The Application of Quantum Simulation to Topological and Open Many-Body Systems

Stuart Flannigan

Quantum Optics and Quantum Many-Body Systems Group

Department of Physics

University of Strathclyde, Glasgow

October 14, 2020

This thesis is the result of the author's original research. It has been composed by the author and has not been previously submitted for examination which has led to the award of a degree.

The copyright of this thesis belongs to the author under the terms of the United Kingdom Copyright Acts as qualified by University of Strathclyde Regulation 3.50. Due acknowledgement must always be made of the use of any material contained in, or derived from, this thesis.

Signed:

Date:

For my mother, father, brother, wife and children

Acknowledgements

When I first sat down to write these acknowledgements I realised just how much my life has changed over the past three years. I became a father (twice), I got married to the mother of my children, my knees began to ache and click when standing up and I supposedly became an expert in a small subfield of theoretical quantum physics. I now feel very old, whether from the physical strain of an intrepid rampaging toddler or through the mental strain of pursuing a doctorate, I am not entirely sure. What I do know is that I would not have been able to cope without the complete support of my wife Becci, whom I'd like to thank first. Secondly, I have to thank my sons Luke and Isaac, who put things into perspective and who cheered me up when my calculations were not working out so well. Thirdly, my father who has always been an incredible role model and now an amazing Grandad. All my family, including my brother, have provided me with invaluable emotional support making me realise that there is more to life than physics.

However, I find (quantum) physics fascinating and incredibly challenging and captivating and so I also want to express my gratitude towards my supervisor, Andrew Daley, for supporting my research and love of the field with his unfailing enthusiasm and incredible knowledge. He has very high standards, which I also want to thank him for because it continually forced me to strive to be better.

I also have to acknowledge the contributions from my fellow PhD students, Liam

Walker, Tom Bintener, Elliott Mansfield, Tomohiro Hashizume, and Mark Carroll and postdocs, François Damanet, Jorge Yago, Rosaria Lena, Gerard Pelegri, Anton Buyskikh and Eduardo Mascarenhas and collaborators, Peter Kirton and Stefan Kuhr for providing incredibly stimulating discussions enabling me to think about interesting physics problems in different ways. Thank you to you all.

Stuart Flannigan, 3rd September 2020

Abstract

Quantum simulation is the notion of experimentally controlling and manipulating physical quantum mechanical resources such that their evolution can be mapped onto a problem that is much harder to solve by any other means. Realising a fully general quantum computer is still a work in progress but we can currently use devices that are purpose built to solve particular classes of problems, so called analogue quantum simulators, to investigate many-body quantum systems.

In this thesis we first consider benchmarking the performance of realistic hardware implementations of quantum simulators through simulations of many-body dynamics, where we are able to demonstrate that even with current levels of experimental errors, analogue simulators in ongoing experiments are able to out-perform the best classical algorithms. We next propose how to use these devices in order to study strongly correlated phases induced by interactions in topological band structures, where we place a strong emphasis on how to experimentally realise, prepare and detect these phases for atoms in a Creutz ladder and in a Lieb lattice. We find that in these systems there is an enhanced tendency for interaction induced pairing, allowing for novel pair superfluid phases to be prepared in experiments with ultracold atoms. Finally, we consider additions to these simulators such that they map more closely to many-body systems in realistic solid state settings by including dissipative mechanisms. Specifically, we demonstrate that we are able to classically simulate this behaviour by modifying and hybridising existing numerical methods to allow for the simulation of open many-body systems beyond the Born-Markov approximation. We benchmark this numerical approach by simulating the dynamics of electrons coupled to a phonon environment, where we find substantial qualitative differences compared to standard open system techniques.

Contents

Part I

Introduction

Chapter 1

Introduction

Many-body quantum mechanical problems are notoriously difficult to solve. This is due to the superposition principle of quantum systems where they can exist in more than one state simultaneously. Thus in order to model these systems we must use a probabilistic approach with complex probability amplitudes resulting in computations that scale exponentially with the size of the system considered.

In order to attempt to solve these problems there have been many methods developed over the past decades to perform classical simulation of specific classes of many-body problems, including restricting the number of variables based on physical arguments, such as tensor network methods [1] or open quantum system approaches [2], or through statistically sampling the Hilbert space with Monte-Carlo approaches [3] or through phase space methods [4]. However, for studying general problems it has become clear that another solution is required, especially for novel out-of-equilibrium situations such as the dynamics of states far from any eigenstate.

An interesting proposal, inspired by an insight from Richard Feynman [5], is to use physical quantum mechanical resources in controlled experimental situations in order to simulate the desired quantum system. This concept, is in principle not

impacted by the scaling issues of a classical simulation as the quantum mechanical bits of information (qubits) naturally encode the correct features needed to describe the quantum states. Additionally, these architectures can collectively work with data that grows exponentially compared to the amount of physical resources utilised. This potentially turns the main barrier in solving quantum mechanical many-body problems into the foundation for an incredibly powerful computational tool, which can in principle be exploited to create a quantum computer.

In the 40 years since this solution was first conceptualised, there has been huge growth in this idea of quantum simulation [6], which has culminated in S. Haroche and D. Wineland being awarded the Nobel prize for their demonstrations of experimentally controlling and manipulating individual quantum mechanical particles [7–10]. This has then lead to proposals and first demonstrations of quantum computation in trapped ions [11], superconducting qubits [12], cold atoms [13] and Rydberg atoms [14], however there are limitations preventing practical universal quantum computers that arise from noise, decoherence and/or heating. These effects are not yet at fundamental levels and so continued development in the field will be able to solve these technological difficulties, while progress on the theoretical side will ensure that these devices are ready to be utilised to their full potential. This has already been illustrated with previous important insights in this area, such as the demonstration that useful classical problems can be mapped to the quantum bits, for instance Shor's factorisation algorithm [15], opening up interest into universal quantum computation [16], and quantum annealing methods [17, 18], to solve complex optimisation problems that are currently relevant to industry

Although a universal quantum computer that has enough physical resources to solve useful problems is still a work in progress, there are many interesting situations that can currently be explored using so called analogue simulation experiments as

a short term alternative to a full digital computation. Analogue simulation is an experimental computation tool that has been purpose built to solve a very specific set of problems, e.g. many interacting particles (both fermions and bosons) in periodic potentials, which for the fermionic case has strong connections to electron dynamics in solids. There are a number of experimental architectures, such as ultracold atoms in optical lattices [19], ion traps [20, 21], cavity QED [22], Rydberg atom arrays [23] and superconducting circuits [24], which can now exhibit precise control over quantum systems that are large enough so that relevant practical calculations can be performed. While all of these platforms are undergoing rapid development, there are still many challenges that need to be overcome in order to apply these systems to larger problems. For the case of cold atoms, the limitation is the ability for single atom addressing and readout and for the others, the main limitation is the ability to scale up the system size.

These experimental simulations have already verified many theoretical predictions and many believe they can already be operated in regimes that go beyond what we can do with a classical simulation. The idea is to use these systems to learn more about the role of noise and dissipation on a many-body system in a controllable setting so that we can either exploit or mitigate these effects to increase the efficiency and scalability of experimental implementations for full universal quantum computation. Over the next decade it is expected that both analogue and digital quantum computation will greatly mature and will be able to demonstrate what the pioneers of quantum simulation first proposed, an unequivocal quantum advantage.

1.1 Overview

In this thesis we demonstrate, by considering a few interesting examples, the power of a quantum simulator and illustrate how it can be used to solve important problems relating to many-body quantum systems. We break this down into three related sub-problems: 1) benchmarking the relative performance of these devices, 2) understanding the microscopic properties of the individual components of a quantum simulator (for example atom-atom and atom-photon interactions) and 3) demonstrating how to realise particular systems and prepare novel many-body states so that their properties can then be studied experimentally.

For problem 1), explicitly demonstrating that a realistic experimental implementation of a quantum simulator can be used to study regimes that are out-with the ability of classical simulation is extremely important as this will demonstrate the sophistication of this growing field, we consider this in Ch. 6. Then in Ch. 7 we focus on problem 2) and demonstrate how knowledge of the microscopic properties of atomic and quantum optical experiments can aid quantum simulation, where we investigate the regime of strong atom-atom interaction and assess the validity of the usual approximations in mapping the behaviour in these experiments to important theoretical models. This analysis will allow future quantum simulation experiments to better define the limitations of these devices as they are applied to solve particular many-body problems. We then consider problem 3), where in Ch. 8 & 9 we consider how to realise and prepare novel systems with topological band structures in cold atom experiments and then in Ch. 10 we consider how to include controlled dissipation in the experimental architectures, such that these systems can more accurately simulate the behaviour in real solid state devices.

Before directly focusing on these problems, we begin by covering the broader

background to this field, where in Ch. 2 we introduce the notion of quantum simulation describing how the properties of quantum mechanics can be exploited for useful applications. We summarise and compare two conceptually different approaches to quantum simulation: digital simulation, which allows for universal quantum computation but where current experimental architectures are limited due to experimental imperfections, and analogue simulation which can be used in the short term to accurately capture the dynamics of a small subset of relevant problems. We describe one particular realisation of analogue simulation, ultracold atoms in an optical lattice which will be the primary focus of the work in this thesis and explain that they can be used to precisely tune and control the parameters of the system. We derive the microscopic scattering properties of interacting atoms where we describe the approximations invoked in mapping these experimental systems into describing seminal models in theoretical physics such as the (Bose-)Hubbard model. Additionally, in Ch. 3 we describe the features of many interacting particles when they are confined to one-dimension where we present a solution for the low energy properties and correlation functions from Luttinger liquid theory.

Then in Ch. 4 we summarise an approach for classically simulating many-body quantum systems, matrix product states. As well as offering many important insights into the fundamental properties of quantum systems, these methods are necessary to develop along side the experimental hardware as they are paramount to being able to benchmark the simulators and ensure confidence in the results. In Ch. 5 we next explain the methods for treating open quantum systems where the system is connected to a much larger environment, which is necessary so that the effects of dissipation or a finite temperature can be included. We summarise the main approximations that are invoked and discuss their validity in quantum optical experiments. We will make use of both of these techniques often throughout the thesis in order to perform

classical simulations of the expected dynamics, which can be used to benchmark and calibrate the experimental resources of the quantum simulator.

We then move on and present the new contributions from this thesis beginning with part II where we focus on benchmarking. First, in Ch. 6 we aim to benchmark quantum simulation generally, where we quantitatively compare the hardware requirements needed to demonstrate a quantum advantage in analogue simulation to universal digital quantum computation for continuous time dynamical simulations. We predict that current experimental architectures for analogue simulation are already able to demonstrate an advantage over state-of-the-art classical algorithms and that the quantum advantage point for digital simulation is within closer reach than many previously expected, for the types of problems considered. This has important implications for the short term development of the field of quantum simulation as a whole. Next in Ch. 7, we consider a more specific example where we present results from our collaboration with an experimental group from the University of Innsbruck. We simulate and understand the microscopic processes behind their observations of atomic losses in terms of three-body recombination effects, which enabled us to better define the regimes in which these loss processes must be considered. This will then allow future experiments to more easily either avoid these regimes or prepare exotic phases that utilise these strong loss features.

We then take a more in depth look into some specific applications for quantum simulation. In part III we consider using the experimental hardware to probe the effects of strong interactions in topological band structures. First in Ch. 8 we analyse the properties of interacting bosonic atoms in a one-dimensional ladder that, due to the geometry, causes a complete suppression of single particle dispersion. We propose an experimental analysis of novel two-body features and many-body phases that are manifested in these systems and we perform proof-of-principle classical simulations

on the ability to prepare these phases experimentally and predict observations of dynamical properties. Next in Ch. 9, we consider a two-dimensional lattice where some of the states have their dispersion suppressed, but others have large kinetic energy. We investigate the interplay of these effects by performing numerical calculations on a one-dimensional ladder strip which preserves the main qualitative features of the full two-dimensional geometry, where we find that the many-body phases for fermions have enhanced cooper pairing perhaps allowing for a realisation of superconductive phases with quantum simulation experiments.

In part IV we describe our incorporation of matrix product state methods into a new promising numerical method for time-evolving open quantum systems in regimes beyond those usually considered. This allows us to simulate the dynamics of open many-body systems well into the non-Markovian and strong coupling regimes. We benchmark this method by applying it to a system of electrons coupled to an environment of dispersive phonons (the dispersive Holstein model) and show that we can capture important distinct features that are out with the range of conventional methods, as well as discussing how this can be realised in cold atom experiments. This work opens up the possibility for future theoretical investigations into the novel effects induced by the combination of many-body features and strong coupling to a non-Markovian environment, and so extends the range of cases that are able to be classically benchmarked.

Finally, in part V we provide a conclusion, discuss the implications of our contributions to the wider field of quantum simulation and discuss possible avenues for future research.

1.2 Contributions during PhD

Publications and preprints connected with this thesis

- M. J. Mark, S. Flannigan, F. Meinert, K. Jag-Lauber, J. P. D'Incao, A. J. Daley and H.-C. Nägerl, *Interplay between coherent and dissipative dynamics of bosonic doublons in an optical lattice*, Phys. Rev. Research 2, 043050 (2020).

  The author of this thesis wrote most of the theoretical and introductory part of the article and performed most of the numerical simulations. This is presented in Ch. 7.

- S. Flannigan and A. J. Daley, *Enhanced repulsively bound atom pairs in topological optical lattice ladders*, Quantum Science and Technology 5, 045017 (2020).

  The author of this thesis performed all of the analytical analysis, numerical simulations, produced all of the figures and wrote most of the article. This publication is presented in Ch. 8.

Other publications

- E. Mascarenhas, F. Damanet, S. Flannigan, L. Tagliacozzo, A. J. Daley, J. Goold, I. de Vega, *Nonreciprocal Quantum Transport at Junctions of Structured Leads*, Phys. Rev. B 99, 245134 (2019).

- L. Madail, S. Flannigan, A. M. Marques, A. J. Daley, and R. G. Dias, *Enhanced localization and protection of topological edge states due to geometric frustration*, Phys. Rev. B 100, 125123 (2019).

- A. Di Carli, C. D. Colquhoun, G. Henderson, S. Flannigan, G. Oppo, A. J. Daley, S. Kuhr, and E. Haller, *Excitation Modes of Bright Matter-Wave Solitons*,

Phys. Rev. Lett. 123, 123602 (2019).

- A. Di Carli, G. Henderson, S. Flannigan, C. D. Colquhoun, M. Mitchell, G. Oppo, A. J. Daley, S. Kuhr, and E. Haller, *Collisionally inhomogeneous Bose-Einstein condensates with a linear interaction gradient*, arXiv:1908.10021 (2020). Accepted in Physical Review Letters.

Papers in preparation

- S. Flannigan, L. Madail, R. G. Dias and A. J. Daley *Hubbard models and state preparation in an optical Lieb lattice*, *In preparation.*

- S. Flannigan, N. Pearson, A. Buyskikh, G.H. Low, I. Bloch, P. Zoller, M. Troyer and A. J. Daley *The practical quantum advantage point for analogue and digital quantum simulators*, *In preparation.*

- S. Flannigan, F. Damanet, R. Lena and A. J. Daley *Non-Markovian state diffusion for open many-body systems*, *In progress.*

Presentations

- Conference presentation, "Topological flat energy bands in an optical lattice", DESOEQ Progress Meeting (Cambrige, UK) 2018

- Poster presentation, "Flat energy bands with quantum simulators", YAO (Glasgow, UK) 2018

- Poster presentation, "Quasi-particles in flat energy bands", SFB-FoQuS International Conference (Innsbruck, Austria) 2019

- Poster presentation, "Quasi-particles in flat energy bands", DESOEQ Progress Meeting (Glasgow, UK) 2019
- Conference presentation, "Pair Superfluidity in bosonic flat band systems", DESOEQ conference (Oxford, UK) 2019
- Poster presentation (virtual), "Achieving a practical quantum advantage in quantum simulation", PQI conference (Pittsburgh, USA) 2020
- Seminar presentation (virtual), "Achieving a practical quantum advantage in quantum simulation", QCS hub seminar (UK) 2020

Chapter 2

Quantum simulators

In this chapter we introduce the ideas behind analogue and digital simulators where we explain that analogue simulation can be used as a short-term alternative to fully universal computation in order to solve important problems related to the dynamics in many-body quantum systems. We describe how to derive, under well-controlled approximations the microscopic many-body models from first principles [25–28]. We emphasise that experiments that aim to investigate the microscopic properties of atom-atom or atom-photon interactions are separate from *quantum simulation*. Of course, detailed knowledge of these mechanisms - which has only been made possible through previous experimental breakthroughs in this area - are paramount for creating a reliable and accurate physical architecture for a quantum simulator which attempt to simulate the properties of a target model or Hamiltonian. The goal of this chapter is to explain the approximations that are required for our quantum optical experimental simulations to give rise to the fundamental many-body Hamiltonians studied in the context of low energy solid state physics.

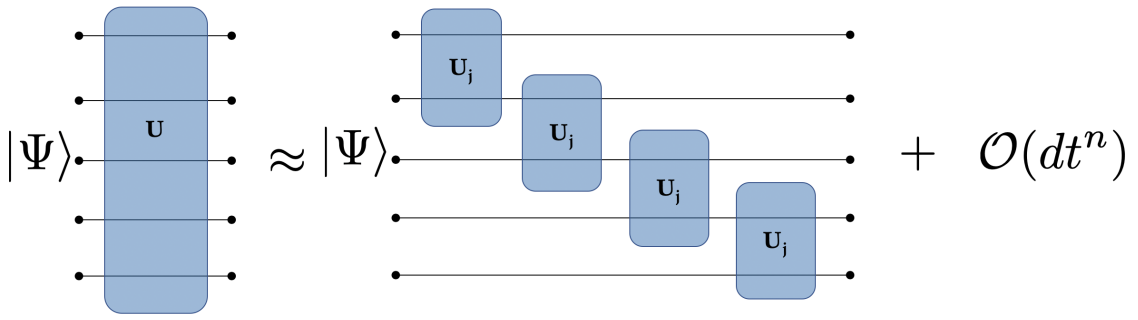

Figure 2.1: Digital Simulation. We can decompose the exact time-evolution operator into a sequence of experimentally feasible two site operations, at the cost of an error that becomes larger with an increasing time-step.

2.1 Analogue and digital simulation

Digital simulation

Experimental advances in quantum optical systems now allow us to create general quantum devices which can be used for a wide range of applications. For example, the ability to trap and localise quantum particles with magnetic or optical fields allows for the manipulation of their internal state through the application of laser pulses. This then gives an experimental realisation of a quantum bit of information, or *qubit*, and offers a way of applying quantum logic gates [21] and then creating sequences of these to perform quantum algorithms which then offers a way of performing universal quantum computation [16]. The great challenge here arises from experimental imperfections which limit the number of gates that can be applied before decoherence effects become important.

More relevant to the context considered here, is that these systems can also be used to simulate the dynamics of many-body quantum systems [29, 30], although at the moment these are limited in system size. Say we want to model the dynamics of

a large many-body quantum system by solving the Schrödinger equation,

$$i\hbar\frac{\partial}{\partial t}|\Psi(t)\rangle = \hat{H}|\Psi(t)\rangle \rightarrow |\Psi(t)\rangle = U(t)|\Psi(0)\rangle, \tag{2.1}$$

where $U(t) = \exp(-i\hat{H}t/\hbar)$ is the unitary time-evolution operator. The concept of digital simulation relies on the ability to discretise this operator through a so called Trotterisation [31], $U(\Delta t) \approx \prod_i U_i$, which naturally comes with an error proportional to the length of the time step, see Fig. 2.1. We must also decompose the discrete time evolution operator into a sequence of the universal quantum gates that the specific architecture can perform which are usually single and two site operations which may come with a further error.

These approaches have been assumed to be non ideal because even with a small error at each time step, this may grow to non-negligible values after many time steps. However, it has been shown recently that for specific circumstances these errors are bounded even for an infinite evolution time [32], which gives these schemes some promise for future applications. We will discuss more the implementations of these features and the accumulated errors when we consider the timescales and hardware requirements necessary to achieve a quantum advantage in Ch. 6.

Analogue simulation

As an alternative to fully universal quantum computation architectures, we can also utilise the control available in quantum optics experiments to create so called analogue quantum simulators. These architectures are highly controllable devices, but do not aim to be fully general purpose quantum computers instead aiming to accurately explore specific questions in many-body dynamics. Example architectures for realising these principles include, ultracold atoms in an optical lattice [19, 33–

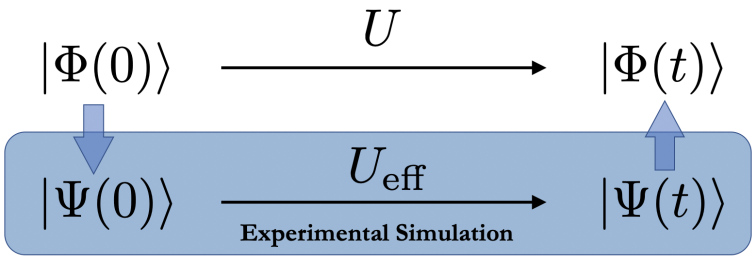

Figure 2.2: Analogue Simulation. The quantum state, $|\Phi(t)\rangle = U|\Phi(0)\rangle$, can be simulated by mapping to a physical experimental system that approximately captures the same effective dynamics, $U_{\text{eff}} \approx U$, and reading out the output by measuring the final state, $|\Psi(t)\rangle$.

36], neutral atoms in optical tweezer arrays [37, 38] or experiments with trapped ions [20, 39, 40].

Most notably, analogue simulation experiments can be used to model the continuous time dynamics of a many-body quantum system and can be used to probe both the equilibrium properties as well as the out-of-equilibrium dynamics induced by various local and global perturbations and/or the application of an applied potential (bias voltage). These principles will allow us to learn more about the role of quantum mechanical interactions in the transport of information through real nano-scale materials and even allow us to incorporate dissipative or driving elements to assess their impact on the performance of quantum electronic devices [41]. See Ch. 10 for an investigation into these effects.

The principle of analogue simulation, see Fig. 2.2, is to create a scale model out of quantum mechanical resources such that the dynamics of the scale model satisfy, $U_{\text{eff}} \approx U$, under well controlled approximations. The quantum state is mapped onto the experimental resources, $|\Phi(0)\rangle \rightarrow |\Psi(0)\rangle$, and the physical system is then allowed to evolve naturally. Finally we map the physical state onto the quantum basis of interest, $|\Psi(t)\rangle \rightarrow |\Phi(t)\rangle$, usually through measurements of the physical resources.

Take for example the case of ultracold atoms confined in an optical lattice. The

quantum system that we want to simulate is usually electrons flowing through a conventional material, where the number of electrons are of the order of Avogadro's number $\sim 6 \times 10^{23}$, and the lattice spacing is of the order of an angstrom 10^{-10} m. We then map this onto an experiment consisting of around 10^6 atoms with a lattice spacing around ~ 0.5 μm. Thus, our quantum simulation can be thought of as a scale model, where in contrast to the usual case in the field of engineering or product design, our model is many orders of magnitude larger. This larger lattice spacing of our scale model gives a number of advantages such as an increased ability to measure the position of individual atoms to within individual lattice sites [42–49].

Comparison

As we can see there are a number of conceptual differences between analogue and digital quantum simulation. The key difference is that realisations for digital simulation are in principle able to perform universal quantum computation, whereas analogue simulators are usually only able to simulate a small class of problems. However, as we will see in Ch. 6, in terms of the current generation of devices, analogue simulators are usually more accurate and usually lead to smaller errors in the problems that they are designed to solve - compared to an equivalent simulation with a digital device. Of course, as the sophistication of the experimental hardware continues to increase realisations of digital simulation will eventually be able to out-perform analogue devices as they will be able to investigate a much wider variety of problems. However, most estimates predict that analogue simulation will be able to lead to useful insights into many important problems in much shorter timescales compared to a digital quantum simulator with many speculating that they are already able to do so (see Ch. 6). For example these analogue devices can already be used to accurately simulate the Hubbard model which has strong connections to solid state

devices and so these experiments have the potential to lead to useful and practical benefits in areas outside of fundamental physics.

2.2 Ultracold atoms in an optical lattice

The experimental achievements in the field of quantum optics have made it possible to engineer optical lattice experiments, where the confined atoms moving through a periodic laser potential play the role of electrons moving through a real material. These systems allow for extreme control over all parameters of this artificial crystal to very high precision [19, 34]. Additionally, due to the sophistication of the experimental architectures, these systems are relatively robust against defects and are extremely well isolated from the environment, thus noise and heating effects play a minimal role on the relevant dynamics of the system, although can be included in a controllable way in order to explore their effects (see Ch. 7 & 10).

The explicit demonstration of the control and versatility of applying these quantum optical principles came with the realisation of the quantum phases transitions between superfluid and Mott insulating phases in bosonic systems [43, 50–53], and then in fermionic systems [54, 55]. Since then, the number of applications of these platforms have gown significantly and they have been used successfully to probe the properties of many-body quantum systems in the presence of disorder [56–60], with driving and dissipation [61], for quenches across a phase transition [62–64], and in novel lattice geometries [65–78].

Motion of an atom in a standing wave potential

If we neglect for the moment the effects of quantum noise, such as spontaneous emission, we can write down the Hamiltonian for a single two-level atom in the

presence of an applied laser,

$$H = \frac{\hat{p}^2}{2m} - \Delta|e\rangle\langle e| - \frac{\Omega(\mathbf{x})}{2}(|g\rangle\langle e| + |e\rangle\langle g|), \tag{2.2}$$

where $\Delta = \omega - \omega_{eg}$ is the detuning of the laser which has a frequency, ω, and the energy spacing ($\hbar = 1$), ω_{eg}, between the ground state, $|g\rangle$ and excited state, $|e\rangle$. The Rabi frequency is defined as $\Omega(\mathbf{x}) = 2\hat{d}_{eg} \cdot \hat{E}(\mathbf{x}, t)$, where $\hat{E}(\mathbf{x}, t)$ is the electric field component of the applied laser field and $\hat{d}_{eg}$ is the dipole matrix element between the two atomic energy levels. For a standing wave potential, $|\hat{E}(\mathbf{x}, t)| = E_0 \cos(\vec{k} \cdot \mathbf{x})$, we can define, $\Omega(\mathbf{x}) \equiv \Omega_0 \cos(\vec{k} \cdot \mathbf{x})$, where $\Omega_0 = 2|\hat{d}_{eg}|E_0$.

Say we have the initial state defined by,

$$|\Psi(\mathbf{x}, t\rangle = \psi_g(\mathbf{x}, t)|g\rangle + \psi_e(\mathbf{x}, t)|e\rangle, \tag{2.3}$$

where $\psi_g(\mathbf{x}, t)$ and $\psi_e(\mathbf{x}, t)$ are complex numbers. We can then solve the Schrödinger equation, which takes the form

$$\begin{aligned} i\frac{\partial\psi_e(\mathbf{x}, t)}{\partial t} &= \left(\frac{\hat{p}^2}{2m} - \Delta\right)\psi_e(\mathbf{x}, t) - \frac{\Omega(\mathbf{x})}{2}\psi_g(\mathbf{x}, t), \\ i\frac{\partial\psi_g(\mathbf{x}, t)}{\partial t} &= \frac{\hat{p}^2}{2m}\psi_g(\mathbf{x}, t) - \frac{\Omega(\mathbf{x})}{2}\psi_e(\mathbf{x}, t). \end{aligned} \tag{2.4}$$

Far detuned case

In the limit of large detuning compared to the system dynamics, such that $\Delta \gg \Omega(\mathbf{x}), \frac{\hat{p}^2}{2m}$, then we can adiabatically eliminate the excited state by setting $\frac{\partial\psi_e(\mathbf{x},t)}{\partial t} \approx 0$. This leads to the new differential equation for the motion of the atom in the ground state,

$$i\frac{\partial\psi_g(\mathbf{x}, t)}{\partial t} = \left(\frac{\hat{p}^2}{2m} + \frac{\Omega_0^2}{4\Delta}\cos^2(\vec{k} \cdot \mathbf{x})\right)\psi_g(\mathbf{x}, t). \tag{2.5}$$

The interpretation of this equation is that an atom in the presence of an applied laser field with a large enough detuning remains effectively in its internal ground state, however the effects of the driving laser are still felt in the form of a potential energy term proportional to the intensity of the applied field. This effective shift of the ground state energy is known as the AC Stark shift. The result is that the atom moves in a periodic potential and so obeys similar dynamics to an electron moving through a real solid state crystal.

Quantum simulation

Simply investigating the dynamics of the atoms confined in this optical potential does not necessarily constitute *quantum simulation*. Of course creating this experiment would allow one to investigate the whether the above approximations are satisfied experimentally and would lead to many insights into the properties of the interactions between atoms and photons and between atoms. However, in order for a similar experiment to be classified as a quantum simulator, we must be able to accurately map an effective Hamiltonian that is responsible for the dynamics of the atoms in this system to that of another model that is perhaps more complex to be realised by another means. For example, as we will see below, it is possible to conduct these optical lattice experiments in particular regimes such that the dynamics of the atoms can be driven by an effective Hamiltonian that is equivalent to the Hubbard model [27]. This is an important theoretical model in the field of condensed matter which describes the (unitary) dynamics of electrons moving in a periodic potential. This means that we can use these quantum optical experiments to perform an experimental simulation of this theoretical model in a variety of parameter regimes allowing us to both better understand the features of the experimental hardware and the behaviour of the target model.

2.3 Effective field theory

Treating interactions in these systems can be a little more complicated as we need to consider many-body field theory. However, we illustrate here that if we assume a low energy limit then the interaction terms can be simplified. In this section we derive the form of this effective Hamiltonian explaining the assumptions and approximations that are used and we explain why they are valid in the experimental systems.

The first assumption that we make is that the atoms are sufficiently dilute so that we only need to take into account two body interaction events. So we can write our field theory Hamiltonian as,

$$\begin{aligned} H = \int d\mathbf{x}\Psi^\dagger(\mathbf{x}) \left(-\frac{\hbar^2}{2m}\nabla^2 + V(\mathbf{x})\right) \Psi(\mathbf{x}) \\ + \frac{1}{2}\int d\mathbf{x}d\mathbf{x}'\Psi^\dagger(\mathbf{x})\Psi^\dagger(\mathbf{x}')\tilde{V}\left(|\mathbf{x}'-\mathbf{x}|\right)\Psi(\mathbf{x}')\Psi(\mathbf{x}), \end{aligned} \tag{2.6}$$

where we have assumed that the two body interaction potential, $\tilde{V}\left(|\mathbf{x}'-\mathbf{x}|\right)$ does not depend on the absolute position, but is simply a function of the relative coordinates. The $\Psi(\mathbf{x})$ are many-body field operators and they satisfy the commutation relation (for fermions this is an anti-commutation relation), $\left[\Psi(\mathbf{x}), \Psi^\dagger(\mathbf{x}')\right] \approx \delta(\mathbf{x}'-\mathbf{x})$. Furthermore we have assumed that we can consider the composite atoms as single (identical) particles, which is valid so long as the scattering wavelengths are sufficiently large so as not to depend on the small scale structure of the atoms. For higher energy scattering processes, or highly dense gases, the composite nature of the atoms will lead to small corrections in the commutation relations.

In a cold atom experiment, this contact interaction is of the Van-der Waals form, $\tilde{V}(r) = -C_6/r^6$, although this does not take into account the behaviour at very small distances, where other effects will come into play such as the repulsion of the

nuclei of the two atoms and so it should be understood that this potential should be modified for short distances such that $\tilde{V}(r) \to +\infty$ as $r \to 0$.

In quantum optical experiments the atoms typically exist at incredibly low energy scales, meaning that their de Broglie wavelengths are large compared to the characteristic length scale of the interaction potential and so the specific microscopic properties are in principle unimportant. It is then possible to replace the form of the interaction with a mathematical expression that is easier to work with but that gives the same scattering behaviour in the low energy limit.

Realistically, the scattering wavefunction for two atoms will have large momentum modes within the range of the interaction potential invalidating a practical perturbation theory. However, due to the diluteness assumption the probability of the atoms being sufficiently close so as to populate these modes is very small* and can be ignored and the most prominent effect of the interactions is to introduce a phase shift in the long range behaviour of this wavefunction. The effects of this phase shift can be completely contained in a single parameter, a_s known as the characteristic scattering length and we can approximate the interaction potential as an infinitely hard sphere with a radius given by this length. This motivates the introduction of an effective Hamiltonian that is mathematically simpler to work with but gives rise to the same low energy scattering behaviour,

$$H = \int d\mathbf{x}\Psi^\dagger(\mathbf{x}) \left(-\frac{\hbar^2}{2m}\nabla^2 + V(\mathbf{x}) \right) \Psi(\mathbf{x}) + \frac{g}{2} \int d\mathbf{x}\Psi^\dagger(\mathbf{x})\Psi^\dagger(\mathbf{x})\Psi(\mathbf{x})\Psi(\mathbf{x}), \quad (2.7)$$

with $g = 4\pi\hbar^2 a_s/2m$. This is an effective field theory where a large momentum cut-off has been introduced, leading to effectively a short distance cut-off over length scales much shorter than this scattering length. We will now justify the simplification

*In a typical ^{87}Rb BEC experiment with a million atoms only around 5 atoms will be close enough to excite these modes [79].

of this interaction term.

Born approximation

At large distances we can write the total wavefunction for two scattering identical particles as a linear superposition of an incoming wave and an outgoing scattered wave,

$$\psi^{(+)}(r) = e^{i\mathbf{k}\cdot\mathbf{r}} + f(k,k')\frac{e^{ikr}}{r}, \tag{2.8}$$

where $\mathbf{r} = |\mathbf{x}' - \mathbf{x}|$ is the relative coordinate of the two particles, $r = |\mathbf{r}|$, $k = |\mathbf{k}|$ and $f(k,k')$ is the scattering amplitude,

$$f(k,k') = -\frac{m}{4\pi\hbar^2}\int d\mathbf{r}' e^{-i\mathbf{k}'\cdot\mathbf{r}'}\tilde{V}(\mathbf{r}')\psi_k^{(+)}(\mathbf{r}'), \tag{2.9}$$

where m is the reduced mass of the two particles and $\mathbf{k}' = \mathbf{r}k/r$. We can then substitute the expression for $\psi^{(+)}(r)$ into the scattering amplitude, which results in an infinite series with increasing numbers of interaction events, this is known as the Born series. However, we can make the Born approximation and only take the first term in this series,

$$f(k,k') \approx -\frac{m}{2\pi\hbar^2}\int d\mathbf{r}' e^{-i(\mathbf{k}'-\mathbf{k})\cdot\mathbf{r}'}\tilde{V}(\mathbf{r}'), \tag{2.10}$$

which is valid for low energy scattering and allows, for certain potentials, for an analytical solution.

Characteristic scattering length

For a completely spherically symmetric scattering potential we can then expand the total wavefunction in terms of angular momentum eigenstates,

$$\psi^{(+)}(r) = \sum_{l=0}^{\infty} \sqrt{\frac{2l+1}{4\pi}} P_l(\cos\theta) \frac{\chi_l(k,r)}{r}, \tag{2.11}$$

where $P_l(\cos\theta)$ are the Legendre polynomials. We can assume that the long range behaviour of the radial wavefunction, $\chi_l(k,r)$, can be expressed as a superposition of forward and backward propagating plane waves,

$$\chi_l(k,r) = A\left((-1)^{l+1}e^{-ikr} + e^{2i\delta_l}e^{ikr}\right), \tag{2.12}$$

where A is a normalisation constant and there is a relative phase in the ingoing and outgoing plane waves based on the parity of l. In this ansatz, we have assumed that at long distances away from the effective range of the scattering potential that we can simply incorporate the scattering effects by a phase shift δ_l. By solving the 1D Schrödinger equation for the radial wavefunction $\chi_l(k,r)$ we can express the scattering amplitude as,

$$f(k,\theta) = \sum_{l=0}^{\infty} (2l+1) \frac{e^{2i\delta_l} - 1}{2ik} P_l(\cos\theta). \tag{2.13}$$

For higher partial wave components, $l > 0$, there is the centrifugal barrier term present in the 1D radial Schrödinger equation $\sim l(l+1)/r^2$ which for sufficiently low scattering energies will dominate the short distance behaviour and these wave components will not even see the interaction potential. We therefore expect that at the energies that cold atom experiments operate (and this has been experimentally

verified [80, 81]) that we can ignore all higher order partial wave components and it is enough simply to consider the $l = 0$ mode, giving,

$$f(k,\theta) \approx f(k) = \frac{e^{2i\delta_0} - 1}{2ik} = \frac{1}{k\cot(\delta_0) - ik}. \tag{2.14}$$

Because we expect that the scattering will be symmetric, we can expand the s-wave phase shift in even powers of k, which by convention (and the reason why will become clear) is done in the following way,

$$k\cot(\delta_0) = -\frac{1}{a_s} + \frac{r_0 k^2}{2} - O(k^4), \tag{2.15}$$

where r_0 is the effective range and a_s is the s-wave scattering length. For an infinitely hard sphere potential such that, $U(r) = 0$ for $r > a$ and $U(r) = \infty$ for $r < a$ gives for the s-wave scattering, $a_s = a$ and for the effective range of the potential, $r_0 = 2a/3$.

In the limit that $kr_0 \ll 1$, we can write the scattering amplitude as,

$$f(k) = -\frac{a_s}{1 + ika_s}. \tag{2.16}$$

And from the relation, $k\cot(\delta_0) \approx -1/a_s$, we can see that a diverging scattering length corresponds to the phase shift approaching $\pm\pi/2$.

Thus it is clear that the low energy description of two-body scattering processes can be completely described by a single parameter, the scattering length a_s. At the very least then, any simplification of the scattering potential must reproduce the low energy description with the same scattering length.

Zero-range pseudopotential

The simplification of the interaction term in the many-body Hamiltonian is through the introduction of a pseudopotential. The simplest form for this is the zero-range pseudopotential [82],

$$\tilde{V}(\mathbf{r}) \to g\delta(\mathbf{r}) \left[\frac{\partial}{\partial r}\left(r\psi(\mathbf{r})\right)\right]_{r=0} \equiv g\delta(\mathbf{r})C[\psi(\mathbf{r})], \tag{2.17}$$

where $g = 4\pi\hbar^2 a_s/m$. Note that this is the simplest possible form with only one free parameter, a_s.

We can see that this gives rise to the same scattering amplitude as before by writing,

$$\begin{aligned} f(k,k') &= -\frac{m}{4\pi\hbar^2}\int d\mathbf{r}' e^{-i\mathbf{k}'\cdot\mathbf{r}'}\tilde{V}(\mathbf{r}')\psi_k^{(+)}(\mathbf{r}') \\ &= -a_s C[\psi^{(+)}(\mathbf{r})]. \end{aligned} \tag{2.18}$$

From which we see that,

$$\psi^{(+)}(r) = e^{i\mathbf{k}\cdot\mathbf{r}} - a_s C[\psi^{(+)}(\mathbf{r})]\frac{e^{ikr}}{r}, \tag{2.19}$$

and allows us to express,

$$\begin{aligned} C[\psi^{(+)}(\mathbf{r})] &= \left[\frac{\partial}{\partial r}\left(r\psi^{(+)}(\mathbf{r})\right)\right]_{r=0} \\ &= \left[\frac{\partial}{\partial r}\left(re^{i\mathbf{k}\cdot\mathbf{r}} - a_s C[\psi^{(+)}(\mathbf{r})]e^{ikr}\right)\right]_{r=0} \\ &= 1 - ika_s C[\psi^{(+)}(\mathbf{r})] \\ &= \frac{1}{1+ika_s}, \end{aligned} \tag{2.20}$$

which gives for the scattering amplitude,

$$f(k) = -\frac{a_s}{1 + ika_s}. \tag{2.21}$$

This is exactly the same expression that we had in Eq. 2.16, thus we have illustrated that the peudopotential gives the same scattering results as the low energy limit for any spherical interaction potential. This is valid as long as $kr_0 \ll 1$, which does not require that the scattering length is small, meaning that this pseudopotential can be used to analyse cold gases in the region of a Feshbach resonance (see below) and diverging a_s. For a typical cold atom experiment with Caesium atoms, the effective range of the Van der Waals interaction is $r_0 \sim 6 \times 10^{-10}$ m [83] and the scattering length can be tuned around $a_s \sim 0 \to 100\ r_0$. This means that the regularisation of the delta function is then a valid approximation for temperatures $T \ll 200$ mK[†], and as typical optical lattice experiments operate in the nano-Kelvin regime this is usually well satisfied.

However, in the limit of small scattering length such that $ka_s \ll 1$, this leads to the approximation that $C[\psi^{(+)}(\mathbf{r})] \approx 1$, which then allows us to write our pseudopotential simply as a delta function. Our interaction Hamiltonian then becomes,

$$\frac{1}{2}\int d\mathbf{x}d\mathbf{x}'\Psi^\dagger(\mathbf{x})\Psi^\dagger(\mathbf{x}')\tilde{V}(|\mathbf{x}' - \mathbf{x}|)\Psi(\mathbf{x}')\Psi(\mathbf{x}) \approx \frac{g}{2}\int d\mathbf{x}\Psi^\dagger(\mathbf{x})\Psi^\dagger(\mathbf{x})\Psi(\mathbf{x})\Psi(\mathbf{x}). \tag{2.22}$$

It is clear then, that for larger values of k that the full regularisation of the delta

[†]The range of temperatures, T, is calculated by,

$$kr_0 \ll 1 \Rightarrow k \ll \frac{1}{r_0} \Rightarrow E \ll \frac{\hbar^2 2\pi^2}{mr_0^2} \Rightarrow T \ll \frac{\hbar^2 2\pi^2}{mr_0^2 k_b},$$

where m is the mass of the atom and k_b is Boltzmann's constant.

function will need to be retained in order to accurately describe the physics. But we can use this effective field theory Hamiltonian for low energy descriptions with the knowledge that we have effectively introduced a cut-off of higher energy modes. For a description of the two-body physics in the strongly interacting regime that properly takes into account this regularisation see Ref. [84, 85] for two atoms confined in a harmonic trap and Ref. [86] for two atoms confined in a lattice.

Feshbach resonance

We can also continuously vary the effective interaction strengths between atoms through the application of an applied magnetic field [87, 88], thus allowing us to realise a wide variety of effective Hamiltonians. For low scattering energies, the interaction strength can be parameterised by a single value, known as the characteristic scattering length, a_s, see Eq. 2.22. Varying an applied magnetic field varies the separation of internal energy states of the atoms, which then modifies the effective coupling of these states through the interactions, thus varying the strength of the effective interaction strength [79]. There are particular values for the magnetic field strength where the effective scattering length is zero, and there are also regions where it diverges, this is known as a Feshbach resonance. See Fig. 2.3 for a plot illustrating the typical features of such a resonance. Near the resonance, we can approximate the scattering length dependence on the strength of the applied magnetic field, B, through the expression,

$$a_s(B) = a_{s,0}\left(1 - \frac{\Delta B}{B - B_{res}}\right), \tag{2.23}$$

where $a_{s,0}$ is the background scattering length, B_{res} is the value at which the resonance occurs and ΔB is referred to as the width of the resonance. These parame-

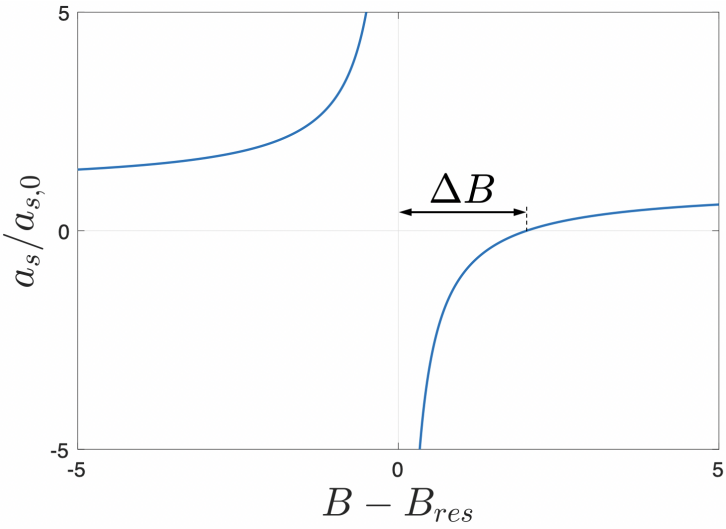

Figure 2.3: Typical features of a Feshbach resonance in arbitrary units.

ters can be calculated by taking into account effective coupling to molecular bound states [89] and have shown to have good agreement to experiments [90]. These Feshbach resonances allow for the realisation of extremely novel phases of matter, for instance they allow for the instantaneous shift from strong repulsive interactions ($a_s \to +\infty$) to strong attractive interactions ($a_s \to -\infty$) by only a relatively small change in the applied field, giving rise to some interesting meta-stable phases [91].

2.4 The Bose-Hubbard model

We can further simplify the above low energy effective field theory by expanding the many-body field theory operators, $\Psi(\mathbf{x})$, in terms of the single particle local Wannier function basis associated with the periodic potential [92], such that $\Psi(\mathbf{x}) = \sum_n w_n^\alpha(\mathbf{x})\hat{b}_n^\alpha$, where $\hat{b}_n^\alpha$ is the annihilation operator for an atom in energy band α at

site $\vec{R}_n$. For a simple periodic potential these Wannier functions are given by

$$w_n^\alpha(\mathbf{x}) = \frac{1}{2\pi}\int dk \phi_k^\alpha(\mathbf{x}) e^{-i\vec{k}\cdot\vec{R}_n}, \tag{2.24}$$

which are centred at site $\vec{R}_n$ and where $\phi_k^\alpha(\mathbf{x})$ are the Bloch functions of the energy band α. Then we can write our many-body Hamiltonian in Eq. 2.7 as a discrete lattice model,

$$H = -\sum_{i,j} J_{i,j}^{n,m}\left(\hat{b}_i^{n\dagger}\hat{b}_j^m + \hat{b}_j^{m\dagger}\hat{b}_i^n\right) + \frac{1}{2}\sum_{i,j,k,l} U_{i,j,k,l}^{n,m,o,p}\hat{b}_i^{n\dagger}\hat{b}_j^{m\dagger}\hat{b}_k^o\hat{b}_l^p, \tag{2.25}$$

where $U_{i,j,k,l}^{n,m,o,p}$ and $J_{i,j}^{n,m}$ are the interaction and hopping parameters respectively,

$$\begin{aligned} U_{i,j,k,l}^{n,m,o,p} &= g\int dr w_i^{n^*}(\vec{r}) w_j^{m^*}(\vec{r}) w_k^o(\vec{r}) w_l^p(\vec{r}), \\ J_{i,j}^{n,m} &= -\int dr w_i^{n^*}(\vec{r})\left(-\frac{\hbar^2}{2m}\nabla^2 + V(\vec{r})\right) w_j^m(\vec{r}). \end{aligned} \tag{2.26}$$

If the lattice potential is sufficiently strong and the interaction strength sufficiently weak then we can approximate the dynamics as being completely confined to the lowest Bloch band, which drastically simplifies the above model. Also note that the Wannier function basis is not unique and by choosing different phase factors in the Bloch functions we can have multiple sets of Wannier functions with different properties, but when these phase factors are chosen so as to be as smoothly varying as possible around the Brillouin zone, this produces unique real Wannier functions that are exponentially localised around each site, $\vec{R}_j$ [92]. The choice of Wannier basis does not change the tunnelling coefficients, $J_{i,j}$ (if no mixing between bands is taken into account, see Ch. 9 for this more general case) but may significantly alter the interaction elements, $U_{i,j,k,l}$. However, as this is simply a basis transfor-

mation, the resulting dynamics and physically observable properties do not change, which can be understood from realising that the local basis corresponding to the Hamiltonian is also altered by using a different Wannier basis. So for a sufficiently localised Wannier basis we can ignore longer ranged interaction terms leading to the Bose-Hubbard model,

$$H = -J \sum_j \left(\hat{b}_j^\dagger \hat{b}_{j+1} + \hat{b}_{j+1}^\dagger \hat{b}_j \right) + \frac{U}{2} \sum_j \hat{b}_j^\dagger \hat{b}_j^\dagger \hat{b}_j \hat{b}_j. \tag{2.27}$$

This has the advantage that all interactions are onsite and that the basis of the Hamiltonian consists of elements that are centred and exponentially localised on each site, which is physically intuitive and convenient to work with.

Many-body features

The Bose-Hubbard model is deceptively simple but has rich physics that are still not completely understood beyond homogeneous equilibrium situations. There is a non-trivial interplay between the kinetic energy term and the quantum mechanical interaction term, which can drastically alter the behaviour of the bosonic gas. For small U, the system has superfluid properties and behaves as a BEC on a lattice, with long range order and linear excitations. But for very large and positive interaction strength the particles become strongly localised and a Mott insulating state is realised, where (for commensurate densities) each particle is localised on a single site and it becomes unfavourable for particles to tunnel to neighbouring sites as this would incur a huge interaction energy. For moderate U the situation is more complicated as the effects of these terms are on more of an equal level and lead to non-trivial features. In 1D the equilibrium properties of this model can be solved numerically to machine precision with matrix product state techniques [93] (see Ch. 4), where

it has been found that the transition between superfluid to insulating behaviour in this model is not continuous as the ratio U/J is varied but has a well defined transition point. At zero temperature this is a quantum phase transition, characterised by a diverging correlation length and a closing of the energy gap in the spectrum [94, 95]. These phases have been experimentally realised both for bosons [43, 50–53] and also for the metal to insulator transition for fermions [54, 55]. Note that the out-of-equilibrium dynamics of this model, with or without the inclusion of dissipative processes or including multi-species, is still a very active area of research [96] (see Ch. 6).

In part III we will investigate the equilibrium and dynamical properties of this model in novel ladder geometries which then modifies the single particle kinetic energy terms and brings with it a more complex interplay between the conventional dynamics and the interactions resulting in novel many-body phases and behaviour.

Controllability

The main advantage of these experimental systems comes in the amount of control that can be placed over the parameters of the system [25, 27, 28, 33]. For example, by varying the intensity of the applied laser controlling the optical potential, we can vary the ratio of the kinetic energy terms to the terms describing interactions and in this way engineer situations where either one type of process dominates the other or where they affect the dynamics equally. Additionally, through the influence of a magnetic field on the internal energy states of the atoms, we can tune the characteristic scattering length (see above) describing the low energy scattering properties allowing for a further tuning of this ratio, and even allowing us to realise either attractive or repulsive effective interactions. These parameters can even be varied time-dependently in a controllable way throughout an experimental sequence, for

example typical timescales for the dynamics of the atoms in an optical lattice are on the order of $J \sim 100 - 1000$ Hz and the parameters of the Hamiltonian can be varied on $>$ 10 kHz timescales [33, 62], allowing for an effective instantaneous quench of the lattice parameters. This then allows these experiments to probe novel highly out-of-equilibrium dynamical features.

Additionally, it is also possible to vary the lattice parameters on timescales much longer than those for the dynamics, allowing for procedures which result in the preparation of strongly correlated eigenstates of a Hamiltonian through adiabatic state preparation. The adiabatic theorem is at the heart of preparing non-trivial many-body ground states in optical lattice experiments, made possible only by the incredible ability to fine tune the experimental lattice parameters. The principle is that if we change the parameters of the Hamiltonian sufficiently slowly, then the physical properties will adjust so that the state is a continuous eigenstate of the time-dependent Hamiltonian. We can explicitly derive a condition for this adiabatic ramp by expanding our state into a superposition of eigenstates of the Hamiltonian at time t,

$$|\Psi(t)\rangle = \sum_n c_n(t)|\phi_n(t)\rangle. \tag{2.28}$$

Substituting this into the Schrödinger equation we obtain the expression for the dynamics of the coefficients, $c_n(t)$,

$$\begin{aligned} i\hbar\frac{\partial}{\partial t}c_n(t) = &\left(E_n(t) - \langle\phi_n(t)|i\hbar\frac{\partial}{\partial t}|\phi_n(t)\rangle\right)c_n(t) \\ &- \sum_{m\neq n}\frac{\langle\phi_n(t)|\frac{\partial}{\partial t}H(t)|\phi_m(t)\rangle}{E_m(t) - E_n(t)}c_m(t). \end{aligned} \tag{2.29}$$

We can see that to avoid mixing between the n^{th} and m^{th} eigenstate that the second term on the right hand side should be zero. We can thus write the condition, such

that there is no time-dependent mixing between eigenstates so that the adiabatic theorem is satisfied as,

$$|\langle\phi_n(t)|\frac{\partial}{\partial t}H(t)|\phi_m(t)\rangle| \ll |E_m(t) - E_n(t)|, \tag{2.30}$$

which indicates that the Hamiltonian should be varied on timescales much longer than the separation of the energy states.

In this way, and by choosing the appropriate initial and final Hamiltonian, we can begin in a state that can be prepared experimentally, such as a product state with an exact number of particles on each site, and produce a non-trivial highly entangled many-body state [97–99]. These features are important for realising many of the proposed physics presented in this thesis (see Ch. 8 & 9).

However, for many interesting situations the ground state of many-body systems are not separated in energy from the excited states in the thermodynamic limit, i.e gapless excitations. In these cases, the condition for adiabaticity in Eq. 2.30 can never be satisfied. Although, in practice realising these phases with a finite lattice size opens up small energy gaps in the spectrum and so makes it in principle possible to prepare these states on timescales proportional to the inverse of this gap. This comes with the caveat that not performing the adiabatic ramps *slow enough* leads to significant errors in the overall state fidelities and many important observables [100, 101]. We will see this explicitly in Ch. 8 & 9 where we observe a reduction in the correlation length in the prepared state compared to the target ground state for ramp times that are too short.

2.5 Summary

Here we have summarised the description of ultracold atoms in optical lattices which is a platform for analogue quantum simulation and will be a heavy focus for realising the physics presented in this thesis. We have explained the well controlled approximations that are valid in these experiments such that they can be used to simulate the behaviour of seminal models in theoretical physics, for example the (Bose-)Hubbard model. In Ch. 6 & 7 we will present benchmarking simulations of these types of quantum simulators, where we directly assess the relative performance in capturing dynamical properties compared to state-of-the-art classical algorithms and then quantitatively analyse the effects of atomic losses.

In this chapter we also illustrated that through precise tuning of the experimental parameters over long or short timescales (compared to the atom dynamics) that novel equilibrium states or highly out-of-equilibrium scenarios respectively can be engineered and probed. We will make use of these features to propose how to experimentally investigate the equilibrium and dynamical behaviour of strongly interacting ladder systems in Ch. 8 & 9 and the dynamics in the presence of strong dissipative mechanisms in Ch. 10.

Chapter 3

One-dimensional quantum systems

In the previous chapter we derived a simplified effective field-operator Hamiltonian for many interacting ultracold atoms, illustrating the controlled approximations that are valid in these experiments making it possible to derive Hubbard type models in the limit of a strong lattice confinement. In this chapter we describe how to more generally analyse the equilibrium and dynamical properties of the effective field theory in one-dimensional systems. As this thesis predominantly focuses on the properties of 1D lattices, understanding the theoretical and analytical results for the general situation in 1D is important, so that we are able to better understand the novel features that are manifested when we consider more specialised situations.

In some cases, restricting the dynamics to one dimension, which results in peculiar features where both bosonic and fermionic systems (in certain limits) share universal behaviour, offers the ability to analytically calculate many important correlation functions by mapping to the so-called Luttinger liquid model [102–105]. However, including additional features into the Luttinger liquid theory, such as inter-spin interactions or a lattice confinement - which are features that we will analyse in this thesis - complicates this simple theory. So in this chapter we summarise some important

known results which we will refer back to often throughout the thesis, in particular in part III when we consider many-body ladder systems with novel coupling terms between each leg.

3.1 The Tomonaga-Luttinger liquid

The problem of interacting quantum particles in a one-dimensional system is not only an interesting theoretical question, but is now becoming increasingly more and more relevant to experimental physics. Using cold atom systems we can now tightly confine atoms in asymmetric traps, such that there is a huge energy cost for exciting particles in the radial directions, producing an effective 1D geometry [106–109]. These experimental capabilities allows us to confirm many novel physical predictions and to now begin to probe exotic regimes that are outwith the grasp of current theoretical or numerical techniques - as we will illustrate in Ch. 6. However, understanding the behaviour of approximate models will allow us to help to benchmark these experimental platforms which throughout this thesis we aim to do through a combination of numerical approaches and the analytical results presented in this (and the previous) chapter.

Features of 1D

In one-dimension, interactions have drastic effects that cannot be captured by a simple effective (perturbative) free quasi-particle theory. This is easy to see by considering that when a particle tries to propagate in 1D it necessarily pushes on its nearest neighbours and the effects of these interactions cannot be mitigated by the particles moving around one another. Thus, excitations in a 1D interacting gas of atoms must behave in a very collective way and the system can have drastically

different properties even for weak interactions. We can compare this to higher dimensions where the effects of interactions can be added perturbatively into most low energy descriptions, see Landau's Fermi liquid theory for example [110].

Furthermore, in higher dimensional systems when creating an excitation with some energy there is an uncertainty to its momentum components because only the magnitude effects the energy, i.e. there are a variety of different momentum vectors that can lead to the same excitation energy. In 1D, this is not the case because the direction of the momentum vectors are extremely limited - they can either be *left* moving or *right* moving. However, for excitations around the Fermi-energy with momentum k_F, processes which transform a right mover into a left mover (or vice-versa) require a large change in momentum, $2k_F$, and so are unlikely, meaning that the low energy particle-hole excitations have *both* a well defined energy and momentum. This meets the minimal requirements for being a well-defined quasi-particle which because they are formed of both a particle and a hole, necessarily have integer spin. Hence the fundamental excitation in 1D is bosonic because they consist of the simultaneous destruction and creation of a fermionic excitation. This observation forms the heart of Luttinger liquid theory and is the key to solving the one-dimensional problem [102–105].

Bosonisation

If we only consider low energy excitations around the Fermi surface, k_F, then we can approximate the excitations with a linear dispersion, $E(k) \approx v_F(k - k_F)$. The difficulty now comes in treating the interaction terms which we cannot straightforwardly diagonalise. However, it has been shown that we can transform to a basis consisting of two bosonic fields which results in a quadratic Hamiltonian of the same form as the non-interacting system [104], and so allows us to treat the interactions

exactly (in the low energy effective field theory) and we find that the excitation spectrum remains qualitatively the same, but with a rescaled velocity. This is the technique referred to as bosonisation, and we sketch out how to transform to this basis [111–113].

We begin with the 1D effective many-body Hamiltonian for free spinless fermions,

$$H = \int dx \psi^\dagger(x) \left(-\frac{1}{2}\nabla^2 \right) \psi(x) + \frac{g}{2} \int dx \psi^\dagger(x)\psi^\dagger(x)\psi(x)\psi(x), \tag{3.1}$$

where $\hbar = m = 1$. This model can be derived by invoking similar approximations as for the bosonic version (see Eq. 2.7) where a higher energy cut-off has been introduced which allows us to regularise the contact interaction. As these are fermionic fields, they satisfy the anti-commutation relations, $\{\psi(x), \psi^\dagger(x')\} \approx \delta(x - x')$. We then decompose our single particle field operators into right movers and left movers,

$$\psi(x) = \psi_L(x) + \psi_R(x). \tag{3.2}$$

Then we define the following two bosonic fields,

$$\begin{aligned} \nabla\phi(x) &= -\pi \left[\psi_R^\dagger(x)\psi_R(x) + \psi_L^\dagger(x)\psi_L(x) \right], \\ \nabla\theta(x) &= \pi \left[\psi_R^\dagger(x)\psi_R(x) - \psi_L^\dagger(x)\psi_L(x) \right], \end{aligned} \tag{3.3}$$

which physically correspond to the density and current fluctuations in the system respectively, and allow us to write the Hamiltonian for non-interacting fermions ($g = 0$) as,

$$H = \frac{v_F}{2\pi} \int dx \left[(\pi\Pi(x))^2 + (\nabla\phi(x))^2 \right]. \tag{3.4}$$

Here the bosonic field $\phi(x)$, and its conjugate momentum density, $\pi\Pi(x) = \nabla\theta(x)$, satisfy the commutation relation, $[\Pi(x), \phi(x')] = i\delta(x - x')$, and v_F is the Fermi

velocity. Note that these fields, $\phi(x)$ & $\theta(x)$, are dimensionless which can be seen from Eq. 3.3 as $\nabla\phi(x)$ & $\nabla\theta(x)$ have dimensions of 1/Length.

This basis transformation may seem strange at first, but it also allows us to write the interaction terms (for spinless fermions),

$$\begin{aligned}\frac{g_4}{2}\left[\psi_R^\dagger(x)\psi_R(x)\psi_R^\dagger(x)\psi_R(x)+\psi_L^\dagger(x)\psi_L(x)\ \psi_L^\dagger(x)\psi_L(x)\right] \\ = \frac{g_4}{4\pi^2}\left[(\nabla\phi(x))^2+(\pi\Pi(x))^2\right],\end{aligned} \tag{3.5}$$

$$g_2\psi_R^\dagger(x)\psi_R(x)\psi_L^\dagger(x)\psi_L(x) = \frac{g_2}{4\pi^2}\left[(\nabla\phi(x))^2-(\pi\Pi(x))^2\right],$$

where we have allowed for the possibility that there are different interaction strengths, g_4, g_2 for the different processes. Here we have ignored the possibility for a left mover to be transformed into a right mover (and vice versa) because this would require a large change in momentum, $\pm 2k_F$, as we have restricted ourselves to excitations around the Fermi-level.

These transformations allow us to write the many-body Hamiltonian as,

$$H = \frac{u}{2\pi}\int dx\left[K(\pi\Pi(x))^2+\frac{1}{K}(\nabla\phi(x))^2\right], \tag{3.6}$$

where we have introduced the rescaled characteristic velocity of the excitations, u and the dimensionless Luttinger liquid parameter, K, which are defined through,

$$\begin{aligned}uK &= v_F\left(1+\frac{g_4}{2\pi v_F}-\frac{g_2}{2\pi v_F}\right), \\ \frac{u}{K} &= v_F\left(1+\frac{g_4}{2\pi v_F}+\frac{g_2}{2\pi v_F}\right).\end{aligned} \tag{3.7}$$

We can see then, that in this bosonized basis, that the form of the Hamiltonian

remains the same with the inclusion of two-body contact interactions. We can see that the effects, are to rescale the characteristic velocity of the low energy linear excitations, u, and also to introduce the so called Luttinger liquid parameter, K, which rescales the relative weighting between the current and density fluctuations.

In order to realise particular values of K we need to start with different initial interaction strengths in the underlying fermion basis. For $K < 1$ the system is dominated by charge density wave fluctuations and corresponds to repulsively interacting fermions, whereas for $K > 1$ the system is dominated by superconducting fluctuations and is realised for attractive interactions. Note that $K = 1$ corresponds to free non-interacting fermions, which can be seen because the Luttinger liquid Hamiltonian in equation 3.6 reduces to the non-interacting case of equation 3.4.

Here we have presented a simple derivation of the Luttinger liquid Hamiltonian which approximates a linear dispersion relation around the Fermi level, however, it is possible to derive this in a much more rigorous way, where it has been shown that it is a valid description of the low energy properties of any massless* one-dimensional system [105], which brings in small corrections to the expressions for the correlation functions that we will present below. In this more general case however, it is not possible to straightforwardly calculate the parameters of this model, u and K, and one must usually resort to finding them through a numerical calculation.

It should also be clear that this Hamiltonian is quadratic, and can thus be diagonalised exactly, and so all low energy properties of Luttinger liquids are completely known once the two parameters, u and K, are obtained. However, we will see below that including additional terms in the model, such as a spin component or a lattice potential, incorporates correction terms making the model no longer quadratic and so not as amenable to finding simple solutions.

*i.e any Hamiltonian that has a gapless linear excitation spectrum.

3.2 Physical consequences

We now summarise some important physical quantities that can be predicted from solving the Hamiltonian in Eq. 3.6, and show that these can be expressed in terms of the Luttinger liquid parameters. We have already stated that the excitation spectrum above the ground state is known, and is directly related to the parameter, u,

$$E_k = u|k|. \tag{3.8}$$

Many thermodynamic properties are also known [102, 114], such as the specific heat,

$$C_V = \frac{TL\pi}{3u}, \tag{3.9}$$

where L is the length of the system, and the compressibility,

$$\kappa = \frac{K}{u\pi}. \tag{3.10}$$

But perhaps more interesting is that the long range correlations can be analytically calculated, giving insights into the quantum features of general one-dimensional systems. To calculate these, we first write the fermionic field operator for the density in terms of the bosonic fields [102],

$$\begin{aligned}\rho(x) &= \psi_L^\dagger(x)\psi_L(x) + \psi_R^\dagger(x)\psi_R(x) + \psi_L^\dagger(x)\psi_R(x) + \psi_R^\dagger(x)\psi_L(x) \\ &= \frac{1}{\pi}\nabla\phi(x) + \frac{1}{2\pi\xi}\left(e^{i2k_Fx}e^{-i2\phi(x)} + e^{-i2k_Fx}e^{i2\phi(x)}\right),\end{aligned} \tag{3.11}$$

where ξ is a short distance cut-off parameter, which is introduced by limiting the effective field theory to low energies similar to the case studied in the previous chapter. In the above equation this means that the coupling between left movers and right

movers only occurs for higher energies when the cut-off, ξ, is small. It should be understood that in all cases where this cut-off appears throughout the chapter that the limit $\xi \to 0$ should be taken, however in certain physical situations, this cut-off could be the lattice spacing, or the effective range of the interactions for example.

We must also use the expressions for the correlations of bosonic fields [102],

$$\begin{aligned} \langle [\phi(x) - \phi(0)]^2 \rangle &= \frac{K}{2} \log \left(\frac{x^2 + (iu|\tau| + \xi)^2}{\xi^2} \right), \\ \langle [\theta(x) - \theta(0)]^2 \rangle &= \frac{1}{2K} \log \left(\frac{x^2 + (iu|\tau| + \xi)^2}{\xi^2} \right), \\ \langle \phi(x)\theta(0) \rangle &= -\frac{i}{2} \arctan \left(\frac{x}{iu\tau + \xi} \right), \end{aligned} \tag{3.12}$$

which as the Hamiltonian is quadratic can be easily derived using the path integral representation, see Ref. [102] for details.

We can then calculate the density-density correlations as a function of space, x and time, τ [102, 111],

$$\langle \rho(x,\tau)\rho(0) \rangle = -\frac{K}{2\pi^2} \frac{u^2\tau^2 + x^2}{\left(x^2 - u^2\tau^2\right)^2} + \frac{2}{(2\pi\xi)^2} \cos(2k_F x) \left(\frac{\xi}{\sqrt{x^2 - u^2\tau^2}} \right)^{2K}. \tag{3.13}$$

It appears then for any physical value for the Luttinger liquid parameter, $K > 0$, that the (zero temperature) correlations decay algebraically. This is a general property of one-dimensional systems [102] and means that it is not possible to achieve phases with real long-range order where the correlations can asymptotically approach a non-zero constant value like the case for Bose-Einstein condensates or superconductivity in three-dimensions. At best in 1D we can achieve only *quasi-long-range* order where the correlations decay algebraically due to the effects of quantum fluctuations, further validating the argument in the beginning of this chapter that interactions in 1D

always play an important role.

We see similar behaviour in other types of correlation functions. In order to derive these we must use another element of the bosonisation toolkit and write the field operators as [102],

$$\psi_r(x) = \frac{U_r}{\sqrt{2\pi\xi}} e^{irk_F x} e^{-i(r\phi(x)-\theta(x))}, \tag{3.14}$$

where $r = L, R$ and U_r is an operator which creates a fermion and commutes with the bosonic fields. Its role is to ensure an exact mapping between the original fermionic basis and the new basis in terms of the bosonic fields, and leads to small corrections in some cases. However, it does not contribute to the correlation functions [102].

We can then calculate the pairing correlations, $O_{SU}(x) = \psi_L(x)\psi_L(x+\xi) + \psi_R(x)\psi_R(x+\xi) + \psi_L(x)\psi_R(x+\xi) + \psi_R(x)\psi_L(x+\xi)$ [102, 111],

$$\langle O^\dagger_{SU}(x,\tau) O_{SU}(0)\rangle = \frac{1}{(\pi\xi)^2}\left(\frac{\xi}{\sqrt{x^2-u^2\tau^2}}\right)^{\frac{1}{2K}}. \tag{3.15}$$

Comparing this to the density-density correlations (Eq. 3.13) we can see that as we increase $K \to \infty$, which corresponds to strong attractive interactions, the density correlations decay faster (in space and time) whereas the pair correlations decay slower. This indicates that for greater attractive interactions that the system manifests more superconductive like pair fluctuations but less charge fluctuations. Contrast this to strong repulsive interactions, $K < 1$, the pair fluctuations are suppressed and the charge fluctuations are enhanced.

Comparing these two correlations to the single particle Greens function [102, 111, 115, 116],

$$\langle \psi_R(x,\tau)\psi_R^\dagger(0)\rangle = \frac{e^{i2k_F x}}{2\pi\xi}\left(\frac{\xi}{\sqrt{x^2-u^2\tau^2}}\right)^{\frac{K+K^{-1}}{2}} \exp\left(\frac{i}{2}\arctan\left(\frac{x}{iu\tau+\xi}\right)\right), \quad (3.16)$$

we see qualitatively different behaviour. Away from $K = 1$, which is the case of non-interacting fermions, the decay of these single particle correlations is increased, indicating that single particle fluctuations in interacting one-dimensional systems are unfavourable.

3.3 Incorporating additional features

The bare Luttinger liquid theory is elegant in its simplicity resulting in a quadratic Hamiltonian which can therefore be used to analytically calculate the form of many important observables. However, including additional features in order to more closely match physical situations results in the appearance of more complicated terms, which are not so straight forward to treat. These additions are particularly relevant when we come to investigate spinful Fermions in Ch. 6, 9 & 10 and bosonic ladder systems in Ch. 8. However in some cases, as we will present here, the effects of these are to simply include corrections to the Luttinger liquid parameters that appear in the expressions for the observables, and so progress can be made by either treating them on a weak perturbative level, applying a renormalisation group analysis or by extracting the parameters from a numerical calculation. The latter can be achieved either by utilising the Bethe ansatz [117] or applying matrix product state techniques - see Ch. 4 for a discussion of these methods and Ch. 8 for a demonstration on how to map the results to the Luttinger liquid theory.

In this section, we summarise the differences to the bare Luttinger liquid theory upon including a spin component in the fermion picture, applying a weak lattice

confinement and when confining bosons to 1D.

Spin

In order to analyse more realistic physical situations in the solid state, as will be considered in Ch. 6 & 10, it becomes necessary to include in the bosonisation analysis both spin components and interactions between them. For spinful fermions we can also perform a similar bosonisation scheme [102, 114, 118], but we now have two degrees of freedom, one for the total charge and one for the total spin,

$$\begin{aligned} \rho(x) &= \frac{1}{\sqrt{2}} \left(\rho_\uparrow(x) + \rho_\downarrow(x)\right), \\ \sigma(x) &= \frac{1}{\sqrt{2}} \left(\rho_\uparrow(x) - \rho_\downarrow(x)\right). \end{aligned} \tag{3.17}$$

We can then define two types of bosonic fields,

$$\begin{aligned} \phi_\rho(x) &= \frac{1}{\sqrt{2}} \left(\phi_\uparrow(x) + \phi_\downarrow(x)\right), \\ \phi_\sigma(x) &= \frac{1}{\sqrt{2}} \left(\phi_\uparrow(x) - \phi_\downarrow(x)\right), \end{aligned} \tag{3.18}$$

and a similar set for the current fluctuations.

The Hamiltonian then decouples in the charge and spin degrees of freedom,

$$H = H_\rho + H_\sigma + g_1 \int dx \cos(2\sqrt{2}\phi_\sigma(x)), \tag{3.19}$$

where g_1 is the inter spin interaction strength and H_ρ & H_σ are of the form given by the bare Luttinger liquid Hamiltonian in equation 3.6, however with different Luttinger liquid parameters. Because there is no need for the Luttinger liquid parameters for the spin and charge sector to be the same, this means that these two

degrees of freedom separate and propagate with different velocities through the system. This separation between spin and charge excitations gives another indication that it is not possible for a single particle to be excited in a purely 1D system, which can be seen by realising that a single particle would carry both a well defined spin and charge which would travel through the system at the same rate.

From the Hamiltonian in Eq. 3.19 we can see that the charge sector is characterised by the bare Luttinger liquid theory, but the spin sector has a cosine term resulting in the sine-Gordon Hamiltonian [119] which can only be treated on an approximate perturbative level [102]. This then allows for an analysis with renormalisation group methods giving us rescaled Luttinger liquid parameters for the emergent effective theory.

Ignoring for the moment the cosine term we can calculate the power law dependence for the charge density wave (CDW) and spin density wave (SDW) density-density correlations using the same techniques described in the previous section [102],

$$\begin{aligned}
\langle O^{\dagger}_{CDW}(x)O_{CDW}(0)\rangle &\propto \left(\frac{\xi}{\sqrt{x^2-u^2\tau^2}}\right)^{K_\rho+K_\sigma}, \\
\langle O^{x\dagger}_{SDW}(x)O^{x}_{SDW}(0)\rangle &\propto \left(\frac{\xi}{\sqrt{x^2-u^2\tau^2}}\right)^{K_\rho+1/K_\sigma}, \\
\langle O^{y\dagger}_{SDW}(x)O^{y}_{SDW}(0)\rangle &\propto \left(\frac{\xi}{\sqrt{x^2-u^2\tau^2}}\right)^{K_\rho+1/K_\sigma}, \\
\langle O^{z\dagger}_{SDW}(x)O^{z}_{SDW}(0)\rangle &\propto \left(\frac{\xi}{\sqrt{x^2-u^2\tau^2}}\right)^{K_\rho+K_\sigma},
\end{aligned} \tag{3.20}$$

for the operators,

$$
\begin{aligned}
O_{CDW}(x) &= \psi^{\dagger}_{R,\uparrow}(x)\psi_{L,\uparrow}(x) + \psi^{\dagger}_{R,\downarrow}(x)\psi_{L,\downarrow}(x), \\
O^{x}_{SDW}(x) &= \psi^{\dagger}_{R,\uparrow}(x)\psi_{L,\downarrow}(x) + \psi^{\dagger}_{R,\downarrow}(x)\psi_{L,\uparrow}(x), \\
O^{y}_{SDW}(x) &= -i\psi^{\dagger}_{R,\uparrow}(x)\psi_{L,\downarrow}(x) + i\psi^{\dagger}_{R,\downarrow}(x)\psi_{L,\uparrow}(x), \\
O^{z}_{SDW}(x) &= \psi^{\dagger}_{R,\uparrow}(x)\psi_{L,\uparrow}(x) - \psi^{\dagger}_{R,\downarrow}(x)\psi_{L,\downarrow}(x),
\end{aligned}
\tag{3.21}
$$

which give us the bare Luttinger liquid theory for the two-component bosonic fields.

One way to analyse the corrections to these correlations arising from the cosine term is to apply a renormalisation group approach [102, 119]. This is valid for weak values for g_1 and it is found that for $K_\sigma > 1$ that the cosine term is irrelevant, meaning that for long length scales it is unimportant and its only effect is to renormalise the Luttinger liquid parameters in the simple quadratic Hamiltonian, meaning that all expressions for the correlation functions map directly over. However, if g_1 is above some critical value, solving the renormalisation group equation results in a non-zero, but finite, weight for the cosine term which opens up a gap in the excitation spectrum for the spin sector, indicating that there are large corrections to this Luttinger liquid theory in the strongly interacting regime, whereas the density sector can retain its Luttinger liquid behaviour. For $K_\sigma < 1$ the cosine term is relevant and so this term dominates over all length scales meaning that the Luttinger liquid behaviour of the spin sector is suppressed and the Luttinger liquid parameter, K_σ flows to smaller and smaller values, meaning that the x and y spin correlations above decay rapidly. In some cases the density sector may retain its Luttinger liquid behaviour and the CDW and the z SDW correlation functions keep their algebraic decay now completely controlled by K_ρ.

Lattice potential

Including a lattice potential also complicates the above analysis on the universal behaviour of one-dimensional systems, meaning that, in general, it is no longer possible to obtain exact, analytical expressions for correlation functions. This is also particularly relevant for the analysis presented in this thesis as throughout we predominantly consider the case of deep potentials in optical lattice experiments such that the dynamics can be described by the (Bose-)Hubbard model, which was derived in the previous section. Therefore in this section we summarise the bosonisation of the Hubbard model [102] and present the Luttinger liquid parameters and discuss the corrections to the Luttinger liquid behaviour in different limits. Note that in certain cases in the limit of strong lattice confinement and strong interactions it is possible to analyse the behaviour by mapping the problem to a spin model which then allows for a direct mapping to the bare Luttinger liquid theory [120, 121]. Here we consider the Hubbard model,

$$H = -J \sum_{n,\sigma} \left(\hat{c}^{\dagger}_{n,\sigma} \hat{c}_{n+1,\sigma} + h.c. \right) + U \sum_{n} \hat{n}_{n,\uparrow} \hat{n}_{n,\downarrow}, \tag{3.22}$$

where, $\hat{c}^{\dagger}_{n,\sigma}$ is the creation operator for a fermion with spin $\sigma = \{\uparrow, \downarrow\}$ on site n, and $\hat{n}_{n,\sigma} = \hat{c}^{\dagger}_{n,\sigma} \hat{c}_{n,\sigma}$. This Hamiltonian is valid for strong lattice confinement and an interaction strength that is much smaller than the spacing between energy bands - this is the fermion version of the Bose-Hubbard model derived in the previous chapter.

In this case we obtain a Hamiltonian of a similar form as Eq. 3.19, but where the Hubbard interaction strength, U controls the sine-Gordon term,

$$H = H_{\rho} + H_{\sigma} + \frac{U}{2\pi^2 \xi^2} \int dx \cos(2\sqrt{2}\phi_{\sigma}(x)). \tag{3.23}$$

The Luttinger liquid parameters are then related to the Hubbard coefficients by,

$$\begin{aligned} u_\rho K_\rho &= u_\sigma K_\sigma = v_F, \\ \frac{u_\rho}{K_\rho} &= v_F \left(1 + \frac{U}{\pi v_F}\right), \\ \frac{u_\sigma}{K_\sigma} &= v_F \left(1 - \frac{U}{\pi v_F}\right). \end{aligned} \tag{3.24}$$

As the form of this Hamiltonian is the same as Eq. 3.19, just with different values for the coefficients, we can apply the same renormalisation group analysis. In order to proceed in the regimes where the effects of the cosine term grows during the renormalisation group flow, then this problem must be approached differently, for example using a numerical method such as matrix product states (see Ch. 4 & 6).

Bosonisation of bosons

A peculiarity of bosonic systems is that the interacting case has very different properties compared to the non-interacing case as for zero interactions all particles occupy the same lowest energy state. This means that it is never possible to begin with the non-interacting theory and incorporate interactions perturbatively like in the case for higher dimensional Fermions. Nevertheless, in 1D we can still solve this problem for repulsive interactions by using the techniques from bosonisation [102, 105]. The Hamiltonian is exactly of the form of the spinless fermion Luttinger liquid Hamiltonian of Eq. 3.6. The results summarised here for one-dimensional boson systems, will play a crucial role in understanding the many-body behaviour of the Creutz ladder that we analyse in Ch. 8.

There are important differences to the fermion theory, for example the field op-

erator (for bosons now) is [102, 105],

$$\psi_B(x) = \sqrt{\rho_0} \sum_p e^{-i2p(\pi\rho_0 x - \phi(x))} e^{i\theta(x)}, \tag{3.25}$$

where ρ_0 is the mean density and p is an integer. Contrast this to the expression for fermions in Eq. 3.14, where $2p = \pm 1$. This leads to the same power law dependence for the density-density correlations [105],

$$\langle \rho(x,\tau)\rho(0)\rangle = \rho_0 - \frac{K}{2\pi^2}\frac{u^2\tau^2 + x^2}{\left(x^2 - u^2\tau^2\right)^2} + \tilde{A}\cos(2\pi\rho_0 x)\left(\frac{1}{\sqrt{x^2 - u^2\tau^2}}\right)^{2K}, \tag{3.26}$$

where $\tilde{A}$ is a model dependent constant. But the differences appear in the expression for the single particle Greens function [105],

$$\langle \psi(x,\tau)\psi^\dagger(0)\rangle \propto \left(\frac{\xi}{\sqrt{x^2 - u^2\tau^2}}\right)^{\frac{1}{2K}}, \tag{3.27}$$

where now for large K, these correlations decay slowly indicating that there can be large single bosons fluctuations. Contrast this to the case for fermions where the exponent was proportional to $K + K^{-1}$, so that if K moved away from one (the non-interacting fermion case) then the correlations decayed faster, meaning that single fermion excitations are suppressed in the interacting case.

We can use these correlation functions to interpret the Luttinger liquid parameter, where we can see that as $K \to \infty$ the charge fluctuations (Eq. 3.26) are suppressed whereas the superfluid fluctuations (Eq. 3.27) are constant, this case corresponds to non-interacting bosons. As K decreases towards one this corresponds to increasing the (repulsive) interaction strength, where the superfluid fluctuations are still dominant over the charge fluctuations. At $K = 1$ the Luttinger liquid model then

describes non-interacting fermions, which through the Jordan-Wigner transformation we know corresponds to hardcore ($U \to \infty$) bosons, which is connected to the fermionisation of bosons [108]. This description in terms of the Luttinger liquid is only valid for repulsively interacting bosons, so there is not so obvious an interpretation for $K < 1$, but from the correlations it is clear that the system is dominated by charge fluctuations. This regime can only be realised if there are longer range repulsive interactions present in the underlying model. In Ch. 8 we will use these results to characterise the many-body phases for interacting bosons in the Creutz ladder.

Extension to ladders

In part III of this thesis we will consider many interacting particles confined in novel ladder geometries and so it is important then to consider how the above results for one-dimensional quantum systems are affected when two 1D chains are connected together to form a simple ladder. In general, including this coupling can significantly affect the long distance behaviour of the correlation functions we presented in the previous section and in some cases can open up a gap in the excitation spectra suppressing the algebraic decay of the correlations. But in other cases it has been found that these ladder systems can also exhibit similar quasi-long-range order and preserve the separation between the charge and spin sectors. It appears then that going a little beyond 1D does not destroy these characteristic features of one-dimensional systems, but leads to a much richer array of physics as we will sketch out below.

For a ladder system of spinless fermions that can be described by a Hubbard model with a nearest neighbour interaction, V, the Hamiltonian in terms of the

boson fields is given by [102],

$$H = H_1 + H_2 - \frac{J_\perp}{2\pi\xi}\int dx \cos\left(\phi_1(x) - \phi_2(x)\right)\cos\left(\theta_1(x) - \theta_2(x)\right), \tag{3.28}$$

where H_1 and H_2 are the bare Luttinger liquid Hamiltonians for each of the two coupled chains and $J_\perp$ describes the tunnelling between chains. Due to the presence of the double cosine term, this means that we must analyse its features using the renormalisation group equations. However, it is much more convenient to analyse this after performing a basis transformation,

$$\begin{aligned}\rho_\rho(x) &= \frac{1}{\sqrt{2}}\left(\psi_1^\dagger(x)\psi_1(x) + \psi_2^\dagger(x)\psi_2(x)\right),\\ \rho_\parallel(x) &= \frac{1}{\sqrt{2}}\left(\psi_1^\dagger(x)\psi_2(x) + \psi_2^\dagger(x)\psi_1(x)\right).\end{aligned} \tag{3.29}$$

This leads to the Hamiltonian,

$$\begin{aligned}H = H_\rho + H_\parallel + \frac{\sqrt{2}J_\perp}{\pi}\int dx \nabla\phi_\parallel(x),\\ + \int dx \frac{2g_\perp}{(2\pi\xi)^2}\cos(\sqrt{8}\phi_\parallel(x)) + \frac{2g_f}{(2\pi\xi)^2}\cos(\sqrt{8}\theta_\parallel(x)),\end{aligned} \tag{3.30}$$

where

$$\begin{aligned}g_\perp &= -V\xi\left(1 - \cos(k_F\xi)\right),\\ g_f &= V\xi\cos(k_F\xi).\end{aligned} \tag{3.31}$$

From this we can observe that the two sets of bosonic fields $\rho_\rho(x)$ and $\rho_\parallel(x)$ are separated and uncoupled. This means that there will be regimes where the power law behaviour in K_ρ, survives for some correlation functions, see Eq. 3.20. In particular, it has been found that this system can host phases dominated by superconducting

like pairs [122, 123], which can be characterised through an algebraic decay of either a symmetric superconductive pairing operator,

$$O^{S}_{SD}(x) = \psi_{L,0}(x)\psi_{R,1}(x) + \psi_{L,1}(x)\psi_{R,0}(x), \tag{3.32}$$

or an antisymmetric operator,

$$O^{A}_{SD}(x) = \psi_{L,0}(x)\psi_{R,1}(x) - \psi_{L,1}(x)\psi_{R,0}(x), \tag{3.33}$$

by tuning the strength of the interactions. In this way realising 1D phases with analogous counterparts in higher dimensions to s-type and d-type superconductivity respectively, indicating that even with two coupled chains that there are features that one would expect from two-dimensions [102]. In contrast to a pure 1D chain, it has been found that in the ladder system the symmetric superconductive pairing is actually robust to the effects of disorder [124], indicating that there are potential advantages in these *quasi-1D* systems compared to the pure 1D case. Ladder systems with spin have also been analysed where it has been shown that similar features for the correlations and phases can also be manifested with certain regimes that are able to realise quasi-long-range order in the superconducting correlations for repulsive interactions [125–130].

Similar analysis has also been carried out on a ladder system of three coupled chains [131, 132] where it has been shown that the system shares more similarities to a single chain compared to the two chain case, and is actually more likely to manifest quasi-long-range order for a wider range of parameters. A qualitative understanding of this is that two chains become strongly coupled and together decouple from the degrees of freedom of the third allowing the fluctuations in this free chain to propa-

gate freely. The crossover to two-dimensions has also been considered as the limit of this analysis to infinite chains [133] where it has been shown that there is a strong even-odd effect where for an odd number of chains the system behaves more like a single chain for similar reasons to the arguments above and for an even number of chains the system behaves more like the two-leg ladder system. Of course, for a real 2D geometry, these unique features of 1D systems should be destroyed, however there are uncertainties as to the precise crossover point of this behaviour [133] and that taking this infinite chain limit is not so straightforward.

3.4 Summary

In this chapter we have summarised the solution of the Luttinger liquid model and presented some of the most important results, such as the long range behaviour of the correlation functions. This is a theory that (in the massless case) can be directly mapped onto the low energy properties of interacting particles confined in one-dimension. As we predominantly consider one-dimensional systems in this thesis, understanding the features of this simple model will allow us to better understand the physics that are unique to the more specific situations that we will analyse. We also presented the effects on the main predictions upon including a strong lattice confinement, which is relevant for comparing to quantum simulations with optical lattice experiments and we considered extending the model to describe spinful Fermions and ladder systems, the results of which we will use to help us analyse many-body effects in topological band structures in part III.

Chapter 4

Methods for classical simulation

The ability to classically simulate many-body quantum systems has led to profound insights into the properties of these systems, but is now becoming even more important in the context of quantum simulation. Given that the goal is to have the simulators operating in a regime beyond what is capable of investigating with classical algorithms, how then are we to confirm that the results are correct? One approach is to benchmark the experimental architecture against state-of-the-art classical algorithms in regimes that are accessible and then gradually extend the parameters of the experiment to regimes beyond those classically obtainable. So in order to ensure the smallest margin of error it is therefore optimal to use classical algorithms that are valid in the largest of possible regimes. In other words it is paramount that we have the best way of benchmarking the experimental architectures for quantum simulation so that we can have confidence that the results are actually correct.

For quantum systems that are too large for a classical computer to manipulate the full set of basis states, matrix product states (MPS) [1, 134–137] are a very powerful but fairly abstract way of representing the state of the system. This representation allows for a reduction in the region of the Hilbert space that must be considered

based on the entanglement properties of the state. As it happens the low energy properties of many one-dimensional Hamiltonians, in particular those that have local interactions and have a gapped excitation spectrum [138], are very amenable to an efficient representation with these matrix product states offering us a way forward in calculating the properties of many-body phases to a high level of accuracy. There have also been algorithms proposed in this language to evolve an MPS in time which have led to many further successes in probing the out-of-equilibrium dynamics of many-body systems after a quench [139–145]. However, in most cases entanglement grows under time-evolution [146] which means that the compression of the MPS becomes less and less accurate leading to the rapid growth of errors, see Ch. 6. These techniques have had extraordinary successes in quantitatively describing the many-body physics of interacting quantum systems in one-dimension and so in this chapter we summarise the main features of some of the algorithms for calculating ground states and performing time-evolution that we will utilise in later chapters.

4.1 Entanglement in many-body systems

Entanglement is a measure of non-classical correlations between two systems [147], where measuring the state of one system not only collapses the wavefunction of that system, but also gives knowledge *and* affects the state of the other. If we think of our total system, Φ, as representing the combined two sub-systems Φ_A and Φ_B, these could be two halves of a 1D system for example, then we can write the total state as a superposition of simple product states through a Schmidt decomposition [147] (also referred to as a singular value decomposition (SVD))

$$|\Phi\rangle = \sum_{m=1}^{r} s_m |\alpha_m\rangle \otimes |\beta_m\rangle, \tag{4.1}$$

where $|\alpha_m\rangle$ and $|\beta_m\rangle$ are orthonormal bases associated with sub-system A and B respectively, r is the Schmidt rank of the bipartition and the s_m are the Schmidt coefficients which are real and satisfy $\sum_m s_m^2 = 1$.

In general the larger the number of terms r in the expansion, the larger the entanglement between the two sub-systems, for example with a product state, $|\Phi\rangle = |\Phi_A\rangle \otimes |\Phi_B\rangle$, there is no entanglement and we can completely describe this with a single term in the decomposition. Entanglement in general pure states can be quantified through the Von-Neumann entropy [148],

$$E = -\sum_{m=1}^{r} s_m \log(s_m). \tag{4.2}$$

The interpretation of this quantity, is how much sub-system B would be affected by performing measurements only on sub-system A. Thus, if the entropy is larger, then projecting A onto particular basis states through projective measurements would affect B more, meaning that there was more entanglement or correlations present between the two sub-systems.

The low energy equilibrium properties of locally interacting, gapped Hamiltonians are such that these systems obey an area law in the entanglement scaling [149], where the entanglement in the system grows with the area of the boundary of a bipartition as opposed to the more general scenario where it could scale with the volume [150]. As the boundary of a bipartition in one dimension remains constant irrespective of the size of the two sub-systems, this means that we can describe these states by only retaining a small number of Schmidt coefficients (and basis states) at each nearest neighbouring bond. We will see below that it is these principles that are behind the success of matrix product state techniques, where it turns out that these types of states that obey area laws are very amenable to an efficient representation

with a compressed matrix product state offering us a way forward in calculating the properties of the many-body phases to a high level of accuracy [151, 152].

Out-of-equilibrium

While the equilibrium properties of the low energy states of these Hamiltonians obey an area law it is a different story when they are driven out-of-equilibrium, for example by applying a instantaneous global quench [139–141]. The entanglement at each bipartition point of the system then grows linearly in time [146, 153, 154] and which in order to achieve a given accuracy with the MPS representation we must exponentially grow the number of Schmidt coefficients that are stored, which can be seen from the logarithm present in Eq. 4.2. This means that we quickly run out of classical resources and it becomes an incredibly intensive calculation in order to evolve these states for any significant length of time.

This feature of out-of-equilibrium entanglement scaling in many-body quantum systems can be understood in terms of the propagation rate of information, which is characterised through the Lieb-Robinson bounds [155, 156]. This states that for a locally interacting Hamiltonian there is an upper bound to the velocity at which correlations spread, and is usually given by a constant linear rate, but there are corrections for systems with long range interactions [142, 144, 145]. This means the number of lattice sites or particles that become correlated or entangled scales linearly with time resulting in the linear growth of entanglement which impedes an efficient classical algorithm. This has led to substantial interest in encoding the problem in physical quantum resources in order for a quantum simulation to help us understand more about the long time thermalisation properties of many-body systems.

4.2 Matrix product state representation

Throughout this chapter we will make use of tensor network diagrams, where each tensor, labelled with three indices α, d, and β for example, is represented as,

$A_{\alpha,d,\beta} =$ 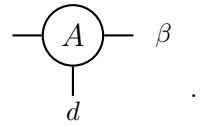

.

Tensor contraction is then depicted through connected edges,

$\sum_\beta A_{\alpha,d_1,\beta} B_{\beta,d_2,\gamma} =$ 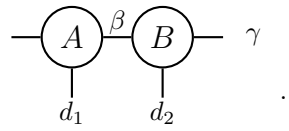

.

The MPS representation involves decomposing our state vector in terms of the local indices. These local dimensions can represent the number of particles on a particular lattice site for example. The decomposition is carried out with successive SVDs at each bipartition, and can be understood in terms of a tensor network diagram,

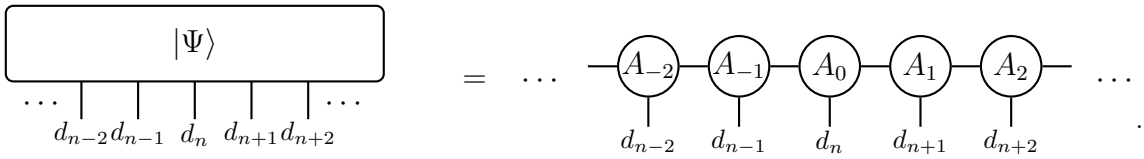

.

At first this appears to only complicate things with no benefit, because in order to capture all states in the Hilbert space, these matrices must grow exponentially as the system size is increased and so suffers from the same scaling in computational complexity as for the state vector representation. However in the MPS form, we have the ability to implement a truncation scheme that allows us to efficiently store

and work with these matrices in practice. This truncation, which incorporates an upper bound in the number of Schmidt coefficients at each bond, limits the amount of entanglement that the MPS can accurately capture as we have discussed in the previous section.

Canonicalising an MPS

Again through SVDs (or equivalently QR decompositions) we can bring the MPS into a so called canonical form,

$|\Psi\rangle = \cdots$ 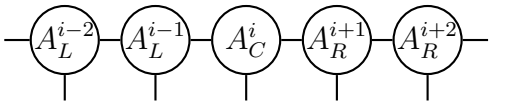 $\cdots$.

where the new left canonicalised tensors, A_L, and the right canonicalised tensors, A_R, satisfy the following contraction properties,

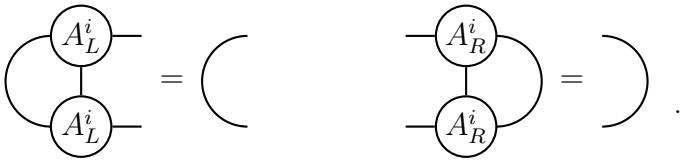 .

And we have also defined a central canonicalised tensor, A_C which is related to A_L and A_R by,

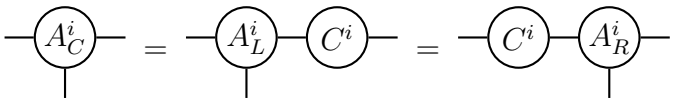 .

The matrices C_i contain the Schmidt coefficients of a bipartition of the system at the bond between site i and $i+1$. We can limit the size of these matrices by removing the smallest Schmidt coefficients and in this way we compress the MPS but retain the components with the largest magnitude and hence of the most importance. It

is this property of the MPS that is responsible for the accurate representation of low entangled many-body states, where the size of these matrices does not need to be too large to exactly capture many important states of the low energy physics of many-body Hamiltonians in one dimension.

4.2.1 Variational ground state search

The most successful algorithm for calculating the ground state involves a local variational optimisation of the parameters contained in the matrices of the MPS. This algorithm is often referred to as the density matrix renormalisation group (DMRG) for historical reasons, [134, 135], which has since been formulated in the MPS language, [1]. The algorithm emphasises another main advantage of the MPS representation: it allows us to optimise the parameters of a small local region rather than attempting to diagonalise the entire state vector. After sweeping this local optimisation procedure from site to site the total energy of the current state should continuously decrease and after many successive sweeps should converge to a well defined value. If the bond dimension of the MPS is sufficiently large, the final state should be (close to) the ground state.

First we must write the Hamiltonian, H, in the form of a matrix product operator (MPO) which is done in a similar way as for a state with SVDs for each local dimension. In the notation for a tensor network diagram, the energy expectation value is given as,

$\langle H \rangle =$ 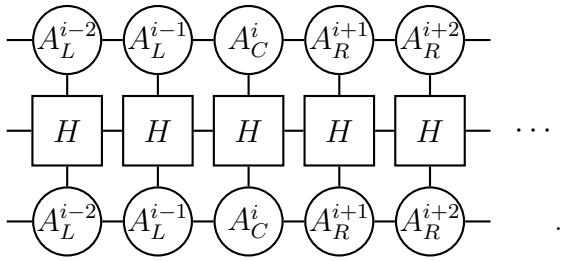

In order to apply the variational optimisation for site i, we must remove the local tensor A_C^i and contract the remaining tensors to obtain an effective left and right environment for the local site,

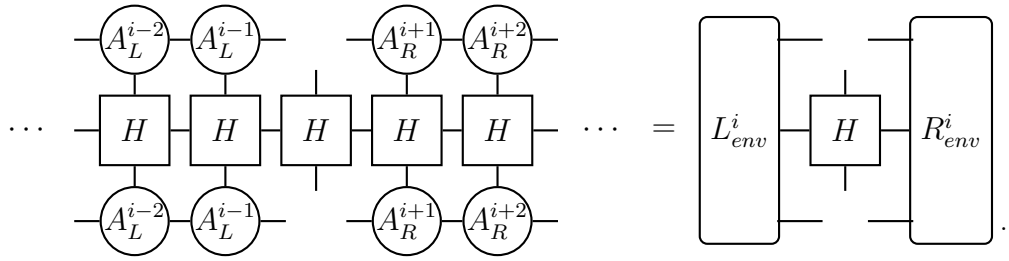

which we can solve for the eigenvector with the lowest eigenvalue. This eigenvector is then our new optimal tensor for A_C^i. We then move the canonicalisation centre with an SVD (or QR decomposition),

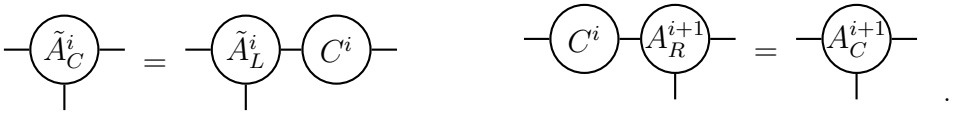

so that we can calculate the new effective left environment in order to optimise A_C^{i+1},

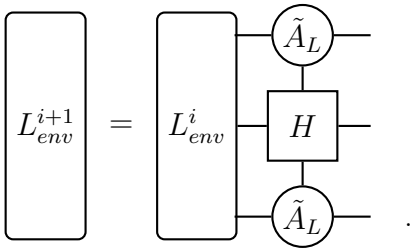

The optimisation procedure sweeps from left to right and right to left like this until subsequent optimisations do not change the state.

4.2.2 Tangent space methods for time evolution

There are many methods for time-evolving an MPS that all have various advantages and disadvantages. The difficulty here is that while there is an efficient representation of the Hamiltonian as an MPO, there is in general no straightforward way to represent the time-evolution operator in MPO form. So various approximations must be used, such as the time evolving block decimation procedure (TEBD), [157, 158], or adaptive time-dependent DMRG, [136, 137], which rely on a decomposition of the total evolution operator into a product of two site gate operators, [31]. Or Runga-Kutta type methods which decompose the evolution operator into a product of global Hamiltonians, [159]. But these methods suffer from an unavoidable growth of the bond dimension of the MPS, requiring a suitable truncation scheme in order to ensure the computational complexity remains practical. This truncation naturally suffers from errors and the most optimal scheme for performing the compression varies from case to case.

Here we summarise a variational optimisation method, known as the time-dependent variational principle (TDVP), [160], which given an MPS, $|\Psi(t)\rangle$, finds the optimal state, $|\Psi(t + dt)\rangle$, such that the bond dimension is preserved. The algorithm is derived by considering the effect of applying a local time-evolution operator and then projecting onto the variational manifold for the MPSs with the given bond dimension.

In a similar way as for the DMRG algorithm above, we compute the left and right environments for a particular site and solve the linear differential equation for the local tensor,

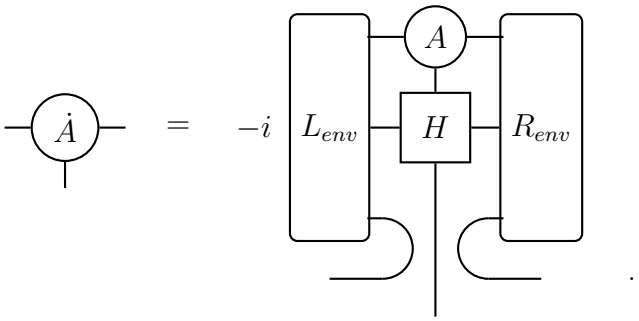

We then shift the canonicalisation centre, but evolve the matrices C *backwards* in time according to the equation,

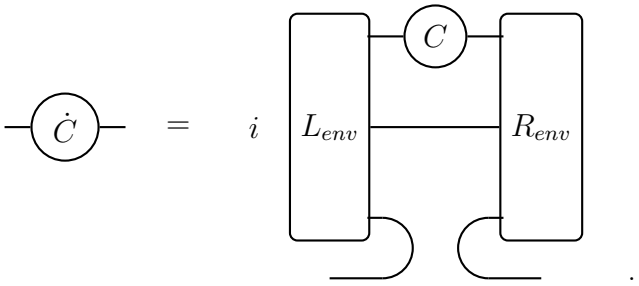

before contracting it with the next site to be evolved. We then sweep through every site from left to right and then right to left, which evolves the state by a single time step with an error scaling of $\mathcal{O}(dt^3)$.

4.3 Summary

In this chapter we explained the importance and impact that matrix product state techniques have had in probing the properties of many-body quantum systems. Throughout this thesis, we will often utilise these techniques to predict the equilibrium and dynamical properties of one-dimensional lattice systems and to perform simulations which can be used to benchmark quantum simulation. In particular, in

Ch. 6 we will utilise these techniques to compare the relative performance of current hardware implementations of analogue simulators to these state-of-the-art classical methods. Additionally, in Ch. 8 & 9 we will exploit the ability to time-evolve these states to simulate adiabatic preparation schemes for strongly correlated ground states of topological ladder systems and in Ch. 10 we will combine these techniques with a promising new numerical algorithm (see Ch. 5) which we demonstrate allows us to simulate open many-body systems beyond the usual weak coupling approximation.

Chapter 5

Open quantum systems

In many realistic experimental situations it is not possible for us to approximate our quantum system of interest as being completely isolated. Naturally there is always an external environment which influences the dynamics of the system. For example, in state-of-the-art quantum optics experiments the atoms in our system are placed in a near perfect isolation, but through spontaneous emission to the electromagnetic vacuum, this can still lead to non-negligible effects. While this can sometimes be neglected on short time scales we must be able to treat these types of effects in more general and complex settings. Unfortunately, we are usually unable to accurately simulate the entire unitary dynamics of the large system-environment Hamiltonian, due to the exponential growth of the size of the Hilbert space.

This problem has inspired a variety of (classical) numerical and analytical methods for the simulation of the effective dynamics of only the system and usually rely on integrating out the state of the environment. These methods, developed due to a need to describe the increasingly sophisticated quantum optical experiments [161–167], have had great successes in modelling the system-environment dynamics in these experimental settings [41, 168–170], offering a way forward if certain approx-

imations are satisfied. In these experiments there is generally a large separation in energy scales between the dynamics of the system and the environment, which allows us to employ the Born-Markov approximation (see below) which can drastically simplify the problem [2]. These allow us to write down an effective equation of motion for the density matrix of the small system, known as the Master equation, which takes into account the energy exchange with the larger environment.

However there is also great interest in going beyond these approximations [171–173], where a necessary criteria is that the environment instantaneously relaxes after exchanging energy with the system, and as such retains no memory of previous interactions. In recent years there has been many studies into the transport of energy and correlations in the presence of environments with memory effects which lead to non-trivial features [173–175], such as the coherent back flow of information from the environment into the system. So, after illustrating the derivation of the Lindblad master equation, we present a promising numerical technique for studying these more novel situations.

5.1 Lindblad Master equation

The notion of constructing a Master equation for a reduced system was first put forward by V. Gorini and A. Kossakowski [176] and G. Lindblad [177], and was formulated to generalise the unitary evolution of closed system Hamiltonians so as to be able to describe irreversible processes, involving energy exchange between the quantum system of interest and the wider environment. Let us write the total Hamiltonian in terms of a contribution from the system, H_S, the rest of the universe (the environment), H_E, and a term that contains all the interaction or coupling

between the system and the environment, H_{SE}. We can write the Hamiltonian as,

$$H = H_S + H_E + H_{SE}. \tag{5.1}$$

And we assume that the total system, H, is itself is a closed system so that the total density matrix evolves unitarily. We can therefore write the time evolution of the total density matrix for the system and environment as ($\hbar = 1$),

$$\frac{d}{dt}\rho_{SE} = -i[H_S + H_E + H_{SE}, \rho_{SE}]. \tag{5.2}$$

This is simply the Schödinger equation but for the density matrix, $\rho = |\Psi\rangle\langle\Psi|$. We then apply a unitary transformation to rotate our Hamiltonian and density matrix from the Schödinger picture to the interaction picture,

$$\begin{aligned} H(t) &= e^{i(H_S+H_E)t} H e^{-i(H_S+H_E)t}, \\ \rho_{SE}(t) &= e^{i(H_S+H_E)t} \rho_{SE} e^{-i(H_S+H_E)t}, \end{aligned} \tag{5.3}$$

which simplifies Eq. 5.2,

$$\frac{d}{dt}\rho_{SE}(t) = -i[H_{SE}(t), \rho_{SE}(t)]. \tag{5.4}$$

We then explicitly integrate this from time $0 \to t$ [178–180],

$$\rho_{SE}(t) = \rho_{SE}(0) - i\int_0^t dt'[H_{SE}(t'), \rho(t')], \tag{5.5}$$

and substitute this back into Eq. 5.4 to obtain [171, 181, 182],

$$\frac{d}{dt}\rho_{SE}(t) = -i[H_{SE}(t), \rho_{SE}(0)] - \int_0^t dt'[H_{SE}(t), [H_{SE}(t'), \rho_{SE}(t')]]. \tag{5.6}$$

And we can always make the first term on the right hand side equal to zero by choosing the correct definition of the coupling Hamiltonian and assuming that the initial state is an uncorrelated state between the system and environment.

But we are only interested in the evolution of our small system, so we integrate out the contributions from the environment in the density matrix by taking the partial trace,

$$\rho(t) = \mathrm{Tr_E}\left(\rho_{SE}(t)\right). \tag{5.7}$$

Which yields (note the partial trace commutes with the time derivative),

$$\frac{d}{dt}\rho(t) = -\int_0^t dt' \mathrm{Tr_E}\left([H_{SE}(t), [H_{SE}(t'), \rho_{SE}(t')]]\right). \tag{5.8}$$

The result of Eq. 5.8 is a Master equation and is so far exact. However, it is incredibly complicated, and numerically costly, to solve in itself even for simple coupling Hamiltonians, so in order to make progress we have to invoke the following approximations.

Born approximation

We assume that the coupling between the system and the environment is weak, such that throughout the entire evolution we can write the total density matrix as a product state [181],

$$\rho_{SE}(t) \approx \rho(t) \otimes \rho_E, \tag{5.9}$$

where ρ_E is the reduced density matrix for the environment, which we assume to be time independent on the system timescales, which is valid if the correlations between the system and the environment decay on timescales much faster than the system dynamics. These approximations make sense if the environment is much larger and is mostly unaffected or influenced by the system.

Markov approximation

In the Markov approximation the environment does not retain any memory of previous interactions with the system [2, 181]. This means that if energy escapes from the system to the environment it is quickly dissipated away from the system and never comes back in the same form. A necessary requirement is that the excitation dynamics of the environment are at much larger frequency scales compared to the dynamics of the system and consequently the environment returns to the equilibrium state very quickly (relative to the system timescales) after being excited.

In terms of our above expression, this means that the density matrix at time t is not dependent on the density matrix from any previous time. So we may replace the argument of the density matrix in the right hand side of Eq. 5.8 by t and we can write our Master equation as (combined with the Born approximation) [181],

$$\frac{d}{dt}\rho(t) = -\int_0^t dt' \mathrm{Tr_E}\left([H_{SE}(t), [H_{SE}(t'), \rho(t) \otimes \rho_E]]\right). \tag{5.10}$$

In order for the Markov approximation to be valid, the environment correlation functions must decay instantly in time and so we may extend the limits of the integral to infinity without consequence to even further simplify the master equation [181],

$$\frac{d}{dt}\rho(t) = -\int_0^\infty dt' \mathrm{Tr_E}\left([H_{SE}(t), [H_{SE}(t'), \rho(t) \otimes \rho_E]]\right). \tag{5.11}$$

It has been shown that invoking these approximations (together referred to as the Born-Markov approximations) results in a Master equation (Eq. 5.11) that is equivalent to taking a perturbative expansion of the exact Master equation (Eq. 5.8) up to terms of second order in the coupling strength [173, 178]. This means that this is only a valid description for a system and environment that are weakly coupled.

Linear coupling and rotating wave approximation

Generally speaking most physical couplings between various systems and environments can be written in the so called linear coupling form. If we have the system operators, c_i and $c_i^\dagger$, and the environment operators, $b_{k,j}$ and $b_{k,j}^\dagger$, then we will have terms in the coupling Hamiltonian given by,

$$H_{SE}(t) = \sum_{i,j} \sum_{k} \alpha_{ij} \left(c_i(t) + c_i^\dagger(t) \right) \left(b_{k,j}(t) + b_{k,j}^\dagger(t) \right), \tag{5.12}$$

where the $\alpha_{i,j}$ are coupling parameters and the sum over k is over the energy modes corresponding to environment j. The operators in the interaction picture, $c_i(t)$, are related to the operators in the Schrödinger picture, $c_i(0)$, as,

$$c_i(t) = c_i(0) e^{-i\omega_i t}, \tag{5.13}$$

where the ω_i are some energy scales of the system (and depends on the specific Hamiltonian considered) and there is a similar expression for the environment operators. We can then write the interaction Hamiltonian as,

$$\begin{aligned} H_{SE}(t) = \sum_{i,j} \sum_{k} \alpha_{i,j} \Big(& c_i(0) b_{k,j}^\dagger(0) e^{-i(\omega_i - \omega_{k,j})t} + c_i^\dagger(0) b_{k.j}(0) e^{i(\omega_i - \omega_{k,j})t} + \\ & c_i(0) b_{k,j}(0) e^{-i(\omega_i + \omega_{k,j})t} + c_i^\dagger(0) b_{k,j}^\dagger(0) e^{i(\omega_i + \omega_{k,j})t} \Big). \end{aligned} \tag{5.14}$$

We assume that the frequency of the relevant environment excitations, $\omega_{k,j}$, are approximately equal to the energy scales of the system, ω_i, and so, $\omega_i - \omega_{k,j} \ll \omega_i + \omega_{k,j}$ for all i and j. Therefore, the third and fourth terms on the right hand side of Eq. 5.14 oscillate much faster than the other two, so when we integrate over the time variable in the master equation (Eq. 5.11) the fast oscillating terms both average to zero. This is the rotating wave approximation. We can write the general form of the coupling Hamiltonian as,

$$H_{SE}(t) = \sum_{i,j} \sum_{k} \alpha_{i,j} \left(c_i(0) b^\dagger_{k,j}(0) e^{-i(\omega_i - \omega_{k,j})t} + c^\dagger_i(0) b_{k,j}(0) e^{i(\omega_i - \omega_{k,j})t} \right). \tag{5.15}$$

So by collecting these approximations together, substituting the coupling Hamiltonian (Eq. 5.15) into our Master equation (Eq. 5.11) and defining the system-environment coupling rates,

$$\begin{aligned} \gamma_i &= \sum_{j,k,k'} |\alpha_{i,j}|^2 \int_0^\infty dt' e^{-i(\omega_i - \omega_{k,j})(t-t')} \langle b_{k,j}(0) b^\dagger_{k',j}(0) \rangle, \\ \gamma^*_i &= \sum_{j,k,k'} |\alpha_{i,j}|^2 \int_0^\infty dt' e^{i(\omega_i - \omega_{k,j})(t-t')} \langle b^\dagger_{k,j}(0) b_{k',j}(0) \rangle, \end{aligned} \tag{5.16}$$

we can write the Markovian master equation in Lindblad form (in the interaction picture and ignoring additional rotating terms) [2, 181],

$$\begin{aligned} \frac{d}{dt}\rho(t) = \mathcal{L}(\rho) = \sum_i \gamma_i \left(2c_i \rho(t) c^\dagger_i - c^\dagger_i c_i \rho(t) - \rho(t) c^\dagger_i c_i \right) \\ + \gamma^*_i \left(2c^\dagger_i \rho(t) c_i - c_i c^\dagger_i \rho(t) - \rho(t) c_i c^\dagger_i \right). \end{aligned} \tag{5.17}$$

Here we denote the dissipation terms by the superoperators, $\mathcal{L}(\rho)$. Note that the terms $\gamma_{i,j}$ correspond to the removal of energy from the system, while the terms $\gamma^*_{i,j}$

correspond to the insertion of energy.

5.2 Unravelling of the Master equation

Unravelling the Master equation refers to the procedure of decomposing the dynamics of the density matrix into an ensemble average of the dynamics of many pure states undergoing a stochastic trajectory in the Hilbert space [2, 173], such that $\rho(t) = \mathcal{E}[|\psi(t)\rangle\langle\psi(t)|]$. The advantages created through this procedure, is that we only have to solve for the dynamics of the state, $|\psi(t)\rangle$, thus saving on computational resources as the state has dimension D as opposed to the density matrix which will have dimension D^2. This approach then allows us to time-evolve many-body systems in the presence of dissipation through the incorporation of matrix product state techniques [41] (see Ch. 4). As we will apply a similar technique in order to treat open many-body quantum systems beyond the Born-Markov approximations in Ch. 10, we briefly summarise the Markovian version here before considering the generalisation of these methods in the next section.

Explicitly, say we have the following Lindblad master equation in the Schrödinger picture,

$$\frac{d}{dt}\rho(t) = -i[H, \rho(t)] + \Gamma L\rho(t)L^\dagger - \frac{\Gamma}{2}L^\dagger L\rho(t) - \frac{\Gamma}{2}\rho(t)L^\dagger L, \tag{5.18}$$

then one possible unravelling is (in Stratonovich form),

$$\frac{d|\psi_t\rangle}{dt} = -iH|\psi_t\rangle + (L - \langle L\rangle)\left(z_t^* - \langle L^\dagger\rangle\right)|\psi_t\rangle - \frac{\Gamma}{2}\left(L^\dagger L - \langle L^\dagger L\rangle\right)|\psi_t\rangle, \tag{5.19}$$

where z_t^* is a complex white noise with the properties $\mathcal{E}[z_t z_{t'}^*] = \Gamma\delta(t - t')$ and $\mathcal{E}[z_t z_{t'}] = 0$, where $\mathcal{E}$ is an ensemble average. It can be shown that averaging of the time-dependent pure state over many simulations (or trajectories) with different

realisations of the stochastic noise term, z_t^*, gives the same results as the Master equation for the average dynamics of the system.

Physical interpretation of the trajectories

The above unravelling of the Master equation is known as a quantum state diffusion equation, but as we have presented it so far, there is no physical interpretation for the individual trajectories. They are simply abstract paths through the Hilbert space which give the correct behaviour for the density matrix when taking the ensemble average. In quantum optics, many unravellings have been formulated with a physical continuous measurement process in mind [2, 183], where one monitors the state of the environment and thus, due to the coupling between the system and environment, gains knowledge on the state of the system without destroying the state (a so called non-demolition measurement). In this context, the type of measurement performed on the environment chooses the form of the unravelling.

For example, a convenient type of unravelling, which has an intuitive physical picture, is a quantum jump process [163, 169], where rather than having continuous stochastic noise terms, involves discrete jumps corresponding to an instantaneous exchange of energy between the system and environment. This was first derived in Ref. [169] to describe the continuous measurement of a single driven multi-level atom interacting with the electromagnetic environment, where if a photon is measured by an external detector, then this corresponds to a spontaneous emission event and the atom is then projected (through a quantum jump) into the ground state. Now each trajectory gives realistic dynamics for an experimental procedure, where averaging over successive experimental runs (or averaging over many trajectories) gives the same predictions as the full master equation for the density matrix.

Additionally, strongly mixing the output photons with a local oscillator before

performing the measurement, so called homodyne detection [165, 166, 183], leads to a physical unravelling with a continuous noise process closer in form to the quantum state diffusion above, but now we can also gain intuitive physical knowledge from each trajectory.

5.3 Beyond the Markov approximation

The Born-Markov approximation is a very special regime of open quantum systems, which has received a great deal of attention in recent years, due to both the simple form of the resulting equations and that it can be easily reached in atomic and quantum optical experiments [2]. However, it is important to assess the effects of going beyond these limits, particularly because these approximations are not usually valid in a solid state setting* [184]. There has been great interest and work along this line over recent years [173], for instance non-Markovian effects have been observed to enhance coherence during quantum transport [174, 185] and to produce entangled steady states [175] .

In this section we describe and derive the hierarchy of pure states (HOPS) method [186, 187], which is a promising numerical strategy for the classical simulation of non-Markovian environments that can also go beyond the weak coupling (Born approximation) regime. The method is an extension to the Markovian stochastic Schrödinger equation described in the previous section, and treats the memory effects of the environment through the introduction of auxiliary states which are coupled with the physical state. The strategy is then to integrate the set of coupled system and auxiliary stochastic differential equations under the influence of

*In quantum optical experiments, there is a large separation in the dominant energy scales between the system and environment making it possible to accurately apply the approximations considered in this chaper. However, this is not usually the case for more general situations.

correlated noise for the pure states and take an ensemble average to reproduce the dynamics for the density matrix. Note that while the original derivation and applications have focused on a bosonic environment, the method has been extended to environments with fermionic modes [188].

Non-Markovian quantum state diffusion

We begin by deriving the non-Markovian generalisation for the stochastic Schrödinger equation [189, 190], which assumes that the system and environment are initially uncorrelated. For a harmonic environment that couples linearly with the system, H_s,

$$H = H_s + \sum_m \omega_m a_m^\dagger a_m + \sum_m g_m (L a_m^\dagger + L^\dagger a_m), \tag{5.20}$$

where a_m and L are the environment and system operators respectively. We expand the state of the environment into a coherent state basis, with $a|z\rangle = z|z\rangle$,

$$|\Psi_T\rangle = \int \frac{d^2z}{\pi} e^{-|z|^2} |\Psi(z^*,t)\rangle \otimes |z\rangle = \int \frac{d^2z}{\pi} e^{-|z|^2} G_z(t)|\psi_0\rangle \otimes |z\rangle, \tag{5.21}$$

where

$$G_z(t) = \langle z^*| \exp\left(-iH_s t - iH_{\rm Int} t\right)|0\rangle. \tag{5.22}$$

Then we can write the Schrödinger equation for the parameterised system state, $|\Psi(t)\rangle \equiv |\Psi(z^*,t)\rangle$, in the interaction picture with respect to the environment as,

$$\begin{aligned} \partial_t|\Psi(t)\rangle =& \partial_t G_z(t)|\psi_0\rangle = -iH_s|\Psi(t)\rangle - iL\sum_m g_m z_m^* e^{i\omega_m t}|\Psi(t)\rangle \\ & - iL^\dagger \sum_m g_m e^{-i\omega_m t}\langle z_m^*|a_m \exp\left(-iH_s t - iH_{\rm Int} t\right)|0\rangle|\psi_0\rangle. \end{aligned} \tag{5.23}$$

Dealing with the final term is a little tricky, but it can be simplified by defining,

$$\tilde{a}_m(t) = \exp\left(iH_s t + iH_{\text{Int}}t\right) a_m \exp\left(-iH_s t - iH_{\text{Int}}t\right), \tag{5.24}$$

which through the Heisenberg equation of motion,

$$\partial_t \tilde{a}_m(t) = -ig_m e^{-i\omega_m t}\tilde{L}(t), \tag{5.25}$$

leads to,

$$\tilde{a}_m(t) = \tilde{a}_m(0) - ig_m \int_0^t ds \tilde{L}(s) e^{i\omega_m s}. \tag{5.26}$$

we can then make the substitution,

$$\frac{\delta|\Psi(t)\rangle}{\delta z_m^*} \equiv \langle z_m^*| \exp\left(-iH_s t - iH_{\text{Int}}t\right) \tilde{L}(t)|0\rangle|\psi_0\rangle, \tag{5.27}$$

which gives us the equation,

$$\begin{aligned} \partial_t|\Psi(t)\rangle = &- iH_s|\Psi(t)\rangle - iL\sum_m g_m z_m^* e^{i\omega_m t}|\Psi(t)\rangle \\ &- L^\dagger \sum_m \int_0^t ds g_m^2 e^{-i\omega_m(t-s)} \frac{\delta|\Psi(t)\rangle}{\delta z_m^*}. \end{aligned} \tag{5.28}$$

Then defining a new noise term,

$$z_t^* = -i\sum_m g_m z_m^* e^{i\omega_m t}, \tag{5.29}$$

we can express the stochastic Schrödinger equation as,

$$\partial_t|\Psi(t)\rangle = -iH|\Psi(t)\rangle + Lz_t^*|\Psi(t)\rangle - L^\dagger \int_0^t ds\alpha^*(t-s)\frac{\delta|\Psi(t)\rangle}{\delta z_s^*}, \tag{5.30}$$

where $\alpha(t-t') = \langle a(t')a^\dagger(t)\rangle = \sum_m g_m^2 e^{i\omega_m(t-t')}$ is the environment correlation function and z_t^* is a complex *coloured* noise with the property, $\mathcal{E}[z_t z_t'^*] = \alpha(t-t')$. This is a quantum state diffusion equation, first put forward in Ref. [189, 190] and is of a similar form as for the Markovian version considered in the previous section.

The hierarchy of pure states

Historically, the difficulty in working with Eq. 5.30 is the functional derivative term on the right hand side, $\delta|\Psi(t)\rangle/\delta z_s^*$. The insight which led to the HOPS algorithm is in writing this as a new auxiliary state,

$$|\Psi^{(1)}(t)\rangle = \int_0^t ds\alpha(t-s)\frac{\delta|\Psi(t)\rangle}{\delta z_s^*} \equiv D_t|\Psi(t)\rangle, \tag{5.31}$$

and deriving a new stochastic equation for its dynamics. Subsequently, we must introduce many more auxiliary states defined through,

$$|\Psi^{(k)}(t)\rangle = D_t^k|\Psi(t)\rangle. \tag{5.32}$$

If for the moment we consider an environment with a single mode which has a correlation function of the form, $\alpha(\tau) = \exp(-wt)$, then this leads to the set of coupled equations for the system ($k=0$) and the auxiliary states ($k>0$),

$$\partial_t|\Psi^{(k)}(t)\rangle = (-iH - kw + Lz_t^*)\,|\Psi^{(k)}(t)\rangle + k\alpha(0)L|\Psi^{(k-1)}(t)\rangle - L^\dagger|\Psi^{(k+1)}(t)\rangle, \tag{5.33}$$

with the initial conditions, $|\Psi^{(0)}(t)\rangle = |\Psi(t)\rangle$ and $|\Psi^{(k)}(t)\rangle = 0$ for $k>0$. The non-Markovianity in these hierarchical equations of motion come in through the time-correlated stochastic noise and through the auxiliary states, where the system state influences the auxiliary states which can then re-influence the system at a later time.

This process works up and down the hierarchy throughout the dynamics. The choice of environment is quite particular, although we can realise this exactly in cavity QED experiments [191–193], but it is possible to extend the hierarchy to sums of m modes with the cost of introducing m indices in the hierarchy, provided all modes have correlation functions of exponential form. For arbitrary bath correlations it is necessary to find a decomposition in terms of a series of exponentials in order to apply this method.

Strictly speaking, for a bosonic environment like this we must have an infinite number of auxiliary states, but it is found that in practice it is possible to truncate the hierarchy at some suitably chosen and problem dependent level - in practice this has to be chosen carefully and for most applications is usually around $k_{\max} \sim 6$, but it must be ensured that the numerical results have converged upon increasing this parameter [186, 187]. There are a variety of ways that have been proposed in order to terminate the hierarchy, for example one choice of terminator for the final auxiliary state at $k = k_{\max}$ is,

$$|\Psi^{(k_{\max})}(t)\rangle = \frac{\alpha(0)}{w} L|\Psi^{(k_{\max}-1)}(t)\rangle, \tag{5.34}$$

but note that the results are usually independent of the choice of terminator for a suitable hierarchy depth [186, 187].

Also presented in Ref. [186, 187] is a modification to this method to make a non-linear stochastic Schrödinger equation which has better convergence properties,

$$\begin{aligned}\partial_t|\Psi^{(k)}(t)\rangle = \left(-iH - kw + \left(z_t^* + \int_0^t ds\alpha^*(s-t)\langle L^\dagger\rangle_s\right)L\right)|\Psi^{(k)}(t)\rangle \\ +k\alpha(0)L|\Psi^{(k-1)}(t)\rangle - \left(L^\dagger - \langle L^\dagger\rangle_t\right)|\Psi^{(k+1)}(t)\rangle,\end{aligned} \tag{5.35}$$

where, $\langle L^\dagger \rangle_t = \langle \Psi^{(0)}(t)|L^\dagger|\Psi^{(0)}(t)\rangle$. As can be seen from the second term on the right hand side, this equation explicitly takes into account previous states of the system in the stochastic noise elements, thereby further incorporating memory effects into the dynamics. It should also be emphasised that although we are assuming that initially the system and environment are uncorrelated the method is able to capture the build up of these correlations time-dependently.

5.4 Summary

In this chapter we introduced the notion of the Lindblad master equation where we presented its derivation and emphasised the Born and Markov approximations that are paramount for its validity. We will utilise these techniques in Ch. 6 & 7 to model realistic mechanisms in optical lattice experiments such as heating due to spontaneous emission and dissipation due to three-body loss respectively.

We also derived the non-Markovian generalisation of the stochastic Schrödinger equation allowing for the simulation of the dynamics of open systems beyond the usual approximations. In Ch. 10 we will make use of these techniques, and in particular the HOPS algorithm that we also presented here, in order to classically simulate the dynamics of electrons in a one-dimensional system that is strongly coupled to a non-Markovian reservoir.

Part II

Benchmarking Quantum Simulators

Chapter 6

Achieving a practical quantum advantage in quantum simulation

Over the past couple of decades there has been an incredible improvement in the experimental capabilities surrounding the control of quantum mechanical resources, which has led to attempts to use physical quantum systems in order to exceed the computational abilities of classical algorithms. In this chapter, we ask the question, what is the most simple, but non-trivial problem, where a quantum simulation can unequivocally demonstrate a practical quantum advantage? A demonstration of this form, will prove the level of sophistication that these quantum devices have reached, and give further validation that they can now be used to probe the properties of novel quantum many-body systems, such as those considered in the subsequent chapters of this thesis. By considering the out-of-equilibrium dynamics of the Hubbard model, which has strong connections to materials science and solid state physics, we quantitatively compare the performance of the state-of-the-art classical algorithms to architectures for quantum simulation, such as ultracold atoms in optical lattices, taking into account realistic sources of errors. By extrapolating beyond

the classically simulable regime, we demonstrate that the quantum advantage point is accessible for current analogue simulators, while for digital simulation the hardware requirements in order to reach these regimes are significantly reduced compared to previous estimates. This is particularly timely due to the recent interest in the notion of *quantum supremacy* where it was recently demonstrated that a quantum computer can out perform classical computation in a particular example which can be used in generating random numbers [194].

6.1 Introduction

The requirements on the experimental hardware in order to demonstrate an advantage over classical computation will, of course, be highly dependent on the particular choice of problem used to perform the comparison. We have chosen the Hubbard model [27, 195], firstly because this has many connections to problems in materials science and so is of interest to fields outside of fundamental physics, and secondly, this model is very well suited to being solved on a realisation of analogue quantum simulation in particular with ultracold atoms in an optical lattice [19, 33–36], but similar seminal lattice models can now be realised in neutral atoms in tweezer arrays [37, 38] or trapped ion experiments [20, 39, 40].

In particular, there has been recent work on comparing the performance through the ability to capture (or prepare) the properties of the many-body ground states [196, 197] but this comparison will be incredibly dependent on the particular parameter regime as well as the model. Here we instead consider the ability for the simulation to capture the dynamical properties of important local observables and two-point correlations after a global quench [117, 198], which offer a much more general way to compare classical, analogue and digital simulation as the resulting dynamics in

many systems obey almost universal behaviour [156, 199, 200].

We should emphasise that this type of continuous time dynamical problem while being very well suited to analogue simulation, is potentially an area where a digital simulation will perform poorly in [16, 29, 30, 201], for example due to errors arising from a discretised time-step, nevertheless this allows for some indication of their relative performance. Of course, we cannot apply a direct comparison between these two simulation approaches as an architecture for digital simulation will in principle be able to realise universal computation and so has a much greater flexibility over the types of problems that it can be applied to, whereas analogue devices are purpose built to solve the types of problems that we are considering. Additionally, there are many different ways that one could optimise the digital logic circuit which is an area that is under constant development [202] and so here we simply compare the errors arising from the discretised time-step neglecting errors from individual logic gates and ignoring considerations about optimising circuit depths and gate counts, which we leave as a future objective.

After introducing the model that we will study, we first explain the limitations of the state-of-the-art classical algorithms where we present the time-dependent errors that are introduced if the numerical precision is limited to numerically tractable values. We then analyse sources of errors in analogue simulators, such as in preparing the initial state, the existence of additional unwanted terms in the Hamiltonian and the effects of heating and dissipation. We show that the dominant source of error in the observables that we consider arise through a calibration error, i.e. an uncertainty in the parameters of the model, but we show that these errors are bounded to values much lower than those introduced in the classical simulation, thus demonstrating that for sufficiently small calibration errors, analogue simulators can currently demonstrate a quantum advantage. Finally, we compare the errors generated to the

errors arising in a digital implementation with a particular value for the discretised time-step with a 4th order Trotter decomposition and discuss balancing this error with the total number of logic gates in the circuit.

The Models

We first consider the Hubbard model which describes a system of many interacting electrons moving through a lattice. This is a seminal model with strong connections to solid state physics [203] and can be realised with ultracold atoms in optical lattices where it can be derived from first principles under well-controlled approximations [25, 27, 28, 33]. Explicitly the Hamiltonian is,

$$H = -J \sum_{n,\sigma} \left(\hat{c}^{\dagger}_{n,\sigma} \hat{c}_{n+1,\sigma} + h.c. \right) + U \sum_{n} \hat{n}_{n,\uparrow} \hat{n}_{n,\downarrow}, \tag{6.1}$$

where, $\hat{c}^{\dagger}_{n,\sigma}$ is the creation operator for a fermion with spin $\sigma = \{\uparrow, \downarrow\}$ on site n, and $\hat{n}_{n,\sigma} = \hat{c}^{\dagger}_{n,\sigma} \hat{c}_{n,\sigma}$ is the number operator. The model is defined by two parameters, J, describing the rate at which electrons tunnel through the system and U, the strength at which electrons interact when occupying the same site. These parameters can be tuned over a wide range of values by varying the intensity of the applied laser producing the lattice confinement and by varying an applied magnetic field around a Feshbach resonance.

Additionally, we will compare some of the results to those in a Transverse Ising model for interacting spins [94], of the form

$$H_S = \sum_{n<m} J^{(n,m)} \hat{S}^n_z \hat{S}^m_z + B \sum_{n} \hat{S}^n_x, \tag{6.2}$$

where $\hat{S}^n_\sigma$ is a spin operator at site n and $\sigma \in \{x, y, z\}$. Here, B corresponds to an

applied transverse field, and $J^{(n,m)}$ describes the strength of Ising coupling between different spins. It is possible to realise this form of coupling matrix with trapped ion systems [204, 205] with $J^{(n,m)} \approx J_0/|n-m|^\alpha$. In the following we consider the case of long-range interactions with $\alpha = 2$.

As opposed to capturing the errors in the total state fidelities, which would characterise the errors in all complex coefficients of the wavefunction, we instead consider errors in the physical observables. Specifically, we calculate the global errors in each observable, O_n according to,

$$\varepsilon = \sqrt{\frac{1}{M}\sum_n |\langle\psi_{\text{sim}}(t)|O_n|\psi_{\text{sim}}(t)\rangle - \langle\psi_{\text{ex}}(t)|O_n|\psi_{\text{ex}}(t)\rangle|^2}, \tag{6.3}$$

where $|\psi_{\text{sim}}(t)\rangle$ is the state as simulated on the experimental hardware with a given source of error and $|\psi_{\text{ex}}(t)\rangle$ is the exact state.

Limits for classical simulation

We perform the classical simulations using state-of-the-art MPS techniques which were discussed in Ch. 4 [1, 136, 137]. These methods utilise the ability to decompose the full state vector into a product of matrices but in order to ensure the problem remains tractable on classical resources the dimension of these matrices (known as the bond dimension D) is truncated to some maximum value. It has been shown that this truncation is equivalent to throwing away the least important basis states of the reduced density matrix of a bipartition at that bond, i.e. restricting to the D basis states that have the largest Schmidt coefficient [1]. But this is only an accurate compression scheme if the values of the Schmidt coefficients decay rapidly, and so if there are many large coefficients which is the case for highly entangled states, then these methods quickly lead to large errors.

In Fig. 6.1(a) we plot the time-dependence of the entanglement entropy beginning in a product state, $|\Psi(0)\rangle = |\uparrow,\downarrow,\uparrow,\downarrow,\cdots\rangle$, and it can be seen that the entanglement grows linearly in time [146, 153, 154]. However, the bond dimension required to capture this linear growth must grow exponentially, and we can see that truncating to only the most important basis states at each time significantly distorts the entanglement growth. Here we have used a 4th order two-site TEBD algorithm [157] with particle number and total spin conservation, and we truncate the bond dimension by performing singular value decompositions on each neighbouring pair of two-site tensor and then only retain components with the D largest singular values.

But we can ask, if we restrict the bond dimension to values that are efficiently simulable on classical computers, how then do the errors in the observables compare to the errors produced through experimental imperfections in analogue simulation? We include the results of this analysis in Fig. 6.1(b-d) for different observables where we compare the values to the case for the calculation with $D = 1024$ using Eq. 6.3. We can see that these errors grow exponentially in time and reach values that are on the order of 100% in some cases. We will see below that these are significantly larger than those from a calibration uncertainty in analogue simulation. This analysis indicates that timescales greater than $tJ \sim 3$ (even in one-dimension) are significantly beyond what is possible to simulate with the state-of-the-art classical algorithms and while it may be possible to extend this using an advanced supercomputer this would not allow for a significant timescale increase due to the need to exponentially scale the number of resources for only a linear increase in performance (see Fig. 6.1(a)). This comparison will also only get worse if we simulate two-dimensional systems, as correlations will still propagate linearly, but now in all directions, meaning that the dynamics can entangle many more particles in the same time compared to 1D.

Note that one could perform this analysis using different MPS time evolution

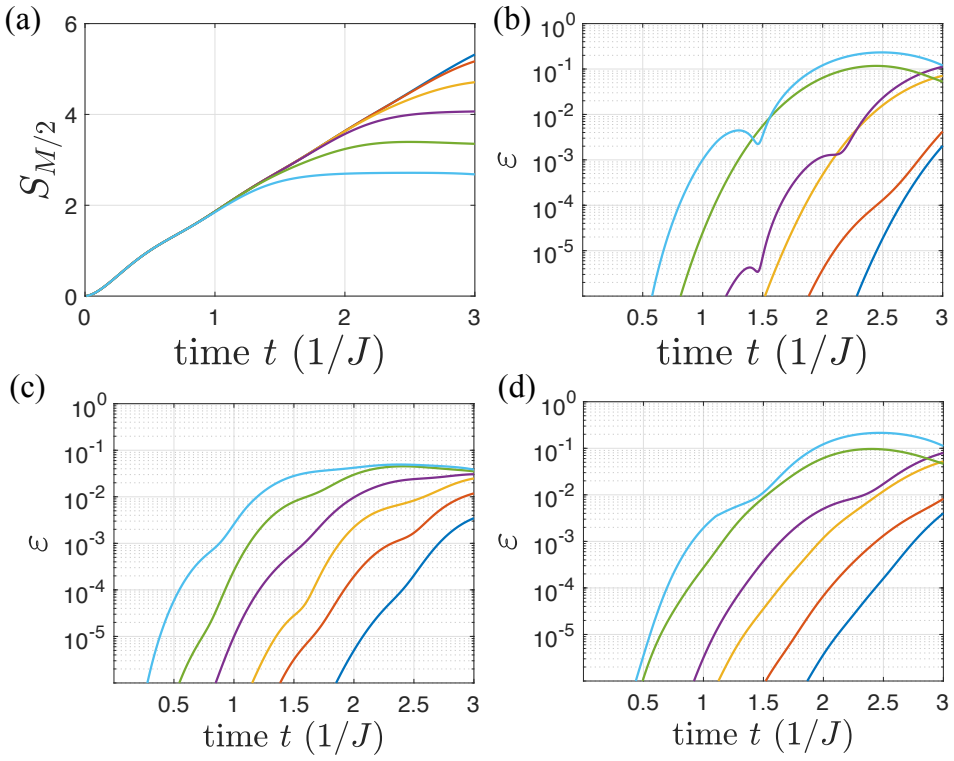

Figure 6.1: Errors in classical simulation of the Hubbard model upon restricting the bond dimension, $D = \{512, 256, 128, 64, 32, 16\}$ (blue,red,yellow,purple,green,cyan), compared to $D = 1024$. (a) Entanglement entropy at the centre bond. (b) Error (Eq. 6.3) in $O_n = c^\dagger_{n,\uparrow} c_{n,\uparrow}$. (c) $O_n = c^\dagger_{M/2,\uparrow} c_{n,\uparrow}$ (d) $O_n = c^\dagger_{M/2,\uparrow} c_{M/2,\uparrow} c^\dagger_{n,\uparrow} c_{n,\uparrow}$. System size, $M = 20$.

algorithms [160, 206] and even different ways that we could perform the compression to a lower bond dimension such as through a variational approach [1]. These will also lead to quantitative differences, but we do not expect any to give a significant advantage or allow a classical simulation to evolve to significantly longer times.

6.2 Sources of errors in analogue simulators

State preparation

In Fig. 6.2 we plot the errors in the observables of the Hubbard model due to an error in the preparation procedure of the initial state, $|\Psi(0)\rangle = |\uparrow,\downarrow,\uparrow,\downarrow,\cdots\rangle$. This can arise from thermal fluctuations during the preparation process which can result in certain particles having enough energy to escape the optical trap creating defects in the periodic initial state. For state-of-the-art experiments this has $\sim 1\%$ chance of occurring, so in the following we assume that in our 20-site system that only one defect will be manifested in a single simulation.

In order to model this we remove a particle from a single lattice site at time $t = 0$ and perform different simulations for the removal at different sites. In (a) we average the global error, Eq. 6.3, over removing the particle at each lattice site. In (b-d) we show the local error upon removing the particle at a particular lattice site, where the initial position of the removed particle is indicated in the legend. We can see that while the average error is large, even at initial times, this is dominated by local errors around the position of the incorrectly prepared site. We can see that at positions far away that the errors are negligible.

Note that these are the error values given that the state has been incorrectly prepared. But as this will only occur $\sim 1\%$ of the time, these values should be multiplied by 10^{-2} before comparing to the errors induced through the calibration errors.

The Hamiltonian

It is also possible that there are additional mechanisms influencing the dynamics in analogue simulation experiments. Typically in optical lattice experiments we

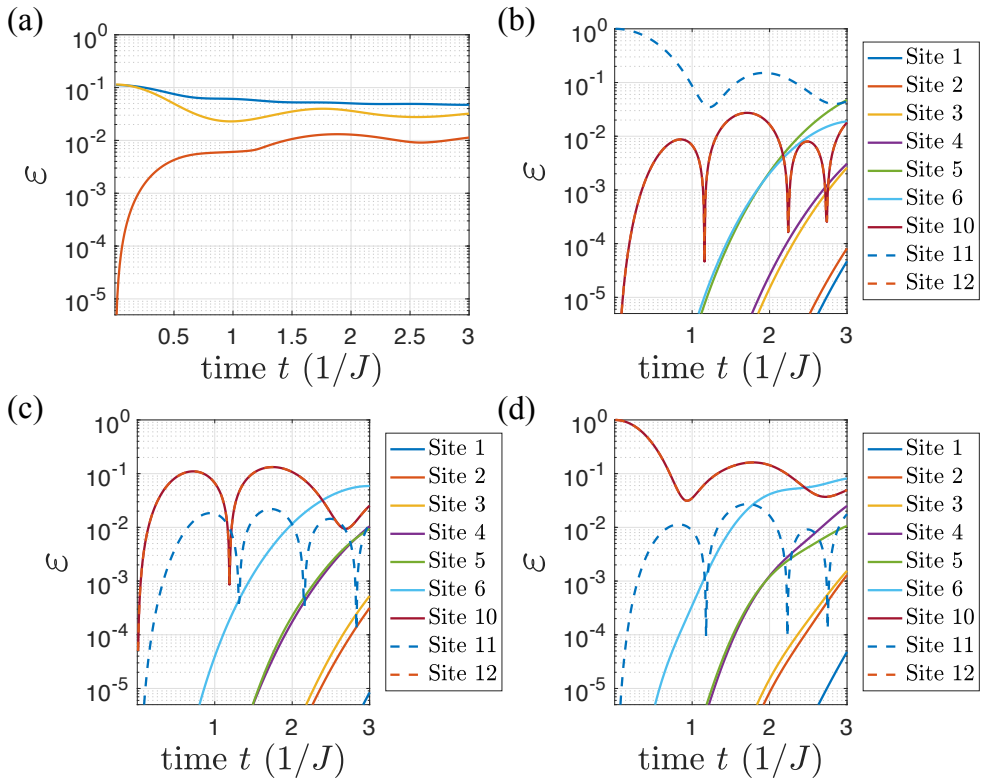

Figure 6.2: Errors in the Hubbard model due to an error in the preparation of the initial state for system size, $M = 20$. (a) Global error (Eq. 6.3) averaged over removing a single particle at one lattice site in the initial state. Errors in $O_n = c^\dagger_{n,\uparrow}c_{n,\uparrow}$ (blue), $O_n = c^\dagger_{M/2,\uparrow}c_{n,\uparrow}$ (red) and $O_n = c^\dagger_{M/2,\uparrow}c_{M/2,\uparrow}c^\dagger_{n,\uparrow}c_{n,\uparrow}$ (yellow). (b-d) Local errors for removing a particle from the initial state at a particular lattice site (indicated in the legends). (b) $O = c^\dagger_{n=11,\uparrow}c_{n=11,\uparrow}$. (c) $O = c^\dagger_{M/2,\uparrow}c_{n=11,\uparrow}$. (d) $O = c^\dagger_{M/2,\uparrow}c_{M/2,\uparrow}c^\dagger_{n=11,\uparrow}c_{n=11,\uparrow}$.

can tune the parameters such that only nearest neighbour tunnelling and onsite interactions are important [25], if the laser intensity is large enough to suppress longer range terms. The first order corrections to this approximation will take the form of a next-nearest neighbour tunnelling,

$$H_{Jnn} = -J_{nn}\sum_{n,\sigma}\left(\hat{c}^\dagger_{n,\sigma}\hat{c}_{n+2,\sigma} + h.c.\right), \tag{6.4}$$

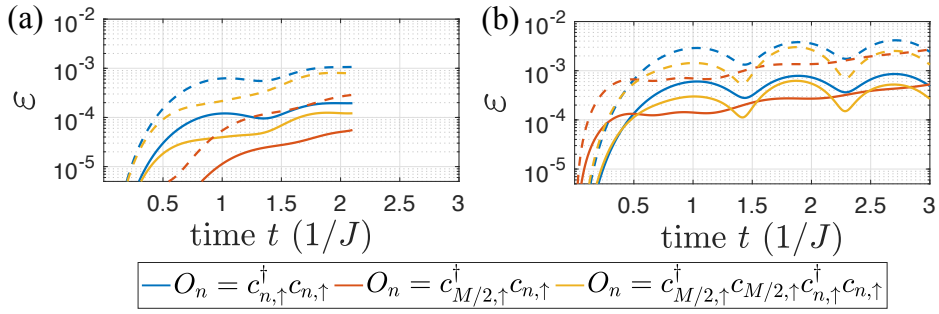

Figure 6.3: Errors in the Hubbard model due to the presence of additional terms in the Hamiltonian for system size, $M = 20$. Errors in $O_n = c^\dagger_{n,\uparrow}c_{n,\uparrow}$ (blue), $O_n = c^\dagger_{M/2,\uparrow}c_{n,\uparrow}$ (red) and $O_n = c^\dagger_{M/2,\uparrow}c_{M/2,\uparrow}c^\dagger_{n,\uparrow}c_{n,\uparrow}$ (yellow). We compare the cases where the terms have a magnitude of 1% (solid) and 5% (dashed) compared to the nearest neighbour tunnelling J and the onsite interactions U. (a) Errors due to the inclusion of a next-nearest neighbour tunnelling term, Eq. 6.4. Due to the increased growth of entanglement in this case, accurate results can only be calculated up to $TJ \sim 2$. (b) Errors due to the inclusion of a nearest neighbour interaction, Eq. 6.5.

or a nearest neighbour interaction,

$$H_{Vnn} = V_{nn} \sum_n \left(\hat{n}_{n,\uparrow} + \hat{n}_{n,\downarrow}\right)\left(\hat{n}_{n+1,\uparrow} + \hat{n}_{n+1,\downarrow}\right). \tag{6.5}$$

The ratio of V_{nn}/U and J_{nn}/J can be tuned by varying the intensity of the applied laser potential, that as the intensity increases these ratios are reduced. However, increasing the intensity also reduces J, which then slows the dynamics manifested in the system. This means that careful tuning of these parameters is necessary in order to mitigate these unwanted terms while ensuring that the tunnelling rates are fast enough in order that sufficient dynamical features can be observed in timescales before the effects of heating and decoherence become important. Typically, these values are $< 1\%$ with values for $J \sim 1$ kHz.

In Fig. 6.3 we plot the resulting errors in the observables upon including one of these additional terms at the level of 1% (solid) and also 5% (dashed) in order to exaggerate their effects and be able to understand their influence. For values around

1% we can see that the errors are smaller than those induced from a calibration error on the level of 0.1%.

Additional corrections could arise from strong interactions mixing with higher energy bands, the dominant effect of this would be to renormalise the onsite and tunnelling coefficients, however, as the band gap energy is typically between $10 - 100$ kHz, and we are considering interactions on the order of J, these effects will give rise to corrections to the J and U terms that are much smaller than the level of calibration errors that we are considering.

Time limits for propagation in analogue simulators

The other element to consider for analogue simulators is that decoherence and heating can create errors that grow in time, and that these will at some point dominate over every other source of error. These come from sources that are again typically well characterised in experiments [207] including spontaneous emission [208, 209] and noise on the trapping lasers [210, 211]. First we incorporate the latter and perform simulations of the Hubbard model with time dependent parameters where the fluctuations in U and J are anti-correlated, i.e. if the laser intensity increases, the potential barrier height increases which gives rise to a lower tunnelling rate but a larger onsite interaction strength. In Fig. 6.4(a-b) we explicitly compare these errors to those produced from a calibration error (see the discussion in the next section), where the calibration uncertainty is equal to the relative uncertainty in the value for the laser intensity, Δ, and we calculate the parameters $U(t)$ and $J(t)$ from the resulting Wannier functions arising from the new potential at each time. The errors in each case have the same qualitative time dependence where they saturate after a rapid initial increase but are at a much lower magnitude compared to the effects from a calibration uncertainty.

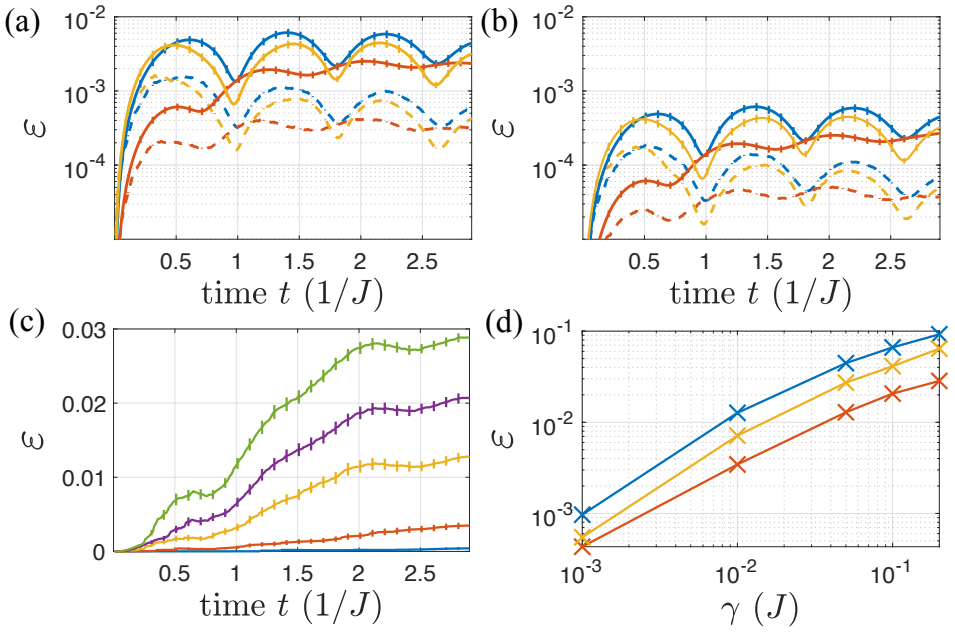

Figure 6.4: (a-b) Comparison of the calibration errors (solid) to the errors from laser fluctuations (dashed) in the Hubbard model for different observables and magnitudes of error, $\Delta = 1\%$ (a) and $\Delta = 0.1\%$ (b). We compare the errors, Eq. 6.3, in $O_n = c^\dagger_{n,\uparrow} c_{n,\uparrow}$ (blue), $O_n = c^\dagger_{M/2,\uparrow} c_{n,\uparrow}$ (red) and $O_n = c^\dagger_{M/2,\uparrow} c_{M/2,\uparrow} c^\dagger_{n,\uparrow} c_{n,\uparrow}$ (yellow). (c) Errors in $O_n = c^\dagger_{M/2,\uparrow} c_{n,\uparrow}$ due to spontaneous emission with rate $\gamma/J = \{0.001, 0.01, 0.05, 0.1, 0.2\}$ (blue, red, yellow, purple, green). (d) Errors due to spontaneous emission at $tJ = 3$ for different observables with the colour coding as in (a-b). System size, $M = 20$.

We also analyse the effects of spontaneous emission by applying a quantum trajectory approach to the Lindblad master equation [2, 41] where we include independent jump operators at each site, $L_n = \sqrt{\gamma}\,(\hat{n}_{n,\uparrow} + \hat{n}_{n,\downarrow})$. In Fig. 6.4(c-d) we plot the errors in observables where we have exaggerated the values of the spontaneous emission rate, γ, in order to make the error scaling more explicit. For $\gamma = 0.001J$ the level of error is comparable to errors due to calibration uncertainty of 0.1%. Note that state-of-the-art analogue simulations are quoting spontaneous emission rates on the order of 10^{-3} Hz [212] which correspond to values for $\gamma \ll 0.001J$ meaning that in realistic experiments the effects will be significantly smaller for the timescales that

we are considering. This analysis of decoherence and heating allows us to conclude that for the timescale we're interested in, that they can be neglected for typical experiments.

Errors in measurement and readout

We have not considered here other potential sources of errors, such as those arising from an imperfect measurement of these observables. In this case, these errors are well understood and will most likely only contribute a small error that is constant throughout the simulation as these will not affect the observables in a dynamical way. Nevertheless these are important considerations and will need to be brought down to minimum levels. The error analysis presented in this chapter assumes that the errors in the measurement can be neglected as they are much smaller than the errors induced through a calibration error.

6.3 Calibration errors and Trotter errors

We apply MPS techniques to capture the errors in the two different approaches for quantum simulation. Firstly, for the calibration error in an analogue simulation, we sample the model parameters from a normal distribution with some standard deviation given by the value of the calibration error. After performing numerous simulations with different realisations of the parameters, we compare the observables to the target model, which corresponds to parameters with the mean value of these distributions. Experimentally, these parameters are set globally, by some external laser for example, and so the errors can be considered homogeneous. With this in mind we take model parameters that are uniform over the entire system for a given simulation, but we have compared this to the case of local calibration errors and

found no qualitative difference.

Secondly, we calculate the errors in the same observables for a digital quantum simulation which approximates the time-evolution operator with a sequence of two-site gates with a particular time-step, τ. The choice of the decomposition can be of the form of a left-right sweep, [31], or a Suzuki-Trotter decomposition of the odd/even bonds, [1] (in the case of the Hubbard model). We have compared the 2nd and 4th order versions of these methods with errors that scale with τ^2 and τ^4 respectively. For the 4th order sweep methods there are additionally several decompositions which have different ratios of errors against complexity. Here we present results using the version of the 4th order decomposition which gives rise to the lowest errors,

$$(1)^T(1)(1)^T(-2)(1)^T(1)^T(1)^T(1)^T(1)(1)^T(1)(1)(1)(1)(-2)^T(1)(1)^T(1), \tag{6.6}$$

where (s) corresponds to a single left-to-right sweep and $(s)^T$ to a right-to-left sweep with a timestep, $s\tau/12$, such that the total cumulated timestep of all sweeps in Eq. 6.6 give τ. For the Hubbard model there is also the additional choice of further decomposing the two-site operator into a contribution from the tunnelling, J, and the onsite interactions, U. We find that it is more experimentally feasible (i.e. requires fewer logic gates) to decompose these into separate time evolution operators even though this results in a slightly larger error. So it is this version that we present here, but note that we include a comparison of different decompositions in the supplementary material of Ref. [213].

In Fig. 6.5 we plot the results of this analysis for the off-diagonal correlation function for the Hubbard model with $J = U = 1$, beginning in the product state $|\Psi(0)\rangle = |\uparrow,\downarrow,\uparrow,\downarrow,\cdots\rangle$ and for the long range transverse Ising model, with $J_{z,0} = 1 = B = 1$, beginning with all spins projected along the s_x direction, $|\Psi(0)\rangle = |+,+,+,+\cdots\rangle$,

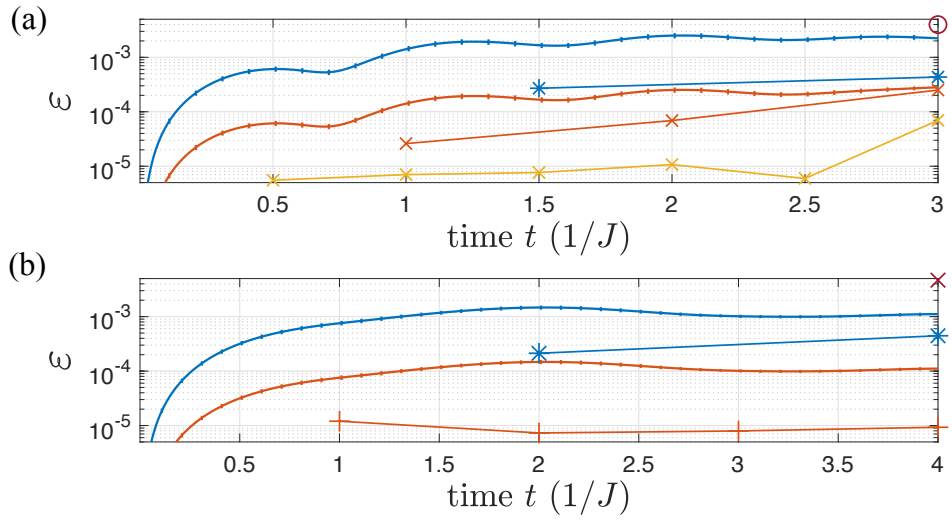

Figure 6.5: (a) Hubbard model, system size $M = 20$. Comparison of the errors in the off-diagonal correlation functions, Eq. 6.3 with $O_n = c^\dagger_{M/2,\uparrow} c_{n,\uparrow}$. For analogue simulation we compare a 1% calibration error (solid blue) and a 0.1% calibration error (solid red). For the digital we have plotted the 4th order decomposition (Eq. 6.6) with a splitting of the interaction and kinetic energy terms, for the time steps $J\tau = 3$ (circles), $J\tau = 3/2$ (stars), $J\tau = 1$ (plus sign) and $J\tau = 1/2$ (crosses). (b) Transverse Ising model, system size $M = 20$. Comparison of the errors in the off-diagonal correlation functions, Eq. 6.3 with $O_n = S^{M/2}_+ S^n_-$. For analogue simulation we compare a 1% calibration error (solid blue) and a 0.1% calibration error (solid red). For the digital we have plotted the 4th order decomposition (Eq. 6.6), for the time steps $J_0\tau = 4$ (crosses), $J_0\tau = 2$ (stars), and $J_0\tau = 1$ (plus sign).

for a system size of 20 lattice sites and spins respectively. The solid lines correspond to the errors in the observable in an analogue simulation comparing a calibration error of 1% (blue) and 0.1% (red). The symbols correspond to the errors in a digital simulation with varying timestep for a 4th order left-right gate sweep. We can see that the errors rapidly increase for short times but then remain approximately constant but with some small oscillation and are similar in both models and simulation approaches.

For the final time ($tJ = 3$ for the Hubbard model and $tJ_0 = 4$ for the Ising model) we extrapolate the critical timestep, τ^*, needed for the errors in the digital simulation to match or exceed the errors in the analogue simulation with a given

level of calibration error. For example, this 4th order decomposition for the Hubbard model has a critical time step of $J\tau^* \approx 2.7$ ($J\tau^* \approx 1$) when comparing to a calibration error of 1% (0.1%), whereas for the Ising model $J_0\tau^* \approx 2.6$ ($J_0\tau^* \approx 1.5$) for a calibration error of 1% (0.1%). Note that these estimates for τ^* only weakly depend on system size and the particular observable, but can be reduced by at most a factor of 3 for some of the more inefficient Trotter decompositions (see Ref. [213]).

Comparing the results for the calibration errors in Fig. 6.5 to the errors in the classical algorithms in Fig. 6.1 it is clear that for sufficiently small levels of calibration errors that the analogue simulation can achieve a much greater accuracy, even for the timescales that we have explicitly considered. Additionally, the errors induced through a calibration uncertainty, are bounded and appear to oscillate around a constant value indicating that the errors will not significantly increase for longer timescales, meaning that we can extrapolate these estimates to benchmark longer time simulations. This then indicates that for this problem, we can accurately simulate the dynamics in regimes that are beyond what we can achieve with the state-of-the-art classical algorithms.

Digital gate count

Specific implementations of digital quantum simulation will involve a competition between the error in the corresponding Trotter decomposition, and the errors associated with individual gates. In order to make some sort of comparison between analogue and digital simulation we have assumed that the total error in a digital simulation arises through the Trotter decomposition which requires either individual gate fidelities of $F > 0.999999$ or a fully fault tolerant algorithm which then comes with additional complexity and restrictions on the types of logic gates that can be applied.

With these considerations taken into account, we calculate the number of logic gates required for a digital simulation to simulate this problem with the same error as the analogue simulation, arising through a calibration error. In particular, we have shown in Ref. [213] that we can extrapolate these results and consider a two-dimensional geometry and simulation times of $TJ = 10$ such that we can go well beyond what we can calculate on a classical computer. We find in this case comparing a 4th order Trotter decomposition to an analogue simulation with a 0.1% calibration error that for NISQ systems, would require on the order of $400,000$ (rotation+CNOT) logic gates and for fully fault tolerant quantum computations with built in error correction, this would require on the order of five million gates (for an inhomogeneous model), which is a factor of 10^3 improvement over previous estimates [201]. This improvement arrises from our problem choice, where we realised that for many applications only the observables need to be accurately simulated and not necessarily the total state fidelities.

6.4 Conclusions

We have quantitatively analysed the effects of various sources of errors in analogue quantum simulators on the dynamics of observables in the Hubbard model, where we have shown that the dominant sources of errors (those due to a calibration uncertainty) give rise to uncertainties that are bounded well below 1% for experimentally achievable levels. This is in contrast to the errors introduced through restricting the precision of classical algorithms to numerically practical levels, indicating that we can currently apply analogue simulators to regimes beyond those that are classically accessible. Furthermore we demonstrated that simulating the dynamics with the same accuracy as the analogue devices on digital simulation is actually within much

closer reach than previous estimates and perhaps this can even be further improved upon finding better optimisations of the logic circuits.

Note also that this comparison was carried out at the quantum advantage point, and so increasing the size of the system (or the length of the time evolution) requires even more digital logic gates to match the accuracy that can be achieved in the analogue experiments. This demonstrates clearly that analogue simulation is the best way to accurately compute observables in these types of problems - provided that the Hamiltonian can be encoded in the native environment of the quantum simulator - and gives a strong indication that analogue simulators can currently demonstrate a quantum advantage.

Chapter 7

Analysis of three body loss in an optical lattice experiment

In this chapter, we present the results of a collaboration with the experimental group of Prof. Hanns-Christoph Nägerl in Innsbruck, where we have studied atomic loss process induced by three-body recombination and the resulting effects on the dynamics of cold atoms in an optical lattice. *

An important aspect for realising quantum simulation is in obtaining detailed and precise knowledge of the microscopic properties of the physical resources in a specific hardware implementation. This is paramount for being able to reliably realise specific dynamical features that can be mapped onto particular target models, see Ch. 2. Throughout this thesis we predominantly consider realising the proposed systems in quantum optical experiments involving ultra-cold atoms confined in an optical lattice and in particular, we are interested in using these systems to explore regimes dominated by strong interactions. However, going beyond the usual ap-

*This work is presented in Ref. [214], for which the theoretical part was written primarily by the author of this thesis. In this chapter we also separately summarise the experimental work for comparison with our theoretical calculations.

proximations presented in Ch. 2 is necessary when considering these experimental systems with dense atomic samples and strong interactions as this can introduce strong Efimov resonances [215] leading to three-body induced losses. This can have a significant impact on the behaviour of the atoms in this system, requiring us to include additional mechanisms in our theoretical description that go beyond the usual Bose-Hubbard model. Although these effects are not always detrimental, for example once these loss effects begin to dominate over the other coherent processes, novel many-body phases have been predicted to form [216–223] which are stabilised through a continuous quantum Zeno suppression of triply populated lattice sites. It is clear then that investigating these features present in these experiments is important, firstly, for defining the regimes where these novel phases can exist so that we are more easily able to realise them with a quantum simulation experiment. But more importantly in the context of this thesis, understanding these loss mechanisms are necessary for evaluating the dominant errors and thus the limitations of applying these experiments as a simulator for Hubbard type models.

7.1 Introduction

As described in Ch. 2, ultracold atomic gases in optical lattices provide a platform for investigating novel many-body coherent and dissipative dynamics in a highly controllable environment [19, 33, 41, 224, 225]. In particular, strong loss processes such as three-body recombination can exhibit the continuous quantum Zeno effect [226–229], where dissipation can prevent certain coherent dynamics from taking place [230, 231]. Although we often seek to avoid these loss mechanisms, there are proposals to use them to realise effective three-body interactions through three-body loss [232–235]. However, there are important open questions related to how these

dynamics work when the loss rates become comparable to or larger than the energy band gap, invalidating a standard Bose-Hubbard (BH) description. In this work, we explore the interplay between coherent and dissipative dynamics for bosonic atom pairs, comparing the dependence of the three-body loss on the interaction strength to theoretical models beyond the standard BH Hamiltonian that combine lattice dynamics with on-site three-body dynamics that takes into account the renormalisation of the coefficients for coherent interactions and loss. Understanding these effects across different regimes provides a path for future studies of exotic quantum phases induced by strong local three-body loss [216–223].

We make use of the control available in optical lattice systems and study interacting Caesium atoms in the vicinity of a broad Feshbach resonance [215], which allows for the s-wave scattering length a_s to be tuned in the experiment and therefore the interactions can be varied from weak to strong and from repulsive ($a_s > 0$) to attractive ($a_s < 0$). The two-body interaction mechanisms of the system are well understood [80, 236, 237] and we can accurately prepare an initial state with two atoms on each site. Quenching to strong interactions then leads to the formation of pairs, known as doublons, which are stable due to a lack of dissipative mechanisms present in the experiment that can remove energy on short timescales [238, 239]. However, by increasing the interaction strength one enters a regime where the energy associated with strong three-body dissipative processes [240, 241] can easily exceed the band gap in the lattice. This raises questions on how to treat this system with an effective BH model [27, 80, 86, 236, 242], including the question whether off-site loss mechanisms become important in understanding the resulting dynamics.

Below, we investigate the effects of strong three-body losses starting with doubly occupied sites and find unexpected phenomena arising from an off-resonant loss process where a single particle tunnels into a virtual triply occupied site. For strong

attractive interactions, we observe an interesting nonlinear dependence of the doublon decay rates on a_s, and attempt to model this with a BH-type model resulting in values for decay rates that are too large if nearest neighbour losses are included, but too low if they are simply ignored. This indicates that the mixing with higher energy bands is causing a renormalisation of both the off-site and the on-site coefficients. When further increasing the attractive interaction strength, we observe a decrease on the decay rate similar to a quantum Zeno type suppression [231], which we expect to manifest in this region and would suppress the occurrence of triply occupied sites through the strong three-body loss terms. However, through first-principle calculations of the on-site losses induced through mixing with three-body Efimov states [240, 241, 243–245], we find that on-site loss rates are too low to induce this type of suppression which instead suggests that the decrease of the decay rates is due to an additional renormalization of the terms responsible for the coherent dynamics.

Experimental set-up

The experiment consists of a pure Bose-Einstein condensate (BEC) of 10^5 Cs atoms confined in a three-dimensional optical lattice. The system is prepared in an $n = 2$ Mott insulating state by an adiabatic ramping of the lattice potential to an initial depth set to $V_{\mathrm{x,y,z}} = 30\, E_{\mathrm{R}}$, where $E_{\mathrm{R}} = h^2/(2m\lambda^2)$ is the atomic recoil energy with the mass m of the Cs atom.

To start the experimental procedure, a magnetic field is ramped around a Feshbach resonance to tune the interaction strength to a particular value of repulsive ($a_s > 0$) or attractive ($a_s < 0$) interactions. The lattice depth in one-direction, V_{z}, is then quenched to the desired value and the system is then allowed to evolve for a particular hold time, t_{H}, after which the dynamics are interrupted by quenching the lattice depth back up to its original value and the remaining number of doublons are

then measured. The doublon decay rate is then extracted from these measurements by fitting a decaying exponential to the measurement data. The resulting experimental values for the doublon decay rates are presented in Fig. 7.1 for different scattering lengths, a_s and lattice potential depths, V_z, where these are then compared to the theoretical predictions which are explained below.

7.2 Analysis of the effects of three-body recombination

We attempt to model the behaviour in the experiment with an extended Bose-Hubbard model, which consists of on-site and nearest-neighbour two-body interactions as well as dissipative on-site three-body loss. The Hamiltonian is given by ($\hbar = 1$),

$$\begin{aligned} H = &-J\sum_{\langle i,j\rangle} b_i^\dagger b_j + \frac{U}{2}\sum_i b_i^\dagger b_i^\dagger b_i b_i + \tilde{U}\sum_i [b_i^\dagger b_i^\dagger b_i b_{i+1} + b_i^\dagger b_{i+1}^\dagger b_{i+1} b_{i+1} + h.c.] \\ &- i\frac{\gamma_3}{12}\sum_i b_i^\dagger b_i^\dagger b_i^\dagger b_i b_i b_i \,. \end{aligned} \tag{7.1}$$

The coefficients, calculated through the Wannier functions associated with the lowest Bloch band centred at a position z_i in the longitudinal direction, $w(z - z_i)$, and r_i in the radial direction, $w_\perp(\vec{r} - r_i)$, are given by

$$\begin{aligned} U &= \frac{4\pi\hbar^2 a_s}{m}\int d\vec{r}|w_\perp(\vec{r} - r_i)|^4 \int dz|w(z - z_i)|^4, \\ \tilde{U} &= \frac{4\pi\hbar^2 a_s}{m}\int d\vec{r}|w_\perp(\vec{r} - r_i)|^4 \int dz|w(z - z_i)|^2 w^*(z - z_i)w(z - z_{i+1}), \\ \gamma_3 &= 2L_3(a_s)\int d\vec{r}|w_\perp(\vec{r} - r_i)|^6 \int dz|w(z - z_i)|^6 \,. \end{aligned} \tag{7.2}$$

Furthermore, a_s denotes the scattering length, J the single particle nearest-neighbour tunnelling amplitude, and $L_3(a_s)$ is the experimentally measured three-body loss parameter that strongly varies with a_s [215]. The approximation of restricting the dynamics to 1D is valid as long as the radial trapping frequency is much larger than the longitudinal trapping frequency, $\omega_r \gg \omega_z$. Additionally, note that we have taken into account three-body Efimov resonances by incorporating the short distance cut-off term, that has to be introduced to regularize the zero range three-body pseudo-potential [246, 247], as a pre-factor for a three-body delta-function contact interaction [232, 248]. These Efimov resonances are large loss features in the energy spectrum for three atoms, each interacting pairwise through a two-body contact interaction. When the two-body scattering length is large enough to strongly couple higher single particle states, these features can manifest themselves strongly rescaling the bare two-body energies and through coupling with molecular bound states introduces renormalised coherent interactions as well as effective decay rates from the optical trap [240, 241].

Note that we neglect terms corresponding to site-to-site three-body loss. For large values of $|a_s|$, it would usually be expected that there would be large contributions from off-site loss processes. However, this picture only holds for sufficiently small loss rates compared to the band separation energy when the lowest-band Wannier functions provide a good local basis. In the presence of large loss rates, as is the case for large $|a_s|$, the Wannier states mix with states from higher bands and we find that the initial overlaps of nearest-neighbouring wavefunctions lead to a very rapid initial decay, although only resulting in a very small loss of atoms. This happens on timescales much faster than the experimental measurements, resulting in renormalised states that are more localized on each lattice site. Atom loss is then driven by on-site decay only, combined with non-resonant tunnelling processes, including

density-assisted tunnelling from nearest neighbour interactions. Furthermore, we believe that this density-induced tunnelling can substantially modify the coupling of the initial state into a virtual triply occupied site which then, through mixing of the on-site three-body eigenstates with diatomic molecular states, leads to decay of atoms from the trap, [240, 241].

We attempt to capture these mechanisms in two complementary approaches. In a first approach, we calculate the lattice coefficients of the extended Bose-Hubbard model using the single-particle Wannier functions associated with the lowest Bloch band, and use for the on-site loss the analytical (zero-range, zero-temperature) fitting function for the three-body recombination rate coefficient L_3 for Cs atoms, with parameters extracted from fitting the experimental data in Ref. [215]. We also include single-particle loss terms, which account for residual heating induced by the lattice light and/or background gas collisions [81]. We then evolve the initial doubly-occupied Mott state using a Lindblad master equation (see Ch. 5), and extract the decay rate from an exponential fit to the computed doublon density. The master equation is given by,

$$\frac{d}{dt}\rho = -i[H_{\text{eff}}, \rho] + 2L\rho(t)L^\dagger + 2L_s\rho(t)L_s^\dagger, \tag{7.3}$$

where $L = \sqrt{\gamma_3/12}b_i^3$. We have included a single particle loss rate, $H_{\text{eff}} = H + H_s$, where

$$H_s = -i\tilde{S}\sum_i b_i^\dagger b_i, \tag{7.4}$$

and $L_s = \sqrt{\tilde{S}}b_i$. For the loss rate, we use a value $\tilde{S} = 0.006\,\text{Hz}$ [81]. We then calculate the time-dependent expectation value of the total doublon number in the system, and fit an exponential to this function, $\langle\hat{N}(t)\rangle/N(0) = \exp(-\Gamma t)$, to extract

the decay rate, Γ.

In our second approach, we again extract the decay rates from the time evolution of the master equation, but account for modified lattice parameters. Specifically, we now use the lowest on-site three-body energy level obtained by using the hyperspherical adiabatic representation [240, 244], which allows for energy shifts to the lowest Bloch band due to three-body interactions mixing with higher energy bands. Similar to Ref. [243], these calculations provide the on-site decay rates of three-body energy levels. For the on-site two-body interactions we also take into account mixing with higher energy bands using the result presented in Ref. [84] for a single harmonic trap. Note that for now, we do not modify the nearest-neighbour tunnelling and interaction terms. Inserting these coefficients into our extended Bose-Hubbard model (Eq. 8.3) allows us to approximate these dynamical features with an effective single band Hubbard model.

In Fig. 7.1, we compare the atomic decay rate obtained from the two approaches with the experimental data. We find that for repulsive interactions the decay rates increase with increasing a_s, in accordance with the predictions. We also find that the first approach (solid lines) predicts a minimum in the decay rate around $a_s = -800\ a_0$, which coincides with the strong Efimov resonance in the L_3 parameter [215], and which is not observed in our lattice experiment. Our second approach (crosses), incorporating mixing with higher energy bands, predicts a suppression of the L_3 resonance and we obtain values for the decay rate that qualitatively match the experiment. This peak suppression is due to the interplay between the Efimov resonance, the mixing with higher bands and the lattice potential, which creates a spread of the particles in momentum space. This spread is of the same magnitude as the temperature-induced energy spread that was found to suppress the Efimov resonance in previous measurements [215, 249]. In addition, effects of mixing with

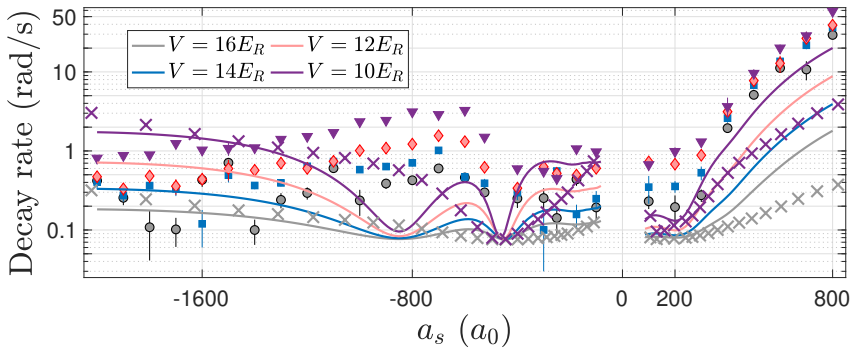

Figure 7.1: Decay rates for strong interactions. Experimentally measured doublon decay rate with V_z =10 (circles), 12 (squares), 14 (diamonds), 16 (triangles) E_R plotted against a_S. Also included are the theory predictions: the solid lines use only the lowest Bloch band whereas for the crosses we have included the renormalised onsite coefficients through mixing with higher energy bands. This figure is partially reproduced from Ref. [214] and includes experimental data from our collaborators as well as theoretical results from the author of this thesis.

higher excited states introduce further modifications to the on-site (which are taken into account with our three-body energy level calculation), but also the off-site (an effect which is not currently included in our model), loss coefficients. A detailed understanding of this will require future analysis on the renormalisation of the nearest neighbour terms, however this part of the analysis confirms that both the off-site and on-site loss coefficients must be modified by mixing with higher energy bands in the lattice. Specifically, we know that the on-site coefficients must be rescaled due to the experiment not observing the large Efimov resonance and we know that the off-site processes must also be affected, because this is the most dominant feature not currently taken into account and would explain the lack of agreement between theory and experiment.

For positive scattering lengths, the calculation with the renormalised onsite coefficients (solid lines with symbols) leads to an even larger discrepancy compared to the naive calculation with the bare coefficients in the lowest band (dotted lines). This is a strong indication that in this regime there are also important corrections

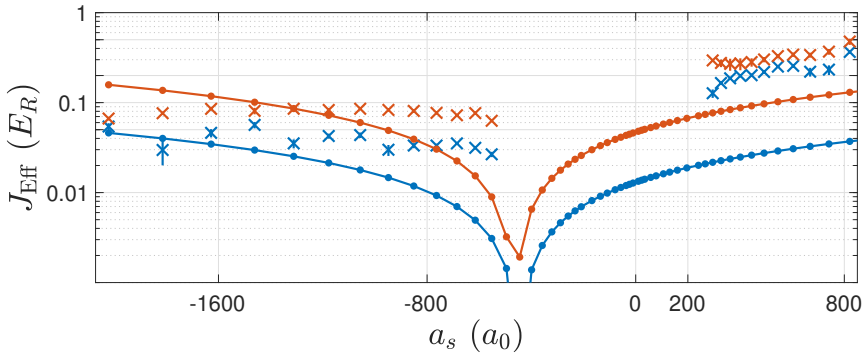

Figure 7.2: The predicted renormalised tunnelling coefficients, $J_{\mathrm{Eff}} = |3\sqrt{6}\tilde{U} - \sqrt{6}J|$ (solid line with crosses) from the model which includes coupling to higher energy bands, such that Eq. 7.5 (which is only valid for $J \ll U$) reproduces the experimentally measured decay rates in Fig. 7.1. We also compare to these tunnelling values predicted from the extended Bose-Hubbard model (dotted line with filled circles), for $V_z = 10(\,\mathrm{red}), V_z = 16(\,\mathrm{blue})$, respectively.

to the nearest-neighbour tunnelling processes arising from the mixing with states in higher energy bands. Additionally, both approaches predict a much larger dependence on the trapping potential than is experimentally observed, indicating that the renormalisation effects may be stronger for tighter trapping potentials.

Furthermore, including corrections from strong interactions (solid lines with symbols) predicts that, for increasingly large attractive interactions, the decay rates also increase, in sharp contrast to the experimental data. We initially interpreted the trend in the measurements to be due to a quantum-Zeno-type suppression of the losses [231], but the values of the renormalised coefficients in our calculation predict on-site loss rate values that are too low for this to occur (see Ref. [214]). Instead, we believe that this trend can be accounted for through the incorporation of two effects not currently taken into account in our model: mixing between ground and excited on-site three-body states [237] and a further renormalisation of the effective tunnelling elements.

The experiment from the Innsbruck group, enables us to estimate what the values

of the rescaled tunnelling coefficients must be, so that the current model reproduces the measured decay rates. This gives us a rough indication of these effects and allows us to predict an upper bound for the rescaling of the coherent tunnelling terms. If we set the single particle loss rate, $\tilde{S} = 0$, we can calculate the decay rate analytically through second-order perturbation theory with $J \ll U$,

$$\Delta E^{(2)} = -2\frac{|3\sqrt{6}\tilde{U} - \sqrt{6}J|^2}{E_{3B}(a_s) - 2U_{2B}}, \tag{7.5}$$

where $E_{3B}(a_s)$ and U_{2B} are the energy shifts due to three and two interacting atoms, respectively. The decay rate is then found through

$$P(t) = \langle\phi|e^{i(\Delta E^{(2)*} - \Delta E^{(2)})t}|\phi\rangle = e^{-i2\mathrm{Imag}(\Delta E^{(2)})t}, \tag{7.6}$$

giving us an expression for the decay rate, $\Gamma = 2\mathrm{Imag}(\Delta E^{(2)})$. We then use this expression to find the rescaled value for $J_{\mathrm{Eff}} = |3\sqrt{6}\tilde{U} - \sqrt{6}J|$, such that the model (with rescaled on-site coefficients) gives rise to the experimentally observed decay rates. Note that we only perform this fit for larger values of $|a_s|$ (where the perturbation theory is most valid) because for lower scattering lengths the calculated decay fits the experimental measurements quite well and is dominated by the single particle losses. Our obtained estimates for J_{Eff} (Fig. 7.2) predict a strong enhancement of the tunnelling rates for positive scattering lengths. For negative a_s there is a saturation of the magnitudes of the rescaled tunnelling rate, an effect that is more pronounced for shallow lattices. This analysis shows that, we can drastically improve the quantitative agreement between the calculations and measurements with only a relatively small variation of the tunnelling terms. This simple estimate and the calculation of the renormalised onsite loss coefficients, indicate that the reduction in the overall decay rate is not due to a continuous quantum Zeno type suppression, but instead

arises from slower coherent dynamics induced by the strong onsite losses mixing with higher energy states. This then has implications for future experiments attempting to realise the novel many-body phases induced by strong three-body losses [232–235].

7.3 Conclusions

In summary we have investigated the dynamics of bosonic doublons across a broad Feshbach resonance. We found that for strong two body interactions (both attractive and repulsive) the dynamics are dominated by off-resonant decay processes induced by on-site three-body losses. We found that there is a large renormalisation of the coefficients in both the dissipative and coherent processes, induced by strong on-site losses and interactions mixing with higher energy bands, which lead to a lack of a quantum Zeno suppression in a regime where we would normally expect to find it. Additionally, we have confirmed that in order to explore the regime of strong interactions in highly dense lattice systems in these experimental architectures, then mechanisms that go beyond the standard Hubbard model must be incorporated to accurately describe the dynamical features.

The reported experiments and our theoretical analysis not only form the basis to elaborate more refined descriptions of strongly interacting and dissipative lattice bosons, which is important for high-fidelity molecular formation, [250], but also opens routes to investigate exotic many-body states, such as antiferromagnetic states formed by attractively bound doublons [216], quantum lattice liquids of repulsively bound doublons [217] or those that are stabilised by an effective three-body hardcore constraint [216–223].

Part III

Interactions in Topological Band Structures

Chapter 8

Superfluid properties of bound pairs in a Creutz ladder

There is a growing interest in using cold-atom systems as a quantum simulator to explore the effects of strong interactions in systems that have band structures characterised by a non-local order parameter, which result in novel global features that are in a separate classification from conventional phases [251, 252], so called topological insulators. While the single particle properties are generally well understood and have recently been measured experimentally [253–255], there are still many open questions relating to interacting quantum systems in these band structures. Recent experimental advances in cold atom systems now allow us to use optical lattice experiments to study these questions and investigate the physics of topological quantum systems in the presence of strong interactions [67–74, 256–258]. In this chapter we investigate the effects of interacting bosons in a topological band structure where the single particle kinetic energy is completely frustrated, [259–269], and find that the topology enhances the formation of bound pairs allowing them to remain stable for higher temperatures. We find that going beyond the regime of perturbative in-

teractions that pair superfluid phases can be engineered, prepared and detected in current optical lattice experiments. This opens up ways of exploring the complex interplay between topological band structures and strongly interacting systems with current analogue quantum simulators allowing for experimental investigations into the effects on the many-body phases and on the resulting dynamical properties.

8.1 Introduction

We analyse the properties of bosons in a Creutz ladder (shown in Fig. 8.1) which is characterised by complex tunnelling amplitudes along the legs of the ladder while also having diagonal tunnelling components between the legs [270]. In this system geometrical frustration results from the combination of these tunnelling terms where there is a destructive interference effect that completely suppresses the single particle kinetic energy and gives rise to flat energy bands. However, it has been proposed that including an onsite interaction can lead to the formation of bound pairs that are stable even for infinitesimal interaction strength which now have dispersion completely dictated by the interactions [263–269]. There is growing interest in repulsively interacting bound pairs in general cold-atom systems [238, 271] as well as in more novel band structures [272–277], but pairs are usually only stable for large interaction strengths compared to the tunnelling. By analysing the dispersion relation for single bound pairs in the Creutz ladder beyond the limit of weak interactions we find that in contrast to those formed in conventional lattices, the pair kinetic energy grows with increasing interaction strength. This shows that the topology of the lattice plays an important role and enhances the formation and properties of these pairs.

After investigating the properties of single pairs we consider the many-body case, where the system has been shown to be able to realise a phase transition between a

charge density wave (CDW) and a superfluid phase made up entirely of pairs [263, 264]. Going beyond the previous works on this system [263, 264] which analyse the properties of these novel phases for low densities, we investigate the system for higher densities and find large density regions where both CDW and pair superfluid phases exist simultaneously, which is an indication of a lattice supersolid, [278–286], but in a regime where there are no contributions from single particles. Additionally, we offer new perspectives in the ability to prepare and detect these phases, by first proposing an experimental preparation scheme for a pair condensate using adiabatic manipulations of the optical lattice potential [97, 287], which can be achieved in timescales that are reachable in current experiments. Secondly, we illustrate that the domination of pair over single particle correlations survives for a large range of finite temperatures. For experimental detection we calculate dynamical properties so as to be able to connect to local measurements following an applied perturbation which also allowed us to analyse the features in the dispersion relations of the excited states. Finally, we determine the properties of these phases by mapping to a universal Luttinger liquid description.

The model

In Fig. 8.1 (a) we include the Creutz ladder which is characterised by complex tunnelling amplitudes that, through a destructive interference effect, gives rise to a dispersion relation with only flat energy bands (see Fig. 8.1 (b)). These two bands are also characterised by a non-zero integer Zaks phase, indicating that they have a non-trivial topology which manifests itself in the existence of edge states [270, 288, 289]. There are various ways to produce this experimentally, for example most proposals utilise a synthetic dimension [270, 290, 291], where each leg of the ladder corresponds to two atomic internal states. However including interactions will then require careful

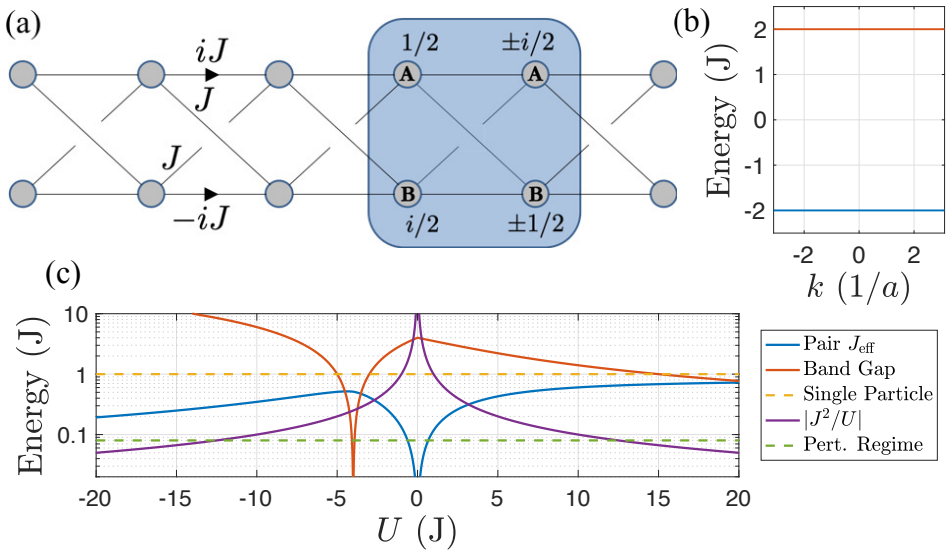

Figure 8.1: Creutz ladder geometry (a) and band structure (b), where a is the lattice spacing between the unit cells and we have highlighted in the blue box all non-zero components of the Wannier functions associated with each (highest $+$, lowest $-$) flat band. We have highlighted the two sites of the unit cell as A and B. (c) For the case $U \equiv U_A = U_B$ a comparison of the effective nearest-neighbour pair-tunnelling in the lowest energy dispersive two-atom bound state, J_{eff} (blue) to that for conventional doublons with a kinetic energy, $|J^2/U|$ (purple). The green dashed line indicates an upper energy bound for the weakly interacting regime and the red line is the energy band gap between the lowest dispersive two-atom band and the first excited one, see blue and red curves in Fig. 8.2.

tuning of the inter-component and intra-component strengths. If there are non-zero inter-component or unequal intra-component interactions then this will result in additional terms appearing, complicating the simple bound state picture presented below, however if they are small, will lead to qualitatively the same features which we demonstrate explicitly below. We also propose an alternative realisation, requiring only atoms in a single internal state confined in a dimerised ladder optical potential, so is not affected by these concerns. All the tunnelling amplitudes, with the correct phase relations, are produced from only two applied fields to facilitate multiple two-photon Raman assisted tunnelling processes (see section 8.4).

Explicitly the Hamiltonian including an onsite two-body contact interaction, U_A

for the A-sites and U_B for the B-sites, is given by ($\hbar = 1$),

$$\begin{aligned} H = \sum_n J \left[\hat{b}_n^\dagger \hat{a}_{n+1} + \hat{a}_n^\dagger \hat{b}_{n+1} + i\hat{b}_n^\dagger \hat{b}_{n+1} - i\hat{a}_n^\dagger \hat{a}_{n+1} + h.c. \right] \\ + \sum_n \left[\frac{U_A}{2} \hat{a}_n^\dagger \hat{a}_n^\dagger \hat{a}_n \hat{a}_n + \frac{U_B}{2} \hat{b}_n^\dagger \hat{b}_n^\dagger \hat{b}_n \hat{b}_n \right], \end{aligned} \tag{8.1}$$

where $\hat{a}_n^\dagger$ ($\hat{b}_n^\dagger$) creates a particle on the A (B) site in the nth unit cell. In order to analyse the bound states in this system, it is advantageous to apply a basis transformation to the local Wannier basis that diagonalises the single particle Hamiltonian. This basis is shown in blue in Fig. 8.1 (a) and the transformation is,

$$\begin{aligned} \hat{a}_n &= \frac{1}{2}\hat{W}_n^+ + \frac{1}{2}\hat{W}_n^- - \frac{i}{2}\hat{W}_{n+1}^+ + \frac{i}{2}\hat{W}_{n+1}^-, \\ \hat{b}_n &= -\frac{i}{2}\hat{W}_n^+ - \frac{i}{2}\hat{W}_n^- + \frac{1}{2}\hat{W}_{n+1}^+ - \frac{1}{2}\hat{W}_{n+1}^-, \end{aligned} \tag{8.2}$$

where the $\hat{W}_n^\pm$ annihilate a boson at unit cell n in the higher/lower band. This transformation allows us to explicitly see that the single particle dynamics are suppressed,

$$\begin{aligned} H = &-2J \sum_n \hat{W}_n^{-\dagger} \hat{W}_n^- + 2J \sum_n \hat{W}_n^{+\dagger} \hat{W}_n^+ \\ &+ \frac{\alpha}{8} \sum_n \left[\frac{1}{4} \hat{W}_n^\dagger \hat{W}_n^\dagger \hat{W}_n \hat{W}_n + \frac{1}{4} \tilde{W}_n^\dagger \tilde{W}_n^\dagger \tilde{W}_n \tilde{W}_n + \hat{W}_n^\dagger \hat{W}_n \tilde{W}_{n+1}^\dagger \tilde{W}_{n+1} \right. \\ &\left. - \frac{1}{4} \hat{W}_n^\dagger \hat{W}_n^\dagger \tilde{W}_{n+1} \tilde{W}_{n+1} - \frac{1}{4} \hat{W}_n \hat{W}_n \tilde{W}_{n+1}^\dagger \tilde{W}_{n+1}^\dagger \right] \\ &- \frac{\beta}{2} \sum_n \left[i\hat{W}_n^\dagger \hat{W}_n^\dagger \hat{W}_n \tilde{W}_{n+1} + i\hat{W}_n^\dagger \tilde{W}_{n+1}^\dagger \tilde{W}_{n+1} \tilde{W}_{n+1} + h.c \right], \end{aligned} \tag{8.3}$$

where $\alpha = U_A + U_B$, $\beta = U_A - U_B$, $\hat{W}_n = \hat{W}_n^+ + \hat{W}_n^-$ and $\tilde{W}_n = \hat{W}_n^+ - \hat{W}_n^-$.

This non-local Wannier function basis makes two novel features of this system apparent: firstly it illustrates the vanishing single particle kinetic energy upon diago-

nalising the single particle Hamiltonian, and secondly it has illuminated the existence of strong pair tunnelling terms, $\hat{W}_n^\dagger \hat{W}_n^\dagger \tilde{W}_{n+1} \tilde{W}_{n+1}$, as well as nearest neighbour interactions, $\hat{W}_n^\dagger \hat{W}_n \tilde{W}_{n+1}^\dagger \tilde{W}_{n+1}$, which are both proportional to the onsite interaction strength. The effect of an imbalance in the interactions, $U_A \neq U_B$, is to introduce complex single particle density assisted tunnelling terms.

8.2 Enhanced topological bound pairs

If we consider the case of, $U \equiv U_A = U_B$ and only two particles, then we can apply an additional basis transformation into a two atom bound state picture. Because the Hamiltonian in Eq. 8.3 does not contain any terms that correspond to the motion of a single particle, we have two types of bound state that cannot mix with one another. One set of states corresponds to two atoms on the same unit cell,

$$\hat{\alpha}_i = \tfrac{1}{\sqrt{2}} \hat{W}_i^- \hat{W}_i^-, \quad \hat{\beta}_i = \tfrac{1}{\sqrt{2}} \hat{W}_i^+ \hat{W}_i^+, \quad \hat{\gamma}_i = \hat{W}_i^+ \hat{W}_i^-, \tag{8.4}$$

and the second set corresponds to the two atoms on neighbouring unit cells,

$$\begin{aligned} \tilde{\alpha}_i &= \hat{W}_i^- \hat{W}_{i+1}^-, \quad \tilde{\gamma}_i = \hat{W}_i^+ \hat{W}_{i+1}^-, \\ \tilde{\beta}_i &= \hat{W}_i^+ \hat{W}_{i+1}^+, \quad \tilde{\kappa}_i = \hat{W}_i^- \hat{W}_{i+1}^+. \end{aligned} \tag{8.5}$$

Transforming to this basis gives rise to a Hamiltonian containing only quadratic terms. If we consider the case where we only have two atoms in the system, then this forms an orthonormal basis set and we can solve the system exactly. Explicitly, the momentum space Hamiltonian is,

$$H = \sum_k \Psi_k^\dagger H_k \Psi_k, \tag{8.6}$$

where

$$\Psi_k = \begin{pmatrix} \hat{\alpha}_k \\ \hat{\beta}_k \\ \hat{\gamma}_k \\ \tilde{\alpha}_k \\ \tilde{\beta}_k \\ \tilde{\gamma}_k \\ \tilde{\kappa}_k \end{pmatrix}, \tag{8.7}$$

and

$$H_k = \begin{pmatrix} -4+U/4(1-\cos k) & U/4(1-\cos k) & iU\sqrt{2}/4\sin k & 0 & 0 & 0 & 0 \\ U/4(1-\cos k) & 4+U/4(1-\cos k) & iU\sqrt{2}/4\sin k & 0 & 0 & 0 & 0 \\ -iU\sqrt{2}/4\sin k & -iU\sqrt{2}/4\sin k & U/2(1+\cos k) & 0 & 0 & 0 & 0 \\ 0 & 0 & 0 & -4+U/4 & -U/4 & U/4 & -U/4 \\ 0 & 0 & 0 & -U/4 & 4+U/4 & -U/4 & U/4 \\ 0 & 0 & 0 & U/4 & -U/4 & U/4 & -U/4 \\ 0 & 0 & 0 & -U/4 & U/4 & -U/4 & U/4 \end{pmatrix}. \tag{8.8}$$

In Fig. 8.1 (c) we plot the resulting dispersion of the lowest bound state band, J_{eff} (blue) as a function of the onsite interaction strength U where there is an asymmetry between repulsive and attractive interactions, which arises through different couplings between the two single particle bands depending on the sign of the interactions. In Fig.8.2 we plot the energy spectrum for repulsive and attractive onsite interaction strength, U, where we can see that changing the sign of the interactions inverts the dispersion relation meaning that the lowest energy band in the repulsive case corresponds to that of the highest band in the attractive interacting case. There are overlaps between two qualitatively different sets of energy bands, one set dispersive, corresponding to a bound state where each single particle is in a Wannier state centred on the same unit cell, and a set of dispersionless bands, corresponding to each single particle centred on a nearest neighbour unit cell. Note that for a single

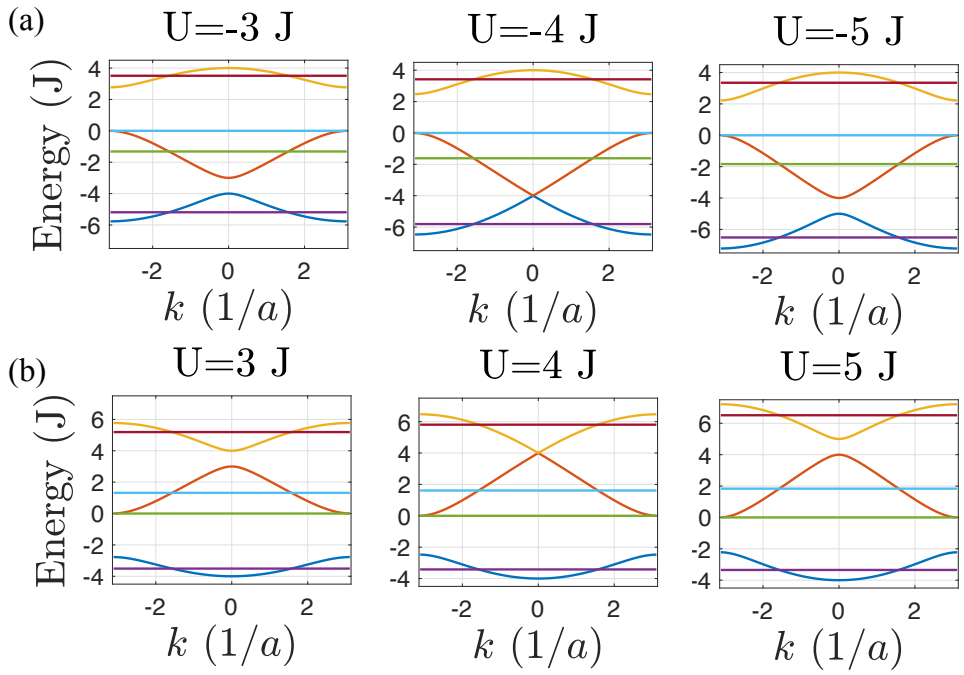

Figure 8.2: Two atom (single bound pair) dispersion relations for $U_A = U_B$, found by diagonalising the effective bound state Hamiltonian, Eq. 8.8, where each line represents the dispersion relation for the different types of two-atom bound state. Many two-atom bands now have some dispersion due to the interactions, but many others remain flat (horizontal lines). Here a is the lattice spacing between the unit cells.

bound state, there are no terms that can mix these two types of bound state. We will see below that in the many-body case there is mixing between these two states, the strength of which varies with density, resulting in a complex phase diagram which one would not observe if these bosonic pairs were not made up of two individual atoms.

The asymmetry in Fig. 8.1 (c) arises from a qualitative difference in the dispersion relations for the lowest dispersive bands (blue) depending on the sign of the interactions, where for attractive interactions a Dirac cone forms in the lower bands, see Fig. 8.2, at the point of maximum bound state kinetic energy and then further increasing the strength of the interaction the width of this band begins to decrease

due to the strong interactions mixing states within the two single-particle bands, explaining the kinetic energy observations for attractive interactions. For repulsive interactions the lowest band is not affected by this mechanism, and although there are still strong mixing between the single-particle bands, this only imposes an upper bound to the dispersion of the bound states making it possible to realise a large kinetic energy for a wide range of interaction strengths.

From Fig. 8.1 (c) we see that for increasing attractive interactions the kinetic energy increases to a maximum and then begins to decrease again, agreeing with previous predictions for excitations on top of a fermion background in the Creutz ladder [268]. This is in contrast to the repulsive side where the kinetic energy asymptotically approaches a value very close to the single particle tunnelling amplitude. In the figure we also include the effective tunnelling for pairs in a simple lattice (purple), which can be calculated in the limit that $U \gg J$ through second order perturbation theory and is J^2/U [271]. Comparing these kinetic energies we can see that on the repulsive side, for interaction strengths large enough so that we expect the conventional pairs to be stable ($U > 10J$), that the topological pairs in this system have a larger kinetic energy by nearly an order of magnitude. This difference in behaviour arrises because the pairing in conventional lattices occurs with both atoms on a single site, whereas in the case of the Creutz ladder, both atoms exist in the same Wannier basis function, shown in Fig. 8.1(a), allowing components to exist where each atom is bound but on different sites. These offsite binding components can then tunnel through the system due to a strong interaction induced nearest neighbour coupling between Wannier states centred at different unit cells, see Eq. 8.3. This has consequences for the critical temperature for superfluidity, which because it is proportional to the tunnelling amplitudes, means that the temperatures required to produce a superfluid with the topological pairs in this system are similar to those

needed for a single particle condensate and is an order of magnitude larger than those needed to prepare one for pairs in a conventional system.

Even though these bound pairs exist in a novel *effective* topological band structure, see Fig. 8.2, the many-body phases will be dominated by pairs condensing in the lowest bands, hence our focus on the kinetic energy of this branch. While in principle there are interesting aspects to the higher energy bands, particularly the Dirac cone at $U = \pm 4J$, we focus on the low-energy properties of the repulsively bound pairs and leave the analysis of these higher-energy features for a future study. Nevertheless, we will see in section 8.5 that the topologically enhanced properties of the lowest effective two-atom energy band leads to shorter timescales for the dynamical features, for example allowing for the preparation of states with (quasi) long range pair correlations in experimentally feasible timescales. Note that previous studies on the properties of interacting pairs in other flat band systems do not observe a strong enhancement of kinetic energy [269], even in those that are also characterised by a topological invariant [292]. This indicates that the enhancement is not a general feature for flat band systems but is unique to the Creutz ladder geometry due to the unique form of the underlying Wannier basis, which are completely localised on only two neighbouring unit cells.

Topological properties of bound pairs

As we have an effective single particle dispersion relation for these bound pairs, an interesting question to ask is if these interacting states retain the topological classification of the underlying single particle Hamiltonian as for those found in an SSH model [276, 277]. Although this effective two-particle model is convenient for analysing the dispersion relations, the basis transformation that is employed does not allow for the usual calculation of the Zaks phase for inversion symmetric lattices.

This is because the effective lattice in this bound state model is not the same as the real space lattice of the Creutz ladder. Instead, we use an ansatz for excitations formulated in the language of uniform matrix product states [293–304] to find the momentum-dependent eigenstates for these interacting bound states with eigenvalues corresponding to the same values as those for the (much simpler) effective model.

This ansatz, which retains the information in the *same* basis as the original real space lattice, allows us to compute the Zaks phase of each quasi-particle branch in the usual way for an inversion symmetric system, which is given by [305]

$$Z_n = \frac{1}{\pi} Arg\left[\langle\psi_{k=0}(B_n)|\hat{\pi}|\psi_{k=0}(B_n)\rangle\langle\psi_{k=\pi}(B_n)|\hat{\pi}|\psi_{k=\pi}(B_n)\rangle\right], \tag{8.9}$$

where n labels the quasi-particle branch and $\hat{\pi}$ is the inversion operator which has a clear physical meaning in the real space basis. Note that while all of the dispersive quasi-particle branches cross a non-dispersive branch and become degenerate at two points in the Brillouin zone ($k = \pm\pi/2$), we can see from the Hamiltonian that there are no terms that couple these dispersive and non-dispersive two particle states, meaning that they are protected from crossing and we can treat these two types of quasi-particles separately when computing the Zaks phase.

We include a chemical potential term, $\mu = 10J$, which allows us to separate out the contributions to the excitation spectrum from single particle states and two particle states. We plot the results in Fig.8.3 where we find that we obtain the same dispersion relation as with the effective model, and we can successfully calculate the correct non-zero Zaks phase for the single particle bands using this excitation ansatz. We also find that all the non-dispersive two particle bound states have a zero Zaks phase indicating that they do not retain the topology of the single particle spectrum. For low onsite interactions ($U < 4\ J$) all three dispersive bound states do retain the

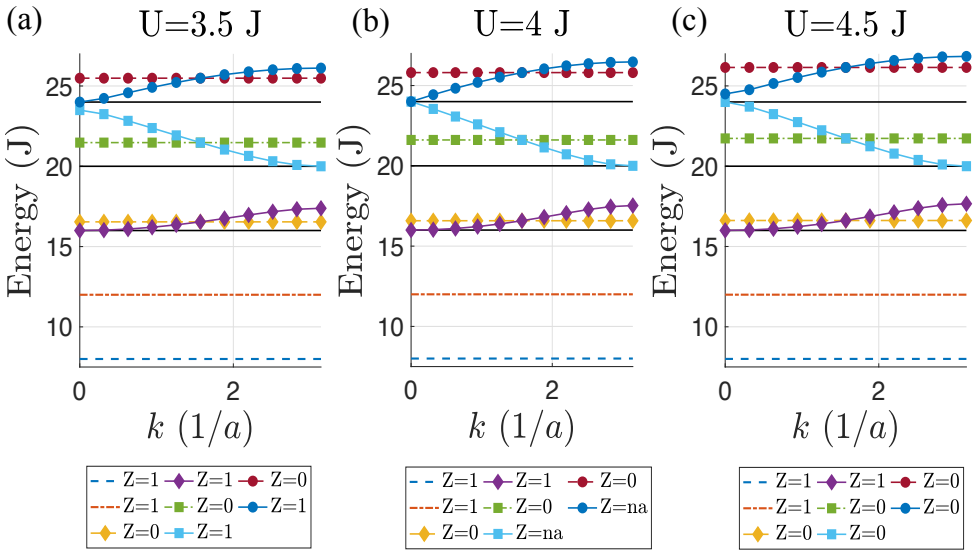

Figure 8.3: Excitation Spectrum for one and two bosons in the Creutz ladder using the uniform matrix product state (uMPS) excitation ansatz [293–304] with an onsite interaction strength $U \equiv U_A = U_B$. Included in the legend are the Zaks phases (see equation 8.9) for each quasi-particle branch. The black (solid) lines are the energy values for two non-interacting particles, and the two bands with the lowest energy (dashed lines) are the single particle solutions. The other branches labelled with coloured markers are the two-particle bound states.

topology and have a non-zero integer Zaks phase. However, at the point $U = 4\ J$ there is a topological transition in the two-particle spectrum and for $U > 4\ J$ the two highest energy dispersive states (squares and circles) have a zero Zaks phase, whereas the lowest energy dispersive state (diamonds) still retains the topology and a non-zero Zaks phase for all U.

8.3 Many-body phases

We now consider the many-body bosonic case and characterise the phases that are manifested by the topological pairs as we vary the density. For the moment we restrict the study to interaction strengths that are symmetric $U \equiv U_A = U_B$ and that are weak compared to the separation of the single particle energy bands by

employing a perturbative Schrieffer-Wolff transformation [263, 264, 266, 306]. This approximation allows us to focus on the lowest flat band in isolation but qualitatively preserves the main features of the full model.

We variationally calculate the ground state directly in the thermodynamic limit using a matrix product state (MPS) algorithm that assumes an infinite and uniform ansatz [307], note that we increase the local dimension such that all bosonic fluctuations are captured. We include a chemical potential term, $(2-\mu)\sum_n \hat{W}_n^{-\dagger}\hat{W}_n^{-}$, in Eq. 8.3 and calculate the pair correlations in the site basis, $\langle \hat{a}_r^\dagger \hat{b}_r^\dagger \hat{a}_0 \hat{b}_0 \rangle$, for a range of densities controlled by the ratio of the chemical potential to the onsite interaction strength, μ/U. In all cases the single particle correlation function is exponentially suppressed, reflecting the lack of single particle dispersion in this system. Additionally, we find that these off-site pair correlation functions dominate over terms of the form, $\langle \hat{a}_r^\dagger \hat{a}_r^\dagger \hat{a}_0 \hat{a}_0 \rangle$, reflecting that the topologically enhanced pairs exist in a superposition of separate sites, in contrast to conventional repulsively bound doublons [271]. The different phases are then characterised by algebraically or exponentially decaying pair correlations for the pair Luttinger liquid (PLL) and pair charge density wave (CDW) phases respectively, examples of which we have included in Fig. 8.4(a-b). The phase diagram is shown in Fig. 8.4(c) where we have highlighted the superfluid pair Luttinger liquid (PLL) phases and the CDW phases and we have also plotted the value of the CDW order parameter [93, 308], which is given by, $O_{DW} = \lim_{r\to\infty}(-1)^r \langle \delta\hat{n}_r \delta\hat{n}_0 \rangle$, where $\delta\hat{n}_i = \hat{W}_i^{-\dagger}\hat{W}_i^{-} - \rho$. Note that analysing the density-density correlation functions (with the exception of the $\rho < 1$ PLL phase, see section 8.7) the component that oscillates with wave-vector $ka = \pi$ is strongly dominant. This is due to the strong nearest neighbour interaction term in Eq. 8.3 which, as there are no longer range interactions present, ensures that this commensurate order is stabilised for all densities considered.

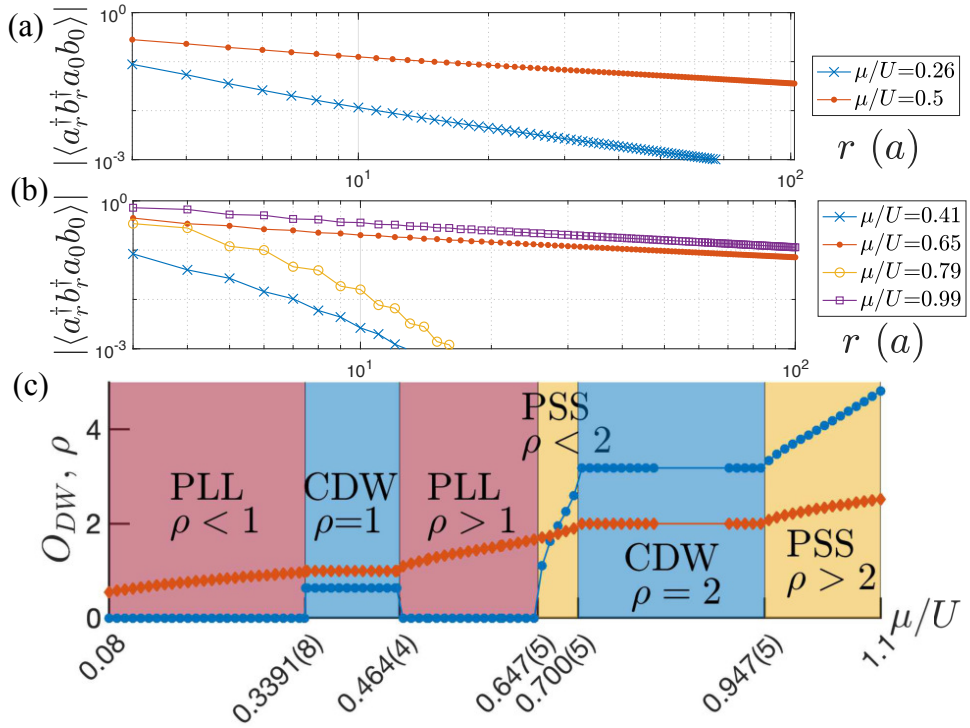

Figure 8.4: (a) Pair correlation functions for the pair Luttinger liquid (PLL) phases. (b) Pair correlation functions for the charge density wave (CDW) and lattice pair supersolid (PSS) phases. (c) Phase diagram for weakly interacting bosons as the chemical potential, μ, is varied relative to the interaction strength, U. The CDW order parameter (blue) and the density (orange) are included. The PLL, CDW and the PSS phases are indicated. Note that there is no physical significance here to the boundaries of the μ/U axis, this is simply the regime where we have focused our analysis.

In all cases the single particle correlation function is exponentially suppressed, reflecting the lack of single particle dispersion in this system. The different phases are then characterised by algebraically or exponentially decaying pair correlations for the PLL and CDW phase respectively, examples of which we have included in Fig. 8.4(a-b), and either a vanishing or finite O_{DW}. We agree with the predictions of Ref. [263, 264] whose authors analyse the same system but restrict their analysis to low densities, where we find a PLL phase for densities between $1/2 < \rho < 1$ (per unit cell) and a phase transition to a CDW for $\rho = 1$. We then investigate larger densities

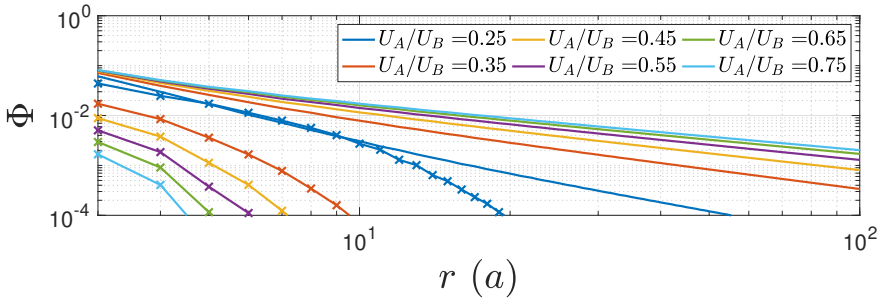

Figure 8.5: Comparison of the pair correlations, $\Phi = |\langle \hat{a}_r^\dagger \hat{b}_r^\dagger \hat{a}_0 \hat{b}_0 \rangle|$ (solid lines) and the single particle correlations, $\Phi = |\langle \hat{a}_r^\dagger \hat{a}_0 \rangle|$ (crosses) for an imbalance between the onsite interactions, $U_A \neq U_B$, in the $\rho < 1$ pair Luttinger liquid (PLL) phase, $\mu/U_A = 0.1$.

where we find a second PLL phase, indicating that the $\rho = 1$ CDW is unstable to the addition of more pairs. Upon further increasing the density we find large regions at incommensurate density where distinct phases exist that share features of both the PLL and CDW. We denote these phases lattice pair supersolid (PSS) and are characterised by algebraically decaying pair correlations but with a non-zero density wave order parameter. Note that if we go beyond the weakly interacting regime, that the coexistence of these phases is suppressed and we either have a PLL or a CDW phase with a clear phase transition point.

Now we include an imbalance between the onsite interaction strengths, $U_A \neq U_B$, and perform the same analysis on the $\rho < 1$ PLL phase. We plot the resulting single particle and pair correlations in Fig. 8.5 where we see that there are still dominant algebraically decaying pair correlations, but now there are exponentially decaying single particle correlations. For values of U_A/U_B close to 1, the pair correlations greatly dominate over the single particle correlations, indicating that the novel properties of this phase survive well into the imbalanced interaction regime. We can see that as U_A/U_B decreases the single particle correlations decay with a smaller correlation length indicating the onset of a conventional superfluid phase for $U_A/U_B \to 0$.

8.4 Experimental realisation of the Creutz ladder

Two experimental realisations of the Creutz ladder have been proposed in Ref. [270, 290], but require the manipulation of two internal states of an atom where each represent each leg of the ladder, which may result in an imbalance between onsite interactions, $U_A \neq U_B$ and potentially lead to a nearest neighbour interaction between sites within the unit cell. This is an interesting regime to investigate in its own right and has been considered in Ref. [309].

Here we propose a different experimental realisation with only a single internal atomic state, allowing us to easily satisfy the considerations above. Our scheme requires one Raman-assisted tunnelling processes and a two-site superlattice see Fig. 8.6. In order to produce this, we find it convenient to redefine the tunnelling amplitudes through a gauge transformation, see Fig. 8.6 (a). This results in the same topological physics because the phases accumulated when moving around loops in the lattice are unmodified. Now the tunnelling elements along each leg of the ladder are real and it is the diagonal tunnelling terms that carry the complex phase. Notice also that there is a dimerisation of the diagonal phase resulting in a doubled periodicity and a larger unit cell and therefore a different local Wannier function basis. The new basis is shown in Fig. 8.6 (b) and is very similar to the one used to derive our effective Hamiltonian where it is also perfectly localised to two unit cells as before. This new basis results in the same single particle spectrum and transforming the many-body Hamiltonian into this basis results in the same model. We confirm that the Creutz ladder shown in Fig. 8.6(a) is able to quantitatively reproduce all features presented in this chapter, while also offering a more viable experimental implementation.

For this scheme we require a particular separation for the onsite energy levels,

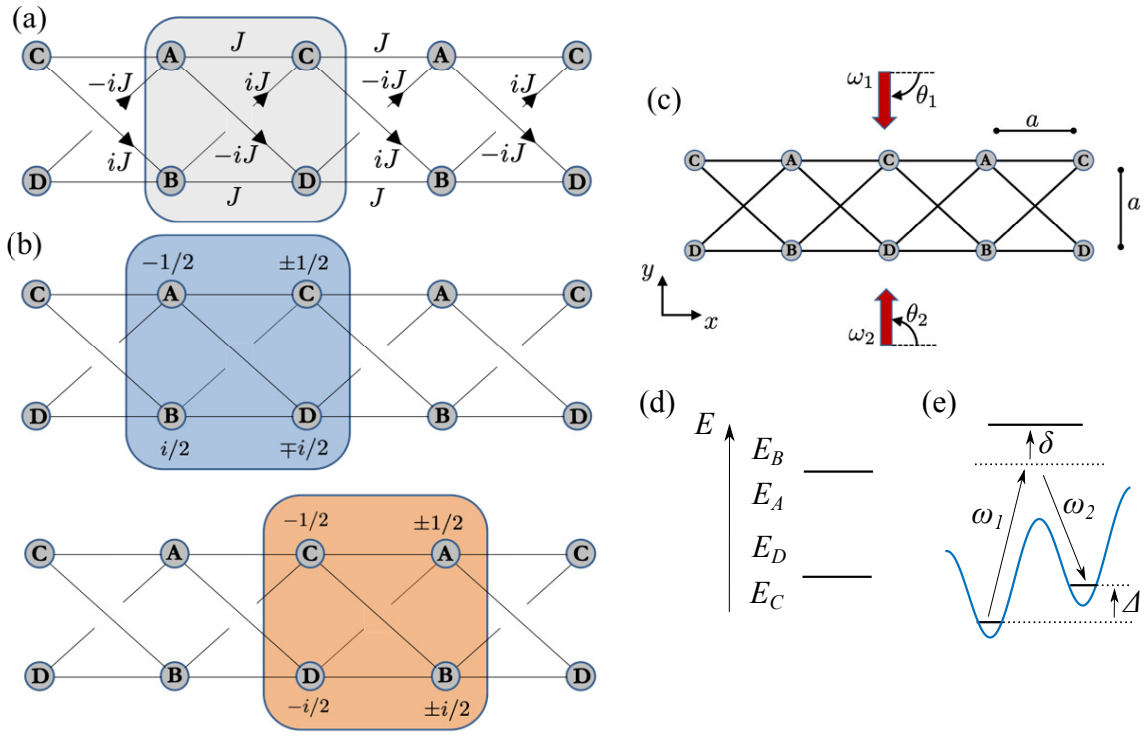

Figure 8.6: Experimental scheme to produce the Creutz ladder in a cold-atom experiment. (a) Illustration of gauge transformed phase components for the tunnelling amplitudes, resulting in the new unit cell highlighted in grey, now consisting of four sites (A,B,C,D). (b) The non-zero components of the four new local Wannier basis functions, where for terms marked with $\pm$ the top is for the lower energy band and the bottom for the higher energy band. (c) One possible configuration for the direction of the applied fields, where $\omega_1 > \omega_2$. Requiring $\lambda_1 \approx \lambda_2 = 4a$ and $\theta_1 = -\pi/2$ and $\theta_2 = \pi/2$ relative to the x-axis. (d) Level scheme showing the distribution of onsite energies for the lattice sites indicated in (c). (e) Illustration of the Raman-assisted tunnelling process for an optical-lattice with an energy offset between neighbouring sites.

shown in Fig. 8.6(d) (note that there is a flexibility in the energy differences). We then apply a Raman assisted tunnelling processes, requiring two fields (shown in Fig. 8.6 (e)), to create the two complex diagonal tunnelling processes and the real processes along the legs. This can be achieved with a single laser with a sideband allowing the necessary phase relations to be easily enforced. The effects of these

applied fields is to induce tunnelling processes between off-resonant sites, [310]

$$J_\alpha = \frac{\Omega_1 \Omega_2^*}{\delta} \int d\vec{r} \phi^*(\vec{r}) e^{i\delta\vec{k}_\alpha \vec{r}} \phi(\vec{r} - a\vec{R}_\alpha), \tag{8.10}$$

where $\phi^*(\vec{r})$ are the onsite Wannier functions, $\delta\vec{k} = \vec{k}_1 - \vec{k}_2$ is the difference between the wave-vectors of the two lasers in a single Raman process, $|\vec{k}_i| = 2\pi a/\lambda_i$, δ is the detuning between ω_1, ω_2 and the excited internal state (see Fig. 8.6(e)) and Ω_i is the Rabi frequency of the applied laser with frequency ω_i.

Assuming that the distance between sites, a, is the same in both directions, then the phase factor in the tunnelling amplitudes between each site labelled in Fig. 8.6(c) is,

$$\begin{aligned} J_{CB} &\propto \exp\left(i\tfrac{a}{2}\left(\delta k_{x,CB} + \delta k_{y,CB}\right)\right); \quad J_{BC} \propto \exp\left(i\tfrac{a}{2}\left(\delta k_{x,BC} - \delta k_{y,BC}\right)\right), \\ J_{DA} &\propto \exp\left(i\tfrac{a}{2}\left(\delta k_{x,DA} - \delta k_{y,DA}\right)\right); \quad J_{AD} \propto \exp\left(i\tfrac{a}{2}\left(\delta k_{x,AD} + \delta k_{y,AD}\right)\right), \\ J_{DB} &\propto \exp\left(i\tfrac{a}{2}\delta k_{x,DB}\right); \qquad\qquad J_{CA} \propto \exp\left(i\tfrac{a}{2}\delta k_{x,CA}\right), \end{aligned} \tag{8.11}$$

where all terms correspond to tunnelling events from left to right in the lattice, along the directions of the arrows in Fig. 8.6(a). The right to left processes are then the complex conjugates.

If we assume that the difference in the frequencies of the two fields in a Raman pulse is much smaller than the magnitudes, $|\omega_1 - \omega_2| \ll \omega_1, \omega_2$, where $\omega_1 > \omega_2$ then we can assume that the wavelengths for each component has the same magnitude, $\lambda \equiv \lambda_1 \approx \lambda_2$, when calculating the phases appearing in the tunnelling amplitudes. Then assuming each field is applied in a general direction in the x-y plane, results in the phases, (where the angles are given relative to the x-axis)

$$
\begin{aligned}
\phi_{CB} &= \frac{a}{2}\left(\delta k_{x,CB} + \delta k_{y,CB}\right) \approx \frac{a\pi}{\lambda}\left(\cos\theta_2 - \cos\theta_1 + \sin\theta_2 - \sin\theta_1\right) \equiv \pi/2, \\
\phi_{BC} &= \frac{a}{2}\left(\delta k_{x,BC} - \delta k_{y,BC}\right) \approx \frac{a\pi}{\lambda}\left(\cos\theta_1 - \cos\theta_2 - \sin\theta_1 + \sin\theta_2\right) \equiv \pi/2, \\
\phi_{DA} &= \frac{a}{2}\left(\delta k_{x,DA} - \delta k_{y,DA}\right) \approx \frac{a\pi}{\lambda}\left(\cos\theta_2 - \cos\theta_1 - \sin\theta_2 + \sin\theta_1\right) \equiv -\pi/2, \\
\phi_{AD} &= \frac{a}{2}\left(\delta k_{x,AD} + \delta k_{y,AD}\right) \approx \frac{a\pi}{\lambda}\left(\cos\theta_1 - \cos\theta_2 + \sin\theta_1 - \sin\theta_2\right) \equiv -\pi/2, \\
\phi_{DB} &= \frac{a}{2}\delta k_{x,DB} \approx \frac{a\pi}{\lambda}\left(\cos\theta_2 - \cos\theta_1\right) \equiv 0, \\
\phi_{CA} &= \frac{a}{2}\delta k_{x,CA} \approx \frac{a\pi}{\lambda}\left(\cos\theta_1 - \cos\theta_2\right) \equiv 0,
\end{aligned}
\tag{8.12}
$$

where on the right we have shown the values that would produce the Creutz ladder shown in Fig. 8.6(a). It is then simply an exercise in finding the optimal direction for the applied fields in order to produce the desired phase differences between each of the tunnelling terms. There is a huge flexibility over the relative angles and the value of the applied λ. The relationship between the angles must satisfy, $\theta_1 = -\theta_2$, and as an example, we plot one possible choice in Fig. 8.6(c) where $\theta_1 = -\pi/2$ and $\theta_2 = \pi/2$, which would then require a wavelength, $\lambda = 4a$.

8.5 Experimental preparation

Here we present a scheme to prepare a many-body eigenstate with strong pair superfluid correlations which can be achieved in a cold-atom experiment by varying the relative intensity of the lasers that create the optical potential. We begin the experimental sequence by applying a large dimerisation to the optical potential such that sites that are populated with atoms are at a much lower energy than neighbouring sites leading to atoms that are strongly localised. We then adiabatically vary the optical potential in order to slowly remove this dimerisation, which amounts to a ramp of onsite energy and allows the atoms to gradually delocalise throughout the

time-dependent ramp which then prepares the eigenstate of the final Hamiltonian if the ramp time is long enough [97, 287].

In cold-atom experiments, if the temperature is much smaller than the critical temperature for condensation then effectively the system is at zero temperature and we can model the dynamics as a pure state. The main consideration in the preparation of low energy eigenstates is in reducing the overall entropy of the many-body state. In adiabatic state preparation this is achieved by first producing a low entropy initial state, in this case by projecting single atoms onto single sites, and ensuring that the state is the ground state of the initial Hamiltonian, in this case by having the onsite energies of populated sites at a much lower energy than the others. This also ensures that the trapped atoms have no dynamics. We then ramp the parameters of the lattice so as to create the final Hamiltonian that we are interested in. If this ramp process is slow enough, so as not to induce unwanted heating effects, but fast enough so that decoherence effects can still be ignored then we can produce the desired low energy eigenstate with also a low entropy.

We begin with atoms populating only particular unit-cells, where the number of populated unit cells is chosen to give the required density and are equally distributed. On a populated unit cell, we have a single atom on each of the two sites, and we have the onsite energies of these populated sites at a significantly lower energy, $E_0/J = -\mu_0$ compared to the rest, $E = 0$. We then ramp the energy of the populated sites to the value of the other sites, using the following exponential ramp,

$$E(t) = -\mu_0 \frac{e^{5(1-t/T)} - 1}{e^5 - 1}, \tag{8.13}$$

where T is the total time for the ramp. We ensure that the initial state is an eigenstate by beginning with a product state where we have the atoms localised on

these initial sites and with all nearest-neighbour tunnelling amplitudes set to zero. We then linearly ramp all tunnelling terms from zero to one in a time $TJ = 10$. The resulting state only has a small amplitude on sites around the ones with a lower onsite energy and has an overlap with the initial product state > 0.9, but there are important phases in these new components which ensure that all tunnelling processes to sites at higher energy (although very highly suppressed in the product state) exactly cancel on the Creutz ladder geometry for the eigenstate.

We consider the case of large interaction strength, $U \equiv U_A = U_B = 6J$, so that we have a large pair kinetic energy (see Fig. 8.1(c)), allowing the correlations to spread to the entire system in timescales that are sufficiently fast so that we can ignore heating and dissipation effects, where we set the initial energy offset to $\mu_0 = 20J$. In principle, once a condensate has been prepared, we can ramp the interaction strength to weak values in order to prepare the phases predicted in the previous section.

In Fig. 8.7 we plot the results of this process for $M = 192$ sites and for $N = 72$ bosons, where it is clear that we can produce a many-body state with significant pair correlations, $\langle \hat{a}_r^\dagger \hat{b}_r^\dagger \hat{a}_0 \hat{b}_0 \rangle$ and vanishing single particle correlations, $\langle b_r^\dagger b_0 \rangle$ and $\langle a_r^\dagger a_0 \rangle$, in experimentally feasibly timescales ($tJ = 210^*$). However, as we are attempting to prepare a phase that is gapless in the thermodynamic limit we expect that as we increase the system size that the total ramp time to achieve the same level of correlation decay will continue to increase. The analysis for short ramp times ($tJ = 40$) indicates that for larger systems we could still produce a pair superfluid in experimentally achievable timescales with the cost of introducing effective finite size effects in the correlations.

Note that the correlations of the time-dependently produced state will always

*Note that compared to the Ch. 6, we can simulate these timescales to a high accuracy because the state remains close to an eigenstate throughout the entire ramp process.

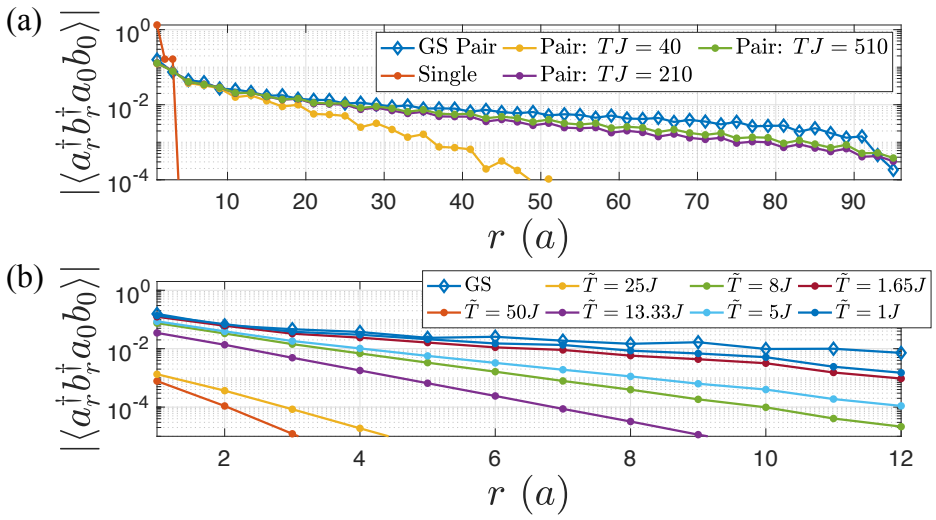

Figure 8.7: (a) Comparison of the single particle and pair correlations for the final produced state of the adiabatic ramp process for a system size of $M = 192$ sites and $N = 72$ bosons. (b) Pair correlations for finite temperatures for $M = 48$ sites, using the technique presented in Ref. [311, 312]. For all cases, $U = 6J$ and $\mu = 1.52J$.

decay faster than the correlations of the ground state. This discrepancy arrises from the breakdown of the adiabatic principle due to the energy gap closing at the end of the ramp process. However the state that is produced is an eigenstate of the many-body Hamiltonian with a low energy variance, and from exact diagonalisation analysis of smaller systems, we find that the prepared state is actually the first excited state.

We also consider the effects of a finite temperature on the pair correlations in the system and we use an imaginary time MPS algorithm which utilises a purification of the density matrix to calculate the state at a given temperature [311, 312]. In Fig. 8.7 (b) we plot the pair correlations at varying temperature and find that the correlations are exponentially suppressed at high temperatures ($\tilde{T} > 20J$) where they become numerically indistinguishable from the exponentially small single particle correlations. Note that at short distances the single particle correlations remain

qualitatively the same as those of the ground state (see. Fig. 8.7 (a)) where they dominate over a distance of several unit cells, simply because the particles are spread into the Wannier basis states. For intermediate temperatures ($2J < \tilde{T} < 15J$), the correlations begin to approximate those of the ground state at short distances but still decay exponentially, with a correlation length that grows as the temperature is decreased. For temperatures $\tilde{T} < 2J$ the pair correlations very closely match the zero temperature case, indicating that these pair superfluid phases are robust to finite temperatures. There are small discrepancies for the longer range tails but these will be experimentally indistinguishable.

8.6 Detection through many-body dynamics

We move on and consider experimental detection of these phases. One possible way to do this is through measurements of the time-dependent onsite particle number after a local quench, in this case after the application of the number operator on a single unit cell. Equivalently, the dynamical structure factors can be experimentally probed use angle-resolved photoemission spectroscopy (ARPES) [313, 314]. To this end we have calculated the dynamical structure factors for each phase (within the weakly interacting and isolated flat band limit) using an MPS algorithm for time evolving infinite systems after a local perturbation [315, 316]. Explicitly we calculate the unequal time two-point correlator, $A(r,t) = \langle \Psi_0 | \delta\hat{n}_r(t)\delta\hat{n}_0(0)|\Psi_0\rangle$, where $|\Psi_0\rangle$ is the initial state and $\delta\hat{n}_r(t) = \hat{W}_r^{-\dagger}(t)\hat{W}_r^{-}(t) - \rho$ where ρ is the density. We then take the Fourier transform which we plot in Fig. 8.8 for the different phases. Note that in all cases, $U_A = U_B$. Additionally, these dynamical structure factors give some knowledge of the spectrum of excitations above the ground state and so we can use this analysis to also determine if the suggestive supersolid like features of the ground

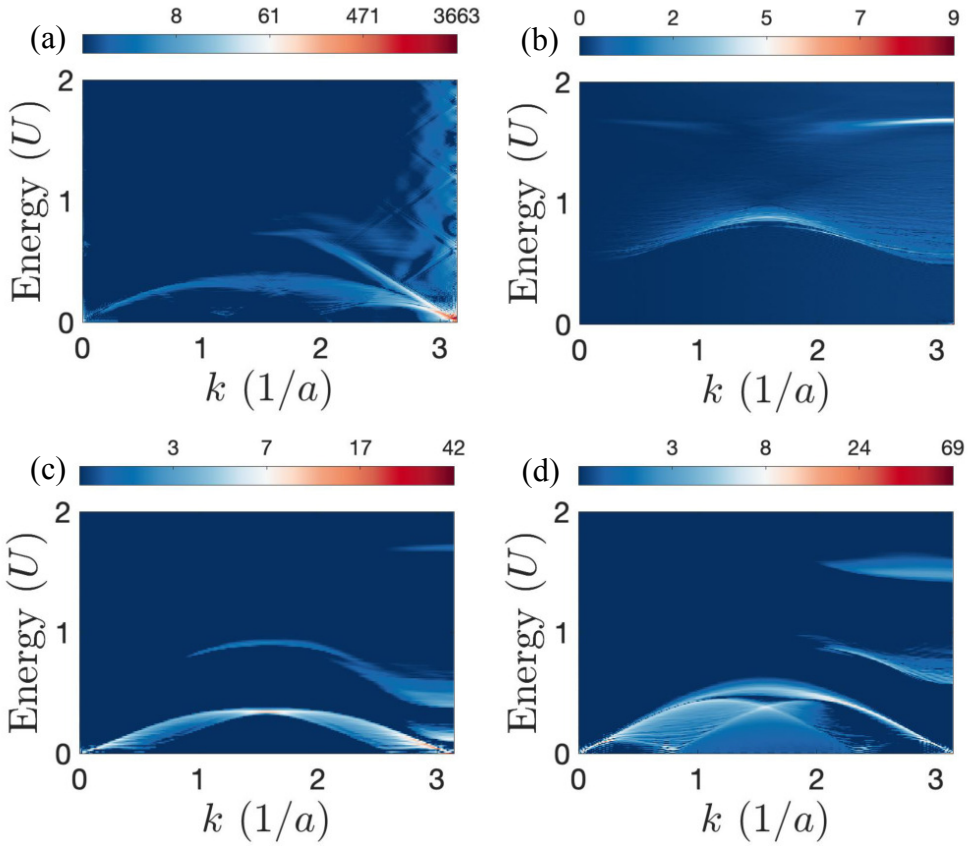

Figure 8.8: Dynamic structure factors for the density-density correlations for each phase. (a) For the $\rho = 1.62$, $\mu/U = 0.63$ pair Luttinger liquid (PLL) phase. (b) The $\rho = 2$, $\mu/U = 0.80$ charge density wave (CDW) phase. (c) The $\rho = 1.84$, $\mu/U = 0.68$ lattice pair supersolid (PSS) phase. (d) The $\rho = 2.25$, $\mu/U = 0.995$ PSS phase (d).

state are also manifested in the excitations.

We can see for the PLL phase (a) there is a dominant linear excitation originating from the $k = \pi$ mode matching the predictions from Luttinger liquid theory (see next section) and for the CDW phase (b) there are well defined gapped energy branches, which can be interpreted as collective quasi-particle excitations. For the lattice supersolid phases (Fig. 8.8(c-d)) we can see gapless excitations that are linear for low energies and originate from $ka = 0$ and $ka = \pi$ which is set by the underlying CDW

order of the ground state, but there are also sinusoidal excitation branches present at higher energies similar to those in the CDW phase indicating the coexistence of the two phases also exists in the excitation spectrum. In Fig. 8.8(c-d) we also observe in the lower energy branches a breaking of translation symmetry as there is a doubled periodicity in $k-$space indicating that the low energy superfluid features exist on top of a dimerised ground state. Additionally in Fig. 8.8(d) there is a local minimum in the low energy dispersion which resembles the helium roton spectrum [317–319], with a roton mode local minimum close to zero gap. These calculations clearly illustrate that the distinct features of each phase are manifested in the excitation spectrum offering a way to experimentally resolve the phases through measurements of the dynamics produced after a local quench.

8.7 Universal behaviour in the pair superfluid phases

As we have a 1D superfluid, we expect to be able to describe the superfluid phases by mapping to a homogeneous Luttinger liquid model (see Ch. 3) [102], ($\hbar = 1$)

$$H = \frac{u}{2\pi} \int dr \left[K(\pi \Pi(r))^2 + \frac{1}{K} (\nabla \phi(r))^2 \right], \tag{8.14}$$

where the bosonic field, $\phi(r)$, and its conjugate momentum density, $\Pi(r)$, satisfy the commutation relation, $[\Pi(r), \phi(r')] = i\delta(r - r')$. All low energy properties of Luttinger liquids are completely known once the two parameters, u and K, are obtained, hence the benefit of mapping our phases into this model. In the following we extract these quantities by first fitting an algebraically decaying function to the off-diagonal pair correlation functions to obtain K,

$$\langle W_r^\dagger W_r^\dagger W_0 W_0 \rangle \sim r^{-1/2K}. \tag{8.15}$$

We use the pair correlation function because we know that the fundamental particles in the superfluid are pairs, and also that the single particle off-diagonal correlation function is zero for all distances. Note that the algebraic decay persists for close to 1000 unit cells before numerical errors destroy this behaviour, allowing us to very accurately extract the decay exponents. We then plug the value for K into the expression for the compressibility to obtain u,

$$\kappa = \frac{d\rho}{d\mu} = \frac{K}{u\pi}, \tag{8.16}$$

where we have evaluated the $d\rho/d\mu$ numerically from our data presented in Fig. 8.4.

The parameter u is the effective speed of sound in the condensate which is the gradient of the linear dispersion of the excitations. The parameter K controls the thermodynamic properties of the system, for example, it has been shown in Ref. [320] that if $K > 1$ then the density transport in the system is completely robust against a single impurity, but for $K < 1$ the effect of an impurity is to completely suppress transport. In Ref. [321] it was shown that K controls the thermal conductivity.

There has also been recent interest in going beyond the assumptions in the Luttinger liquid theory, namely assuming that the excitations follow a linear dispersion relation. We can compute the leading order correction to this, the effective mass, m^*, for a non-linear Luttinger liquid theory [322], through,

$$\frac{1}{m^*} = \frac{u}{K}\frac{d}{d\mu}(u\sqrt{K}). \tag{8.17}$$

We begin with the $\rho < 1$ superfluid phase and apply the Luttinger liquid formalism. Ref. [263] maps this phase onto a spin 1/2 system where $|2\rangle = |\uparrow\rangle$ and $|0\rangle = |\downarrow\rangle$, and while they test the validity of this mapping for small system sizes, we find that the mapped spin 1/2 system does not yield the same physics as the full

boson model for the infinite system considered here. We find that we need to account for the possibility of up to four bosons existing on a given site in order to properly account for all the bosonic fluctuations. Our predictions are not qualitatively different, but the critical value for the chemical potential at the phase transition is shifted. However, if this mapping was valid then this commensurate-incommensurate quantum phase transition at $\rho = 1$ would be mathematically equivalent to that for gapped spin 1/2 chains in a magnetic field [102, 121]. By comparing the correlation functions of the bosonic ground state to these predictions we can quantify the deviations away from the spin 1/2 regime. If the mapping was valid, then we would be able to exactly derive the critical exponents of the phase transition on the incommensurate side simply by knowing the value of the Luttinger liquid parameters at the phase transition point. Because the deviations away from the spin 1/2 regime are small, we can still estimate these quantities.

We extract the Luttinger liquid parameters numerically through the procedure described above and plot these in Fig. 8.9 (a). The Luttinger liquid parameter K is always less than one, indicating that the superfluid is dominated by charge fluctuations induced by the effective nearest neighbour interactions, and the value at the phase transition point can be extrapolated, $K^* \approx 0.3$.

We also plot the inverse effective mass, $1/m^*$ in Fig. 8.9(a) where we see that for smaller values of the chemical potential it is much smaller than the other parameters, indicating that there are only small corrections to the conventional Luttinger liquid theory. However, for larger chemical potentials - and so larger densities - the values become negative with magnitudes that are larger than the u, signifying that there may be features beyond that of a Luttinger liquid.

The long distance behaviour of the density-density correlation functions for a

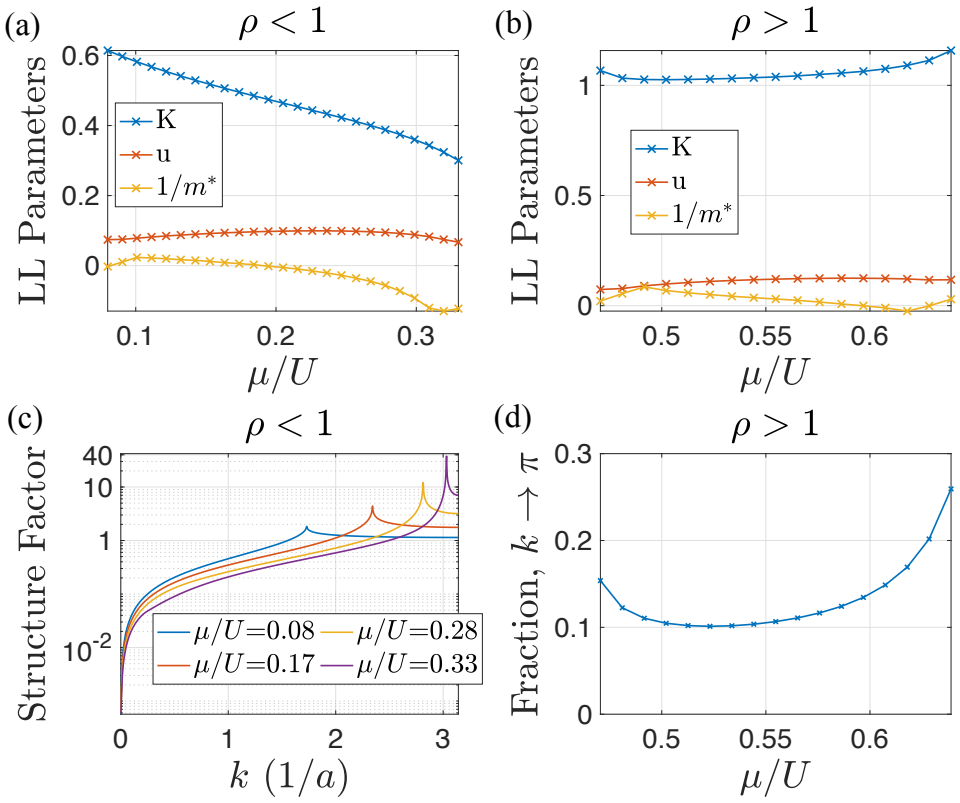

Figure 8.9: Luttinger liquid parameters for the $\rho < 1$ PLL phase (a) and for $\rho > 1$ (b). (c) Static structure factors for the density-density correlation functions for $\rho < 1$, on a log scale. (d) The fraction of the static structure factor in close to the $k = \pi$ mode for $\rho > 1$.

spin 1/2 system in the presence of an applied magnetic field is given by,

$$\langle \hat{n}_r \hat{n}_0 \rangle \sim \cos\{\pi(1 + 2\delta\rho)r\} r^{-2K}, \tag{8.18}$$

where $\delta\rho$ is the deviation in the spin magnetisation (or the density for the bosonic system considered here) from the commensurate regime. This correlation function predicts peaks in the Fourier transform (static structure factor) at values of $q_\pm = \pi(1 \pm 2\delta\rho)$. We calculate these structure factors for our system and plot these in Fig. 8.9 (c) for a range of μ/U and we find that the peaks do indeed correspond to

the values predicted by the Luttinger liquid theory. Even though there are terms present in the model which give rise to an effective nearest neighbour interaction (see Eq. 8.3) these are clearly negligible in this phase as the features can be predicted from the Luttinger liquid theory. This can be understood by realising that the relative magnitudes of the terms in the Hamiltonian will be dependent on density, for example $\langle W_n^\dagger W_n W_{n+1}^\dagger W_{n+1}\rangle \approx \rho^2$, and so the nearest neighbour interactions are dominated by the other processes in this phase. A similar analysis was carried out in Ref. [265] on a Sawtooth lattice but the commensurate phase is a $\rho = 1/2$ CDW made stable by the dispersionless energy band and the incommensurate phase occurs for increasing densities. Here we find qualitatively the same features but our gapless commensurate phase is a CDW stabilised by the effective nearest neighbour interactions.

For the superfluid phase for $\rho > 1$ it is not possible to map to the results from the spin 1/2 theories, however we apply the same numerical strategy and find that the Luttinger liquid parameters are always ≥ 1, (see Fig. 8.9 (b)) indicating that the phase is dominated by superfluid fluctuations and the effects of the nearest neighbour repulsion becomes suppressed. What is quite interesting is that there is a region around $\mu = 0.5U$ where $K \approx 1$ which corresponds to the case for hard-core bosons [102], indicating that we can realise a regime where the physical onsite interactions are weak but the effective onsite interactions are infinite.

The values for the inverse effective mass approach the same magnitude as the u values for smaller chemical potential values, indicating that there may be additional features present that are beyond Luttinger liquid theory. In particular we can see from Fig. 8.8(a) that the excitation spectrum in this phase is dominated by a linear branch, which is predicted from Luttinger liquid theory, but there is also clearly a sinusoidal branch present further indicating that there are additional features present

here.

We also calculate the density-density structure factors and find that it is peaked at $k = \pi$ for all μ/U, which is due to the strong nearest neighbour interaction in Eq. 8.3. While in this phase these terms do not give rise to a charge density wave, they lead to features that oscillate with a given period and set the commensurate ordering in k-space. In Fig. 8.9(d) we plot the fraction of the population that is in this peak, which indicates that the system is strongly condensed for larger μ/U and when $K \approx 1$ the condensate peak is somewhat suppressed by the strong effective interactions.

8.8 Conclusions

We have considered the experimental opportunities of using the Creutz ladder to investigate the interplay between topological band structures and strong interactions. By analysing the properties of single repulsively bound pairs we found that the topology greatly enhances the stability and kinetic energy of formed pairs making it possible to realise and investigate pair superfluid phases in experiments with cold atoms. We considered the ability to prepare and detect these phases where we illustrated an experimentally feasible preparation scheme allowing us to prepare a pair superfluid in realistic timescales and demonstrated that these phases can be resolved through measurements of the dynamical properties. This opens up opportunities for understanding and exploring the unique many-body phases that can be produced with strong interactions in more general topological band structures.

While previous analysis on other systems with flat energy bands have found similar superfluid phases dominated by bound pairs that share qualitative features as the pair superfluid phases presented here, such as in the sawtooth and Kagome lat-

tice [266] or the diamond chain [323] they have not been considered in the context of practicalities for experimental detection. In particular, the latter system must have a very precise value for the tunnelling phases in order for it to manifest a pair superfluid, in contrast to the robustness of these phases in the Creutz ladder to similar phase deviations [264] and even to an interaction imbalance or finite temperatures as analysed here. The stability of these features in the Creutz ladder is due to the enhanced properties for single repulsively bound pairs, which in contrast to the sawtooth lattice [269] or the diamond chain [292], we find have a kinetic energy that grows with increasing interaction strength, arising from the particular topology of the Creutz ladder. This distinct behaviour for the Creutz ladder opens up many questions relating to the features of other flat band systems, in particular those with additional dispersive energy bands [324].

Chapter 9

Enhanced pair correlations in a Lieb ladder

Inspired by growing interest in probing many-body phases in novel two-dimensional lattice geometries [75, 256–258, 325–331], in this chapter we consider how to use ultracold atoms in optical lattices in order to perform a quantum simulation of these systems and investigate the role of strong interactions. We noted in the previous chapter that there has been great interest recently in exploiting the features of novel lattices in order to realise unique many-body phases that have superfluid [266, 331, 332] or superconducting features [324] dominated by interaction induced pairing that have been enhanced by the presence of flat energy bands which we explicitly demonstrated for a 1D system. However, classical methods for quantitatively analysing these phases in two-dimensions are not currently practical for large systems. While there has been some recent numerical analysis on a minimal quasi-2D model for superconductivity [333], it is an interesting opportunity to potentially use quantum simulators to improve the understanding of strongly correlated phases in two-dimensions. To this end, we consider an experimental realisation of

an optical Lieb lattice, where we directly calculate experimentally realistic values for the coefficients in the many-body Hubbard model as a function of the parameters of the optical potential, allowing for a mapping between experimental and theoretical parameters. We demonstrate how to prepare the ground state of attractively interacting fermions at half filling, where the excitations are dominated by states in the flat band and we perform benchmarking calculations of the correlations in a 1D Lieb ladder where we show that the pair correlations greatly dominate over the single particle correlations for a range of strong attractive interactions. These calculations enable the investigation into the strongly interacting phases manifested in the Lieb lattice and raise interesting questions regarding the behaviour of the correlations for the full two-dimensional Lieb lattice which can be accessed with the aid of this presented experimental proposal.

9.1 Introduction

The Lieb lattice is shown in Fig. 9.1, and is characterised by a novel band structure with a flat energy band that touches a dispersive band at a single k-point. This dispersionless (or flat) single particle energy band arises through a destructive interference effect of the single particle wavefunction, [259–262], leading to an infinite energy degeneracy without a well defined energy minima in the band. One consequence is that conventional single particle correlations are suppressed due to the effective mass $\rightarrow \infty$ and the effective tunnelling amplitudes $\rightarrow 0$. It has been shown that interactions allow the atoms to form into bound pairs, breaking the energy degeneracy and leading to mobility [269]. For bosons these pairs can push the system into condensing into a pair superfluid even for infinitesimal interaction strength [263–265, 332, 334]. For fermions there is a similar enhancement of pair

correlations [324, 335] where it has been shown that the critical temperature for superconductivity can be much larger than for conventional systems [336, 337]. However, most analysis on two-dimensional systems exploit mean field approximations but there are questions here on the validity of a conventional BCS treatment in a flat band, as the interactions strength dominates the dynamics resulting in strongly correlated phases even for weak interactions. A full quantum treatment in 1D has also been explored [268, 338], but usually only in the isolated flat band approximation. However, there are additional questions here as to the effects on these properties in systems that have a flat band as well as dispersive bands, such as the Lieb lattice, and in particular when the interaction strengths are strong enough to mix states in different bands.

In order to allow future experiments to more easily explore these questions, we derive experimentally realistic values for the coefficients in a Hubbard model as a function of the laser intensity through calculating the single particle Wannier functions localised on each site. We then consider the many-body fermion case at half filling where we show that pair correlations appear quasi-long range, strongly dominate over exponentially suppressed single particle correlations and are at sufficiently large magnitudes to be resolved experimentally. Furthermore we show that the pair correlations become further enhanced when there is greater mixing between states in the flat band and in the higher dispersive bands due to increasing the interaction strength. Finally, in order to be able to realise these phases experimentally we describe and demonstrate an experimentally feasible adiabatic ramp process for preparing these ground states.

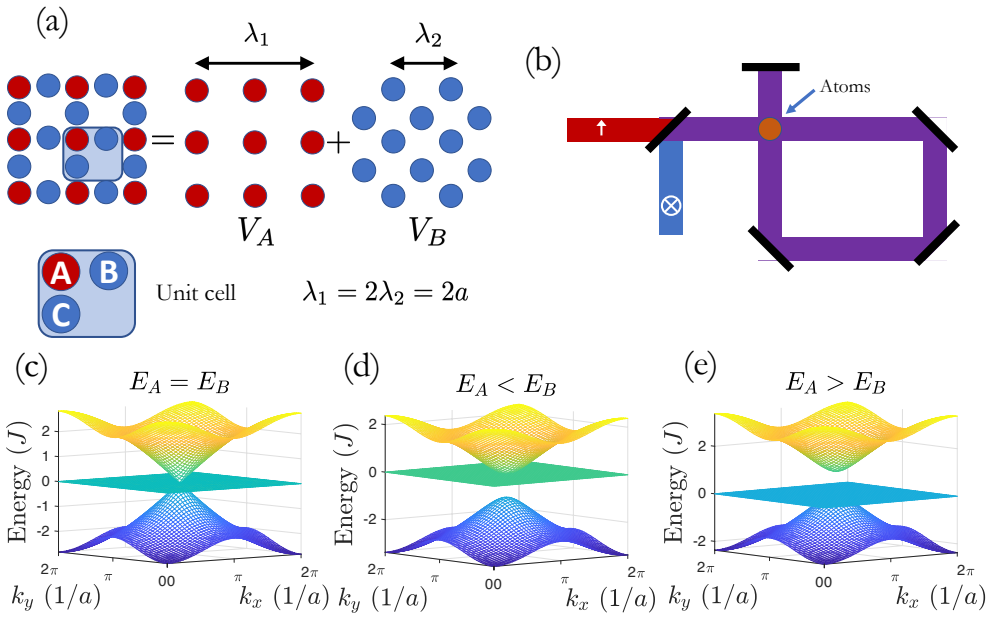

Figure 9.1: (a) Creation of an optical Lieb lattice by superimposing two optical potentials, $\{V_A, V_B\}$ given by Eq. 9.1. (b) Beam configuration and polarisation for each optical potential, reproduced from Ref. [331]. (c-e) Single particle energy band structure for tight binding model on the Lieb lattice for different ratios of the onsite energies, $\{E_A, E_B, E_C\}$, for each site of the unit cell ($E_C = E_B$ for all), given in units of the nearest neighbour tunnelling rate, J, and the unit cell spacing, a.

9.2 Hubbard coefficients

In the Lieb lattice for the case where every site is degenerate the system manifests a three band touching point, with a Dirac cone that crosses the flat band, but by tuning the ratio of the onsite energies it is possible to realise different energy gaps, see Fig. 9.1. Here we consider producing the Lieb lattice experimentally by superimposing two optical potentials [331],

$$\begin{aligned} V_A(x,y) &= -V_1[\cos^2(k_1 x) + \cos^2(k_1 y)], \\ V_B(x,y) &= -\frac{V_2}{4}[\cos(k_2 x) - \cos(k_2 y)]^2, \end{aligned} \tag{9.1}$$

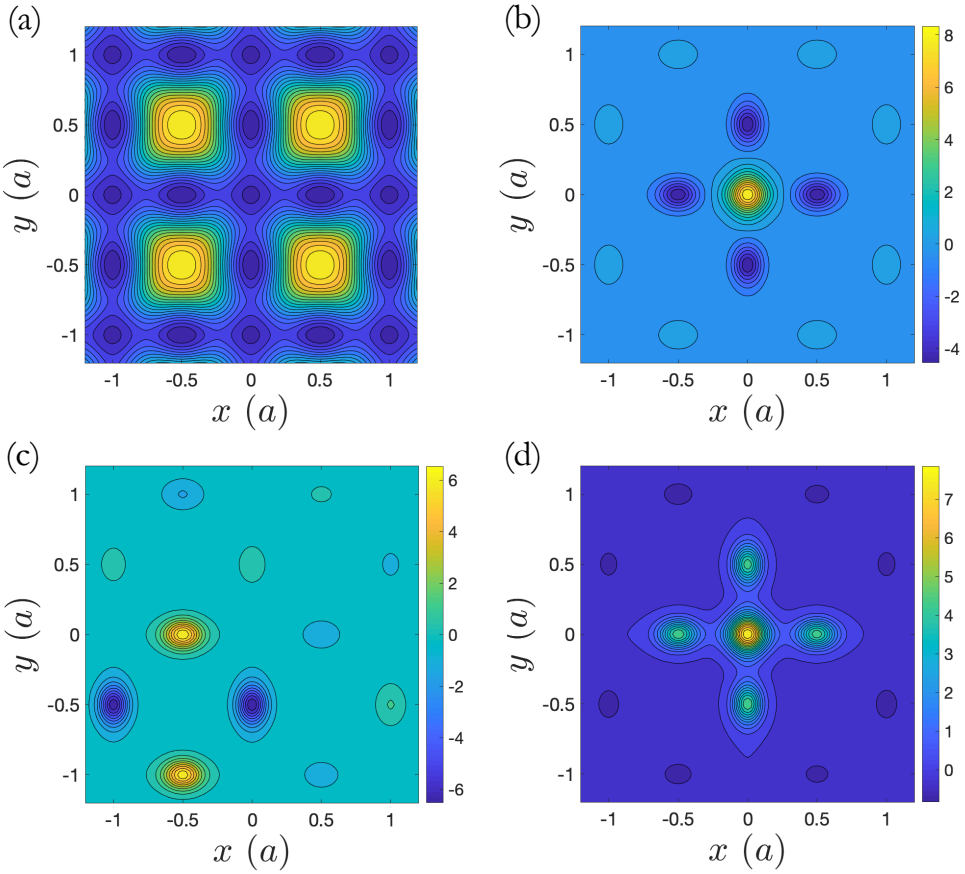

Figure 9.2: (a) Optical potential for the Lieb lattice produced using Eq. 9.1 with $V_1 = 34.5E_{R2}$ and $R = V_2/V_1 = 1.07$. The Wannier functions associated with each energy band for a single particle in the optical potential. (b) Higher band. (c) Flat band. (d) Lower band.

where the wavevector $k_i = 2\pi/\lambda_i$, and $\lambda_1 \approx 2\lambda_2$. In Fig. 9.1(a) we illustrate the direction of the beams and the values required for the wave-vectors. Usually, V_1, V_2 are expressed in units of the recoil energy, $E_{Ri} = \hbar^2 k_i^2/2m$. The above potential can be produced experimentally using the configuration shown in Fig. 9.1(b) which has been reproduced from Ref. [331]. For V_A (red) we use laser light that is polarised in the plane of the lattice and for V_B (blue) we use a polarisation that is orthogonal to the plane.

By tuning the ratio $R = V_2/V_1$ (achieved experimentally by varying the intensities

of the two superimposed lasers) around 1, the relative depth of the trap at the A sites and the B, C sites can be varied, which then modifies the single particle energy band structure, see Fig. 9.1(c-e). Under well controlled approximations it has been shown that atoms confined in an optical lattice can be described with a Hubbard model [27] for sufficiently large potential depths. We will see below that for the Lieb lattice we require laser intensities of around $V_1, V_2 \sim 40E_{R2}$ so that the next nearest neighbour tunnelling rates are below 1% of the nearest neighbour components. In this case the Hubbard model on this geometry takes the form,

$$\begin{aligned} H = &\sum_{n,\sigma} E_A a^\dagger_{\sigma,A,n} a_{\sigma,A,n} + E_B a^\dagger_{\sigma,B,n} a_{\sigma,B,n} + E_C a^\dagger_{\sigma,C,n} a_{\sigma,C,n} \\ &- J\left(a^\dagger_{\sigma,A,n} a_{\sigma,B,n} + a^\dagger_{\sigma,A,n} a_{\sigma,C,n} + a^\dagger_{\sigma,B,n} a_{\sigma,A,n-\vec{x}} + a^\dagger_{\sigma,C,n} a_{\sigma,A,n+\vec{y}} + h.c\right) \\ &+ U_A a^\dagger_{\sigma,A,n} a^\dagger_{\bar{\sigma},A,n} a_{\bar{\sigma},A,n} a_{\sigma,A,n} + U_B a^\dagger_{\sigma,B,n} a^\dagger_{\bar{\sigma},B,n} a_{\bar{\sigma},B,n} \\ &+ U_C a^\dagger_{\sigma,C,n} a^\dagger_{\bar{\sigma},C,n} a_{\bar{\sigma},C,n} a_{\sigma,C,n} a_{\sigma,C,n}, \end{aligned} \tag{9.2}$$

where $a^\dagger_{\sigma,\kappa,n}$ creates an atom at the unit cell n on site κ. The index σ runs over the distinguishable species, and for bosons, $\sigma = \bar{\sigma}$.

In order to analyse the effects of strongly interacting systems in novel band structures it is necessary to derive the coefficients of this model so that we are able to accurately describe the dynamics induced in these systems. While it is now routine to realise Hubbard models in simple periodic potentials, up to well controlled approximations [25, 27, 28, 33], it can still be a challenging task to derive the coefficients in models for more complicated lattices. So in order to allow future experiments to more easily explore these questions in the Lieb lattice, we first derive experimentally realistic values for the coefficients in a Hubbard model as a function of the laser intensity through calculating the single particle Wannier functions localised on each

site [339].

Single particle Wannier functions can be found by first diagonalising the single particle Hamiltonian, to obtain the Bloch functions, $\phi_k^m(\vec{r})$, associated with each band m,

$$w_j^n(\vec{r}) = \frac{1}{2\pi} \int dk U_{n,m}^k \phi_k^m(\vec{r}) e^{-i\vec{k}\cdot\vec{R}_j}, \tag{9.3}$$

where $U_{n,m}^k$ is a k-dependent 3×3 unitary matrix. For the case where each U^k is diagonal and we find the appropriate choice for the phase factors then we can obtain unique and real Wannier functions that are exponentially localised to a single unit cell and each represent particles in an individual energy band [92]. This phase is chosen so that the Bloch functions are as smoothly varying as possible around the Brillouin zone. In this way, the Wannier functions for the Lieb lattice can be found as shown in Fig. 9.2.

However, calculating the terms in the Hubbard model using these ordinary Wannier functions would result in a model with many long range tunnelling and interaction processes. It is then advantageous to calculate a new set of basis states which themselves are localised on individual sites, and will allow for the realisation of a Hubbard model of the form of Eq. 9.2 with only nearest neighbour processes. In general, this can be a non-trivial task particularly when the lattice geometry has a complicated spatial structure and connectivity. To this end, we use the method presented in Ref. [339] which finds the optimal superposition of the ordinary Wannier functions, by iteratively optimising each $U_{n,m}^k$, such that we obtain a new set of orthogonal functions, but which are much more localised. The effect of the off-diagonal elements of $U_{n,m}^k$ is to mix the Bloch functions of each energy band, thus the new basis set corresponds to particles localised on individual lattice sites, but which exist in a superposition of the three energy bands.

This new maximally localised onsite basis is most convenient for calculating the coefficients of a Hubbard model because we can use them to obtain the tunnelling amplitudes between nearest neighbouring sites and the onsite energy and interaction coefficients as a function of the optical lattice laser potential values which is important for experimentally realising theoretical predictions that require knowledge of the interaction strength and are paramount for being able to reliably explore the physics of many-body systems in complex geometries. These coefficients are shown in Fig. 9.3 for the regimes where the tight binding spectrum is well approximated, where we can see that the onsite interaction strengths can be tuned to values close to the tunnelling rates for moderate scattering lengths.

Note that compared to a conventional square lattice, which requires intensities of $V_0 \sim 10 - 50E_R$ in order to accurately approximate a tight binding model, we find here that we must be in the upper limit of this range to reproduce a spectrum similar to the tight binding case in Fig. 9.1(c-e). However, as can be seen from Fig. 9.2(a) the potential is greatly dominated by the large peaks which creates the distinct pattern of the Lieb lattice and the potential barriers between nearest neighbouring sites are much lower, giving values for the nearest neighbour tunnelling rates on the order of $J \sim 1$ kHz for all parameters considered in Fig. 9.3. This means that while we require a higher laser power to produce the tight binding spectrum compared to conventional lattices, the dynamics manifested in this system will be at a similar rate.

We are also able to calculate corrections to a standard Hubbard model and in Fig. 9.3(b) we also plot the next-nearest neighbour tunnelling and a nearest neighbour density induced tunnelling coefficient where we can see that these values are on the order of 1% for the potential values illustrated here. The most dominant effect of the next nearest neighbour tunnelling term is to introduce a small curvature

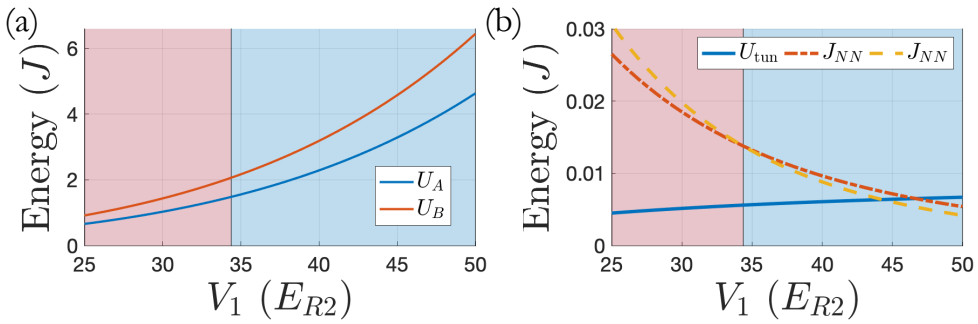

Figure 9.3: Hubbard coefficients produced from Eq. 9.1 as a function of the laser intensity, where U_A (U_B) are the onsite interaction strengths for the A (B) sites of the unit cell, where $U_C = U_B$. J_{NN} are the next-nearest neighbour tunnelling rates between A (B) sites in different unit cells, red (yellow) and U_{tun} are the dominant interaction strengths between nearest neighbour sites. With $V_2 = 1.07V_1$, the wavelength $\lambda_1 = 1024$ nm, a harmonic trap in the z-direction with $\omega_z = 2\pi\times200$ Hz and for a scattering length $a_s = 250\ a_0$. For all values the nearest neighbour tunnelling is on the order of $J \sim$ kHz.

and band width for the flat energy band, however, this is also much smaller than the dominant nearest neighbour tunnelling rates ($< 1\%$) indicating that these corrections will have a negligible effect on the dynamics as they are significantly dominated by the conventional Hubbard terms.

9.3 Many-body correlations at half filling

In order to perform a quantitative analysis of the many-body phases produced in the Lieb lattice we focus on a one-dimensional ladder cut, shown in Fig. 9.4, and variationally calculate the ground state using matrix product states [1] (see Ch. 4). This allows us to quantitatively calculate the properties of the ground state in the strongly interacting regimes while also preserving the main qualitative features of the full Lieb lattice, where we have an energy band structure with a flat band and a Dirac cone (see Fig. 9.4). In the following we consider the case of fermions at half filling as in this regime the lower two energy bands are filled and the flat band is

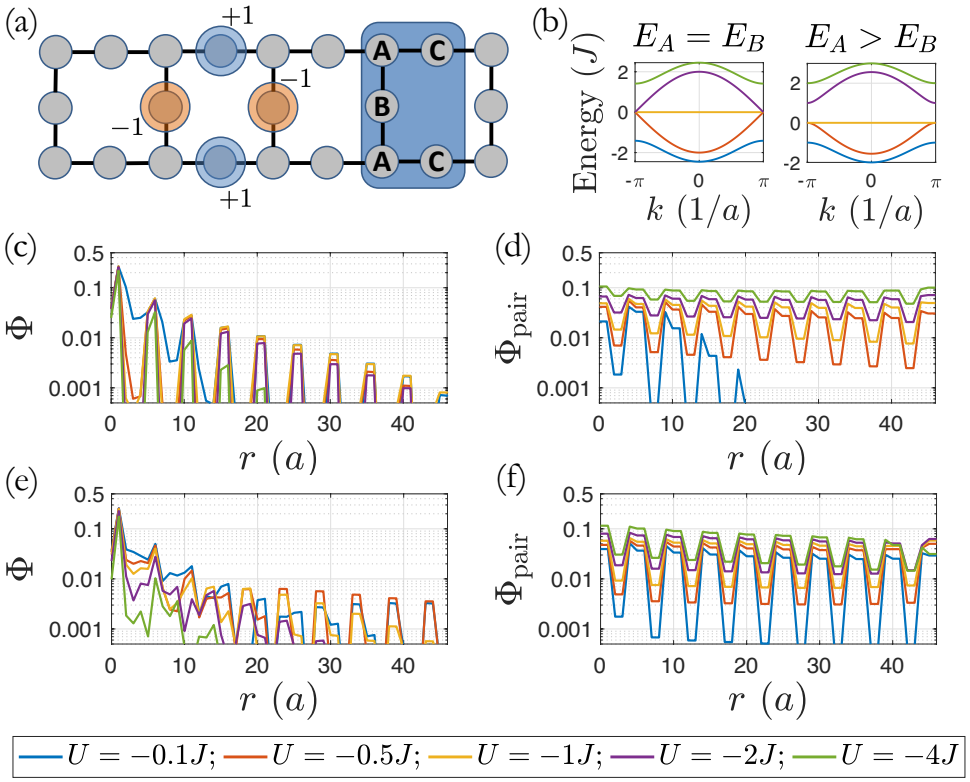

Figure 9.4: (a) One-dimensional Lieb ladder strip with the most dominant components of the maximally localised flat band states highlighted, compare to Fig. 9.2(b). (b) Energy band structures for the ladder, $E_B = E_C$ for all. (c-f) Matrix product state calculation (bond dimension, $D = 1024$) of the ground states at half filling where we compare the single particle (Eq. 10.49) and pair correlations (Eq. 9.5) for $E_A = E_B = E_C = 0$ (c-d) and $E_A = J$; $E_B = E_C = 0$ (e-f). System size of 20 unit cells (100 sites) and 50 spin up and 50 spin down fermions.

half filled, meaning that all excitations and dynamics around the Fermi level will be dominated by states in the flat band.

We calculate the ground state for attractive interactions as the interaction strength is increased for the two band structures illustrated in Fig. 9.4. We calculate the single particle correlations,

$$\Phi(r) = \langle a^\dagger_{\uparrow,A} a_{\uparrow,r} \rangle, \tag{9.4}$$

where we first apply the creation operator on the A site in the centre of the system

and then apply the destruction operator at every other site to the right in the system. We compare these to the cooper pair correlations

$$\Phi_{\text{pair}}(r) = \langle \Delta_B^\dagger \Delta_r \rangle, \tag{9.5}$$

where

$$\Delta_r = a_{\uparrow,r} a_{\downarrow,r}, \tag{9.6}$$

and we first apply the pair creation operator to the B site in the centre of the system. We plot the results in Fig. 9.4, where we can see that for non-zero interactions the pair correlations dominate over the single particle correlations for both regimes.

Due to the spatial distribution of the flat band eigenstates (shown in Fig. 9.4) we find that the dominant pair correlations occur between B and C sites, where the noticeable dips in the plots for lower interaction strengths occur when the subsequent destruction operator is applied to an A site. As the interaction strength is increased these features are washed out, indicating that there is strong mixing with Wannier states associated with the higher energy bands, but intriguingly, the overall decay of the correlations seems to actually be enhanced by this mixing, whereas the single particle correlations become further suppressed.

We can also see that in the regime $E_A = E_B = E_C$ with the Dirac cone (a-b), that the pair correlations are suppressed for weak interactions, but for strong interactions the pair correlations seem to become even larger than the case with a gap in the band structure ($E_A = J$) and for $U = -4J$ appear to remain almost constant over the entire length of the system that we have considered. Of course, with these long range correlations, finite size effects become important, making it difficult to really unequivocally determine if these correlations decay algebraically, or simply have a correlation length that is larger than the system. Nevertheless, these results are very

suggestive of quasi-long range superconducting pairing, and also demonstrate that strongly mixing with dispersive energy bands, rather than destroying the novel pair dominated phases in flat bands, can actually enhance these properties.

9.4 State preparation

We consider the ability of preparing these novel many-body phases in a realisation of the Lieb lattice with an optical lattice. This preparation scheme is based on adiabatic state preparation [97, 287] and utilises the ability of these systems to time-dependently vary the onsite energies, interaction strengths and tunnelling amplitudes. In order to achieve this experimentally requires precise knowledge of the relationship between the parameters of the optical potential and the coefficients in the effective Hubbard model which can be understood with the help of the analysis presented in the previous sections.

We require the preparation of an initial product state where a single fermion is projected onto each of the blue sites shown in Fig. 9.5(a). Our initial state in this process is the case where all tunnelling rates are zero which can be achieved with strong laser intensity creating large potential barriers and where the onsite interaction strengths are also zero, which can be tuned with a magnetic field around a Feshbach resonance [340]. Additionally, we require a large detuning between onsite energies with much lower energies for the sites that are initially populated, which can be achieved by varying the relative intensity of the two optical potentials creating our lattice in Eq. 9.1. We then simultaneously time dependently ramp the tunnelling, the onsite energy and the onsite interaction strength to the desired value.

First in Fig. 9.5(b) we consider the case for zero interactions, with $E_A = 1$; $E_B = E_C = 0$, where we linearly ramp the parameters in the Hubbard model.

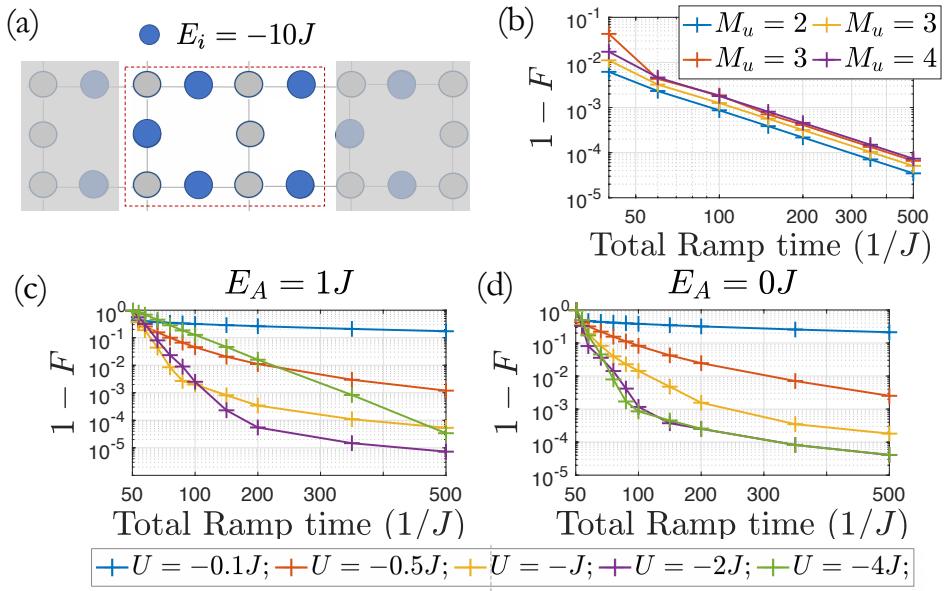

Figure 9.5: (a) Initial onsite energies for the adiabatic preparation process and the time dependence for the parameters. (b) The error in the fidelity, $F = |\langle \Psi_{\text{gs}} | \psi_T \rangle|^2$. of the time-dependently produced state compared to the non-interacting fermion ground state as a function of the total ramp time, T (linear ramp) and for different number of 5 site unit cells (shown in Fig. 9.4(a)). For an even number of unit cells ($M_u = 2$ & $M_u = 4$) these states are at half filling, for an odd number of unit cells ($M_u = 3$) the states are at half filling ± 1 atom (yellow/red). (c-d) ED results for the adiabatic preparation of the interacting ground state at half-filling for $M_u = 2$, with the ramp process in Eq. 9.7, where E_A is the onsite energy of the A sites, see Fig. 9.4(a), which is constant throughout the ramp.

For the non-interacting case the ground state is highly degenerate so we plot the projection of the final state onto the ground state manifold for small system sizes using exact diagonalisation. We can see that for ramp times that are achievable before decoherence effects begin to lead to errors ($TJ \sim 200$) we can achieve fidelities $> 1 - 1 \times 10^{-3}$ for the system sizes considered here.

Next we investigate the more interesting case of interacting ground states. We begin with the same initial state, but we now apply an exponential ramp for the parameters,

$$
\begin{aligned}
E(t) &= -E_{in}\frac{e^{5(1-t/T)}-1}{e^5-1}, \\
J(t) &= J\left(1-\frac{e^{5(1-t/T)}-1}{e^5-1}\right), \\
U(t) &= U\left(1-\frac{e^{5(1-t/T)}-1}{e^5-1}\right),
\end{aligned}
\tag{9.7}
$$

from $t = 0$ to $t = T$. As the energy gap between the ground state and first excited state decreases as we ramp these parameters, with the final state being gapless in the thermodynamic limit we find it optimal to apply this exponential ramp which ensures that there is a slower change in the parameters as the gap decreases. This ensure that the adiabatic principle is not as strongly violated compared to the case for a linear ramp. Fig. 9.5(c) we plot the projection of the final state onto the ground state using exact diagonalisation on a small system for both band structures with $E_A = J$ and $E_A = 0$. We consider a range of attractive interaction strengths where we can see that as we increase the interaction strength, the projection on the ground state improves. It is also apparent that we can achieve near perfect fidelities for experimentally achievable ramp times ($TJ \sim 200$) for strong interaction strengths, which are the phases with the most dominant pair correlations, see Fig. 9.4.

Of course, as this analysis was carried out on small system sizes, we are only able to prepare these states so accurately due to finite size effects introducing effective energy gaps in the spectra. So, we also simulate the same ramp processes on larger system sizes using time-evolution techniques with MPS [159, 206], where in Fig. 9.6 we compare the correlations produced through the time-dependent preparation to those for the ground state, again for both band structures, $E_A = J$ (a) and $E_A = 0$ (b).

We can see that as we increase the total ramp time, the correlations of the pre-

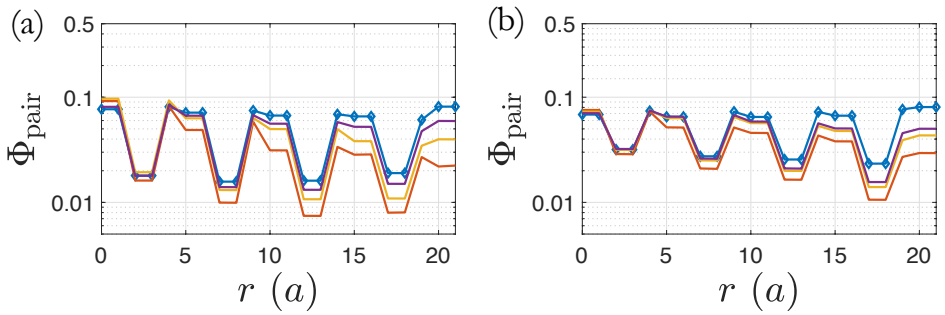

Figure 9.6: Comparison of the pair correlations in the half filled ground state (blue diamonds) with the time-dependently prepared state with a total ramp time, $TJ = (50, 100, 200) =$ (red,yellow,purple), for $E_A = J$ (a) and $E_A = 0$ (b). $U = -2J$ and system size of 10 unit cells (50 sites). Calculated with a 4th order Runge-Kutta MPS time evolution algorithm [159] with $J\tau = 0.1$ and $D = 512$.

pared state quickly approach those of the ground state, where for experimentally feasible ramp times ($TJ \sim 100$) the deviations become too small to be resolved experimentally. Note that in all cases, the single particle correlations are exponentially suppressed. These states are gapless in the thermodynamic limit, so as the size of the system is increased the total ramp time needed to accurately prepare the ground state will increase due to the closing of the energy gap. Therefore, we have also included the correlations for the state produced with a faster ramp time, $TJ = 50$, which shows that while there are deviations at larger distances, the short distance behaviour of the pair correlations is preserved. This analysis indicates that while preparing these ground states with near perfect fidelities may not be possible using adiabatic preparation schemes, due to the fact that the states are gapless in the thermodynamic limit, it is clear that we can feasibly prepare states with strong pair correlations that have a similar dependence to those of the true ground state for short distances. In this way we introduce an effective finite size for our condensate, with the benefit of being able to prepare them in realistic timescales before decoherence effects begin to dominate.

9.5 Conclusions

We have considered an experimental realisation of the Lieb lattice and how to prepare phases that have enhanced Cooper pair correlations. By performing numerical calculations on a one-dimensional ladder system we quantitatively demonstrated that we can prepare the half filled fermion ground state in experimentally realistic timescales. Additionally we provided predictions for the ground state correlations for attractive interactions where we found that due to the flat energy band the pair correlations dominate and can be further enhanced by increasing the interaction strength such that there is strong mixing with the higher dispersive energy bands. We also found that in the strongly interacting regime, mixing between the flat band states and states close to the Dirac cone resulted in correlations that were almost constant throughout the full system that we considered.

On the theoretical side this work has implications for understanding strongly interacting phases in flat band systems and how mixing with additional dispersive bands affects the properties of these phases. Additionally, our analysis also has potential to impact quantum simulation more generally, as our experimental proposal demonstrates that it is in principle possible to realise phases with strong Cooper pair correlations in current cold atom experiments.

Part IV

Simulating Open Systems Beyond Weak Coupling

Chapter 10

Non-Markovian state diffusion for open many-body systems

In this chapter we develop and apply a new method for classically simulating open quantum systems beyond the Born and Markov approximations to study dynamics of open many-body quantum systems in one-dimension strongly connected to a non-Markovian environment. We have hybridised a recently proposed technique, the hierarchy of pure states [186, 187] (see Ch. 5) and incorporated matrix product state algorithms allowing us to generalise the method to many-body systems, which is particularly relevant for understanding quantum dynamics in real materials, as the Born-Markov approximation is usually strongly violated in a solid state setting [184]. As well as opening up new avenues for theoretically investigating these novel systems, this algorithm allows us to extend the regimes that we are able to classically benchmark which is important for calibrating future quantum simulators.

As an initial proof-of-principle for the algorithm, in this chapter we present the simulation of dynamics of a system that cannot be treated, or can only be treated approximately, by other means. In particular, we consider immersing an optical lattice

system in a Bose-Einstein condensate (BEC) such that our quantum simulator can be better mapped to real world materials through the incorporation of the effects of interactions between electrons (lattice atoms) and phonons (BEC excitations). Classically simulating these effects is very computationally expensive, as it results in a combined electron-phonon Hilbert space that is too large to accurately handle, even with matrix product states and progress cannot be made with a conventional open quantum system approach as this results in very non-Markovian properties for the phonon environment. While this system is unlikely to lead to a quantum enhancement, it is equally as important to understand as finding any regimes where the effects of lattice phonons somewhat preserves quantum correlations would potentially allow for better practical real world quantum devices to be developed. Additionally, we have already seen in Ch. 6 that the correlations and entanglement grow rapidly in time and we quickly go beyond what we are able to simulate classically, but an obvious question is then how does this situation change for a system with realistic material properties and how can this be investigated with a quantum simulator?

10.1 Non-Markovian treatments of open systems in quantum optics

Advances in cold atom systems offer a controlled experimental way of probing the effects on dissipative and coherent dynamics in many-body systems through strong coupling to a non-Markovian environment [174, 341]. By utilising the controllability of cold atom experiments it is possible to accurately tune parameters allowing us to probe the transition from Markovian to non-Markovian induced dynamics [342–344]. However, there are still important open questions regarding the numerical

simulation of many-body systems that are strongly coupled to a non-Markovian environment. While there are previous techniques for going beyond the Born-Markov approximations, such as the hierarchical equations of motion (HEOM) [345, 346] or the time evolving matrix product operator technique (TEMPO) [347, 348], these studies have been limited to small systems. For larger systems, there are quantum trajectory techniques [41] which have proved invaluable for understanding dissipation in a many-body context but are usually only valid within weak coupling approximations. Thus new methods must be developed in order to benchmark or describe these novel experimental situations. To this end, by combining the recently developed hierarchy of pure states (HOPS) method [186, 187], which is a numerically exact quantum stochastic diffusion (QSD) equation, with matrix product state (MPS) techniques [1, 136, 158] we have been able to derive a numerical algorithm that is capable of quantitively calculating the dynamics of an open many-body system (in one-dimension) in regimes beyond those available within standard Born-Markov approximations [2]. This opens up opportunities for future studies to answer important questions related to the effects on many-body dynamics due to being strongly coupled to a reservoir and to quantitatively calculate the resulting non-Markovian features without invoking strong physical approximations.

We benchmark this method by considering the out-of-equilibrium dynamics of the Holstein model [349–359] going beyond the limit of dispersionless phonons. This regime has only been explored by applying approximate methods, (such as quantum Monte Carlo approaches [360–363]), because a full quantum treatment requires applying open quantum system techniques, and due to the nature of this system the resulting dynamics (in regimes that are interesting, such as for strong coupling) can only be described by going beyond conventional quantum trajectory methods [41]. Although we find that compared to the dispersionless phonon limit, (previously mod-

elled with closed system MPS techniques [364]), the physics remains qualitatively the same, our approach here allows us to more easily incorporate additional features such as correlations within the environment or finite temperatures. This study demonstrates an excellent proof-of-principle for our numerical technique where we are able to illustrate that we can access physics in an open many-body system beyond the weak coupling and Markov approximations.

10.2 The HOPS + MPS algorithm

The hierarchy of pure states (HOPS) method is a QSD equation that can be applied to a wide range of problems where it is numerically exact. There are very few approximations invoked in its derivation (see section 5.3): 1) we assume that the environment can be expressed in a coherent state basis, 2) we assume that the system and environment are linearly coupled and 3) we assume that initially, the system and environment are uncorrelated. In general however, the stronger the violation of the Born-Markov approximations the more numerically costly the algorithm becomes, and so in a practical sense we are somewhat limited in the scope of problems that can be solved with this method. Additionally, in order to apply the method we must know the correlation function for the environment operators that couple with the system, which in most cases can only be analytically derived for environments with quadratic Hamiltonians. This means that in general, in order to reliably apply this method to interesting problems more detailed knowledge of the form of the coupling between the system and environment must be obtained, compared to a conventional Born-Markov treatment.

Here we consider the case that we have N different effective environments, each coupled locally to a single site, labelled by n. One requirement for HOPS is that the

correlation function of the environment must be expanded into a sum of exponentials, so for the moment we assume that the properties of each environment n can be approximated with a Lorentzian spectral density giving rise to a correlation function of the form,

$$\alpha_{n,m}(t-t') = \langle \hat{a}_n(t)\hat{a}_m^\dagger(t')\rangle = e^{-b|n-m|}e^{-\kappa|t-t'|-i\omega(t-t')}, \tag{10.1}$$

where b is a parameter controlling the spatial correlations between environments coupled to site n & m, κ controls the decay of the temporal correlations and ω is the dominant energy mode in the environment. We assume a linear coupling between the system and environment,

$$H_{\text{Int}} = \sum_n L_n\hat{a}_n^\dagger + L_n^\dagger\hat{a}_n, \tag{10.2}$$

where L_n and $\hat{a}_n$ are the system and environment operators respectively. We can then write the (non-linear) HOPS algorithm as [186, 187]

$$\begin{aligned}\partial_t|\Psi^{\vec{k}}(t)\rangle = &\left(-iH - \sum_n k_n\left(\kappa + i\omega\right) + \sum_n \tilde{z}_n(t)L_n\right)|\Psi^{\vec{k}}(t)\rangle \\ &+ \sum_n L_n k_n|\Psi^{\vec{k}-\vec{u}_n}(t)\rangle - \sum_n \left(L_n^\dagger - \langle L_n^\dagger\rangle_t\right)|\Psi^{\vec{k}+\vec{u}_n}(t)\rangle,\end{aligned} \tag{10.3}$$

where, $\vec{k}$ is an N dimensional vector representing the auxiliary state component for each environment mode, $\vec{u}_n$ is a unit vector in the n^{th} direction of the hierarchy, $\langle L_n^\dagger\rangle_t = \langle\Psi^{(0)}(t)|L_n^\dagger|\Psi^{(0)}(t)\rangle$ and the noise terms have the properties, $\mathcal{E}[z_n(t)z_m(t')^*] = \alpha_{n,m}(t-t')$, which in the non-linear version of HOPS are modified time dependently according to,

$$\tilde{z}_n(t) = z_n(t) + \sum_m \int_0^t ds\alpha_{n,m}^*(t-s)\langle L_m^\dagger\rangle_s. \tag{10.4}$$

This form of noise effectively takes into account modifications to the environment modes due to being coupled to the system. See the next section for a numerical way for generating noise with the required statistics. Additionally, we truncate each direction of the hierarchy (where each run from $k_n = 0 \rightarrow k_{n,\max}$) with the terminator

$$|\Psi^{k_{n,\max}}(t)\rangle = \frac{\alpha(0)}{\kappa + i\omega} L_n |\Psi^{k_{n,\max} - \vec{u}_n}(t)\rangle. \tag{10.5}$$

It should be understood here that the index, $k_{n,\max}$, in the above expression should be a vector with the coefficient $k_{n,\max}$ in the n^{th} direction of the hierarchy and arbitrary coefficients in all other directions. The choice of terminator does not have a significant effect on the dynamics, for a suitable hierarchy depth [186]. Nevertheless this choice of terminator has been proposed because when the limit $k_{\max} = 0$ is taken we recover a single equation of the same form as a conventional Markovian quantum state diffusion (QSD) equation [186].

Notice that due to the simple system-environment coupling, that we can split the Hamiltonian into pieces that act locally. We will now exploit this to re-write the time-evolution in terms of an MPS algorithm. We simply incorporate the auxiliary states in the hierarchy of an environment mode into each local tensor. We do this by connecting a set of new tensors K_n,

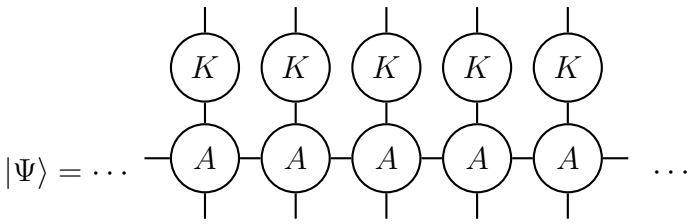

where the dimension of each hierarchy, σ, is represented by the open indices at the top. We initialise this new tensor network by setting all elements except the physical $\sigma = 0$, to zero and incorporate the initial (pure) state in the A tensors. For the

case considered here where each environment has a Lorentzian spectral density the dimension for each K_n is simply, $\sigma = k_{n,\max}$, however, if more general environments are considered, such that we must approximate the spectral density for each environment (where environments are coupled to individual sites) as a sum of p Lorentzians then naively the dimension of each K_n then must grow according to, $\sigma = (k_{n,\max})^p$.

This tensor network works well for the applications considered here, but note that it is in principle possible to extend this method to more complicated situations, even those with a non-local system-environment coupling with terms of the form $L_m L_n^\dagger a_n$, with the cost of including bonds between each K tensor. There are still open questions to how well this method would perform upon truncating the dimension of these bonds to numerically tractable sizes.

We then evolve the state with a TEBD algorithm, [136, 158], where we split the evolution of the physical degrees of freedom d_n and the hierarchy σ_n and apply two separate sets of local time-evolution operators, $U_{d_n,d_{n+1}}^{d'_n,d'_{n+1}}$, which evolve the physical dimensions, d_n, and then $\tilde{U}_{d_n,\sigma_n}^{d'_n,\sigma'_n}$, which mixes the auxiliary states by including the contributions from the HOPS algorithm.

The dimension of this hierarchy can be quite large, around ~ 6 for a single mode, and can be considerably larger if we consider environment correlations that must be approximated by a sum of exponentials. So after each application of the time-evolution operator, we include an additional step where we transform the hierarchy indices to an optimal local basis, then truncate the terms with the lowest weight, similar to that performed in [353, 364]. To implement this procedure we first, for each tensor, calculate the reduced density matrix,

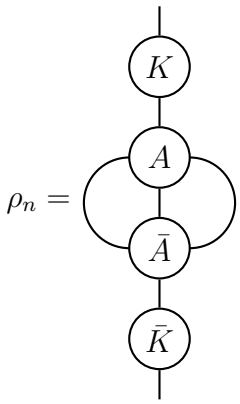

then we diagonalise this matrix and truncate elements with eigenvalues smaller than some cut-off value, $E \to E_0$,

$$\rho_n = RER^\dagger \approx R_0 E_0 R_0^\dagger. \tag{10.6}$$

This gives us a transformation to a new basis of a lower dimension. We then transform the hierarchy indices of the state and the time-evolution operator for the auxiliary states,

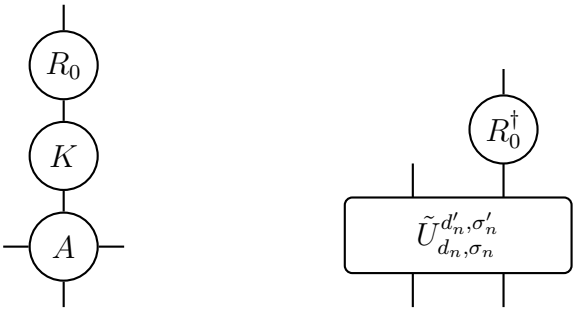

thereby reducing the number of basis states needed to represent the hierarchy. Note that only one of the hierarchy indices of $\tilde{U}^{d'_n,\sigma'_n}_{d_n,\sigma_n}$ is transformed, because we must ensure that the time-evolution operator is able to allow the state to access to the full basis during the evolution. If instead we transformed both indices, σ'_n & σ_n the

state would remain in the reduced basis leading to errors.

Numerical generation of coloured noise in the time domain

First we must define a response function, $R(t)$,

$$R(t) = \frac{1}{2\pi}\int_{-\infty}^{\infty} d\omega G(\omega) e^{-i\omega t}, \tag{10.7}$$

where $G(\omega)$ is related to the correlation function through,

$$G(\omega) = \left(\int_{-\infty}^{\infty} dt \alpha(t) e^{i\omega t}\right)^{1/2}. \tag{10.8}$$

Finally, we then calculate the coloured noise, $z(t)$, through,

$$z(t) = \int_{-\infty}^{\infty} ds R(s)\xi(t-s), \tag{10.9}$$

where $\xi(\tau) = 1/\sqrt{2}\left(\xi'(\tau) + i\xi''(\tau)\right)$ and $\xi'(\tau)$, $\xi''(\tau)$ are real independent gaussian white noise terms. The coloured noise then has the desired properties,

$$\begin{aligned} M\left[z(t)z^*(t)\right] &= \alpha(t-t'), \\ M\left[z(t)z(t)\right] &= 0. \end{aligned} \tag{10.10}$$

Numerical generation of coloured noise in the frequency domain

This derivation follows Ref. [187]. Usually the correlation function (including all examples in this note) is given in terms of a spectral density,

$$\alpha(\tau) = \frac{1}{\pi}\int_0^{\infty} \Omega(\omega) e^{-i\omega\tau} \equiv \frac{1}{\pi}\int_{-\infty}^{\infty} \tilde{\Omega}(\omega) e^{-i\omega\tau}, \tag{10.11}$$

which we can approximate this by the Riemann sum,

$$\frac{1}{\pi}\int_{-\infty}^{\infty}\tilde{\Omega}(\omega)e^{-i\omega\tau} \approx \sum_{k=0}^{n-1}\frac{\Delta\omega}{\pi}\tilde{\Omega}(\omega_k)e^{-i\omega_k\tau}, \tag{10.12}$$

allowing us to define the coloured noise through,

$$z(t) = \sum_{k=0}^{n-1}\sqrt{\frac{\Delta\omega\tilde{\Omega}(\omega_k)}{\pi}}\xi(k)e^{-i\omega_k t}, \tag{10.13}$$

where $\xi(k)$ is a complex gaussian white noise process, satisfying,

$$\begin{aligned} M\left[\xi(k)\xi^*(k')\right] &= \delta(k-k'), \\ M\left[\xi(k)\xi(k')\right] &= 0 \end{aligned} \tag{10.14}$$

This corresponds to a numerical integration from $\omega_0 - \Delta\omega/2$ to $\omega_1 + \Delta\omega/2$, using the midpoint rule. In practice I find it optimal to choose a particular value of dt and $\Delta\omega$, which gives rise to the number of terms in the sum n through, $n\Delta\omega dt = 2\pi$. Choosing $\omega_0 = \Delta\omega/2$ then allows us to calculate ω_1, and we should check that the value of $\tilde{\Omega}(\omega_1)$ is close to zero so that the spectral function is reliably approximated. We can actually compute this coloured noise very efficiently using the Fast Fourier Transform (FFT),

$$z(t) = e^{-i\omega_0 t}\sqrt{\frac{\Delta\omega}{\pi}}FFT\left(\sqrt{\tilde{\Omega}(\omega_k)}\xi(k)\right). \tag{10.15}$$

10.3 Benchmarking: CDW melting in the dispersive Holstein model

We then benchmark this algorithm by applying it to solve for the out-of-equilibrium dynamics of a Holstein model going beyond the approximation of dispersionless phonons. We take a phenomenological approach, where we assume that we can capture the phonon dispersion with a Lorentzian spectral density and that each site of the lattice couples to its own effective phonon environment. This approximation is useful as this form of spectral density is efficiently simulable with HOPS and it can be easily seen that upon taking the phonon dispersion to zero we recover the seminal model for dispersionless phonons, which results in a highly non-Markovian environment with an infinite correlation time.

At the end of this chapter, we will consider the possibility of creating this system in cold atom experiments by immersing a lattice system in a weakly interacting BEC. We show that in certain limits it may be possible to experimentally model the dynamics that we are classically simulating here, with effective independent environments with Lorentzian spectral densities.

We will approximate the Hamiltonian for a one-dimensional lattice, taking for the moment spinless fermions, immersed in a global (also 1D) phonon environment with a model where each lattice site is connected to its own environment,

$$H = \omega_0 \sum_n c_n^\dagger c_n - J \sum_n \left(c_n^\dagger c_{n+1} + c_n c_{n+1}^\dagger \right) + g \sum_n \hat{n}_n \left(\hat{a}_n + \hat{a}_n^\dagger \right), \tag{10.16}$$

where $\hat{a}_n$, $\hat{a}_n^\dagger$ are the environment operators with correlations of the form,

$$\alpha_n(t - t') = \langle \hat{a}_n(t) \hat{a}_n^\dagger(t') \rangle = e^{-\kappa|t-t'| - i\omega(t-t')}, \tag{10.17}$$

where a is the spacing between lattice sites, ω is the phonon energy level in the environment and κ is the gradient of the linearly dispersive phonons. Taking the limit of $\kappa \to 0$ we recover the Holstein model which describes dispersionless phonons. In the following, we set $\omega_0 = 1/2J$ and $\omega = J$, and vary κ and g.

For an experimental realisation in quantum optical experiments, we can usually make the approximation that $ka \gg 1$ allowing us to neglect spatial correlations between the environment modes which gives rise to a model where each site is connected to an independent environment. However, we note here that a feature of HOPS is that it can also be used to describe situations where this approximation is relaxed without additional computational cost, if one can find a way to numerically generate the coloured noise terms, $z_n(t)$, with the required statistics and correlations.

As we make use of a QSD equation we must integrate the equations of motion many times with different realisations of the noise terms and average the observables to obtain the results predicted from a full density matrix description, however in practice these trajectories can be solved in parallel. Note that for the calculation of observables within this framework follows a similar process as for conventional QSD. For each trajectory we calculate expectation values using only the physical state, i.e

$$O_{n,m}(t) = \langle \Psi^0(t) | O_{n,m} | \Psi^0(t) \rangle. \tag{10.18}$$

Charge density wave melting

Following Ref. [364] we begin with the initial state, $|1, 0, 1, 0, \cdots\rangle$, and calculate a charge density wave order parameter,

$$O_{\mathrm{CDW}}(t) = \frac{1}{M} \sum_n (-1)^n \langle \hat{n}_n(t) \rangle. \tag{10.19}$$

We plot this in Fig. 10.1(a) for different coupling strengths, g and phonon dispersions, κ. We find the same qualitative behaviour as the case for dispersionless phonons, where for weak coupling, $g = 0.1J$, the dynamics are similar to the closed system ($g = 0$) case where there are oscillations, but for non-zero dissipation, the CDW *melts* into a homogeneous steady state. Increasing the coupling strength to $g = J$ these oscillations are damped and quickly approach the steady state value. Further increasing the coupling strength we can see that the the charge density wave melting is somewhat suppressed and slowed for short times and the oscillations become completely damped for $g = 5J$.

This is similar to the features observed for the dispersionless phonon case [364], however they observe a very pronounced plateau in the order parameter which is then followed by a decay towards zero, as opposed to this constant decay to zero observed here. This indicates that having some dispersion to the phonons reduces the effects on the system dynamics, and indeed, if we increase the phonon dispersion κ we see a reduction in this effect. Note that previous analysis for time-evolution in the dispersionless phonon case was carried out on system sizes up to $M = 13$ [364], but we can go beyond this limit with the HOPS + MPS algorithm.

We compare the results to that of a conventional quantum state diffusion (QSD) equation valid in the Born-Markov limit (BML). This is achieved by setting $k_{max} = 1$ and $\alpha_{n,m}(\tau) = \Gamma\delta_{n,m}\delta(\tau)$, which physically corresponds to the approximation that the phonon dispersion is large. In order to match this limit of HOPS with a standard Markovian QSD equation, we use $\Gamma = 2/\kappa$. Note that we use the non-linear version of this equation, see Eq. 5.19 in Ch. 5. We see that this model completely fails to predict the suppression of the order parameter at short times, although agrees with the steady state behaviour. Also note that the dynamics are now independent of κ.

It is also clear that the observables captured with HOPS for stronger coupling

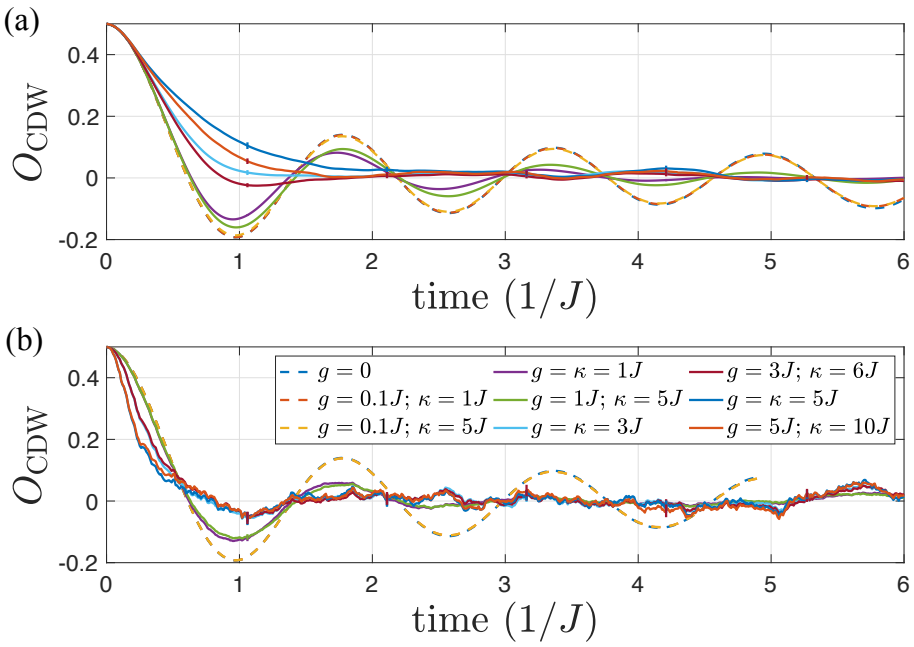

Figure 10.1: The charge density wave order parameter, increasing the coupling strength g, suppresses the melting somewhat for short times. (a) HOPS, $k_{max} = 8$, $D = 128$, $Jdt = 0.01$, $N_{\mathrm{traj}} = 100$. (b) Born-Markov Limit (BML), $N_{\mathrm{traj}} = 100$. System size, $M = 20$. Error bars represent statistical uncertainty in the mean value over all trajectories - where error bars are not visible they are smaller than the width of the curves.

are less noisy compared to the BML even though there are the same number of trajectories. This is due to the coloured noise term which is correlated in time, meaning that on average there are not as many large jumps in the noise processes compared to the white noise used for the BML. Additionally, from Eq. 10.4 we can see that the noise terms are also weighted by the correlation function and system observables from previous times, which will further smooth out the random processes. This is a nice feature of the non-linear version of HOPS, which is not observed as prominently in the linear version [186, 187] (see Eq. 5.33 in Ch. 5), indicating that this is most likely a numerical effect rather than a physical one.

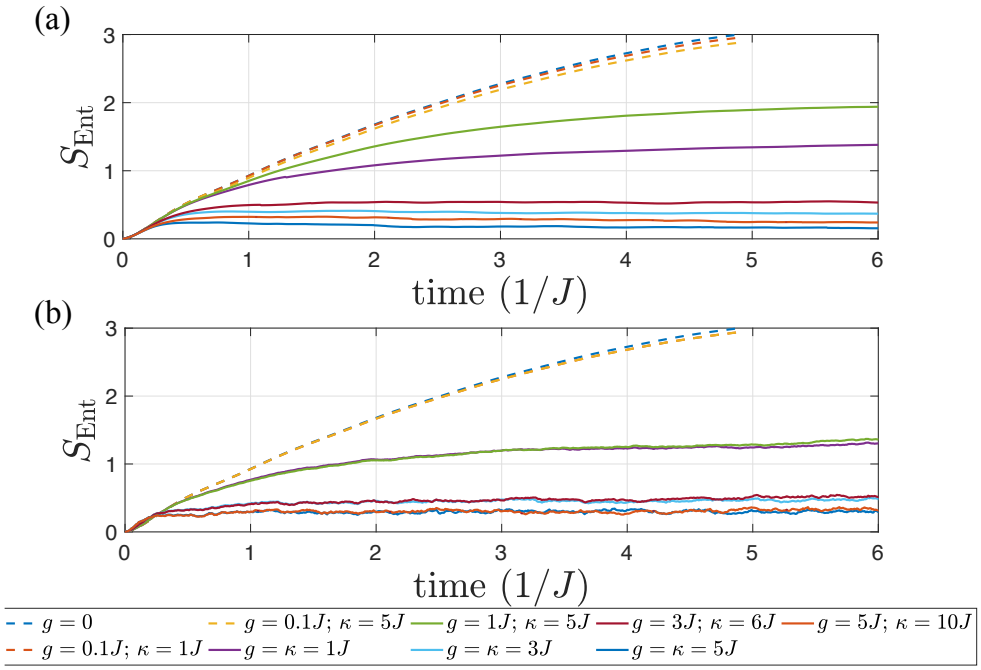

Figure 10.2: The average entanglement entropy at each bond. (a) HOPS, $k_{max} = 8$, $D = 128$, $Jdt = 0.01$, $N_{\mathrm{traj}} = 100$. (b) Born-Markov Limit, $N_{\mathrm{traj}} = 100$. System size, $M = 20$. Error bars represent statistical uncertainty in the mean value over all trajectories - where error bars are not visible they are smaller than the width of the curves.

Entanglement scaling

We then consider the entanglement properties of the system. We calculate the Von-Neuman entropy of each bond,

$$E = -\sum_{m=1}^{r} s_m \log(s_m), \tag{10.20}$$

where s_m are the Schmidt coefficients at each bond. We plot the average over all bonds in Fig. 10.2, where we find that as the phonon coupling is increased, the entanglement in the system decreases. This indicates that the presence of phonons prevents motion of particles in the system and also suppresses the build up of entanglement and correlations. We also observe that as the phonon dispersion is increased,

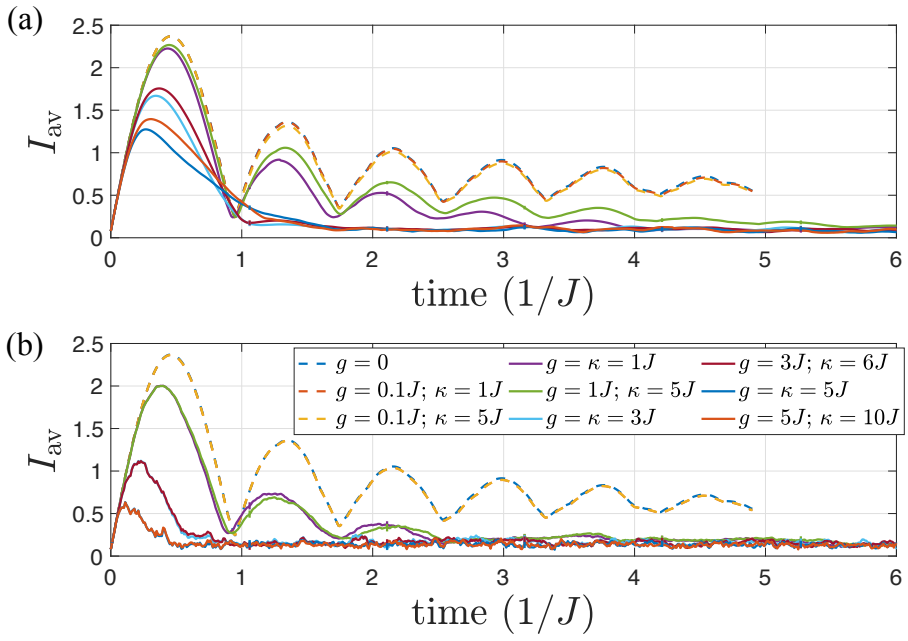

Figure 10.3: The average magnitude of the particle current at each bond (see Eq. 10.21). (a) HOPS, $k_{max} = 8$, $D = 128$, $Jdt = 0.01$, $N_{\mathrm{traj}} = 100$. (b) Born-Markov Limit, $N_{\mathrm{traj}} = 100$. System size, $M = 20$. Error bars represent statistical uncertainty in the mean value over all trajectories - where error bars are not visible they are smaller than the width of the curves.

then the entanglement can grow to larger values indicating that the phonons do not have as much time to affect the system before moving away from the site at which they were created. Again we compare to the BML and we see that there is qualitative agreement between the two methods, but in particular note that the case with $g = J$, $\kappa = 5J$ has larger entropy compared to those predicted in the BML.

Currents

In Fig. 10.3 we compare the particle currents predicted by the HOPS+MPS method and the BML. We calculate the current at each bond between neighbouring sites,

$$I_n = 4i\left(c_n^\dagger c_{n+1} - c_n c_{n+1}^\dagger\right). \tag{10.21}$$

As we are simulating a global quench here without any applied bias there is no preferred direction to the currents, but we can still obtain information about the directionless particle motion in the system by calculating the magnitude of the above expression. We plot the average at each bond in Fig. 10.3, where we see that as the coupling strength increases, the current is suppressed and decays towards zero at an increased rate. Similar to the case of charge density wave melting, the BML fails to reliably capture the short time dynamics, but predicts a reliable estimate for the steady state where all motion has been suppressed by the dissipation.

Environment correlations

Through features arising from the HOPS algorithm, we can calculate time-dependent observables within the environment, thus enabling us to quantify the deviation away from the initial phonon population as well as capturing the build up of correlations between the system and the environment. This allows us to directly calculate the extent of which a Born approximation would be invalid*. In order to derive the expression for these quantities, we must exploit one of the assumptions of HOPS where we can expand the state of the environment in a basis of coherent states, which allows us to write the total state as,

$$|\Psi_T\rangle = \int \frac{d^2z}{\pi} e^{-|z|^2} |\psi_s(z,t)\rangle \otimes |z\rangle. \tag{10.22}$$

We can then calculate observables by,

$$\langle a^\dagger a \hat{S}\rangle = \mathrm{Tr}\left[a^\dagger a \hat{S}|\Psi_T\rangle\langle\Psi_T|\right] = \int \frac{d^2z}{\pi} e^{-|z|^2} \langle\psi_s(z,t)|\hat{S}|\psi_s(z,t)\rangle\langle z|a^\dagger a|z\rangle, \tag{10.23}$$

*However, this does not necessarily mean that there would be errors in the dynamics for the system in this approximation [365].

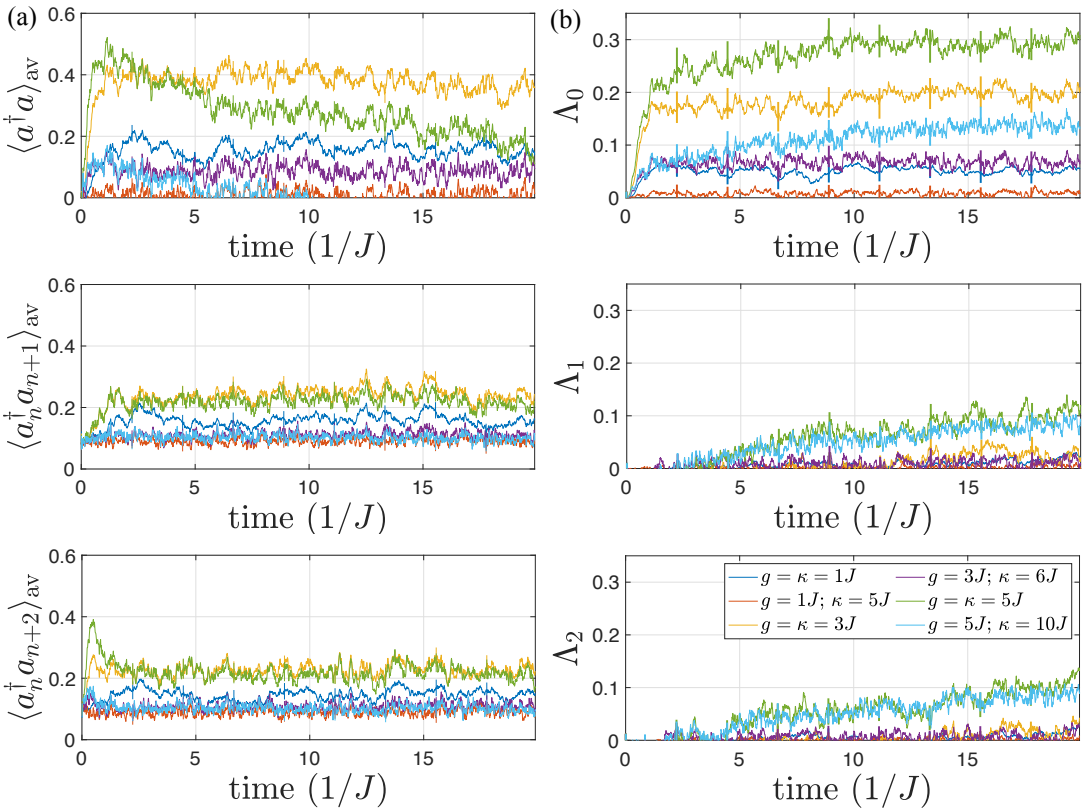

Figure 10.4: (a) Phonon-phonon correlations. (b) Electron-phonon correlations (see Eq. 10.25). For a Born approximation to be valid these would all need to be zero. HOPS, $k_{max} = 8$, $D = 128$, $Jdt = 0.01$, $N_{\rm traj} = 100$. Error bars represent statistical uncertainty in the mean value over all trajectories - where error bars are not visible they are smaller than the width of the curves.

where $\hat{S}$ and $a^\dagger a$ act on the system and environment Hilbert spaces respectively. Like the dynamical evolution of the state $|\psi_s(z,t)\rangle$ we can compute this quantity stochastically,

$$\langle a^\dagger a \hat{S} \rangle = \mathcal{E}\left[\langle \psi_s(z,t)|\hat{S}|\psi_s(z,t)\rangle \langle z|a^\dagger a|z\rangle\right] = \mathcal{E}\left[\langle \psi_s(z,t)|\hat{S}|\psi_s(z,t)\rangle |z|^2\right]. \quad (10.24)$$

For the dispersive Holstein model we plot the correlations generated in the environment in Fig. 10.4(a). Firstly, it is apparent that these values have a larger

uncertainty associated with them, indicating that in order to obtain reliable quantitative predictions for these observables many more trajectories are needed compared to the system observables. Nevertheless they allow us to assess the qualitative features, where we can see that as the coupling strength is increased the phonon population $\langle a^\dagger a\rangle_{\rm av} = 1/M\sum_n \langle a_n^\dagger a_n\rangle$ increases. We also see that as the dispersion of the phonons is increased that this population decreases and we can see that the (average) correlations between spatially separated phonon modes in the environment share a similar dependence. In Fig. 10.4(b) we plot the correlations between the system and environment,

$$\Lambda_m = \frac{1}{M-m}\sum_p \langle \hat{n}_{p+m} a_p a_p^\dagger\rangle - \langle \hat{n}_{p+m}\rangle\langle a_p a_p^\dagger\rangle. \tag{10.25}$$

We see similar behaviour, which also illustrates why the BML equations failed for stronger coupling. Firstly from (a) there is a significant deviation away from the initial zero phonon state, meaning that the environment does not relax back to thermal equilibrium which may lead an invalidation of the memoryless bath and the Markov approximation. But more importantly, from (b) we can see there are significant correlations built up between the system and environment which directly invalidates the Born approximation.

Finite temperature

We follow Ref. [187] and generalise the HOPS algorithm for environments initially in thermal states, by simply incorporating a hermitian stochastic contribution to the system Hamiltonian,

$$H = H_S + L^\dagger y(t) + L y^*(t), \tag{10.26}$$

where the stochastic noise elements, $y(t)$, satisfy, $\mathcal{E}[y(t)y^*(t')] = (\exp(\beta\omega)-1)^{-1}\alpha(t-t')$ for the case of a single mode, where β is the inverse temperature, $\beta = 1/k_b T$. But

more generally,

$$\mathcal{E}[y(t)y^*(t')] = \frac{1}{\pi}\int_0^\infty d\omega n(\beta,\omega)\Omega(\omega)e^{-i\omega(t-t')}, \tag{10.27}$$

where $n(\beta,\omega) = (\exp(\beta\omega)-1)^{-1}$ and the spectral density $\Omega(\omega)$ is related to the (zero temperature) correlation function through,

$$\alpha(t-t') = \frac{1}{\pi}\int d\omega\Omega(\omega)e^{-i\omega(t-t')}. \tag{10.28}$$

We can derive Eq. 10.26 by considering the P-representation of the full density matrix for an environment initially in a thermal coherent state,

$$\rho_T(t) = \int d^2y \frac{1}{\pi\bar{n}} e^{-|y|^2/\bar{n}} U(t)\rho_s(0)\otimes|y\rangle\langle y|U^\dagger(t), \tag{10.29}$$

where $|y\rangle$ is a normalised coherent state. We can make use of the coherent state displacement operator, $|y\rangle = D(y)|0\rangle$, where $|0\rangle$ is the vacuum,

$$\rho_T(t) = \int d^2y \frac{1}{\pi\bar{n}} e^{-|y|^2/\bar{n}} U(t)D(y)\rho_s(0)\otimes|0\rangle\langle 0|D^\dagger(y)U^\dagger(t). \tag{10.30}$$

Making use of the relation, $D(y)D^\dagger(y) = 1$, and the cyclical properties of the trace, we can define a new time evolution operator,

$$\tilde{U}(t) = D^\dagger(y)U(t)D(y), \tag{10.31}$$

which acts on an initial state with a zero temperature environment, and leads to the modified Hamiltonian,

$$\tilde{H} = D^\dagger(y)HD(y) = H_S + Ly^*(t) + L^\dagger y(t) + H_{\rm Int}. \tag{10.32}$$

We can then write the time evolution for the density matrix as,

$$\rho_T(t) = \int d^2y \frac{1}{\pi\bar{n}} e^{-|y|^2/\bar{n}} \tilde{U}(t)\rho_s(0) \otimes |0\rangle\langle 0|\tilde{U}^\dagger(t) = \int d^2y \frac{1}{\pi\bar{n}} e^{-|y|^2/\bar{n}} |\tilde{\Psi}_T\rangle\langle\tilde{\Psi}_T|, \tag{10.33}$$

where

$$|\tilde{\Psi}_T\rangle = \int \frac{d^2z}{\pi} e^{-|z|^2} |\tilde{\psi}_s(z, y, t)\rangle \otimes |z\rangle. \tag{10.34}$$

This then gives us,

$$\rho_T(t) = \int d^2y \frac{1}{\pi\bar{n}} e^{-|y|^2/\bar{n}} \int d^2z \frac{1}{\pi} e^{-|z|^2} |\tilde{\psi}_s(z, y, t)\rangle\langle\tilde{\psi}_s(z, y, t)| \otimes |z\rangle\langle z|, \tag{10.35}$$

This means that in order to reproduce this density matrix, we now have to perform two averages over these two noise realisations, y and z. The two integrals over coherent states in Equ. 10.35 can be interpreted in a Monte Carlo sense, [187], by sampling trajectories with different realisations of the noise terms which satisfy,

$$\begin{aligned} \mathcal{E}[z(t)z^*(t')] &= \frac{1}{\pi}\int_0^\infty d\omega \Omega(\omega) e^{-i\omega(t-t')} = \alpha(t-t'), \\ \mathcal{E}[y(t)y^*(t')] &= \frac{1}{\pi}\int_0^\infty d\omega n(\beta, \omega)\Omega(\omega) e^{-i\omega(t-t')}. \end{aligned} \tag{10.36}$$

This means that we can simply apply the same zero temperature HOPS algorithm with the only modification to the time-evolution of the individual trajectories being the addition of the new hermitian stochastic contribution, $Ly^*(t) + L^\dagger y(t)$. We note that to reproduce the correct statistics it is likely that we will need to perform more trajectories compared to the zero temperature case.

In Fig. 10.5 we plot the results, where we see that the suppression of the CDW melting is enhanced for increasing temperatures. This is because there is a non-zero population of phonons in the initial state, allowing for a greater effect on the short

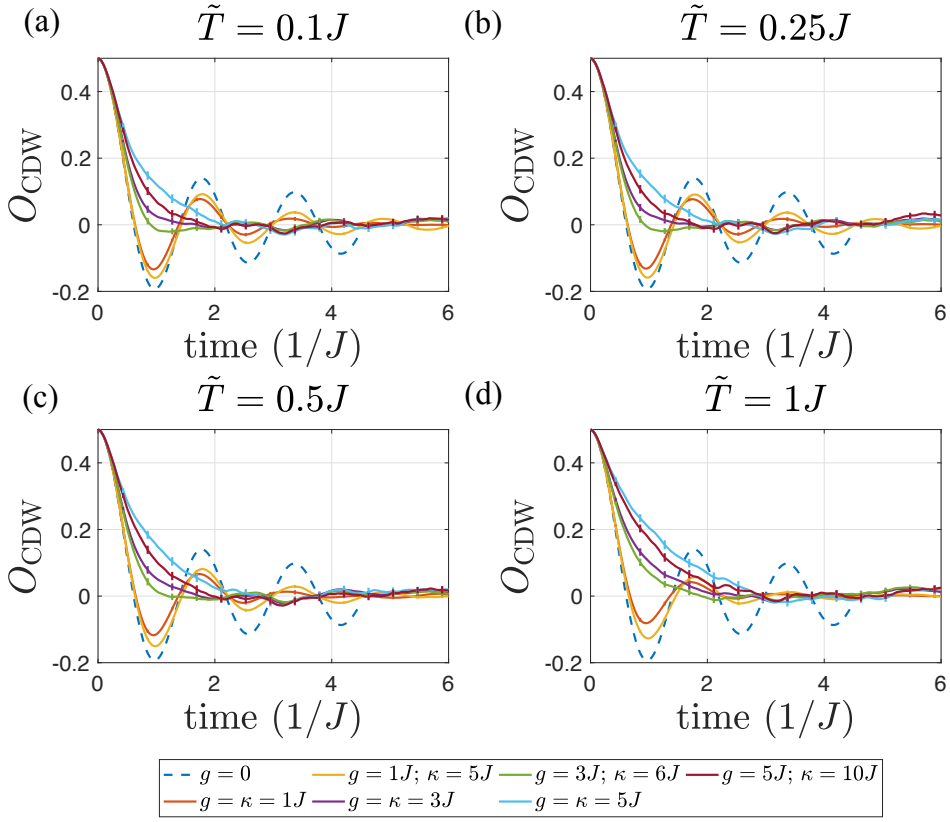

Figure 10.5: Finite temperature analysis of the charge density wave order parameter with HOPS, $k_{max} = 8$, $D = 128$, $Jdt = 0.01$, $N_{\mathrm{traj}} = 100$. System size, $M = 20$. Error bars represent statistical uncertainty in the mean value over all trajectories - where error bars are not visible they are smaller than the width of the curves.

time dynamics. This is one prominent advantage of the presented numerical approach to solving for the dynamics in the Holstein model compared to previous closed system simulations of the dispersionless case. Even though the qualitative behaviour is very similar, we can then go beyond the previous studies and investigate the quantitative corrections to the dynamics induced by finite temperatures, which is an important consideration for real solid state devices.

10.3.1 Correlation spreading in the XXZ model

We attempt now to capture the effects of interactions between particles in this system and so we consider two component fermion (spin) states. In this section we assume the limit of strong onsite interactions, such that we can neglect the motion of the particles and we derive an effective spin model describing super-exchange processes [366, 367]. If we have two component fermions with onsite contact interactions that satisfy $U_{\uparrow\uparrow}, U_{\downarrow\downarrow} \gg U_{\uparrow\downarrow} \gg J$, where J is the nearest neighbour tunnelling rate and if we have unit density with $\rho_\uparrow + \rho_\downarrow = 1$, then we have a Mott insulating state with a single fermion on each site. But we can then have a process that comes with an exchange of the $\uparrow$ and $\downarrow$ species on neighbouring sites through a super-exchange interaction, which can be derived through second order perturbation theory as $J^2/U_{\uparrow\downarrow}$. For bosonic atoms the super-exchange between the same component can be neglected because $U_{\uparrow\uparrow}, U_{\downarrow\downarrow} \gg U_{\uparrow\downarrow}$, whereas for fermions the Pauli blocking completely suppresses these terms. We can then write this as a flip-flop spin model by mapping which gives rise to the Hamiltonian,

$$H_{XY} = \omega_0 \sum_n \sigma_n^z - \frac{J^2}{U_{\uparrow\downarrow}} \sum_n \left(\sigma_n^+ \sigma_{n+1}^- + h.c\right), \tag{10.37}$$

where $\omega_0 = E_\uparrow - E_\downarrow$.

Then including a nearest neighbour density-density two-body interaction,

$$H_V = \sum_m \left(V_{\uparrow\uparrow}\hat{n}_{\uparrow,m}\hat{n}_{\uparrow,m+1} + V_{\downarrow\downarrow}\hat{n}_{\downarrow,m}\hat{n}_{\downarrow,m+1} + V_{\uparrow\downarrow}\hat{n}_{\uparrow,m}\hat{n}_{\downarrow,m+1} + V_{\uparrow\downarrow}\hat{n}_{\downarrow,m}\hat{n}_{\uparrow,m+1}\right), \tag{10.38}$$

leads to the effective spin model,

$$H_V = \sum_n \left(\tilde{V} \sigma_n^z \sigma_{n+1}^z + \tilde{V} \sigma_n^z \right), \tag{10.39}$$

where $\tilde{V} = V_{\uparrow\uparrow} + V_{\downarrow\downarrow} - 2V_{\uparrow\downarrow}$. Combining these pieces together we obtain the XXZ model,

$$H_{XXZ} = \tilde{\omega}_0 \sum_n \sigma_n^z + \sum_n \left(-\frac{2J^2}{U_{\uparrow\downarrow}} \sigma_n^x \sigma_{n+1}^x - \frac{2J^2}{U_{\uparrow\downarrow}} \sigma_n^y \sigma_{n+1}^y + \tilde{V} \sigma_n^z \sigma_{n+1}^z \right), \tag{10.40}$$

In the XXZ model it is clear that the total occupation number on each site is a conserved quantity. This means that in terms of the interaction Hamiltonian of Eq. 10.61, $c_n^\dagger c_n + \bar{c}_n^\dagger \bar{c}_n$ in the spin model is an identity and so we can neglect the effects of this term. We then only consider the Heisenberg limit of the XXZ model where all couplings between different spin components are equal. Combining these things together, we can write the Hamiltonian as

$$H = \tilde{\omega}_0 \sum_n \sigma_n^z + J \sum_n \left(\sigma_n^x \sigma_{n+1}^x + \sigma_n^y \sigma_{n+1}^y + \sigma_n^z \sigma_{n+1}^z \right) + \sum_n g \left(\hat{a}_n + \hat{a}_n^\dagger \right) \sigma_n^x, \tag{10.41}$$

where in the following we consider, $\tilde{\omega}_0 = 1/2J$ and we again approximate the environment correlations as

$$\alpha_{n,m}(t - t') = \langle \hat{a}_n(t) \hat{a}_m^\dagger(t') \rangle = \delta_{n,m} e^{-\kappa |t-t'| - i\omega(t-t')}, \tag{10.42}$$

with $\omega = J$.

In Fig. 10.6 we plot the correlations within the system beginning in a charge density wave state, $|\uparrow, \downarrow, \uparrow, \downarrow, \cdots\rangle$. We note here that we required a much larger number of trajectories compared to the previous section in order to obtain a low sampling error in these observables, $N_{\text{traj}} = 1000$. In terms of the physics we can

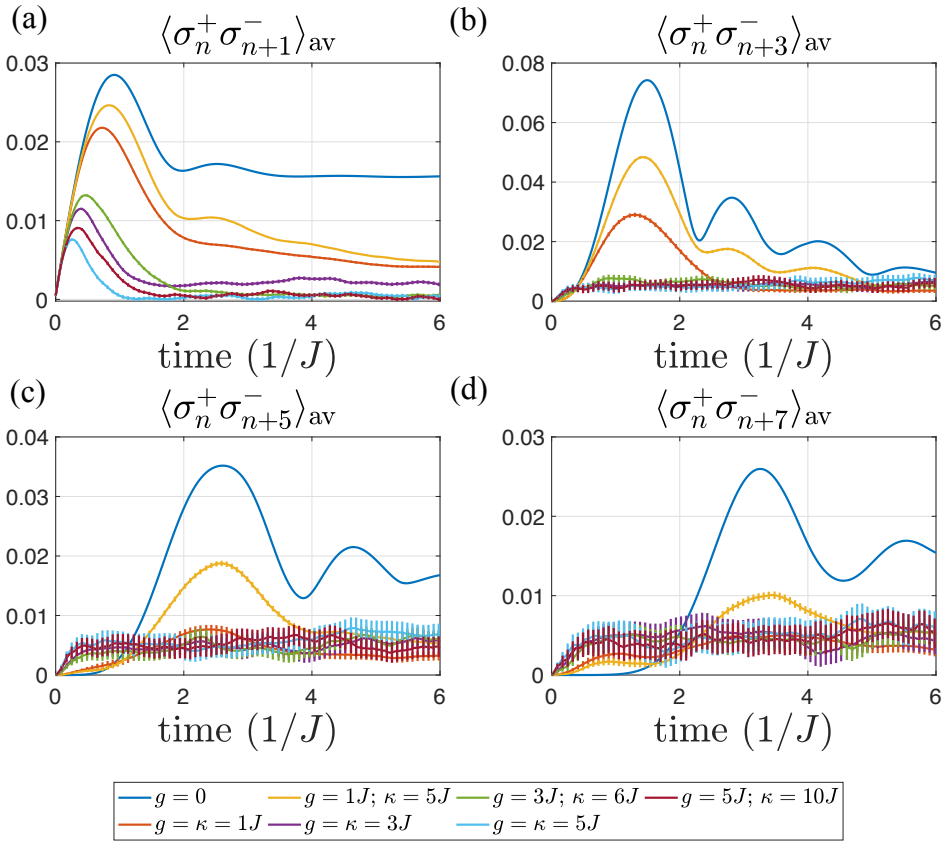

Figure 10.6: Correlation spreading in the XXZ model with dissipation. Calculated with HOPS, $k_{max} = 6$, $D = 128$, $Jdt = 0.01$, $N_{\text{traj}} = 1000$. System size, $M = 20$. Error bars represent statistical uncertainty in the mean value over all trajectories - where error bars are not visible they are smaller than the width of the curves.

see from (a) that increasing the coupling strength suppresses the magnitude of the nearest neighbour correlations and decreasing κ (i.e. increasing the memory of the environment) also suppresses these correlations. This indicates that effects beyond the Born-Markov approximations will in general result in a suppression of the maximum correlations in this model. For longer range correlations (b-d), firstly it is clear that there is more uncertainty, but it appears that the correlations grow faster for strong coupling ($g = 3J$ & $g = 5J$), albeit reaching much smaller values. In all cases,

the steady state appears to be around the same non-zero value, indicating that in some cases strong coupling does not destroy all correlations.

This analysis demonstrates that we can efficiently simulate the dynamics of spin models in the presence of dissipative effects beyond the Born-Markov approximation with this numerical technique and we have shown that we can consider different couplings between the system and environment which results in different physical features, but does not significantly impact the performance of the method.

10.4 The extended Hubbard-Holstein model

We now consider the full model of two-species fermions taking into account both their kinetic energy and their interactions. Explicitly this is given by

$$\begin{aligned} H = \omega_0 \sum_{n,\sigma} c^\dagger_{n,\sigma} c_{n,\sigma} - J \sum_{n,\sigma} \left(c^\dagger_{n,\sigma} c_{n+1,\sigma} + c_{n,\sigma} c^\dagger_{n+1,\sigma} \right) + U \sum_n \hat{n}_{n,\uparrow} \hat{n}_{n,\downarrow} \\ + \frac{g}{2} \sum_n \left(\hat{n}_{n,\uparrow} + \hat{n}_{n,\downarrow} + c^\dagger_{n,\uparrow} c_{n,\downarrow} + c^\dagger_{n,\downarrow} c_{n,\uparrow} \right) \left(\hat{a}_n + \hat{a}^\dagger_n \right). \end{aligned} \tag{10.43}$$

If there were no spin flip processes, $c^\dagger_{n,\uparrow} c_{n,\downarrow}$ and $c^\dagger_{n,\downarrow} c_{n,\uparrow}$ then this would be known as the Hubbard-Holstein model [368–372], however, our derivation of this model in cold atom experiments, presented in the next section, means that we may also include them, which leads to novel features that we will see below. We refer to this case as the *extended* Hubbard-Holstein model.

It has been shown that in the Hubbard-Holstein model the coupling to the phonons shifts the effective electron-electron interaction strength which if the coupling is large enough can give rise to an effective attractive interaction that can lead to phases with superconductive like pairing [373–375]. This can be understood by considering the large phonon frequency limit, $\omega \gg J$, which gives then an effective

interaction strength of $U_{\text{eff}} \to U - 2g^2/\omega$. Below we will assess the dynamical behaviour of this model away from this simple limit, specifically for the case where $\omega = J$. Additionally we will allow for dispersive phonons such that the correlation functions are,

$$\alpha_{n,m}(t-t') = \langle \hat{a}_n(t)\hat{a}_m^\dagger(t')\rangle = \delta_{n,m} e^{-\kappa|t-t'|-i\omega(t-t')}. \tag{10.44}$$

By applying our MPS + HOPS algorithm to this problem we are able to assess the fully quantum corrections to the previous predictions with the complimentary approach of quantum Monte Carlo techniques [373–375], although we then limit ourselves to one-dimensional systems, where the previous studies are also valid. In the following we begin in the initial product state, $|\uparrow,\downarrow,\uparrow,\downarrow,\cdots\rangle$ and consider the parameters, $\omega_0 = 1/2J$; $U = J$; $\omega = J$. Similar to the previous sections we then vary g and κ.

Additionally, we find that the increased dimension for the local Hilbert space and the resulting increased growth of entanglement means that we are limited in the length of time evolution for a similar range of numerical parameters as in the previous sections. However, we are still able to capture the most interesting features which occur during the short time transient regime.

Charge density wave melting

First we calculate the charge density wave order parameter,

$$O_{\text{CDW}}(t) = \frac{1}{M}\sum_n (-1)^n \langle \hat{n}_{n,\uparrow}(t)\rangle, \tag{10.45}$$

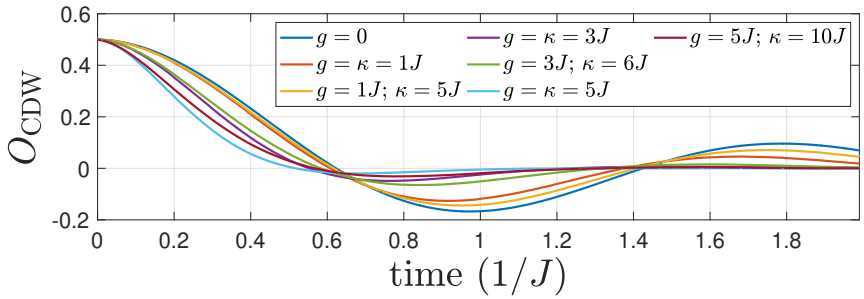

Figure 10.7: The charge density wave order parameter in the extended Hubbard-Holstein model. HOPS, $k_{max} = 8$, $D = 128$, $Jdt = 0.01$, $N_{\mathrm{traj}} = 500$. Error bars represent statistical uncertainty in the mean value over all trajectories - where error bars are not visible they are smaller than the width of the curves.

and plot this in Fig. 10.7 for different coupling strengths, g, and values for the phonon dispersion, κ. We can see that in contrast to the spinless case (see Fig. 10.1), that the melting of the charge density wave is enhanced for stronger coupling and/or smaller phonon dispersion where the oscillations (present for small coupling, $g = J$) are strongly damped for $g = 3J$ and $g = 5J$. We believe that this is due to two features of the coupling Hamiltonian: firstly, the total particle number operator, $\hat{n}_\uparrow + \hat{n}_\downarrow$, which when two species are on a single site will allow them to interact stronger with the phonon environment meaning that it is more favourable for the initial state, with a single particle on each site, to melt into the case where there two particles on each site. This is related to the manifestation of the effective attractive interaction strength along the lines detailed above. Secondly the presence of the additional spin flip dissipative terms will further enhance this melting. The steady state values in this case, where the dynamics have been suppressed are similar to the behaviour for the spinless case.

Currents

To get an insight into the dynamical features of the system we calculate the particle, spin and pair currents. Again, as we are simulating a global quench with no favourable direction, we simply compare the average magnitudes of the currents at each bond. This will allow us to get an idea of the ability for the system to conduct a net current, in the event that an applied bias voltage is included.

In Fig. 10.8, we compare the particle current,

$$I_{n,\sigma} = 4i\left(c^{\dagger}_{n,\sigma}c_{n+1,\sigma} - c_{n,\sigma}c^{\dagger}_{n+1,\sigma}\right), \tag{10.46}$$

the spin current,

$$I_{n,\text{spin}} = 4i\left(\sigma^{+}_{n}\sigma^{-}_{n+1} - \sigma^{-}_{n}\sigma^{+}_{n+1}\right), \tag{10.47}$$

where, $\sigma^{+}_{n} = (\sigma^{-}_{n})^{\dagger} = c^{\dagger}_{n,\uparrow}c_{n,\downarrow}$, and the pair current,

$$I_{n,\text{pair}} = 4i\left(\Delta^{\dagger}_{n}\Delta_{n+1} - \Delta_{n}\Delta^{\dagger}_{n+1}\right), \tag{10.48}$$

where $\Delta_n = c_{n,\uparrow}c_{n,\downarrow}$.

We can see that similar to the spinless case, the single particle currents are suppressed for stronger coupling and lower phonon dispersion. We also compare the spin currents which have different qualitative behaviour compared to the particle currents and peak at later times, due to the spin charge separation of one-dimensional systems (see Ch. 3), although are also similarly suppressed. In the figure we also compare the pairing currents, where for the case of no coupling to the phonons, $g = 0$, there is no net motion for pairs. We can see here that as the coupling to the phonon environment is increased, there is an enhancement of the pairing currents, although these values are at magnitudes much smaller than the single particle currents, it

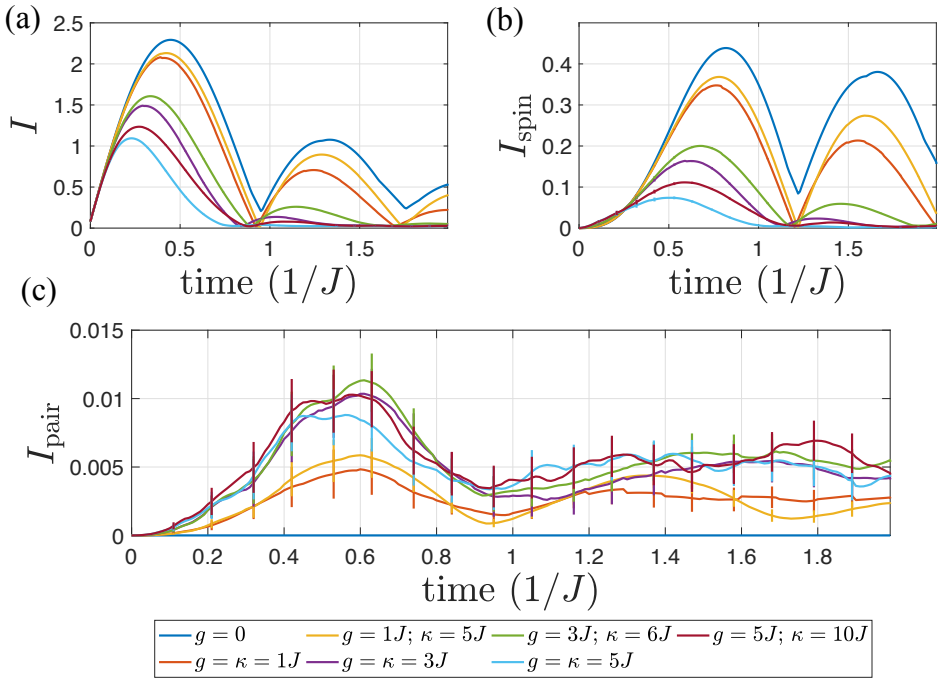

Figure 10.8: Comparison of the (a) single particle (Eq. 10.46), (b) spin (Eq. 10.47) and (c) cooper pair (Eq. 10.48) currents in the extended Hubbard-Holstein model to the case where $g = 0$ (blue line). The average magnitude of the current at each bond. HOPS, $k_{max} = 8$, $D = 128$, $Jdt = 0.01$, $N_{\text{traj}} = 500$. Error bars represent statistical uncertainty in the mean value over all trajectories - where error bars are not visible they are smaller than the width of the curves.

is clear that these grow if the coupling strength is increased. These features bring in interesting questions regarding how to exploit this enhanced pairing for practical uses in quantum transport experiments. In particular, for systems to exhibit superconductive transport, it is not a necessary requirement to have superfluid pair correlations [124]. A future analysis would involve investigating these features in the presence of a potential gradient, or upon attaching leads to either end of the system, in order to investigate if the system can host pair transport that is robust to imperfections or defects.

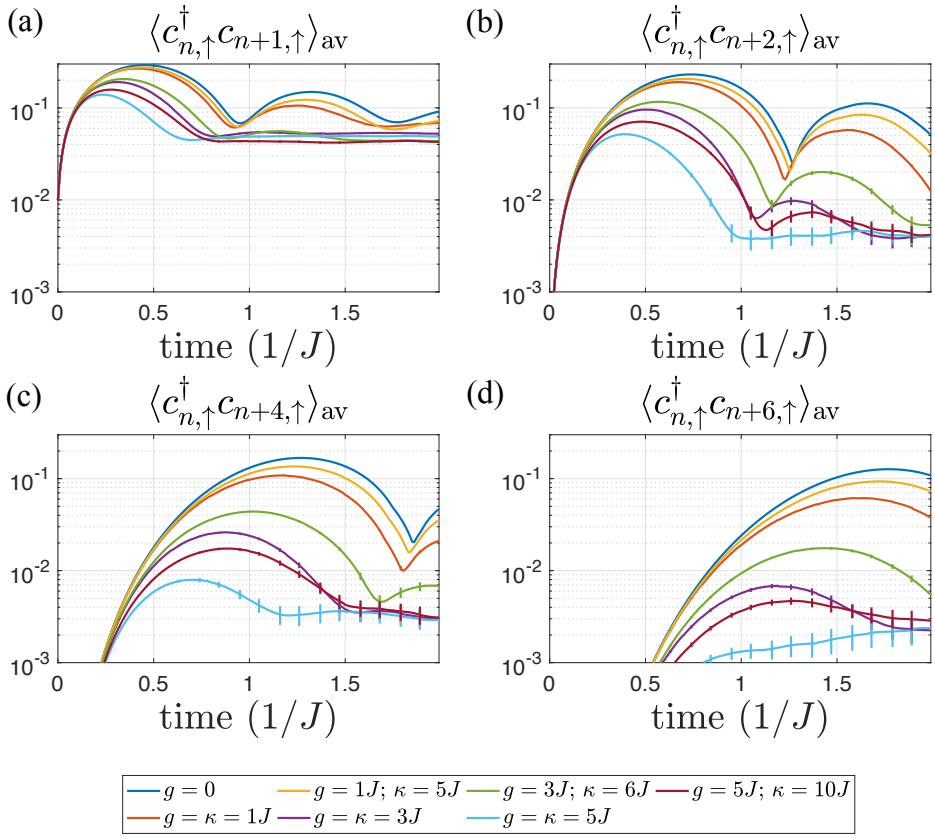

Figure 10.9: Single particle correlation functions in the extended Hubbard-Holstein model. Averaged over values for n in the 10 central sites of the system. Calculated with HOPS, $k_{max} = 8$, $D = 128$, $Jdt = 0.01$, $N_{\text{traj}} = 500$. System size, $M = 20$. Error bars represent statistical uncertainty in the mean value over all trajectories - where error bars are not visible they are smaller than the width of the curves.

Correlations

We also calculate the correlations that are generated in this system, where we compare the single particle correlations

$$\langle c^\dagger_{n,\uparrow} c_{n+r,\uparrow} \rangle, \tag{10.49}$$

to the spin correlations,

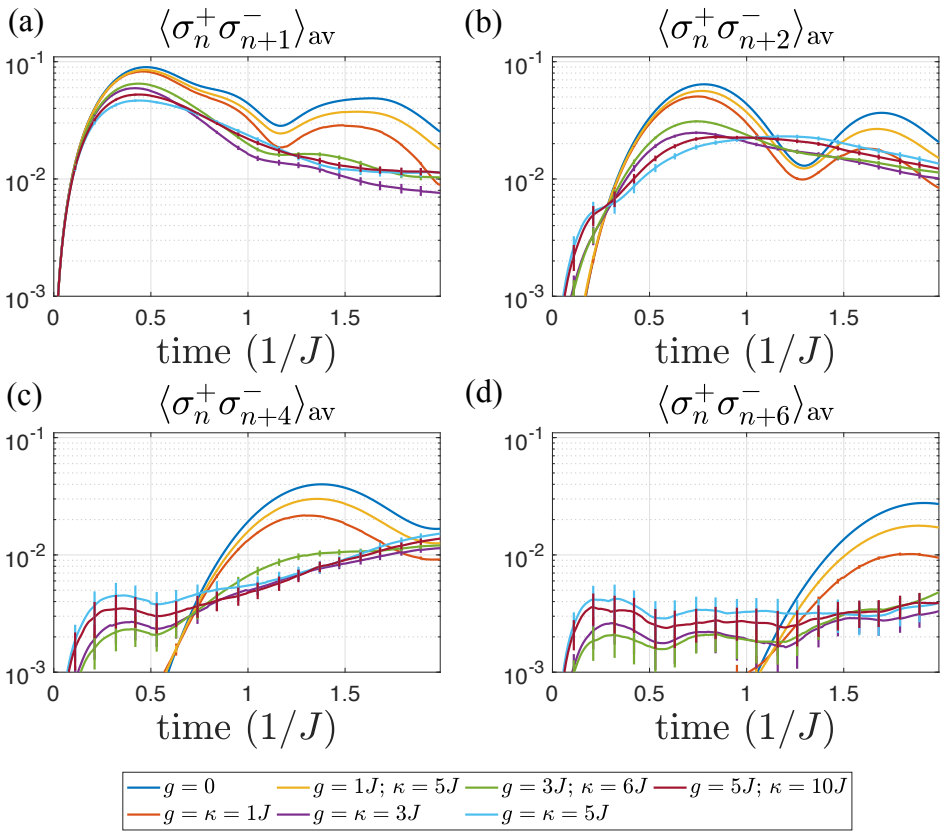

Figure 10.10: Spin correlation functions in the extended Hubbard-Holstein model. Averaged over values for n in the 10 central sites of the system. Calculated with HOPS, $k_{max} = 8$, $D = 128$, $Jdt = 0.01$, $N_{\rm traj} = 500$. System size, $M = 20$. Error bars represent statistical uncertainty in the mean value over all trajectories - where error bars are not visible they are smaller than the width of the curves.

$$\langle\sigma_n^+\sigma_{n+r}^-\rangle, \tag{10.50}$$

where $\sigma_n^+ = (\sigma_n^-)^\dagger = c_{n,\uparrow}^\dagger c_{n,\downarrow}$. In Fig. 10.9 the single particle correlations are shown, where we can see that as the coupling strength is increased or the phonon dispersion is reduced that these correlations are more suppressed. This indicates that the phonon environment reduces the quantum correlations in the system.

Additionally, in Fig. 10.10 we illustrate the spin correlations. Where we can see

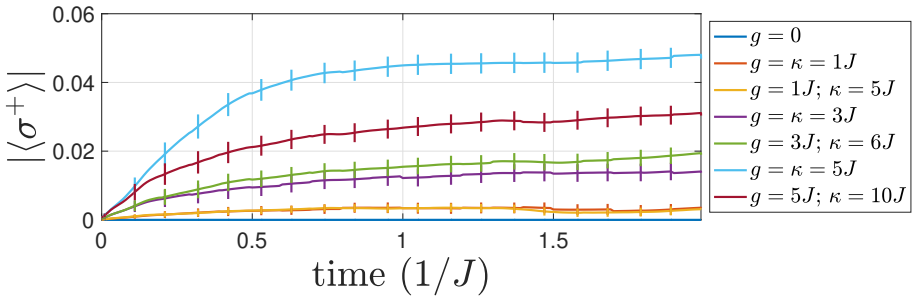

Figure 10.11: Average spin superfluid order parameter, $\langle\sigma^+\rangle_{\text{av}}$, in the extended Hubbard-Holstein model. HOPS, $k_{max} = 8$, $D = 128$, $Jdt = 0.01$, $N_{\text{traj}} = 500$. Error bars represent statistical uncertainty in the mean value over all trajectories - where error bars are not visible they are smaller than the width of the curves.

again that the magnitudes of these correlation functions decrease as the coupling strength increases. However, similar to the XXZ model considered in the previous section (see Fig. 10.6) the correlations seem to grow faster at short times for stronger coupling, which is due to the spin-flip processes in the coupling Hamiltonian. These correlations for strong coupling, although at an overall lower magnitude, appear to decay at a slower rate spatially, indicating that perhaps there is a small superfluid weight which would result in an algebraic decay of the correlations. Indeed, in Fig. 10.11, we plot the order parameter for a spin superfluid, which is zero for the closed system and increases for increasing coupling strength and for lower phonon dispersion. Note that the pair superfluid and single particle superfluid order parameters remain zero for all coupling strengths considered here, indicating that this may be a phase dominated by superfluid correlations in the spin sector, but suppressed correlations in the charge sector. While it is difficult to unequivocally decide if this is a spin superfluid, as we cannot reliably calculate the exponent for the algebraic decay due to the small system size considered here, these results are quite suggestive and indicate that coupling to a dissipative environment does not completely suppress quantum correlations in all cases.

We should also note that these results allow us to get an understanding into the numerical performance of the HOPS+MPS method that we have derived. The values for the correlation functions in this case have a relatively low error arising from the sampling over the trajectories. They indicate that we can achieve accurate results for certain correlation functions with this numerical method with a feasible number of numerical resources, opening up a way to study future non-Markovian systems that may exhibit even more novel properties.

10.5 Experimental realisation of non-Markovian systems

Physical systems where there are non-Markovian effects on the dynamics are fairly ubiquitous, in particular there are many examples in solid-state physics [184], however, it would be beneficial to be able to produce these interesting features in highly controlled quantum optical experiments. In order to realise dissipative systems with strong non-Markovian features with cold atom experiments there are a number of proposals involving extending current schemes for dissipative cooling [343, 376–382] where a system of impurity atoms (confined in a harmonic trap or optical lattice) is immersed in a weakly interacting BEC that is produced with a different species of atoms, leading to system dynamics that are strongly influenced by the presence of the BEC environment. The idea is that the BEC atomic species does not see the optical potential, but can interact with the trapped atoms [343, 344]. The contact interaction of the (single species) atoms in the lattice and the atoms in the BEC is,

$$H_{\text{Int}} = g_{ab} \int d^3r \Psi^\dagger(r)\Phi^\dagger(r)\Phi(r)\Psi(r), \tag{10.51}$$

where $\Psi(r)$ ($\Phi(r)$) is the many-body field theory operator for the atoms in the lattice (BEC) and we have already made the Born approximation allowing us to replace the two-body contact interaction with a delta function, see section 2.3.

First, we expand the BEC operators into a classical component, $\sqrt{\rho}$, and a quantum fluctuation [343, 344],

$$\Phi(x) = \sqrt{\rho} + \frac{1}{\sqrt{V}} \sum_k \left(u_k b_k e^{-ikr} + v_k b_k^\dagger e^{ikr} \right), \tag{10.52}$$

where V is the volume of the BEC, u_k & v_k are coefficients used to enforce the correct commutation relations and b_k is the annihilation operator for a Bogoliubov quasi-particle with wavevector, k, that has the dispersion relation [383],

$$E_k = \hbar \sqrt{c^2 |k|^2 + \hbar^2 \frac{|k|^4}{4m^2}}, \tag{10.53}$$

where m is the mass of the atoms in the BEC and $c^2 = g_b \rho / m$ is the effective speed of sound. We then insert this expansion into the interaction Hamiltonian but we keep only terms linear in the Bogoliubov operators,

$$H_{\text{Int}} = g_{ab} \sqrt{\frac{\rho}{V}} \int d^3 r \Psi^\dagger(r) \Psi(r) \sum_k \sqrt{S(k)} \left(b_k^\dagger e^{ikr} + b_k e^{-ikr} \right), \tag{10.54}$$

where $S(k) = (u_k + v_k)^2 = |k|^2 / 2mE_k$, is the static structure factor. For a quantitative evaluation of the effects of the additional terms that are quadratic in the Bogoliubov operators see Ref. [344].

Next we expand the lattice operator in terms of a localised basis, but we allow for the atom to be in one of two possible internal states, c_n and $\bar{c}_i$ respectively,

$$\Psi(r) = \sum_{n,\alpha} \left(w_\alpha(r - r_n) c_{n,\alpha} + w_\alpha(r - r_n) \bar{c}_{n,\alpha} \right), \tag{10.55}$$

where r_n is the lattice vector and we have assumed that the Wannier basis functions, $w_\alpha(r - r_n)$, are the same for both internal states, n labels the lattice site and α labels the energy level (band). Also transforming the sum over k to an integral $1/V \sum_k \to \int dk$, then leads to the linear interaction Hamiltonian,

$$H_{\text{Int}} = \sum_n \int d^3k \left(G^n(k) b_k + G^{*n}(k) b_k^\dagger \right) \left(c_n^\dagger c_n + \bar{c}_n^\dagger c_n + c_n^\dagger \bar{c}_n + \bar{c}_n^\dagger \bar{c}_n \right), \tag{10.56}$$

where

$$G^{i,j}_{\alpha,\beta}(k) = g_{ab} \sqrt{S(k)\rho V} e^{-ikr_i} \int d^3r w^*_\alpha(r) w_\beta(r + r_i - r_j) e^{-ikr}, \tag{10.57}$$

We assume that the lattice confinement is sufficiently strong so that the localised basis can be approximated by harmonic oscillator eigenstates and that the overlaps of nearest neighbouring functions are zero, such that,

$$G^{i,j}_{\alpha,\beta}(k) = \delta_{i,j} G^{i,j}_{\alpha,\beta}(k) \equiv e^{-ikr_i} G_{\alpha,\beta}(k). \tag{10.58}$$

Giving us,

$$G_{\alpha,\beta}(k) = g_{ab} \sqrt{S(k)\rho V} I_R \int dz \phi^*_\alpha(z) \phi_\beta(z) e^{-ik_z z}, \tag{10.59}$$

where $I_R = 1/2\pi a_R^2$ ($I_R = \exp(-k_R^2 a_R^2/4)$) for a 1D (3D) BEC, with a_R the characteristic length of the radial trap (assuming identical trapping for the lattice and BEC atoms) and

$$\phi_n(z) = \frac{1}{\sqrt{2^n n!}} (\pi a_z^2)^{-1/4} e^{-\frac{z^2}{2a_z^2}} H_n\left(\frac{z}{a_z}\right), \tag{10.60}$$

where H_n are the (physicists) Hermite polynomials and $a_z = \sqrt{\hbar/m\omega_z}$ is the characteristic harmonic oscillator length. We also assume that the separation between energy bands is sufficiently large, that the first excited energy level is never populated, meaning that we only need to consider the terms $\alpha = \beta = 0$. This will lead to the case of onsite non-Markovian dephasing for the case of a single species of impurity atoms, but there are also additional terms describing transitions between the two internal energy states,

$$H_{\text{Int}} = \sum_n \left(\hat{a}_n + \hat{a}_n^\dagger\right)\left(c_n^\dagger c_n + \bar{c}_n^\dagger c_n + c_n^\dagger \bar{c}_n + \bar{c}_n^\dagger \bar{c}_n\right). \tag{10.61}$$

where the effective environment modes are given by,

$$\hat{a}_n = \int d^3k e^{-ik_z an}\tilde{G}(k)b_k \tag{10.62}$$

where a is the spacing between lattice sites, and

$$\tilde{G}(k) = g_{ab}\sqrt{S(k)\rho V}I_R e^{-\frac{k_z^2 a_z^2}{4}}. \tag{10.63}$$

The correlation functions for the effective environment can be calculated (for zero temperature) as,

$$\alpha_n(t-t') = \langle \hat{a}_n(t)\hat{a}_n^\dagger(t')\rangle = g_{ab}^2\rho V\int dk S(k) I_R^2 e^{-\frac{k_z^2 a_z^2}{2}} e^{-i\omega_k(t-t')}, \tag{10.64}$$

where we have ignored the spatial correlations by assuming that $k_z a \gg 1$. If the relevant modes are in the phonon regime of the Bogoliubov dispersion ($E_k \approx c\hbar k$, $S(k) \approx k/2mc\hbar$) and we assume a 1D BEC then this gives (omitting the index n),

$$\alpha(t-t') = \tilde{g}\int d\omega\omega e^{-\frac{\omega^2}{2\tilde{c}^2}} e^{-i\omega(t-t')}, \tag{10.65}$$

where $\tilde{c} = c/a_z$ and,

$$\tilde{g} = \frac{g_{ab}^2 N}{8\pi^2 m c^3 a_R^4 \hbar}. \tag{10.66}$$

In order to qualitatively map this proposed experimental realisation, to the numerical simulations in the previous sections of this chapter, it is convenient to attempt to derive an approximate form of the above correlation function in terms of a single (complex) exponential. When benchmarking our HOPS+MPS algorithm we used environments with Lorentzian spectral densities, due to the method being significantly more efficient when using a single exponential for the correlation function and it is an interesting question to ask how well this approximation is able to capture the features of this experimental realsiation.

To this end we substitute for the full correlation function in Eq. 10.65 with the exponential correlation function of the form,

$$\tilde{\alpha}(\tau) \to \tilde{g}' \exp\left(-\frac{\tilde{c}}{2}|\tau|\right), \tag{10.67}$$

where,

$$\tilde{g}' \approx \frac{c^2}{\pi a_z^2}\tilde{g} = \frac{\hbar^2 a_s^2 N}{\pi m_{\text{red}}^2 m a_R^4 a_z^2 c}, \tag{10.68}$$

as $g_{ab} = 4\pi\hbar^2 a_s/m_{\text{red}}$, where a_s is the characteristic scattering length for the intra-species interaction.

In Fig. 10.12, we explicitly compare the correlation function given by Eq. 10.65 and the approximate form given by Eq. 10.67, where we can see that for short times, the dependence is qualitatively preserved. In the full correlations there are additional oscillations not captured by the exponential form, but these should provide

a good initial estimate for the dynamics. In the figure, we also compared the spectral densities, $\Omega(\omega)$, which are defined through,

$$\alpha(t-t') = \int d\omega \Omega(\omega) e^{-i\omega(t-t')}. \tag{10.69}$$

We can see that the most dominant energy modes are well approximated, however, the behaviour around $\omega \to 0$ is qualitatively different, with the real spectral density going to zero in contrast to our approximate form which goes to a non-zero (but small) value. As these low energy modes only strongly influence the long time dynamics we should in principle be able to accurately capture the short time transient behaviour with this approximation. Given that the HOPS method is significantly more efficient when using a single exponential for the correlation function, this approximation offers us a nice way of initially benchmarking the numerical method and gaining insight into the resulting dynamics, but note that investigating the dynamics using the full correlation function (Eq. 10.65) is part of our short term future objectives.

In the previous sections we have simulated the lattice dynamics for these parameters with $\tilde{g}'$ and $\tilde{c}$ around order $1-10$ in units relating to the nearest neighbour tunnelling amplitude, J. To get an estimate on typical experimental values for the velocity of sound in a BEC and the effective coupling term, we consider Caesium atoms in an optical lattice with $\{V_z, V_{x,y}\} = \{5, 50\}E_R$ and a lattice spacing of $a = 512$nm immersed in a BEC of $N = 1000$ atoms of a species that has half the mass of the Caesium atoms. We then have a sound velocity of $c = 1 \times 10^{-3}\text{ms}^{-1} = \sqrt{g_b \rho/m}$, which in dimensionless units corresponds to $c \approx 3.5aJ/\hbar$, and chemical potential, $\mu = mc^2 \approx 2.5J$. This means that for energies around $E_k \sim J$, the Bogoliubov excitation spectrum (Eq. 10.53) is well approximated by the linear phonon regime.

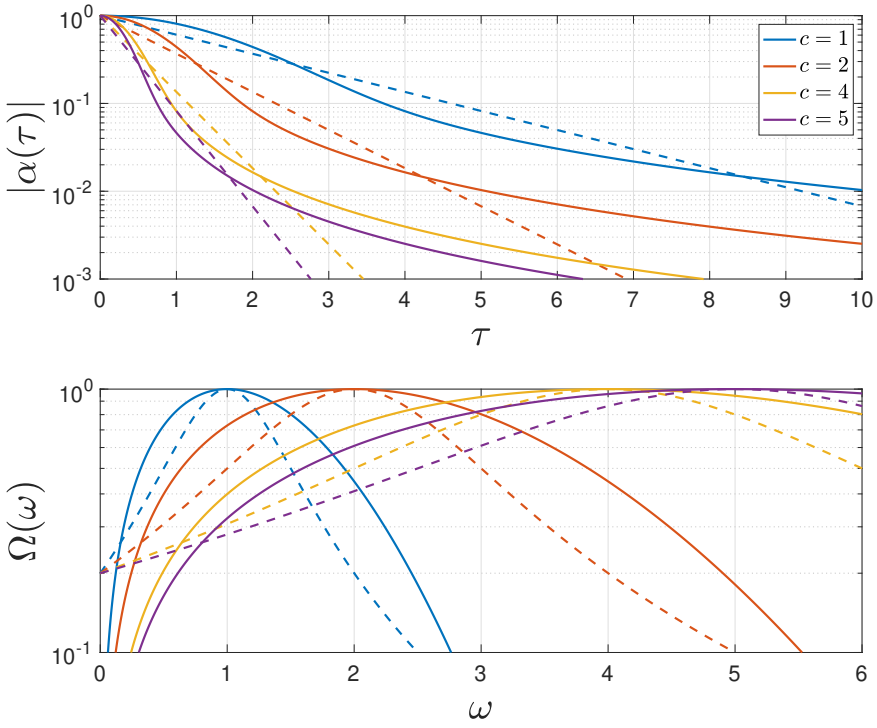

Figure 10.12: Comparison of the short time dependence of the correlation function (left) given by Eq. 10.65 (solid) to the approximate correlation function given by Eq. 10.67 (dashed). The correlation functions have been normalised at $\tau = 0$. Similar comparison of the resulting spectral densities (right) where the maximum values have been frequency shifted to overlap.

Then for an intra-species scattering length of $0.25\mathrm{a}_0$, the dimensionless interaction strength is,

$$\frac{g_{ab} I_R}{a_z} \approx 0.06J, \tag{10.70}$$

where J is the nearest neighbour tunnelling amplitude for the lattice atoms. This then gives, $\tilde{g}' \approx 0.66\mathrm{ms}^{-2}$, which in dimensionless units corresponds to $\tilde{g}' \approx 4aJ^2\hbar^{-2}$. This indicates that we can realise the desired range of parameter regimes considered below with these experimental values combined with varying the characteristic scattering lengths using a Feshbach resonance.

10.6 Discussion

The results for the dynamics of the dispersive Holstein model are consistent with what is expected from previous analysis of similar models. Increasing the phonon dispersion means that the phonons have less effect on the system because they can move away from the point where they were created and the environment around the site can then relax. We also compared this to the case for phonons with infinite dispersion such that the environment instantaneously relaxes and a Born-Markov approximation is valid which results in even smaller effects. These cases are in contrast to a dispersionless excitation which remains in the vicinity of its creation point which can then influence the dynamics of the particles in the system to a much greater extent. Upon increasing the temperature of the phonon environment, we observed a greater effect and an increased suppression of the melting of the charge density wave which arrises because there is now an initial non-zero phonon occupation which can then interact with the atoms in the system leading to a greater effect on the short time dynamics.

Of course, the case considered here of dispersive phonons is the more natural one compared to the dispersionless case, as it is similar to the behaviour of real physical systems and thus it is actually incredibly useful to be able to explore and to understand in a completely quantitative way. Even though the corrections compared to the dispersionless limit are small, they could be very important when considering practical real world examples, such as the thermal and electrical conduction properties of realistic materials, where even tiny quantitative differences can have a huge impact on practical considerations.

Additionally the analysis of the extended Hubbard-Holstein model allowed us to further benchmark our numerical method where we illustrated that even with the

increased numerical intensity for the spinfull case we were able to capture the interesting short time dynamics. We observed that with a feasible number of trajectories we could obtain a relatively low error in many important two-point correlation functions. In terms of the physics we found some qualitative differences to the spinless case where there is an enhanced melting of the charge density wave, and we observed features hinting towards the ability for the system to host superconductive currents and to generate spin superfluid phases in the steady state.

More generally however, our combination of the HOPS algorithm with MPS techniques opens up the ability to explore a wide range of new and interesting regimes that were previously only possible to simulate qualitatively and/or through invoking some strong approximation. By considering the dispersive Holstein model, which is the simplest possible example, and extending this to the Hubbard-Holstein model, we demonstrated that we can simulate the dynamics of open many-body systems well into the non-Markovian and strong coupling regimes.

Part V

Conclusions and Outlook

In this thesis we have discussed quantum simulation and how it can be used to solve problems in many-body quantum physics that are beyond the capabilities of classical computers. We quantitatively demonstrated that even with the current generation of experimental hardware that purpose-built analogue simulators are able to go beyond state-of-the-art classical algorithms in out-of-equilibrium dynamical problems in many-body quantum physics models. These simulations are particularly relevant to problems in materials science or in the field of nano-electronic devices as the microscopic behaviour of electrons in these systems can be well captured by the Hubbard model [384] and the dissipative effects of lattice phonons can also be included by employing the Hubbard-Holstein model [368–372].

Additionally we demonstrated that these simulators can also be used to investigate novel lattice geometries with topological band structures which are outside the usual phase classification scheme. In particular, we illustrated that quantum simulation can be used to quantitatively probe the properties of strongly correlated phases induced by strong interactions in these novel band structures. We explicitly considered systems with flat energy bands where we demonstrated experimentally feasible ways of producing, preparing and detecting the features of the novel phases that are dominated by interacting bound pairs. This offers a roadmap towards experimentally probing the effects of strong quantum mechanical interactions in regimes where conventional single particle dynamics are suppressed and perhaps also allowing for an investigation of strongly interacting regimes in more general topological systems.

Finally we considered additional incorporations to the simulators in order to controllably simulate the dissipative effects of phonon modes on the dynamics of particles confined in the lattice, such that we are able to simulate dynamics in a way that is more akin to the solid state. We demonstrated that by modifying a new numerical technique we can classically benchmark the quantum simulators in these

situations beyond the usual approximations of weak coupling and fast environment dynamics. This classical algorithm opens up new opportunities for increasing our theoretical understanding of one-dimensional many-body systems strongly coupled to non-Markovian environments in much more general situations than considered in this thesis and it also allows for the direct calibration of quantum simulation devices that aim to probe these novel regimes.

The research presented in this thesis, while giving insights into many interesting regimes, naturally raised many additional questions and so below we briefly summarise the potentially most fruitful lines of future research.

Hardware requirements for demonstrating quantum advantage

For the most part, in Ch. 6 we considered the comparison in performance of analogue simulators to classical algorithms. Although we briefly discussed the hardware requirements for fully universal digital simulation, where we assumed that all the errors arise from the discretisation of the time-step. This requires either gates with a near perfect fidelity, which is not realistic with current experimental hardware, or an implementation of fully fault tolerant and error corrected algorithms which, in order to apply this needs an incredibly large number of gates. So, a future objective would be to better benchmark digital simulators where the errors and sources of noise are explicitly taken into account in an experimentally realistic way.

Additionally, in our analysis, we decomposed the time-evolution operator into discrete two site operations in a way that is optimal for the classical algorithms, i.e. through a trotter decomposition [1]. But recently there has been some interesting work along the lines of producing better approximations to the time-evolution operator [385] that are optimised for the quantum hardware. So, during our future benchmarking of the digital simulators for the types of continuous time dynamical

problems that have been the focus of this thesis we should utilise this recent work and derive more refined and optimal quantum logic circuits.

Non-Markovian open many-body quantum systems

In Ch. 10 we described and benchmarked our hybridisation of matrix product state algorithms and the hierarchy of pure states method, allowing us to classically simulate one-dimensional open many-body systems strongly coupled to a non-Markovian environment. We benchmarked this method by considering the Holstein model, which is important for understanding quantum effects on dynamical properties in real materials, where in general, features beyond the Born-Markov approximations lead to a reduction in the correlations present in the system. It has been shown that Markovian dissipation can in some cases gives rise to steady states that have quantum enhanced properties for use in metrological applications [386, 387] and so an interesting question here is to ask if non-Markovian features can be used in a similar way. Can these effects be tuned in order to give an advantage over Markovian dissipation such that either the produced states have further enhanced properties or they can be prepared faster?

Separately, there are many interesting experiments (both in the solid state and with cold atoms) probing transport properties, where a small system is connected to much larger leads at either end [388]. Upon varying either a chemical potential or thermal bias between the leads the currents produced through the system are measured. In particular there has been some recent work in this context upon applying methods from open quantum systems in order to study these features in the Born-Markov regimes [389, 390] and an obvious extension would be to consider these transport properties in the presence of non-Markovian dissipation or in the regime of strong coupling to the leads.

Bibliography

[1] U. Schollwöck, "The density-matrix renormalization group in the age of matrix product states," Annals of Physics **326**, 96 (2011).

[2] C. Gardiner and P. Zoller, *Quantum Noise* (Springer, 2004).

[3] M. Suzuki, *Quantum Monte Carlo Methods in Condensed Matter Physics* (World Scientific, 1993).

[4] B. Zhu, A. M. Rey, and J. Schachenmayer, "A generalized phase space approach for solving quantum spin dynamics," New Journal of Physics **21**, 082001 (2019).

[5] R. P. Feynman, "Simulating physics with computers," International Journal of Theoretical Physics **21**, 467 (1982).

[6] I. M. Georgescu, S. Ashhab, and F. Nori, "Quantum simulation," Rev. Mod. Phys. **86**, 153 (2014).

[7] P. Goy, J. M. Raimond, M. Gross, and S. Haroche, "Observation of cavity-enhanced single-atom spontaneous emission," Phys. Rev. Lett. **50**, 1903 (1983).

[8] M. Brune, J. M. Raimond, P. Goy, L. Davidovich, and S. Haroche, "Realization of a two-photon maser oscillator," Phys. Rev. Lett. **59**, 1899 (1987).

[9] J. C. Bergquist, R. G. Hulet, W. M. Itano, and D. J. Wineland, "Observation of quantum jumps in a single atom," Phys. Rev. Lett. **57**, 1699 (1986).

[10] D. Leibfried, R. Blatt, C. Monroe, and D. Wineland, "Quantum dynamics of single trapped ions," Rev. Mod. Phys. **75**, 281 (2003).

[11] R. Blatt and D. Wineland, "Entangled states of trapped atomic ions," Nature **453**, 1008 (2008).

[12] D. Dong, C. Chen, B. Qi, I. R. Petersen, and F. Nori, "Robust manipulation of superconducting qubits in the presence of fluctuations," Scientific Reports **5**, 7873 (2015).

[13] I. Bloch, "Quantum coherence and entanglement with ultracold atoms in optical lattices," Nature **453**, 1016 (2008).

[14] C. J. Picken, R. Legaie, K. McDonnell, and J. D. Pritchard, "Entanglement of neutral-atom qubits with long ground-rydberg coherence times," Quantum Science and Technology **4**, 015011 (2018).

[15] P. W. Shor, in *Proceedings 35th Annual Symposium on Foundations of Computer Science* (1994), pp. 124–134.

[16] S. Lloyd, "Universal quantum simulators," Science **273**, 1073 (1996).

[17] S. Kirkpatrick, C. D. Gelatt, and M. P. Vecchi, "Optimization by simulated annealing," Science **220**, 671 (1983).

[18] E. Farhi, J. Goldstone, S. Gutmann, J. Lapan, A. Lundgren, and D. Preda, "A quantum adiabatic evolution algorithm applied to random instances of an np-complete problem," Science **292**, 472 (2001).

[19] I. Bloch, J. Dalibard, and S. Nascimbene, "Quantum simulations with ultracold quantum gases," Nat Phys **8**, 267 (2012).

[20] R. Blatt and C. F. Roos, "Quantum simulations with trapped ions," Nature Physics **8**, 277 (2012).

[21] P. Schindler, D. Nigg, T. Monz, J. T. Barreiro, E. Martinez, S. X. Wang, S. Quint, M. F. Brandl, V. Nebendahl, C. F. Roos, et al., "A quantum information processor with trapped ions," New Journal of Physics **15**, 123012 (2013).

[22] C.-L. Hung, A. González-Tudela, J. I. Cirac, and H. J. Kimble, "Quantum spin dynamics with pairwise-tunable, long-range interactions," Proceedings of the National Academy of Sciences **113**, E4946 (2016).

[23] H. Labuhn, D. Barredo, S. Ravets, S. de Léséleuc, T. Macrì, T. Lahaye, and A. Browaeys, "Tunable two-dimensional arrays of single rydberg atoms for realizing quantum ising models," Nature **534**, 667 (2016).

[24] A. A. Houck, H. E. Türeci, and J. Koch, "On-chip quantum simulation with superconducting circuits," Nature Physics **8**, 292 (2012).

[25] D. Jaksch, C. Bruder, J. I. Cirac, C. W. Gardiner, and P. Zoller, "Cold bosonic atoms in optical lattices," Phys. Rev. Lett. **81**, 3108 (1998).

[26] T. Esslinger, "Fermi-hubbard physics with atoms in an optical lattice," Annual Review of Condensed Matter Physics **1**, 129 (2010).

[27] D. Jaksch and P. Zoller, "The cold atom hubbard toolbox," Annals of Physics **315**, 52 (2005).

[28] M. Müller, S. Diehl, G. Pupillo, and P. Zoller, *Engineered Open Systems and Quantum Simulations with Atoms and Ions* (Academic Press, 2012), vol. 61 of *Advances in Atomic, Molecular, and Optical Physics*, pp. 1–80.

[29] A. Smith, M. S. Kim, F. Pollmann, and J. Knolle, "Simulating quantum many-body dynamics on a current digital quantum computer," npj Quantum Information **5**, 106 (2019).

[30] L. Clinton, J. Bausch, and T. Cubitt, "Hamiltonian simulation algorithms for near-term quantum hardware," arXiv:2003.06886 (2020).

[31] A. T. Sornborger and E. D. Stewart, "Higher-order methods for simulations on quantum computers," Phys. Rev. A **60**, 1956 (1999).

[32] L. M. Sieberer, T. Olsacher, A. Elben, M. Heyl, P. Hauke, F. Haake, and P. Zoller, "Digital quantum simulation, trotter errors, and quantum chaos of the kicked top," npj Quantum Information **5**, 78 (2019).

[33] I. Bloch, J. Dalibard, and W. Zwerger, "Many-body physics with ultracold gases," Rev. Mod. Phys. **80**, 885 (2008).

[34] I. Bloch, "Ultracold quantum gases in optical lattices," Nature Physics **1**, 23 (2005).

[35] J.-y. Choi, S. Hild, J. Zeiher, P. Schauß, A. Rubio-Abadal, T. Yefsah, V. Khemani, D. A. Huse, I. Bloch, and C. Gross, "Exploring the many-body localization transition in two dimensions," Science **352**, 1547 (2016).

[36] A. Mazurenko, C. S. Chiu, G. Ji, M. F. Parsons, M. Kanász-Nagy, R. Schmidt, F. Grusdt, E. Demler, D. Greif, and M. Greiner, "A cold-atom fermi–hubbard antiferromagnet," Nature **545**, 462 (2017).

[37] A. Browaeys and T. Lahaye, "Many-body physics with individually controlled rydberg atoms," Nature Physics **16**, 132 (2020).

[38] H. Bernien, S. Schwartz, A. Keesling, H. Levine, A. Omran, H. Pichler, S. Choi, A. S. Zibrov, M. Endres, M. Greiner, et al., "Probing many-body dynamics on a 51-atom quantum simulator," Nature **551**, 579 (2017).

[39] J. Zhang, G. Pagano, P. W. Hess, A. Kyprianidis, P. Becker, H. Kaplan, A. V. Gorshkov, Z.-X. Gong, and C. Monroe, "Observation of a many-body dynamical phase transition with a 53-qubit quantum simulator," Nature **551**, 601 (2017).

[40] T. Brydges, A. Elben, P. Jurcevic, B. Vermersch, C. Maier, B. P. Lanyon, P. Zoller, R. Blatt, and C. F. Roos, "Probing rényi entanglement entropy via randomized measurements," Science **364**, 260 (2019).

[41] A. J. Daley, "Quantum trajectories and open many-body quantum systems," Advances in Physics **63**, 77 (2014).

[42] W. S. Bakr, J. I. Gillen, A. Peng, S. Fölling, and M. Greiner, "A quantum gas microscope for detecting single atoms in a hubbard-regime optical lattice," Nature **462**, 74 (2009).

[43] J. F. Sherson, C. Weitenberg, M. Endres, M. Cheneau, I. Bloch, and S. Kuhr, "Single-atom-resolved fluorescence imaging of an atomic mott insulator," Nature **467**, 68 (2010).

[44] E. Haller, J. Hudson, A. Kelly, D. A. Cotta, B. Peaudecerf, G. D. Bruce, and S. Kuhr, "Single-atom imaging of fermions in a quantum-gas microscope," Nature Physics **11**, 738 (2015).

[45] L. W. Cheuk, M. A. Nichols, M. Okan, T. Gersdorf, V. V. Ramasesh, W. S. Bakr, T. Lompe, and M. W. Zwierlein, "Quantum-gas microscope for fermionic atoms," Phys. Rev. Lett. **114**, 193001 (2015).

[46] M. Miranda, R. Inoue, Y. Okuyama, A. Nakamoto, and M. Kozuma, "Site-resolved imaging of ytterbium atoms in a two-dimensional optical lattice," Phys. Rev. A **91**, 063414 (2015).

[47] R. Yamamoto, J. Kobayashi, T. Kuno, K. Kato, and Y. Takahashi, "An ytterbium quantum gas microscope with narrow-line laser cooling," New Journal of Physics **18**, 023016 (2016).

[48] R. Yamamoto, J. Kobayashi, K. Kato, T. Kuno, Y. Sakura, and Y. Takahashi, "Site-resolved imaging of single atoms with a faraday quantum gas microscope," Phys. Rev. A **96**, 033610 (2017).

[49] D. Mitra, P. T. Brown, E. Guardado-Sanchez, S. S. Kondov, T. Devakul, D. A. Huse, P. Schauß, and W. S. Bakr, "Quantum gas microscopy of an attractive fermi–hubbard system," Nature Physics **14**, 173 (2018).

[50] M. Greiner, O. Mandel, T. Esslinger, T. W. Hänsch, and I. Bloch, "Quantum phase transition from a superfluid to a mott insulator in a gas of ultracold atoms," Nature **415**, 39 (2002).

[51] N. Gemelke, X. Zhang, C.-L. Hung, and C. Chin, "In situ observation of incompressible mott-insulating domains in ultracold atomic gases," Nature **460**, 995 (2009).

[52] T. Fukuhara, S. Sugawa, M. Sugimoto, S. Taie, and Y. Takahashi, "Mott in-

sulator of ultracold alkaline-earth-metal-like atoms," Phys. Rev. A **79**, 041604 (2009).

[53] W. S. Bakr, A. Peng, M. E. Tai, R. Ma, J. Simon, J. I. Gillen, S. Fölling, L. Pollet, and M. Greiner, "Probing the superfluid–to–mott insulator transition at the single-atom level," Science **329**, 547 (2010).

[54] R. Jördens, N. Strohmaier, K. Günter, H. Moritz, and T. Esslinger, "A mott insulator of fermionic atoms in an optical lattice," Nature **455**, 204 (2008).

[55] U. Schneider, L. Hackermüller, S. Will, T. Best, I. Bloch, T. A. Costi, R. W. Helmes, D. Rasch, and A. Rosch, "Metallic and insulating phases of repulsively interacting fermions in a 3d optical lattice," Science **322**, 1520 (2008).

[56] M. Schreiber, S. S. Hodgman, P. Bordia, H. P. Lüschen, M. H. Fischer, R. Vosk, E. Altman, U. Schneider, and I. Bloch, "Observation of many-body localization of interacting fermions in a quasirandom optical lattice," Science **349**, 842 (2015).

[57] J. Billy, V. Josse, Z. Zuo, A. Bernard, B. Hambrecht, P. Lugan, D. Clément, L. Sanchez-Palencia, P. Bouyer, and A. Aspect, "Direct observation of anderson localization of matter waves in a controlled disorder," Nature **453**, 891 (2008).

[58] B. Deissler, M. Zaccanti, G. Roati, C. D'Errico, M. Fattori, M. Modugno, G. Modugno, and M. Inguscio, "Delocalization of a disordered bosonic system by repulsive interactions," Nature Physics **6**, 354 (2010).

[59] C. D'Errico, E. Lucioni, L. Tanzi, L. Gori, G. Roux, I. P. McCulloch, T. Giamarchi, M. Inguscio, and G. Modugno, "Observation of a disordered bosonic

insulator from weak to strong interactions," Phys. Rev. Lett. **113**, 095301 (2014).

[60] S. S. Kondov, W. R. McGehee, W. Xu, and B. DeMarco, "Disorder-induced localization in a strongly correlated atomic hubbard gas," Phys. Rev. Lett. **114**, 083002 (2015).

[61] T. Tomita, S. Nakajima, I. Danshita, Y. Takasu, and Y. Takahashi, "Observation of the mott insulator to superfluid crossover of a driven-dissipative bose-hubbard system," Science Advances **3** (2017).

[62] M. Cheneau, P. Barmettler, D. Poletti, M. Endres, P. Schauß, T. Fukuhara, C. Gross, I. Bloch, C. Kollath, and S. Kuhr, "Light-cone-like spreading of correlations in a quantum many-body system," Nature **481**, 484 (2012).

[63] P. Barmettler, D. Poletti, M. Cheneau, and C. Kollath, "Propagation front of correlations in an interacting bose gas," Phys. Rev. A **85**, 053625 (2012).

[64] S. Braun, M. Friesdorf, S. S. Hodgman, M. Schreiber, J. P. Ronzheimer, A. Riera, M. del Rey, I. Bloch, J. Eisert, and U. Schneider, "Emergence of coherence and the dynamics of quantum phase transitions," Proceedings of the National Academy of Sciences (2015).

[65] K. Viebahn, M. Sbroscia, E. Carter, J.-C. Yu, and U. Schneider, "Matter-wave diffraction from a quasicrystalline optical lattice," Phys. Rev. Lett. **122**, 110404 (2019).

[66] J. Ruostekoski, "Optical kagome lattice for ultracold atoms with nearest neighbor interactions," Phys. Rev. Lett. **103**, 080406 (2009).

[67] Y. J. Lin, K. Jiménez-García, and I. B. Spielman, "Spin–orbit-coupled bose–einstein condensates," Nature **471**, 83 (2011).

[68] J. Struck, C. Ölschläger, R. Le Targat, P. Soltan-Panahi, A. Eckardt, M. Lewenstein, P. Windpassinger, and K. Sengstock, "Quantum simulation of frustrated classical magnetism in triangular optical lattices," Science **333**, 996 (2011).

[69] J. Struck, C. Ölschläger, M. Weinberg, P. Hauke, J. Simonet, A. Eckardt, M. Lewenstein, K. Sengstock, and P. Windpassinger, "Tunable gauge potential for neutral and spinless particles in driven optical lattices," Phys. Rev. Lett. **108**, 225304 (2012).

[70] G. Jotzu, M. Messer, R. Desbuquois, M. Lebrat, T. Uehlinger, D. Greif, and T. Esslinger, "Experimental realization of the topological haldane model with ultracold fermions," Nature **515**, 237 (2014).

[71] M. Aidelsburger, M. Atala, S. Nascimbène, S. Trotzky, Y.-A. Chen, and I. Bloch, "Experimental realization of strong effective magnetic fields in an optical lattice," Phys. Rev. Lett. **107**, 255301 (2011).

[72] H. Miyake, G. A. Siviloglou, C. J. Kennedy, W. C. Burton, and W. Ketterle, "Realizing the harper hamiltonian with laser-assisted tunneling in optical lattices," Phys. Rev. Lett. **111**, 185302 (2013).

[73] N. Fläschner, B. S. Rem, M. Tarnowski, D. Vogel, D. S. Lühmann, K. Sengstock, and C. Weitenberg, "Experimental reconstruction of the berry curvature in a floquet bloch band," Science **352**, 1091 (2016).

[74] M. Tarnowski, M. Nuske, N. Fläschner, B. Rem, D. Vogel, L. Freystatzky, K. Sengstock, L. Mathey, and C. Weitenberg, "Observation of topological bloch-state defects and their merging transition," Phys. Rev. Lett. **118**, 240403 (2017).

[75] M. Aidelsburger, S. Nascimbene, and N. Goldman, "Artificial gauge fields in materials and engineered systems," Comptes Rendus Physique **19**, 394 (2018).

[76] M. Aidelsburger, M. Atala, M. Lohse, J. T. Barreiro, B. Paredes, and I. Bloch, "Realization of the hofstadter hamiltonian with ultracold atoms in optical lattices," Phys. Rev. Lett. **111**, 185301 (2013).

[77] S. H. Kooi, A. Quelle, W. Beugeling, and C. Morais Smith, "Genesis of the floquet hofstadter butterfly," Phys. Rev. B **98**, 115124 (2018).

[78] A. Quelle, C. Weitenberg, K. Sengstock, and C. M. Smith, "Driving protocol for a floquet topological phase without static counterpart," New Journal of Physics **19**, 113010 (2017).

[79] C. Gardiner and P. Zoller, *The Quantum World of Ultra-Cold Atoms and Light Book III: Ultra-Cold Atoms* (World Scientific, 2017).

[80] M. J. Mark, E. Haller, K. Lauber, J. G. Danzl, A. J. Daley, and H.-C. Nägerl, "Precision measurements on a tunable mott insulator of ultracold atoms," Phys. Rev. Lett. **107**, 175301 (2011).

[81] M. J. Mark, E. Haller, K. Lauber, J. G. Danzl, A. Janisch, H. P. Büchler, A. J. Daley, and H.-C. Nägerl, "Preparation and spectroscopy of a metastable mott-insulator state with attractive interactions," Phys. Rev. Lett. **108**, 215302 (2012).

[82] K. Huang, *Statistical Mechanics* (Wiley, 1987).

[83] G. F. Gribakin and V. V. Flambaum, "Calculation of the scattering length in atomic collisions using the semiclassical approximation," Phys. Rev. A **48**, 546 (1993).

[84] T. Busch, B.-G. Englert, K. Rzażewski, and M. Wilkens, "Two cold atoms in a harmonic trap," Foundations of Physics **28**, 549 (1998).

[85] Z. Idziaszek and T. Calarco, "Two atoms in an anisotropic harmonic trap," Phys. Rev. A **71**, 050701 (2005).

[86] H. P. Büchler, "Microscopic derivation of hubbard parameters for cold atomic gases," Phys. Rev. Lett. **104**, 090402 (2010).

[87] S. Inouye, M. R. Andrews, J. Stenger, H. J. Miesner, D. M. Stamper-Kurn, and W. Ketterle, "Observation of feshbach resonances in a bose–einstein condensate," Nature **392**, 151 (1998).

[88] E. Timmermans, P. Tommasini, M. Hussein, and A. Kerman, "Feshbach resonances in atomic bose–einstein condensates," Physics Reports **315**, 199 (1999).

[89] B. J. Verhaar, E. G. M. van Kempen, and S. J. J. M. F. Kokkelmans, "Predicting scattering properties of ultracold atoms: Adiabatic accumulated phase method and mass scaling," Phys. Rev. A **79**, 032711 (2009).

[90] D. J. Papoular, S. Bize, A. Clairon, H. Marion, S. J. J. M. F. Kokkelmans, and G. V. Shlyapnikov, "Feshbach resonances in cesium at ultralow static magnetic fields," Phys. Rev. A **86**, 040701 (2012).

[91] E. Haller, M. Gustavsson, M. J. Mark, J. G. Danzl, R. Hart, G. Pupillo, and H.-C. Nägerl, "Realization of an excited, strongly correlated quantum gas phase," Science **325**, 1224 (2009).

[92] W. Kohn, "Analytic properties of bloch waves and wannier functions," Phys. Rev. **115**, 809 (1959).

[93] D. Rossini and R. Fazio, "Phase diagram of the extended bose–hubbard model," New Journal of Physics **14**, 065012 (2012).

[94] S. Sachdev, *Quantum Phase Transitions* (Cambridge University Press, 2011).

[95] M. P. A. Fisher, P. B. Weichman, G. Grinstein, and D. S. Fisher, "Boson localization and the superfluid-insulator transition," Phys. Rev. B **40**, 546 (1989).

[96] G. Kordas, D. Witthaut, and S. Wimberger, "Non-equilibrium dynamics in dissipative bose-hubbard chains," Annalen der Physik **527**, 619 (2015).

[97] J. Simon, W. S. Bakr, R. Ma, M. E. Tai, P. M. Preiss, and M. Greiner, "Quantum simulation of antiferromagnetic spin chains in an optical lattice," Nature **472**, 307 (2011).

[98] A. Friedenauer, H. Schmitz, J. T. Glueckert, D. Porras, and T. Schaetz, "Simulating a quantum magnet with trapped ions," Nature Physics **4**, 757 (2008).

[99] A. S. Sørensen, E. Altman, M. Gullans, J. V. Porto, M. D. Lukin, and E. Demler, "Adiabatic preparation of many-body states in optical lattices," Phys. Rev. A **81**, 061603 (2010).

[100] O. Lychkovskiy, O. Gamayun, and V. Cheianov, "Time scale for adiabaticity breakdown in driven many-body systems and orthogonality catastrophe," Phys. Rev. Lett. **119**, 200401 (2017).

[101] O. Lychkovskiy, O. Gamayun, and V. Cheianov, "Quantum many-body adiabaticity, topological thouless pump and driven impurity in a one-dimensional quantum fluid," AIP Conference Proceedings **1936**, 020024 (2018).

[102] T. Giamarchi, *Quantum Physics in One Dimension*, International Series of Monographs on Physics (Oxford University Press, 2003).

[103] S.-i. Tomonaga, "Remarks on Bloch's Method of Sound Waves applied to Many-Fermion Problems," Progress of Theoretical Physics **5**, 544 (1950).

[104] J. M. Luttinger, "An exactly soluble model of a many-fermion system," Journal of Mathematical Physics **4**, 1154 (1963).

[105] F. D. M. Haldane, "Effective harmonic-fluid approach to low-energy properties of one-dimensional quantum fluids," Phys. Rev. Lett. **47**, 1840 (1981).

[106] M. Greiner, I. Bloch, O. Mandel, T. W. Hänsch, and T. Esslinger, "Exploring phase coherence in a 2d lattice of bose-einstein condensates," Phys. Rev. Lett. **87**, 160405 (2001).

[107] H. Moritz, T. Stöferle, M. Köhl, and T. Esslinger, "Exciting collective oscillations in a trapped 1d gas," Phys. Rev. Lett. **91**, 250402 (2003).

[108] T. Kinoshita, T. Wenger, and D. S. Weiss, "Observation of a one-dimensional tonks-girardeau gas," Science **305**, 1125 (2004).

[109] B. Paredes, A. Widera, V. Murg, O. Mandel, S. Fölling, I. Cirac, G. V. Shlyapnikov, T. W. Hänsch, and I. Bloch, "Tonks–girardeau gas of ultracold atoms in an optical lattice," Nature **429**, 277 (2004).

[110] L. D. Landau, "On the theory of the fermi liquid," Sov. Phys. JETP **8**, 70 (1958).

[111] F. D. M. Haldane, "'luttinger liquid theory' of one-dimensional quantum fluids. i. properties of the luttinger model and their extension to the general 1d interacting spinless fermi gas," Journal of Physics C: Solid State Physics **14**, 2585 (1981).

[112] D. C. Mattis, "New wave-operator identity applied to the study of persistent currents in 1d," Journal of Mathematical Physics **15**, 609 (1974).

[113] A. Luther and I. Peschel, "Single-particle states, kohn anomaly, and pairing fluctuations in one dimension," Phys. Rev. B **9**, 2911 (1974).

[114] D. C. Mattis and E. H. Lieb, "Exact solution of a many-fermion system and its associated boson field," Journal of Mathematical Physics **6**, 304 (1965).

[115] V. Meden and K. Schönhammer, "Spectral functions for the tomonaga-luttinger model," Phys. Rev. B **46**, 15753 (1992).

[116] J. Voit, "Charge-spin separation and the spectral properties of luttinger liquids," Phys. Rev. B **47**, 6740 (1993).

[117] F. Essler, H. Frahm, F. Göhmann, A. Klümper, and V. Korepin, *The One-Dimensional Hubbard Model* (Cambridge University Press, 2005).

[118] F. D. M. Haldane, "Coupling between charge and spin degrees of freedom in the one-dimensional fermi gas with backscattering," Journal of Physics C: Solid State Physics **12**, 4791 (1979).

[119] R. Heidenreich, B. Schroer, R. Seiler, and D. Uhlenbrock, "The sine-gordon equation and the one-dimensional electron gas," Physics Letters A **54**, 119 (1975).

[120] I. Affleck, "Quantum spin chains and the haldane gap," Journal of Physics: Condensed Matter **1**, 3047 (1989).

[121] R. Chitra and T. Giamarchi, "Critical properties of gapped spin-chains and ladders in a magnetic field," Phys. Rev. B **55**, 5816 (1997).

[122] A. A. Nersesyan, A. Luther, and F. V. Kusmartsev, "Scaling properties of the two-chain model," Physics Letters A **176**, 363 (1993).

[123] F. m. c. Crépin, N. Laflorencie, G. Roux, and P. Simon, "Phase diagram of hard-core bosons on clean and disordered two-leg ladders: Mott insulator–luttinger liquid–bose glass," Phys. Rev. B **84**, 054517 (2011).

[124] E. Orignac and T. Giamarchi, "Effects of disorder on two strongly correlated coupled chains," Phys. Rev. B **56**, 7167 (1997).

[125] M. Fabrizio, "Role of transverse hopping in a two-coupled-chains model," Phys. Rev. B **48**, 15838 (1993).

[126] A. M. Finkel'stein and A. I. Larkin, "Two coupled chains with tomonaga-luttinger interactions," Phys. Rev. B **47**, 10461 (1993).

[127] D. V. Khveshchenko and T. M. Rice, "Spin-gap fixed points in the double-chain problem," Phys. Rev. B **50**, 252 (1994).

[128] L. Balents and M. P. A. Fisher, "Weak-coupling phase diagram of the two-chain hubbard model," Phys. Rev. B **53**, 12133 (1996).

[129] H. J. Schulz, "Phases of two coupled luttinger liquids," Phys. Rev. B **53**, R2959 (1996).

[130] S. R. White, I. Affleck, and D. J. Scalapino, "Friedel oscillations and charge density waves in chains and ladders," Phys. Rev. B **65**, 165122 (2002).

[131] E. Arrigoni, "Spin and charge excitations in a three-legs fermionic ladder: a renormalization-group study," Physics Letters A **215**, 91 (1996).

[132] T. Kimura, K. Kuroki, and H. Aoki, "Correlation functions in the three-chain hubbard ladder," Phys. Rev. B **54**, R9608 (1996).

[133] H.-H. Lin, L. Balents, and M. P. A. Fisher, "n-chain hubbard model in weak coupling," Phys. Rev. B **56**, 6569 (1997).

[134] S. R. White, "Density matrix formulation for quantum renormalization groups," Phys. Rev. Lett. **69**, 2863 (1992).

[135] S. R. White, "Density-matrix algorithms for quantum renormalization groups," Phys. Rev. B **48**, 10345 (1993).

[136] A. J. Daley, C. Kollath, U. Schollwöck, and G. Vidal, "Time-dependent density-matrix renormalization-group using adaptive effective hilbert spaces," Journal of Statistical Mechanics: Theory and Experiment **2004**, P04005 (2004).

[137] S. R. White and A. E. Feiguin, "Real-time evolution using the density matrix renormalization group," Phys. Rev. Lett. **93**, 076401 (2004).

[138] N. Schuch, M. M. Wolf, F. Verstraete, and J. I. Cirac, "Entropy scaling and simulability by matrix product states," Phys. Rev. Lett. **100**, 030504 (2008).

[139] P. Jurcevic, B. P. Lanyon, P. Hauke, C. Hempel, P. Zoller, R. Blatt, and C. F. Roos, "Quasiparticle engineering and entanglement propagation in a quantum many-body system," Nature **511**, 202 (2014).

[140] P. Richerme, Z.-X. Gong, A. Lee, C. Senko, J. Smith, M. Foss-Feig, S. Michalakis, A. V. Gorshkov, and C. Monroe, "Non-local propagation of correlations in quantum systems with long-range interactions," Nature **511**, 198 (2014).

[141] Z.-X. Gong and L.-M. Duan, "Prethermalization and dynamic phase transition in an isolated trapped ion spin chain," New Journal of Physics **15**, 113051 (2013).

[142] P. Hauke and L. Tagliacozzo, "Spread of correlations in long-range interacting quantum systems," Phys. Rev. Lett. **111**, 207202 (2013).

[143] L. Cevolani, J. Despres, G. Carleo, L. Tagliacozzo, and L. Sanchez-Palencia, "Universal scaling laws for correlation spreading in quantum systems with short- and long-range interactions," Phys. Rev. B **98**, 024302 (2018).

[144] J. Schachenmayer, B. P. Lanyon, C. F. Roos, and A. J. Daley, "Entanglement growth in quench dynamics with variable range interactions," Phys. Rev. X **3**, 031015 (2013).

[145] A. S. Buyskikh, M. Fagotti, J. Schachenmayer, F. Essler, and A. J. Daley, "Entanglement growth and correlation spreading with variable-range interactions in spin and fermionic tunneling models," Phys. Rev. A **93**, 053620 (2016).

[146] N. Schuch, M. M. Wolf, K. G. H. Vollbrecht, and J. I. Cirac, "On entropy growth and the hardness of simulating time evolution," New Journal of Physics **10**, 033032 (2008).

[147] M. A. Nielsen and I. L. Chuang, *Quantum Computation and Quantum Information: 10th Anniversary Edition* (Cambridge University Press, 2010).

[148] G. Vidal and R. F. Werner, "Computable measure of entanglement," Phys. Rev. A **65**, 032314 (2002).

[149] J. Eisert, M. Cramer, and M. B. Plenio, "Colloquium: Area laws for the entanglement entropy," Rev. Mod. Phys. **82**, 277 (2010).

[150] S. K. Foong and S. Kanno, "Proof of page's conjecture on the average entropy of a subsystem," Phys. Rev. Lett. **72**, 1148 (1994).

[151] U. Schollwöck, "The density-matrix renormalization group," Rev. Mod. Phys. **77**, 259 (2005).

[152] K. A. Hallberg, "New trends in density matrix renormalization," Advances in Physics **55**, 477 (2006).

[153] P. Calabrese and J. Cardy, "Evolution of entanglement entropy in one-dimensional systems," Journal of Statistical Mechanics: Theory and Experiment **2005**, P04010 (2005).

[154] N. Schuch, M. M. Wolf, F. Verstraete, and J. I. Cirac, "Simulation of quantum many-body systems with strings of operators and monte carlo tensor contractions," Phys. Rev. Lett. **100**, 040501 (2008).

[155] E. H. Lieb and D. W. Robinson, "The finite group velocity of quantum spin systems," Communications in Mathematical Physics **28**, 251 (1972).

[156] M. Kliesch, C. Gogolin, and J. Eisert, *Lieb-Robinson Bounds and the Simulation of Time-Evolution of Local Observables in Lattice Systems* (Springer International Publishing, 2014), pp. 301–318.

[157] G. Vidal, "Efficient classical simulation of slightly entangled quantum computations," Phys. Rev. Lett. **91**, 147902 (2003).

[158] G. Vidal, "Efficient simulation of one-dimensional quantum many-body systems," Phys. Rev. Lett. **93**, 040502 (2004).

[159] J. J. García-Ripoll, "Time evolution of matrix product states," New Journal of Physics **8**, 305 (2006).

[160] J. Haegeman, C. Lubich, I. Oseledets, B. Vandereycken, and F. Verstraete, "Unifying time evolution and optimization with matrix product states," Phys. Rev. B **94**, 165116 (2016).

[161] C. W. Gardiner and M. J. Collett, "Input and output in damped quantum systems: Quantum stochastic differential equations and the master equation," Phys. Rev. A **31**, 3761 (1985).

[162] C. W. Gardiner and M. J. Collett, in *International Quantum Electronics Conference* (Optical Society of America, 1984).

[163] C. W. Gardiner, A. S. Parkins, and P. Zoller, "Wave-function quantum stochastic differential equations and quantum-jump simulation methods," Phys. Rev. A **46**, 4363 (1992).

[164] H. M. Wiseman, "Quantum theory of continuous feedback," Phys. Rev. A **49**, 2133 (1994).

[165] H. M. Wiseman and G. J. Milburn, "Interpretation of quantum jump and diffusion processes illustrated on the bloch sphere," Phys. Rev. A **47**, 1652 (1993).

[166] H. M. Wiseman and G. J. Milburn, "Quantum theory of field-quadrature measurements," Phys. Rev. A **47**, 642 (1993).

[167] A. Barchielli, "Measurement theory and stochastic differential equations in quantum mechanics," Phys. Rev. A **34**, 1642 (1986).

[168] A. M. Smith and C. W. Gardiner, "Three-level atom laser model with results and applications," Phys. Rev. A **41**, 2730 (1990).

[169] P. Zoller, M. Marte, and D. F. Walls, "Quantum jumps in atomic systems," Phys. Rev. A **35**, 198 (1987).

[170] A. S. Parkins, C. W. Gardiner, and M. L. Stéyn-Ross, "The effect of dissipation on coherent quantum tunnelling in a double-well system: Two-level model using an adjoint equation approach," Zeitschrift für Physik B Condensed Matter **83**, 413 (1991).

[171] A. G. Redfield, "On the theory of relaxation processes," IBM Journal of Research and Development **1**, 19 (1957).

[172] A. G. Redfield and J. S. Waugh, *The Theory of Relaxation Processes* (Academic Press, 1965), vol. 1, pp. 1–32.

[173] I. de Vega and D. Alonso, "Dynamics of non-markovian open quantum systems," Rev. Mod. Phys. **89**, 015001 (2017).

[174] C. Maier, T. Brydges, P. Jurcevic, N. Trautmann, C. Hempel, B. P. Lanyon, P. Hauke, R. Blatt, and C. F. Roos, "Environment-assisted quantum transport in a 10-qubit network," Phys. Rev. Lett. **122**, 050501 (2019).

[175] S. F. Huelga, A. Rivas, and M. B. Plenio, "Non-markovianity-assisted steady state entanglement," Phys. Rev. Lett. **108**, 160402 (2012).

[176] V. Gorini, A. Kossakowski, and E. C. G. Sudarshan, "Completely positive dynamical semigroups of n-level systems," Journal of Mathematical Physics **17**, 821 (1976).

[177] G. Lindblad, "On the generators of quantum dynamical semigroups," Comm. Math. Phys. **48**, 119 (1976).

[178] C. Cohen-Tannoudji, J. Dupont-Roc, and G. Grynberg, *Atom-Photon Interactions: Basic Processes and Applications* (Wiley Interscience, 992).

[179] H.-P. Breuer, B. Kappler, and F. Petruccione, "Stochastic wave-function method for non-markovian quantum master equations," Phys. Rev. A **59**, 1633 (1999).

[180] N. G. Van Kampen, "A cumulant expansion for stochastic linear differential equations. i," Physica **74**, 215 (1974).

[181] H.-P. Breuer and F. Petruccione, *The Theory of Open Quantum Systems* (Oxford University Press, 2002).

[182] K. Blum, *Density Matrix Theory and Applications* (Plenum Press, New York, London, 1981).

[183] M. J. Collett, R. Loudon, and C. W. Gardiner, "Quantum theory of optical homodyne and heterodyne detection," Journal of Modern Optics **34**, 881 (1987).

[184] U. Weiss, *Quantum Dissipative Systems* (World Scientific, 1993).

[185] P. Ribeiro and V. R. Vieira, "Non-markovian effects in electronic and spin transport," Phys. Rev. B **92**, 100302 (2015).

[186] D. Suess, A. Eisfeld, and W. T. Strunz, "Hierarchy of stochastic pure states for open quantum system dynamics," Phys. Rev. Lett. **113**, 150403 (2014).

[187] R. Hartmann and W. T. Strunz, "Exact open quantum system dynamics using the hierarchy of pure states (hops)," Journal of Chemical Theory and Computation **13**, 5834 (2017).

[188] D. Suess, W. T. Strunz, and A. Eisfeld, "Hierarchical equations for open system dynamics in fermionic and bosonic environments," Journal of Statistical Physics **159**, 1408 (2015).

[189] L. Diósi and W. T. Strunz, "The non-markovian stochastic schrödinger equation for open systems," Physics Letters A **235**, 569 (1997).

[190] L. Diósi, N. Gisin, and W. T. Strunz, "Non-markovian quantum state diffusion," Phys. Rev. A **58**, 1699 (1998).

[191] F. Damanet, A. J. Daley, and J. Keeling, "Atom-only descriptions of the driven-dissipative dicke model," Phys. Rev. A **99**, 033845 (2019).

[192] F. Dimer, B. Estienne, A. S. Parkins, and H. J. Carmichael, "Proposed realization of the dicke-model quantum phase transition in an optical cavity qed system," Phys. Rev. A **75**, 013804 (2007).

[193] K. Baumann, C. Guerlin, F. Brennecke, and T. Esslinger, "Dicke quantum phase transition with a superfluid gas in an optical cavity," Nature **464**, 1301 (2010).

[194] F. Arute, K. Arya, R. Babbush, D. Bacon, J. C. Bardin, R. Barends, R. Biswas, S. Boixo, F. G. S. L. Brandao, D. A. Buell, et al., "Quantum supremacy using a programmable superconducting processor," Nature **574**, 505 (2019).

[195] C. S. Chiu, G. Ji, A. Mazurenko, D. Greif, and M. Greiner, "Quantum state engineering of a hubbard system with ultracold fermions," Phys. Rev. Lett. **120**, 243201 (2018).

[196] P. Dallaire-DeStechły, M., J. Gonthier, N. Bashige, J. Romero, and Y. Cao, "An application benchmark for fermionic quantum simulations," arXiv:2003.01862 (2020).

[197] C. Cade, L. Mineh, A. Montanaro, and S. Stanisic, "Strategies for solving the fermi-hubbard model on near-term quantum computers," arXiv:1912.06007 (2020).

[198] J. P. F. LeBlanc, A. E. Antipov, F. Becca, I. W. Bulik, G. K.-L. Chan, C.-M. Chung, Y. Deng, M. Ferrero, T. M. Henderson, C. A. Jiménez-Hoyos, et al.

(Simons Collaboration on the Many-Electron Problem), "Solutions of the two-dimensional hubbard model: Benchmarks and results from a wide range of numerical algorithms," Phys. Rev. X **5**, 041041 (2015).

[199] D. Poulin, M. B. Hastings, D. Wecker, N. Wiebe, A. C. Doberty, and M. Troyer, "The trotter step size required for accurate quantum simulation of quantum chemistry," Quantum Inf. Comput. **15**, 361 (2015).

[200] A. M. Childs, Y. Su, M. C. Tran, N. Wiebe, and S. Zhu, "A theory of trotter error," arXiv:1912.08854 (2019).

[201] A. M. Childs, D. Maslov, Y. Nam, N. J. Ross, and Y. Su, "Toward the first quantum simulation with quantum speedup," Proceedings of the National Academy of Sciences **115**, 9456 (2018).

[202] P. Poggi, N. Lysne, K. Kuper, I. Deutsch, and P. Jessen, "Quantifying the sensitivity to errors in analog quantum simulation," arXiv:2007.01901 (2020).

[203] L. Tarruell and L. Sanchez-Palencia, "Quantum simulation of the hubbard model with ultracold fermions in optical lattices," Comptes Rendus Physique **19**, 365 (2018).

[204] D. Porras and J. I. Cirac, "Effective quantum spin systems with trapped ions," Phys. Rev. Lett. **92**, 207901 (2004).

[205] T. Graß and M. Lewenstein, "Trapped-ion quantum simulation of tunable-range heisenberg chains," EPJ Quantum Technology **1**, 8 (2014).

[206] S. Paeckel, T. Köhler, A. Swoboda, S. R. Manmana, U. Schollwöck, and C. Hubig, "Time-evolution methods for matrix-product states," Annals of Physics **411**, 167998 (2019).

[207] D. C. McKay and B. DeMarco, "Cooling in strongly correlated optical lattices: prospects and challenges," Reports on Progress in Physics **74**, 054401 (2011).

[208] H. Pichler, A. J. Daley, and P. Zoller, "Nonequilibrium dynamics of bosonic atoms in optical lattices: Decoherence of many-body states due to spontaneous emission," Phys. Rev. A **82**, 063605 (2010).

[209] F. Gerbier and Y. Castin, "Heating rates for an atom in a far-detuned optical lattice," Phys. Rev. A **82**, 013615 (2010).

[210] H. Pichler, J. Schachenmayer, J. Simon, P. Zoller, and A. J. Daley, "Noise- and disorder-resilient optical lattices," Phys. Rev. A **86**, 051605 (2012).

[211] H. Pichler, J. Schachenmayer, A. J. Daley, and P. Zoller, "Heating dynamics of bosonic atoms in a noisy optical lattice," Phys. Rev. A **87**, 033606 (2013).

[212] A. Heinz, A. J. Park, N. Šantić, J. Trautmann, S. G. Porsev, M. S. Safronova, I. Bloch, and S. Blatt, "State-dependent optical lattices for the strontium optical qubit," Phys. Rev. Lett. **124**, 203201 (2020).

[213] S. Flannigan, N. Pearson, A. Buyskikh, G. Low, I. Bloch, P. Zoller, M. Troyer, and A. J. Daley, "The practical quantum advantage point for analogue and digital quantum simulators," In preparation (????).

[214] M. J. Mark, S. Flannigan, F. Meinert, J. P. D'Incao, A. J. Daley, and H.-C. Nägerl, "Interplay between coherent and dissipative dynamics of bosonic doublons in an optical lattice," Phys. Rev. Research **2**, 043050 (2020).

[215] T. Kraemer, M. Mark, P. Waldburger, J. G. Danzl, C. Chin, B. Engeser, A. D. Lange, K. Pilch, A. Jaakkola, H. C. Nägerl, et al., "Evidence for efimov quantum states in an ultracold gas of caesium atoms," Nature **440**, 315 (2006).

[216] B. Schmidt, M. Bortz, S. Eggert, M. Fleischhauer, and D. Petrosyan, "Attractively bound pairs of atoms in the bose-hubbard model and antiferromagnetism," Phys. Rev. A **79**, 063634 (2009).

[217] D. Petrosyan, B. Schmidt, J. R. Anglin, and M. Fleischhauer, "Quantum liquid of repulsively bound pairs of particles in a lattice," Phys. Rev. A **76**, 033606 (2007).

[218] Y.-C. Chen, K.-K. Ng, and M.-F. Yang, "Quantum phase transitions in the attractive extended bose-hubbard model with a three-body constraint," Phys. Rev. B **84**, 092503 (2011).

[219] A. Privitera, I. Titvinidze, S.-Y. Chang, S. Diehl, A. J. Daley, and W. Hofstetter, "Loss-induced phase separation and pairing for three-species atomic lattice fermions," Phys. Rev. A **84**, 021601 (2011).

[220] Y.-W. Lee and M.-F. Yang, "Superfluid-insulator transitions in attractive bose-hubbard model with three-body constraint," Phys. Rev. A **81**, 061604 (2010).

[221] L. Bonnes and S. Wessel, "Pair superfluidity of three-body constrained bosons in two dimensions," Phys. Rev. Lett. **106**, 185302 (2011).

[222] A. Kantian, M. Dalmonte, S. Diehl, W. Hofstetter, P. Zoller, and A. J. Daley, "Atomic color superfluid via three-body loss," Phys. Rev. Lett. **103**, 240401 (2009).

[223] B. Capogrosso-Sansone, S. Wessel, H. P. Büchler, P. Zoller, and G. Pupillo, "Phase diagram of one-dimensional hard-core bosons with three-body interactions," Phys. Rev. B **79**, 020503 (2009).

[224] M. Lewenstein, A. Sanpera, and V. Ahufinger, *Ultracold Atoms in Optical Lattices: Simulating quantum many-body systems* (Oxford Scholarship Online, 2012).

[225] M. Müller, S. Diehl, G. Pupillo, and P. Zoller, "Engineered open systems and quantum simulations with atoms and ions," Advances in Atomic, Molecular, and Optical Physics **61**, 1 (2012).

[226] N. Syassen, D. M. Bauer, M. Lettner, T. Volz, D. Dietze, J. J. García-Ripoll, J. I. Cirac, G. Rempe, and S. Dürr, "Strong dissipation inhibits losses and induces correlations in cold molecular gases," Science **320**, 1329 (2008).

[227] B. Yan, S. A. Moses, B. Gadway, J. P. Covey, K. R. A. Hazzard, A. M. Rey, D. S. Jin, and J. Ye, "Observation of dipolar spin-exchange interactions with lattice-confined polar molecules," Nature **501**, 521 (2013).

[228] B. Zhu, B. Gadway, M. Foss-Feig, J. Schachenmayer, M. L. Wall, K. R. A. Hazzard, B. Yan, S. A. Moses, J. P. Covey, D. S. Jin, et al., "Suppressing the loss of ultracold molecules via the continuous quantum zeno effect," Phys. Rev. Lett. **112**, 070404 (2014).

[229] R. Schützhold and G. Gnanapragasam, "Quantum zeno suppression of three-body losses in bose-einstein condensates," Phys. Rev. A **82**, 022120 (2010).

[230] W. M. Itano, D. J. Heinzen, J. J. Bollinger, and D. J. Wineland, "Quantum zeno effect," Phys. Rev. A **41**, 2295 (1990).

[231] M. J. Gagen, H. M. Wiseman, and G. J. Milburn, "Continuous position measurements and the quantum zeno effect," Phys. Rev. A **48**, 132 (1993).

[232] A. J. Daley, J. M. Taylor, S. Diehl, M. Baranov, and P. Zoller, "Atomic three-body loss as a dynamical three-body interaction," Phys. Rev. Lett. **102**, 040402 (2009).

[233] M. Roncaglia, M. Rizzi, and J. I. Cirac, "Pfaffian state generation by strong three-body dissipation," Phys. Rev. Lett. **104**, 096803 (2010).

[234] S. Diehl, M. Baranov, A. J. Daley, and P. Zoller, "Quantum field theory for the three-body constrained lattice bose gas. i. formal developments," Phys. Rev. B **82**, 064509 (2010).

[235] S. Diehl, M. Baranov, A. J. Daley, and P. Zoller, "Quantum field theory for the three-body constrained lattice bose gas. ii. application to the many-body problem," Phys. Rev. B **82**, 064510 (2010).

[236] B. Kraus, H. P. Büchler, S. Diehl, A. Kantian, A. Micheli, and P. Zoller, "Preparation of entangled states by quantum markov processes," Phys. Rev. A **78**, 042307 (2008).

[237] O. Jürgensen, F. Meinert, M. J. Mark, H.-C. Nägerl, and D.-S. Lühmann, "Observation of density-induced tunneling," Phys. Rev. Lett. **113**, 193003 (2014).

[238] K. Winkler, G. Thalhammer, F. Lang, R. Grimm, J. Hecker Denschlag, A. J. Daley, A. Kantian, H. P. Büchler, and P. Zoller, "Repulsively bound atom pairs in an optical lattice," Nature **441**, 853 (2006).

[239] N. Strohmaier, D. Greif, R. Jördens, L. Tarruell, H. Moritz, T. Esslinger, R. Sensarma, D. Pekker, E. Altman, and E. Demler, "Observation of elastic doublon decay in the fermi-hubbard model," Phys. Rev. Lett. **104**, 080401 (2010).

[240] J. P. D'Incao, "Few-body physics in resonantly interacting ultracold quantum gases," Journal of Physics B: Atomic, Molecular and Optical Physics **51**, 043001 (2018).

[241] E. Braaten and H.-W. Hammer, "Universality in few-body systems with large scattering length," Phys. Rep. **428**, 259 (2006).

[242] L.-M. Duan, E. Demler, and M. D. Lukin, "Controlling spin exchange interactions of ultracold atoms in optical lattices," Phys. Rev. Lett. **91**, 090402 (2003).

[243] A. Goban, R. B. Hutson, G. E. Marti, S. L. Campbell, M. A. Perlin, P. S. Julienne, J. P. D'Incao, A. M. Rey, and J. Ye, "Emergence of multi-body interactions in few-atom sites of a fermionic lattice clock," Nature **563**, 369 (2018).

[244] J. Wang, J. P. D'Incao, and C. H. Greene, "Numerical study of three-body recombination for systems with many bound states," Phys. Rev. A **84**, 052721 (2011).

[245] V. Efimov, "Energy levels of three resonantly interacting particles," Nucl. Phys. A **210**, 157 (1973).

[246] V. Efimov, "Energy levels arising from resonant two-body forces in a three-body system," Physics Letters B **33**, 563 (1970).

[247] P. F. Bedaque, H.-W. Hammer, and U. van Kolck, "Renormalization of the three-body system with short-range interactions," Phys. Rev. Lett. **82**, 463 (1999).

[248] P. Naidon and S. Endo, "Efimov physics: a review," Reports on Progress in Physics **80**, 056001 (2017).

[249] J. P. D'Incao, H. Suno, and B. D. Esry, "Limits on universality in ultracold three-boson recombination," Phys. Rev. Lett **93**, 123201 (2004).

[250] G. Thalhammer, K. Winkler, F. Lang, S. Schmid, R. Grimm, and J. H. Denschlag, "Long-lived feshbach molecules in a three-dimensional optical lattice," Phys. Rev. Lett. **96**, 050402 (2006).

[251] A. Bansil, H. Lin, and T. Das, "Colloquium: Topological band theory," Rev. Mod. Phys. **88**, 021004 (2016).

[252] M. Z. Hasan and C. L. Kane, "Colloquium: Topological insulators," Rev. Mod. Phys. **82**, 3045 (2010).

[253] M. Aidelsburger, M. Lohse, C. Schweizer, M. Atala, J. T. Barreiro, S. Nascimbène, N. R. Cooper, I. Bloch, and N. Goldman, "Measuring the chern number of hofstadter bands with ultracold bosonic atoms," Nature Physics **11**, 162 (2015).

[254] L. Asteria, D. T. Tran, T. Ozawa, M. Tarnowski, B. S. Rem, N. Fläschner, K. Sengstock, N. Goldman, and C. Weitenberg, "Measuring quantized circular dichroism in ultracold topological matter," Nature Physics **15**, 449 (2019).

[255] M. Tarnowski, F. N. Ünal, N. Fläschner, B. S. Rem, A. Eckardt, K. Sengstock, and C. Weitenberg, "Measuring topology from dynamics by obtaining the chern number from a linking number," Nature Communications **10**, 1728 (2019).

[256] N. R. Cooper and J. Dalibard, "Reaching fractional quantum hall states with optical flux lattices," Phys. Rev. Lett. **110**, 185301 (2013).

[257] A. G. Grushin, A. Gómez-León, and T. Neupert, "Floquet fractional chern insulators," Phys. Rev. Lett. **112**, 156801 (2014).

[258] E. Anisimovas, G. Žlabys, B. M. Anderson, G. Juzeliūnas, and A. Eckardt, "Role of real-space micromotion for bosonic and fermionic floquet fractional chern insulators," Phys. Rev. B **91**, 245135 (2015).

[259] D. Leykam, A. Andreanov, and S. Flach, "Artificial flat band systems: from lattice models to experiments artificial flat band systems: from lattice models to experiments artificial flat band systems: from lattice models to experiments," arXiv:1801.09378v3 (2018).

[260] Z. Liu, F. Liu, and Y.-S. Wu, "Exotic electronic states in the world of flat bands: From theory to material," Chinese Physics B **23**, 077308 (2014).

[261] J. Vidal, R. Mosseri, and B. Douçot, "Aharonov-bohm cages in two-dimensional structures," Phys. Rev. Lett. **81**, 5888 (1998).

[262] S. Mukherjee and R. R. Thomson, "Observation of localized flat-band modes in a quasi-one-dimensional photonic rhombic lattice," Opt. Lett. **40**, 5443 (2015).

[263] S. Takayoshi, H. Katsura, N. Watanabe, and H. Aoki, "Phase diagram and pair tomonaga-luttinger liquid in a bose-hubbard model with flat bands," Phys. Rev. A **88**, 063613 (2013).

[264] M. Tovmasyan, E. P. L. van Nieuwenburg, and S. D. Huber, "Geometry-induced pair condensation," Phys. Rev. B **88**, 220510 (2013).

[265] G. Möller and N. R. Cooper, "Correlated phases of bosons in the flat lowest band of the dice lattice," Phys. Rev. Lett. **108**, 045306 (2012).

[266] S. D. Huber and E. Altman, "Bose condensation in flat bands," Phys. Rev. B **82**, 184502 (2010).

[267] K.-E. Huhtinen, M. Tylutki, P. Kumar, T. I. Vanhala, S. Peotta, and P. Törmä, "Spin-imbalanced pairing and fermi surface deformation in flat bands," Phys. Rev. B **97**, 214503 (2018).

[268] M. Tovmasyan, S. Peotta, L. Liang, P. Törmä, and S. D. Huber, "Preformed pairs in flat bloch bands," Phys. Rev. B **98**, 134513 (2018).

[269] P. Törmä, L. Liang, and S. Peotta, "Quantum metric and effective mass of a two-body bound state in a flat band," Phys. Rev. B **98**, 220511 (2018).

[270] J. Jünemann, A. Piga, S.-J. Ran, M. Lewenstein, M. Rizzi, and A. Bermudez, "Exploring interacting topological insulators with ultracold atoms: The synthetic creutz-hubbard model," Phys. Rev. X **7**, 031057 (2017).

[271] A. Deuchert, K. Sakmann, A. I. Streltsov, O. E. Alon, and L. S. Cederbaum, "Dynamics and symmetries of a repulsively bound atom pair in an infinite optical lattice," Phys. Rev. A **86**, 013618 (2012).

[272] L. Lin, Y. Ke, and C. Lee, "Interaction-induced topological bound states and thouless pumping in a one-dimensional optical lattice," Phys. Rev. A **101**, 023620 (2020).

[273] Y. Ke, X. Qin, Y. S. Kivshar, and C. Lee, "Multiparticle wannier states and thouless pumping of interacting bosons," Phys. Rev. A **95**, 063630 (2017).

[274] X. Qin, F. Mei, Y. Ke, L. Zhang, and C. Lee, "Topological magnon bound states in periodically modulated heisenberg xxz chains," Phys. Rev. B **96**, 195134 (2017).

[275] X. Qin, F. Mei, Y. Ke, L. Zhang, and C. Lee, "Topological invariant and cotranslational symmetry in strongly interacting multi-magnon systems," New Journal of Physics **20**, 013003 (2018).

[276] M. Di Liberto, A. Recati, I. Carusotto, and C. Menotti, "Two-body physics in the su-schrieffer-heeger model," Phys. Rev. A **94**, 062704 (2016).

[277] A. M. Marques and R. G. Dias, "Topological bound states in interacting su–schrieffer–heeger rings," Journal of Physics: Condensed Matter **30**, 305601 (2018).

[278] V. W. Scarola and S. Das Sarma, "Quantum phases of the extended bose-hubbard hamiltonian: Possibility of a supersolid state of cold atoms in optical lattices," Phys. Rev. Lett. **95**, 033003 (2005).

[279] V. W. Scarola, E. Demler, and S. Das Sarma, "Searching for a supersolid in cold-atom optical lattices," Phys. Rev. A **73**, 051601 (2006).

[280] M. Iskin, "Route to supersolidity for the extended bose-hubbard model," Phys. Rev. A **83**, 051606 (2011).

[281] Y.-M. Wang and J.-Q. Liang, "Quantum phases of bose gases on a lattice with pair-tunneling," Chinese Physics B **21**, 060305 (2012).

[282] L. Mathey, I. Danshita, and C. W. Clark, "Creating a supersolid in one-dimensional bose mixtures," Phys. Rev. A **79**, 011602 (2009).

[283] I. Danshita and C. A. R. Sá de Melo, "Stability of superfluid and supersolid phases of dipolar bosons in optical lattices," Phys. Rev. Lett. **103**, 225301 (2009).

[284] S. Diehl, M. Baranov, A. J. Daley, and P. Zoller, "Observability of quantum criticality and a continuous supersolid in atomic gases," Phys. Rev. Lett. **104**, 165301 (2010).

[285] C. Trefzger, C. Menotti, and M. Lewenstein, "Pair-supersolid phase in a bilayer system of dipolar lattice bosons," Phys. Rev. Lett. **103**, 035304 (2009).

[286] A. Hu, L. Mathey, I. Danshita, E. Tiesinga, C. J. Williams, and C. W. Clark, "Counterflow and paired superfluidity in one-dimensional bose mixtures in optical lattices," Phys. Rev. A **80**, 023619 (2009).

[287] P. Richerme, C. Senko, J. Smith, A. Lee, S. Korenblit, and C. Monroe, "Experimental performance of a quantum simulator: Optimizing adiabatic evolution and identifying many-body ground states," Phys. Rev. A **88**, 012334 (2013).

[288] S. Gholizadeh, M. Yahyavi, and B. Hetényi, "Extended creutz ladder with spin-orbit coupling: A one-dimensional analog of the kane-mele model," EPL (Europhysics Letters) **122**, 27001 (2018).

[289] N. Sun and L.-K. Lim, "Quantum charge pumps with topological phases in a creutz ladder," Phys. Rev. B **96**, 035139 (2017).

[290] S. Mugel, A. Celi, P. Massignan, J. K. Asbóth, M. Lewenstein, and C. Lobo, "Topological bound states of a quantum walk with cold atoms," Phys. Rev. A **94**, 023631 (2016).

[291] J. H. Kang, J. H. Han, and Y. Shin, "Creutz ladder in a resonantly shaken 1d optical lattice," New Journal of Physics **22**, 013023 (2020).

[292] G. Pelegrí, A. M. Marques, V. Ahufinger, J. Mompart, and R. G. Dias,

"Interaction-induced topological properties of two bosons in flat-band systems," arXiv:2005.10810 (2020).

[293] J. Haegeman, B. Pirvu, D. J. Weir, J. I. Cirac, T. J. Osborne, H. Verschelde, and F. Verstraete, "Variational matrix product ansatz for dispersion relations," Phys. Rev. B **85**, 100408 (2012).

[294] L. Vanderstraeten, F. Verstraete, and J. Haegeman, "Scattering particles in quantum spin chains," Phys. Rev. B **92**, 125136 (2015).

[295] J. Haegeman, T. J. Osborne, and F. Verstraete, "Post-matrix product state methods: To tangent space and beyond," Phys. Rev. B **88**, 075133 (2013).

[296] V. Zauner, D. Draxler, L. Vanderstraeten, M. Degroote, J. Haegeman, M. M. Rams, V. Stojevic, N. Schuch, and F. Verstraete, "Transfer matrices and excitations with matrix product states," New Journal of Physics **17**, 053002 (2015).

[297] S. Östlund and S. Rommer, "Thermodynamic limit of density matrix renormalization," Phys. Rev. Lett. **75**, 3537 (1995).

[298] S. Rommer and S. Östlund, "Class of ansatz wave functions for one-dimensional spin systems and their relation to the density matrix renormalization group," Phys. Rev. B **55**, 2164 (1997).

[299] J. Haegeman, S. Michalakis, B. Nachtergaele, T. J. Osborne, N. Schuch, and F. Verstraete, "Elementary excitations in gapped quantum spin systems," Phys. Rev. Lett. **111**, 080401 (2013).

[300] L. Vanderstraeten, J. Haegeman, F. Verstraete, and D. Poilblanc, "Quasiparticle interactions in frustrated heisenberg chains," Phys. Rev. B **93**, 235108 (2016).

[301] L. Vanderstraeten, M. Van Damme, H. P. Büchler, and F. Verstraete, "Quasiparticles in quantum spin chains with long-range interactions," Phys. Rev. Lett. **121**, 090603 (2018).

[302] B. Pirvu, J. Haegeman, and F. Verstraete, "Matrix product state based algorithm for determining dispersion relations of quantum spin chains with periodic boundary conditions," Phys. Rev. B **85**, 035130 (2012).

[303] F. Keim and G. S. Uhrig, "Effective one-dimensional models from matrix product states," The European Physical Journal B **88**, 154 (2015).

[304] L. Vanderstraeten, J. Haegeman, and F. Verstraete, "Simulating excitation spectra with projected entangled-pair states," Phys. Rev. B **99**, 165121 (2019).

[305] L. Fu and C. L. Kane, "Topological insulators with inversion symmetry," Phys. Rev. B **76**, 045302 (2007).

[306] S. Bravyi, D. P. DiVincenzo, and D. Loss, "Schrieffer–wolff transformation for quantum many-body systems," Annals of Physics **326**, 2793 (2011).

[307] V. Zauner-Stauber, L. Vanderstraeten, M. T. Fishman, F. Verstraete, and J. Haegeman, "Variational optimization algorithms for uniform matrix product states," Phys. Rev. B **97**, 045145 (2018).

[308] T. D. Kühner and H. Monien, "Phases of the one-dimensional bose-hubbard model," Phys. Rev. B **58**, R14741 (1998).

[309] M. Buser, C. Hubig, U. Schollwöck, L. Tarruell, and F. Heidrich-Meisner, "Interacting bosonic flux ladders with a synthetic dimension: Ground-state phases and quantum quench dynamics," arXiv:2006.13862 (2020).

[310] A. J. Daley and J. Simon, "Effective three-body interactions via photon-assisted tunneling in an optical lattice," Phys. Rev. A **89**, 053619 (2014).

[311] A. S. Buyskikh, L. Tagliacozzo, D. Schuricht, C. A. Hooley, D. Pekker, and A. J. Daley, "Resonant two-site tunneling dynamics of bosons in a tilted optical superlattice," Phys. Rev. A **100**, 023627 (2019).

[312] F. Verstraete, J. J. García-Ripoll, and J. I. Cirac, "Matrix product density operators: Simulation of finite-temperature and dissipative systems," Phys. Rev. Lett. **93**, 207204 (2004).

[313] P. T. Brown, E. Guardado-Sanchez, B. M. Spar, E. W. Huang, T. P. Devereaux, and W. S. Bakr, "Angle-resolved photoemission spectroscopy of a fermi–hubbard system," Nature Physics **16**, 26 (2020).

[314] B. Lv, T. Qian, and H. Ding, "Angle-resolved photoemission spectroscopy and its application to topological materials," Nature Reviews Physics **1**, 609 (2019).

[315] H. N. Phien, G. Vidal, and I. P. McCulloch, "Infinite boundary conditions for matrix product state calculations," Phys. Rev. B **86**, 245107 (2012).

[316] H. N. Phien, G. Vidal, and I. P. McCulloch, "Dynamical windows for real-time evolution with matrix product states," Phys. Rev. B **88**, 035103 (2013).

[317] L. Landau, "Theory of the superfluidity of helium," J. Phys. U.S.S.R. **11**, 91 (1947).

[318] R. P. Feynman, "Atomic theory of the two-fluid model of liquid helium," Phys. Rev. **94**, 262 (1954).

[319] L. Chomaz, R. M. W. van Bijnen, D. Petter, G. Faraoni, S. Baier, J. H. Becher, M. J. Mark, F. Wächtler, L. Santos, and F. Ferlaino, "Observation of roton mode population in a dipolar quantum gas," Nature Physics **14**, 442 (2018).

[320] C. L. Kane and M. P. A. Fisher, "Transport in a one-channel luttinger liquid," Phys. Rev. Lett. **68**, 1220 (1992).

[321] C. L. Kane and M. P. A. Fisher, "Thermal transport in a luttinger liquid," Phys. Rev. Lett. **76**, 3192 (1996).

[322] A. Imambekov, T. L. Schmidt, and L. I. Glazman, "One-dimensional quantum liquids: Beyond the luttinger liquid paradigm," Rev. Mod. Phys. **84**, 1253 (2012).

[323] C. Cartwright, G. De Chiara, and M. Rizzi, "Rhombi-chain bose-hubbard model: Geometric frustration and interactions," Phys. Rev. B **98**, 184508 (2018).

[324] A. Julku, S. Peotta, T. I. Vanhala, D.-H. Kim, and P. Törmä, "Geometric origin of superfluidity in the lieb-lattice flat band," Phys. Rev. Lett. **117**, 045303 (2016).

[325] N. R. Cooper, J. Dalibard, and I. B. Spielman, "Topological bands for ultracold atoms," Rev. Mod. Phys. **91**, 015005 (2019).

[326] L. Barbiero, L. Santos, and N. Goldman, "Quenched dynamics and spin-charge separation in an interacting topological lattice," Phys. Rev. B **97**, 201115 (2018).

[327] L. Cardarelli, S. Greschner, and L. Santos, "Hidden order and symmetry protected topological states in quantum link ladders," Phys. Rev. Lett. **119**, 180402 (2017).

[328] D. Raventós, T. Graß, B. Juliá-Díaz, L. Santos, and M. Lewenstein, "Topological phases of lattice bosons with a dynamical gauge field," Phys. Rev. A **93**, 033605 (2016).

[329] S. Greschner, D. Huerga, G. Sun, D. Poletti, and L. Santos, "Density-dependent synthetic magnetism for ultracold atoms in optical lattices," Phys. Rev. B **92**, 115120 (2015).

[330] X. Deng and L. Santos, "Topological transitions of interacting bosons in one-dimensional bichromatic optical lattices," Phys. Rev. A **89**, 033632 (2014).

[331] M. Di Liberto, A. Hemmerich, and C. Morais Smith, "Topological varma superfluid in optical lattices," Phys. Rev. Lett. **117**, 163001 (2016).

[332] S. Flannigan and A. J. Daley, "Enhanced repulsively bound atom pairs in topological optical lattice ladders," **5**, 045017 (2020).

[333] A. Kantian, M. Dolfi, M. Troyer, and T. Giamarchi, "Understanding repulsively mediated superconductivity of correlated electrons via massively parallel density matrix renormalization group," Phys. Rev. B **100**, 075138 (2019).

[334] T. Mishra, S. Greschner, and L. Santos, "Frustration-induced supersolids in the absence of intersite interactions," Phys. Rev. B **92**, 195149 (2015).

[335] M. Tylutki and P. Törmä, "Spin-imbalanced fermi superfluidity in a hubbard model on a lieb lattice," Phys. Rev. B **98**, 094513 (2018).

[336] N. B. Kopnin, T. T. Heikkilä, and G. E. Volovik, "High-temperature surface superconductivity in topological flat-band systems," Phys. Rev. B **83**, 220503 (2011).

[337] T. T. Heikkilä, N. B. Kopnin, and G. E. Volovik, "Flat bands in topological media," JETP Letters **94**, 233 (2011).

[338] M. Tovmasyan, S. Peotta, P. Törmä, and S. D. Huber, "Effective theory and emergent SU(2) symmetry in the flat bands of attractive hubbard models," Phys. Rev. B **94**, 245149 (2016).

[339] R. Walters, G. Cotugno, T. H. Johnson, S. R. Clark, and D. Jaksch, "Ab initio derivation of hubbard models for cold atoms in optical lattices," Phys. Rev. A **87**, 043613 (2013).

[340] C. Chin, R. Grimm, P. Julienne, and E. Tiesinga, "Feshbach resonances in ultracold gases," Rev. Mod. Phys. **82**, 1225 (2010).

[341] J. Roos, J. I. Cirac, and M. C. Bañuls, "Markovianity of an emitter coupled to a structured spin-chain bath," Phys. Rev. A **101**, 042114 (2020).

[342] F. Cosco, M. Borrelli, J. J. Mendoza-Arenas, F. Plastina, D. Jaksch, and S. Maniscalco, "Bose-hubbard lattice as a controllable environment for open quantum systems," Phys. Rev. A **97**, 040101 (2018).

[343] A. Griessner, A. J. Daley, S. R. Clark, D. Jaksch, and P. Zoller, "Dissipative dynamics of atomic hubbard models coupled to a phonon bath: dark state cooling of atoms within a bloch band of an optical lattice," New Journal of Physics **9**, 44 (2007).

[344] T. Lausch, A. Widera, and M. Fleischhauer, "Prethermalization in the cooling dynamics of an impurity in a bose-einstein condensate," Phys. Rev. A **97**, 023621 (2018).

[345] A. Ishizaki and Y. Tanimura, "Quantum dynamics of system strongly coupled to low-temperature colored noise bath: Reduced hierarchy equations approach," Journal of the Physical Society of Japan **74**, 3131 (2005).

[346] A. Kato and Y. Tanimura, "Quantum heat current under non-perturbative and non-markovian conditions: Applications to heat machines," The Journal of Chemical Physics **145**, 224105 (2016).

[347] A. Strathearn, P. Kirton, D. Kilda, J. Keeling, and B. W. Lovett, "Efficient non-markovian quantum dynamics using time-evolving matrix product operators," Nature Communications **9**, 3322 (2018).

[348] D. Gribben, A. Strathearn, J. Iles-Smith, D. Kilda, A. Nazir, B. W. Lovett, and P. Kirton, "Exact quantum dynamics in structured environments," Phys. Rev. Research **2**, 013265 (2020).

[349] T. Holstein, "Studies of polaron motion: Part i. the molecular-crystal model," Annals of Physics **8**, 325 (1959).

[350] T. Holstein, "Studies of polaron motion: Part ii. the "small"polaron," Annals of Physics **281**, 725 (2000).

[351] E. Fradkin and J. E. Hirsch, "Phase diagram of one-dimensional electron-phonon systems. i. the su-schrieffer-heeger model," Phys. Rev. B **27**, 1680 (1983).

[352] J. E. Hirsch and E. Fradkin, "Phase diagram of one-dimensional electron-phonon systems. ii. the molecular-crystal model," Phys. Rev. B **27**, 4302 (1983).

[353] E. Jeckelmann, C. Zhang, and S. R. White, "Metal-insulator transition in the one-dimensional holstein model at half filling," Phys. Rev. B **60**, 7950 (1999).

[354] G. L. Goodvin, M. Berciu, and G. A. Sawatzky, "Green's function of the holstein polaron," Phys. Rev. B **74**, 245104 (2006).

[355] M. Hohenadler, "Charge and spin correlations of a peierls insulator after a quench," Phys. Rev. B **88**, 064303 (2013).

[356] H. Hashimoto and S. Ishihara, "Photoinduced charge-order melting dynamics in a one-dimensional interacting holstein model," Phys. Rev. B **96**, 035154 (2017).

[357] G. De Filippis, V. Cataudella, E. A. Nowadnick, T. P. Devereaux, A. S. Mishchenko, and N. Nagaosa, "Quantum dynamics of the hubbard-holstein model in equilibrium and nonequilibrium: Application to pump-probe phenomena," Phys. Rev. Lett. **109**, 176402 (2012).

[358] P. Werner and M. Eckstein, "Field-induced polaron formation in the holstein-hubbard model," EPL (Europhysics Letters) **109**, 37002 (2015).

[359] F. Hébert, B. Xiao, V. G. Rousseau, R. T. Scalettar, and G. G. Batrouni, "One-dimensional hubbard-holstein model with finite-range electron-phonon coupling," Phys. Rev. B **99**, 075108 (2019).

[360] M. Zoli, "Nonlocal electron-phonon correlations in a dispersive holstein model," Phys. Rev. B **71**, 184308 (2005).

[361] N. C. Costa, T. Blommel, W.-T. Chiu, G. Batrouni, and R. T. Scalettar, "Phonon dispersion and the competition between pairing and charge order," Phys. Rev. Lett. **120**, 187003 (2018).

[362] D. J. J. Marchand and M. Berciu, "Effect of dispersive optical phonons on the behavior of a holstein polaron," Phys. Rev. B **88**, 060301 (2013).

[363] C. E. Creffield, G. Sangiovanni, and M. Capone, "Phonon softening and dispersion in the 1d holstein model of spinless fermions," The European Physical Journal B - Condensed Matter and Complex Systems **44**, 175 (2005).

[364] J. Stolpp, J. Herbrych, F. Dorfner, E. Dagotto, and F. Heidrich-Meisner, "Charge-density-wave melting in the one-dimensional holstein model," Phys. Rev. B **101**, 035134 (2020).

[365] Á. Rivas, A. D. K Plato, S. F. Huelga, and M. B Plenio, "Markovian master equations: a critical study," New Journal of Physics **12**, 113032 (2010).

[366] A. Venegas-Gomez, A. S. Buyskikh, J. Schachenmayer, W. Ketterle, and A. J. Daley, "Dynamics of rotated spin states and magnetic ordering with two-component bosonic atoms in optical lattices," arXiv:1912.10028 (2020).

[367] A. Venegas-Gomez, J. Schachenmayer, A. S. Buyskikh, W. Ketterle, M. L. Chiofalo, and A. J. Daley, "Adiabatic preparation of entangled, magnetically ordered states with cold bosons in optical lattices," arXiv:2003.10905 (2020).

[368] G. Beni, P. Pincus, and J. Kanamori, "Low-temperature properties of the one-dimensional polaron band. i. extreme-band-narrowing regime," Phys. Rev. B **10**, 1896 (1974).

[369] Y. Takada and A. Chatterjee, "Possibility of a metallic phase in the charge-density-wave–spin-density-wave crossover region in the one-dimensional hubbard-holstein model at half filling," Phys. Rev. B **67**, 081102 (2003).

[370] R. T. Clay and R. P. Hardikar, "Intermediate phase of the one dimensional half-filled hubbard-holstein model," Phys. Rev. Lett. **95**, 096401 (2005).

[371] T. Hotta and Y. Takada, "Effect of electron correlation on phonons in a strongly coupled electron-phonon system," Phys. Rev. B **56**, 13916 (1997).

[372] G. Sangiovanni and O. Gunnarsson, "Electron-phonon interaction in strongly correlated electron systems: relevance of antiferromagnetic correlations.," Journal of Physics: Conference Series **108**, 012012 (2008).

[373] T. Ohgoe and M. Imada, "Competition among superconducting, antiferromagnetic, and charge orders with intervention by phase separation in the 2d holstein-hubbard model," Phys. Rev. Lett. **119**, 197001 (2017).

[374] S. Karakuzu, L. F. Tocchio, S. Sorella, and F. Becca, "Superconductivity, charge-density waves, antiferromagnetism, and phase separation in the hubbard-holstein model," Phys. Rev. B **96**, 205145 (2017).

[375] B. Xiao, N. Costa, E. Khatami, G. Batrouni, and R. Scalettar, "Charge density wave and superconductivity in the disordered holstein model," arXiv:1910.08703 (2019).

[376] R. G. Lena and A. J. Daley, "Dissipative dynamics and cooling rates of trapped impurity atoms immersed in a reservoir gas," Phys. Rev. A **101**, 033612 (2020).

[377] J. J. Hope, G. M. Moy, M. J. Collett, and C. M. Savage, "Steady-state quantum statistics of a non-markovian atom laser," Phys. Rev. A **61**, 023603 (2000).

[378] M. A. Cirone, G. D. Chiara, G. M. Palma, and A. Recati, "Collective decoherence of cold atoms coupled to a bose–einstein condensate," New Journal of Physics **11**, 103055 (2009).

[379] R. Scelle, T. Rentrop, A. Trautmann, T. Schuster, and M. K. Oberthaler, "Motional coherence of fermions immersed in a bose gas," Phys. Rev. Lett. **111**, 070401 (2013).

[380] D. Chen, C. Meldgin, and B. DeMarco, "Bath-induced band decay of a hubbard lattice gas," Phys. Rev. A **90**, 013602 (2014).

[381] A. J. Daley, P. O. Fedichev, and P. Zoller, "Single-atom cooling by superfluid immersion: A nondestructive method for qubits," Phys. Rev. A **69**, 022306 (2004).

[382] A. Griessner, A. J. Daley, S. R. Clark, D. Jaksch, and P. Zoller, "Dark-state cooling of atoms by superfluid immersion," Phys. Rev. Lett. **97**, 220403 (2006).

[383] C. J. Pethick and H. Smith, *Bose-Einstein Condensation in Dilute Gases* (Cambridge University Press, New York, 2008).

[384] J. Hubbard and B. H. Flowers, "Electron correlations in narrow energy bands," Proceedings of the Royal Society of London. Series A. Mathematical and Physical Sciences **276**, 238 (1963).

[385] T. Jones and S. Benjamin, "Quantum compilation and circuit optimisation via energy dissipation," arXiv:1811.03147 (2020).

[386] V. Giovannetti, S. Lloyd, and L. Maccone, "Advances in quantum metrology," Nature Photonics **5**, 222 (2011).

[387] R. Belyansky, P. Bienias, Y. Kharkov, A. Gorshkov, and B. Swingle, "A minimal model for fast scrambling," arXiv:2005.05362 (2020).

[388] M. Lebrat, P. Grišins, D. Husmann, S. Häusler, L. Corman, T. Giamarchi, J.-P. Brantut, and T. Esslinger, "Band and correlated insulators of cold fermions in a mesoscopic lattice," Phys. Rev. X **8**, 011053 (2018).

[389] F. Damanet, E. Mascarenhas, D. Pekker, and A. J. Daley, "Controlling quantum transport via dissipation engineering," Phys. Rev. Lett. **123**, 180402 (2019).

[390] F. Damanet, E. Mascarenhas, D. Pekker, and A. J. Daley, "Reservoir engineering of cooper-pair-assisted transport with cold atoms," New Journal of Physics **21**, 115001 (2019).